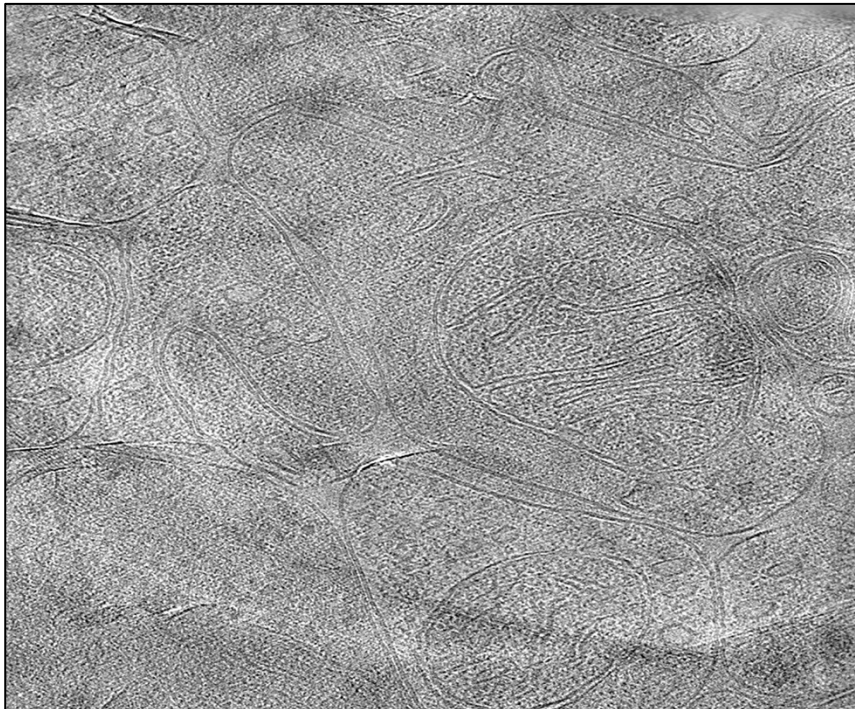


The in-tissue molecular architecture of synapses in memory circuits

Charlie Lovatt

Submitted in accordance with the requirements for the degree of “Doctor of Philosophy”.



The University of Leeds
Faculty of Biological Sciences
School of Biomedical Sciences

March 2024

Intellectual Property and Publication Statements

I confirm that the work submitted is my own, except where work which has formed part of jointly authored publications has been included. My contribution and the other authors to this work has been explicitly indicated below. I confirm that appropriate credit has been given within the thesis where reference has been made to the work of others.

Chapter 3 contains work from a jointly authored paper available as a preprint at: Peukes et al., 2021. bioRxiv. 2021.02.19.432002. Within the preprint, I performed sample preparation, high-pressure freezing, cryoFM and cryoET imaging, and reconstruction and analysis of tomograms from cryo-sections. Sample preparation, imaging and analysis of tissue homogenate was performed by co-authors, predominantly Julia Peukes and René Frank, which is not included within this thesis. All authors contributed to the writing of the manuscript. Conny Leistner and Martin Fuller collected and imaged the resin-embedded conventional EM synapses included in this thesis.

Chapter 4 contains stereotactic surgery and conditional fear training performed by Clara Ortega-de San Luis. Thomas O'Sullivan contributed towards cryo-sectioning of tissue. All other sample preparation, optimisation and analysis was carried out by me. This work is currently unpublished.

Chapter 5 contains work from a jointly authored paper available at: Lovatt et al., 2022. Faraday Discuss., 240, 114-126. Within the paper, data collection was performed by me and Conny Leistner. I performed data analysis. The manuscript was written by me and René Frank. Chapter 5 also contains an image of a lamella courtesy of Nayab Fatima, Andreas Schertel, Madeleine Gilbert and Yehuda Halfon from their paper available as a preprint at: Gilbert et al., 2023. bioRxiv. 2023.07.17.549278.

This copy has been supplied on the understanding that it is copyright material and that no quotation from the thesis may be published without proper acknowledgement. The right of Charlie Lovatt to be identified as Author of this work has been asserted by Charlie Lovatt in accordance with the Copyright, Designs and Patents Act 1988.

Acknowledgements

Firstly, I would like to thank my supervisor, René Frank, for his support and advice. I would also like to thank the rest of the Frank group, past and present, particularly Conny Leistner for training me in cryo-sectioning; Maddie Gilbert for the best hours of tomogram staring and constant provision of entertainment, love, and support; and Josh Jenkins for help with subtomogram averaging.

Thank you to Sally Boxall and Ruth Hughes at the bioimaging facility, and to everyone at the EM facility, especially Tom O'Sullivan for the cryo-sectioning help after my injury and Becky Thompson for the fantastic support through difficult times.

Thank you to Julia Peukes and Jerome Boulanger for collaborating on the synapse project in chapter 3, providing some of the MatLab scripts used in this thesis. Thank you to Tomás Ryan and Clara Ortega-de San Luis at Trinity College Dublin for collaborating with us on the engram project in chapter 4, particularly Clara for performing the engram labelling included in this thesis. Thank you to Nayab Fatima, Andreas Schertel, Madeleine Gilbert and Yehuda Halfon for providing the image of a lamella used within chapter 5 of this thesis.

This thesis would not have been possible without the Whiterose DTP BBSRC (BB/M011151/1) for providing the opportunity, training, and funds for me to carry out this project- thank you. It was a privilege to be a part of this programme. Additionally, thank you to the University of Leeds and the Wellcome trust for funding the Titan Krios microscopes (108466/Z/15/Z) and the Leica EM ICE, UC7 cryo-ultramicrotome and cryoCLEM systems (208395/Z/17/Z).

Of course, I would like to thank my friends and family for supporting me during my PhD studies and for encouraging me to follow my dreams- I hope I have made you all proud.

Last, but definitely not least, I would like to thank everyone at the NHS, LGI, and St James' hospital, especially Dr Hogarth and Dr Holmes, without whom I would not have been able to complete this project.

List of Abbreviations

AMPA - α -amino-3-hydroxy-5-methyl-4-isoxazole propionic acid receptor

CA1 - Cornu Ammonis layer 1

CA3 - Cornu Ammonis layer 3

CaMKII - Ca²⁺ /calmodulin-dependent protein kinase II

CEMOVIS - Cryo-electron Microscopy of Vitreous Sections

cryoEM - Cryogenic Electron Microscopy

cryoET - Cryogenic Electron Tomography

cryoFM - Cryogenic Fluorescence Microscopy

cryoCLEM - Cryogenic Correlated Light and Electron Microscopy

DG - Dentate Gyrus

DOX - Doxycycline

EC - Entorhinal Cortex

EM - Electron Microscopy

FIB - Focussed Ion Beam

FM - Fluorescence Microscopy

GFP - Green Fluorescent Protein

hACSF - HEPES-buffered Artificial Cerebrospinal Fluid

iGluR - Ionotropic Glutamate Receptor

LTD - Long-term depression

LTP - Long-term Potentiation

mGluR - Metabotropic Glutamate Receptor

NMDAR - N-methyl-D-aspartate Receptor

NMDG - N-Methyl-D-glucamine

OCT- Optimal Cutting Temperature compound

PreSM- Presynaptic Membrane

PoSM- Postsynaptic Membrane

PSD - Postsynaptic Density

SD - Standard Deviation

SEM - Scanning Electron Microscopy

SPA - Single Particle Analysis

STA - Subtomogram Averaging

TBS -Tris Buffered Saline

TRE - Tetracycline Responsive Element

tTA- Tetracycline Trans-Activator

WT - Wild-Type

Abstract

The brain encodes information as changes to ensembles of cells, termed engram cells, that are wired into complex neuroanatomical circuitry incorporating multiple brain regions. At the molecular level, mnemonic properties have been attributed to neuronal plasticity involving the rewiring of circuitry via junctions called synapses, which use neurotransmitters such as glutamate for electrochemical communication. However, the architectural structures at such synapses underlying memory functions remain to be elucidated. Here, two workflows were developed to label and visualize mammalian glutamatergic synapses and synapses between engram cells, respectively, within their cryopreserved in-tissue environment. These workflows encompassed mouse genetics (including knockin mice, engram labelling technology, and learning paradigms), cryogenic correlated light and electron microscopy, and cryogenic electron tomography. Through application of these workflows, this thesis reveals the first in-tissue 3D architectures of synapses between engram cells within the dorsal Cornu Ammonis layer 1 (CA1) of the hippocampus, in addition to those of glutamatergic synapses in the cortex, Cornu Ammonis layer 3 (CA3) and dentate gyrus (DG). These tomograms unveiled diverse synapses with molecular resolution containing organelles, macromolecular complexes and proteins, encapsulating the known heterogeneity of synapses. Synaptic constituents were quantitatively assessed, including F-Actin number, cleft geometry and organelle composition. Furthermore, subtomogram averaging was applied to classify molecular features of the synaptic cleft. These workflows initiate a voyage of discovery into the structural basis of memory, synaptic architecture and input specificity of neuronal circuits.

Table of Contents

List of Abbreviations	4
List of Tables	9
List of Figures	9
Chapter 1: An Introduction to Memory	13
1.1. The Psychology and Neurobiology of Memory	13
1.2. Synapses as Candidates for the Acquisition of Long-term Memory	17
1.3 Synaptic Plasticity in Learning and Memory	19
1.4 Spine Dynamics in Learning and Memory	21
1.5 Ionotropic Glutamate Receptors at Synapses	23
1.6 Translational and Transcriptional Changes Associated with Long-term Memory	28
1.7 The Current Outlook and Future Directions.....	33
1.8 Aims and Hypotheses.....	35
Chapter 2. Materials and Methods	37
2.1 Buffers and solutions	37
2.2 Sample preparation.....	38
<i>Laboratory animals and stereotactic surgery</i>	38
<i>Preparation of cryoEM grids via plunge-freezing</i>	43
<i>Preparation of acute slices</i>	43
<i>Live labelling and immunohistochemistry</i>	43
<i>Conventional EM of fixed brain tissue</i>	45
<i>High-pressure freezing</i>	46
<i>Cryogenic fluorescence microscopy of carriers</i>	46
<i>Cryo-ultramicrotomy</i>	47
<i>Cryogenic fluorescence microscopy of grids</i>	47
<i>Cryogenic correlative light and electron microscopy and cryo-electron tomography</i>	47
2.3 Data presentation and analysis.....	61
<i>Ultrastructural analysis</i>	61
<i>Subtomogram averaging</i>	65
Chapter 3: The in-tissue Molecular Architecture of Glutamatergic Synapses... 70	
3.1 The in-tissue architectures of glutamatergic cortical and hippocampal synapses in cryo-sections have variable postsynaptic density (PSD) distribution	73
3.2 The CA3 hippocampal region contains a sub-population of larger postsynaptic compartments	84
3.3 The hippocampus has greater incidence of postsynaptic mitochondria than the cortex.....	88
3.4 The CA3 region has greater vesicle occupancy and vesicle tethering, inferring a presynaptic-mediated mechanism of activity	91
3.5 Glutamatergic synapses have variable cleft height and distribution of iGluRs in the synaptic clefts across brain regions	94

3.6 Glutamatergic postsynaptic compartments contained extensive actin-associated cytoskeletal networks, particularly in the CA3 region	99
3.7 Concluding comments	104
Chapter 4: The in-tissue Architecture of Engram-labelled Synapses	108
4.1 Engram cell labelling in mice	110
4.2 Developing and optimising the engram preparation for cryoCLEM and cryoET	115
4.3 Compositional analysis of engram-labelled synapses	121
4.4 Quantitative analysis of engram synaptic architecture revealed diverse features	126
4.5 Macromolecular constituents of the synaptic cleft demonstrated vast heterogeneity	131
4.6 Postsynaptic compartments exhibit F-Actin-associated cytoskeletal networks	138
4.7 Vicinal engram-labelled features	141
4.8 Concluding comments	144
Chapter 5: CryoCLEM and CryoET Workflow Development.....	148
5.1. Choosing a method for fluorescently labelling molecular targets for cryoCLEM and cryoET.....	149
5.2. Preparing tissue sections for cryoCLEM and cryoET	154
5.3. Optimising and screening signal detection, ice thickness and vitrification.....	158
5.4. Concluding Comments.....	164
Chapter 6: General Discussion and Conclusions	166
6.1 A workflow was developed, enabling the collection of tomograms of engram-labelled cells, including synapses.....	167
6.2 Engram-specific differences were not detected in synaptic architecture.....	167
6.3 Glutamatergic synapses obtained from different neuroanatomical brain regions exhibited variability in synaptic architecture, with some region-specific observations indicated for further studies	169
6.4 Ionotropic glutamate receptors were detected within glutamatergic synapses and engram-labelled synapses	170
6.5 Live labelling enabled the identification of proteins with cryoCLEM but was not suitable for a cryoCLEM/cryoET workflow	171
6.6 Concluding comments	172
Appendices.....	173
Ethics statement.....	173
Supplementary Tables	174
Supplementary figures	188
Bibliography.....	204

List of Tables

Table Number	Title	Page Number
2.1	<i>Buffers made in-house.</i>	37
2.2.1	<i>Excitation/emission spectra for each fluorophore used for immunohistochemistry.</i>	45
2.2.2	<i>Collection parameters for tomograms of glutamatergic synapses discussed in chapter 3.</i>	48
2.2.3	<i>Collection parameters for tomograms of engram synapses discussed in chapter 4.</i>	56
2.3.1	<i>Criteria for the identification of ultrastructural constituents within cryo-tomograms.</i>	61
2.3.2	<i>Search parameters for subtomogram averaging of synaptic proteins using membrane oversampling.</i>	66
2.3.3	<i>Search parameters for the subtomogram averaging of microtubules.</i>	66
2.3.4	<i>Search parameters for the subtomogram averaging of putative ionotropic glutamate receptors.</i>	67
Supp.1	<i>Constituents of tomograms containing glutamatergic synapses.</i>	174
Supp.2	Constituents of tomograms containing engram-labelled synapses.	182

List of Figures

Figure number	Title	Page number
1.1.1	<i>The psychological stages of memory.</i>	14
1.1.2	<i>The neurological circuitry that underlies memory.</i>	16

1.5	<i>The molecular mechanisms of NMDAR-dependent plasticity.</i>	25
2.2.1	<i>Schematic depicting the application of engram labelling technology.</i>	40
2.2.2	<i>Schematic summary of in situ workflows.</i>	60
2.3.1	<i>Flow diagrams showing processing workflows.</i>	68
2.3.2	<i>Flow diagrams depicting protocols used for subtomogram averaging.</i>	69
3.1.1	<i>Graphical representation of constituents within tomograms of glutamatergic synapses from the cortex, CA3 and DG brain regions.</i>	74
3.1.2	<i>The in-tissue architecture of native glutamatergic cortical synapses in cryo-sections.</i>	76
3.1.3	<i>Identification of anatomical region in high-pressure frozen brain biopsies based on cell body labelling.</i>	79
3.1.4	<i>Cryo-preserved vitreous glutamatergic synapses had variable molecular crowding profiles independent of brain region.</i>	81
3.1.5	<i>The PSD is not always significantly more molecularly dense than regions distal to the membrane in cryopreserved tissue.</i>	83
3.2	<i>The diversity of post-synaptic compartment size in confocal microscopy of fixed acute slices, cryoFM of cryo-sections, and cryoET of cryo-sections.</i>	85
3.3	<i>Postsynaptic mitochondria are more abundant in hippocampal synapses.</i>	91
3.4	<i>The CA3 region demonstrated signatures of presynaptic-mediated plasticity.</i>	94
3.5	<i>Molecular constituents of the synaptic cleft.</i>	98

3.6	<i>Postsynaptic compartments contained extensive cytoskeletal networks, with more F-Actin in the CA3 region.</i>	102
4.1.1	<i>Labelling of engram synapses with engram labelling technology.</i>	111
4.1.2	<i>Confocal microscopy of engram-labelled cells in the hippocampal dorsal CA1 region.</i>	113
4.2.1	<i>In situ molecular architecture of plunge-frozen engram-labelled neurons.</i>	117
4.2.2	<i>A workflow to detect engram synapses within cryopreserved tissue for cryoCLEM and cryoET.</i>	120
4.3.1	<i>Constituents of tomograms containing engram-labelled synapses.</i>	122
4.3.2	<i>CryoCLEM and cryoET of engram-labelled synapses within cryo-sections.</i>	124
4.4	<i>Variability in prevalence of cellular organelles in engram-labelled synapses.</i>	129
4.5.1	<i>Engram-labelled synapses demonstrated variable distribution of synaptic cleft height.</i>	132
4.5.2	<i>Classification of molecular features in synaptic clefts revealed variability.</i>	136
4.6	<i>Ultrastructural analysis of F-Actin in engram-labelled cells revealed variability.</i>	138
4.7	<i>CryoCLEM of extracellular non-synaptic engram-labelled constituents.</i>	141
5.1	<i>Developing a live-labelling workflow to detect NMDA receptors within cryopreserved synapses.</i>	152
5.2	<i>Sample preparation methods for in situ cryoET.</i>	157
5.3.1	<i>Detecting fluorescent signals in high-pressure frozen tissue within gold carriers via cryoFM.</i>	159
5.3.2	<i>Optimising ice thickness and fluorescence detection in cryo-samples.</i>	161

5.3.3	<i>Testing for devitrification in cryo- samples.</i>	163
Supp.Fig.1	<i>All cryoFM, cryoEM and cryoCLEM of Psd95-EGFP-labelled glutamatergic synapses in chapter 3.</i>	188
Supp.Fig 2	<i>All cryoFM, cryoEM and cryoCLEM of engram-labelled synapses in chapter 4.</i>	197

Chapter 1: An Introduction to Memory

1.1. The Psychology and Neurobiology of Memory

Memory is the process by which the brain encodes, retains, and recalls information to accordingly alter future behaviour (Josselyn et al., 2015; Josselyn and Tonegawa, 2020; Ortega-De San Luis and Ryan, 2022).

Experimental psychological tests of cognition categorised memory into the three stages: encoding, consolidation and retrieval (Stangor and Walinga, 2014) (Fig. 1.1.1). Sensory inputs, including auditory, olfactory, mechanical, visual and gustatory, deliver information to neuronal circuits encoding memory (Itskov et al., 2011; Itskov et al., 2012; Igarashi et al., 2014; Stangor and Walinga, 2014). For rapid short-term memory functions, such as sound localisation, this information is used and discarded, whereas information which requires storage for future use is encoded and then consolidated into long-term memory, predominantly during sleep (Stangor and Walinga, 2014; Klinzing et al., 2019). Subsequently, memories can be retrieved from long-term storage (Stangor and Walinga, 2014), allowing the information to be used and updated (Liu et al., 2012; Josselyn and Tonegawa, 2020). Thus, memory has mechanisms that operate on a temporal scale from encoding to consolidation and reconsolidation (Squire, 2004; Stangor and Walinga, 2014).

Furthermore, cognitive tests classified the types of memory based on whether they are consciously or unconsciously learnt, referred to as “explicit/declarative” or “implicit/procedural” memory, respectively. Explicit memory was further classified relating to experiences or facts, named “episodic” and “semantic”, respectively (Martin-Ordas et al., 2014; Stangor and Walinga, 2014). These functions have been mapped to specific anatomical locations by cognitive neurologists, suggesting that individual functions can be attributed, at least to some extent, to specific brain regions (Squire, 2004; Chapi Mori, 2016; López-Madróna et al., 2017; Billig et al., 2022).

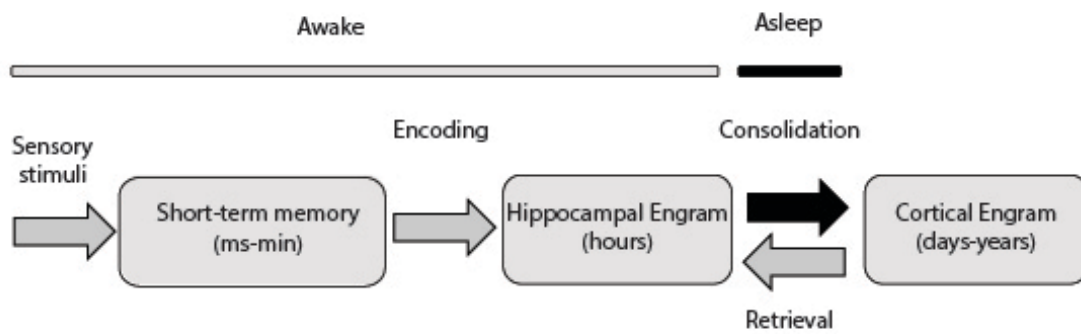


Figure 1.1.1: The psychological stages of memory.

Sensory stimuli are detected, which can be incorporated into short-term memory. Information is encoded in the hippocampus. Consolidation then forms a long-term memory, which can be retrieved, used and updated. Consolidation can include multiple phases, known as re-consolidation.

Adapted from (Stangor and Walinga, 2014).

The anatomical basis of the psychological phenomena was provided through the neurological study of patients afflicted by cognitive deficits due to brain injury, stroke or epilepsy. These observations evidenced the roles of various brain regions for the acquisition of different types of memory (Fig. 1.1.2A) (Squire, 2004). For example, it was observed that removal of the temporal lobe from a patient suffering with epileptic seizures prevented the recall of memories (retrograde amnesia) and the formation of new memories (anterograde amnesia) relating to episodic memory (Scoville and Milner, 1957), inferring that episodic memory was formed and stored in the temporal lobe. The limbic system of the temporal lobe, which includes the hippocampus, was identified as critical for many types of memory (Scoville and Milner, 1957; Josselyn et al., 2017). Accordingly, the hippocampus is required for the formation and consolidation of episodic memories (Squire, 2004; Fastenrath et al., 2014). Such functions rely upon hippocampal circuitry (Johnston and Amaral, 2004; Squire, 2004; López-Madrona et al., 2017).

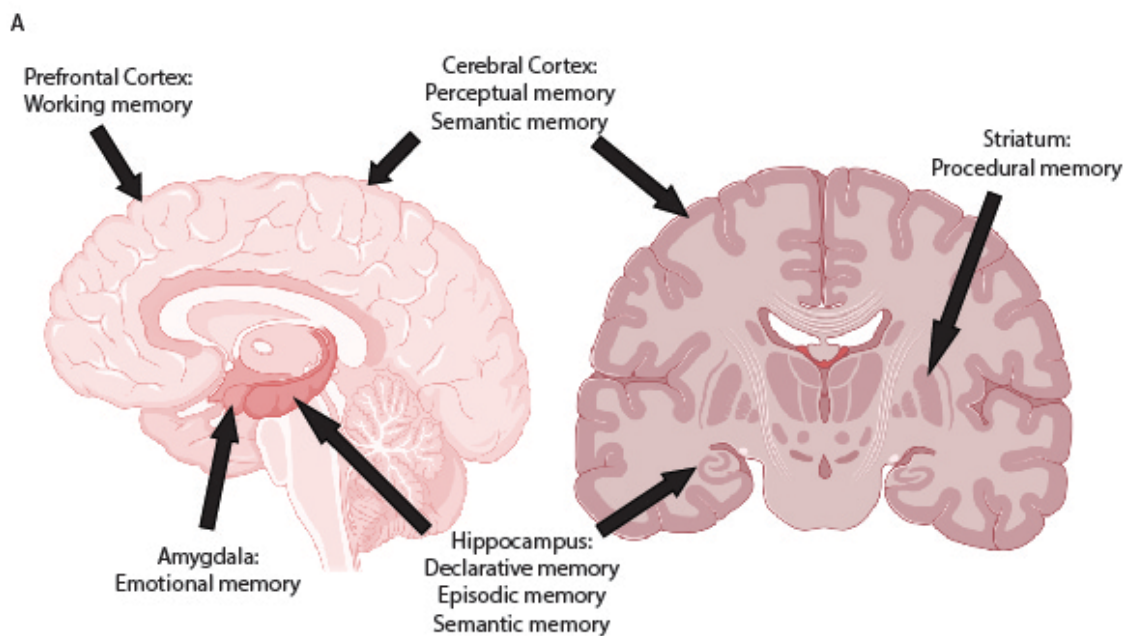
The hippocampus is sub-divided into neuroanatomical regions, identifiable based on the relative locations to the granular layer, a laminar structure encompassing densely

packed cell bodies (Ramón y Cajal, 1909; Johnston and Amaral, 2004). The hippocampus is composed of the hippocampus proper (*Cornu Ammonis* layers 1-3 (CA1-CA3) regions), the dentate gyrus (DG) and the entorhinal cortex (EC) (Squire et al., 2004; López-Madrona et al., 2017). Within this system there are two parallel circuits: the perforant tri-synaptic circuit and the monosynaptic temporo-anatomic circuit (De Benedictis et al., 2014; López-Madrona et al., 2017) (Fig. 1.1.2B). In the perforant tri-synaptic circuit, EC layer II projects to the DG, which relays activity via the mossy fibres to the CA3. CA3 Schaffer collateral neurons then project to the CA1 region to synapse with CA1 pyramidal neurons, which re-enter the deep layers of the EC. In contrast, in the temporo-anatomic monosynaptic circuit, the CA1 neurons receive a direct projection from EC layer III (López-Madrona et al., 2017; Billig et al., 2022). Additionally, the hippocampus receives input from the contralateral side; the CA1 receives contralateral input via the commissural fibres (Tao et al., 2021).

Although the hippocampus is critical for many types of memory, other types of memory, such as procedural, are hippocampus-independent (Fig. 1.1.2A), as shown in the case of the violist able to learn a new piece of music despite severe hippocampal damage due to herpes simplex encephalitis (Valtonen et al., 2014). In contrast, the circuitry of the striatum is critical for procedural memory (Fig. 1.1.2A) (Willuhn and Steiner, 2009; Chapi Mori, 2016). Accordingly, specific memory circuits were evidenced to contribute towards learning and memory, including working (Ojemann, 2003), semantic and episodic (Platel, 2005) and emotional (Fastenrath et al., 2014) memories. Therefore, distinct neuroanatomical circuits underlie specific forms of memory (Fig.1.1.2A), and thus, physiological explanations at the circuit level were provided for the psychological observations. Additionally, the hippocampus was identified to act as a hub for information correlation and processing, with the cortex acting as long-term storage for memories, divided into discrete information cortices (Chklovskii et al., 2004; Miller et al., 2010; Tanaka et al., 2014; Tonegawa et al., 2015).

However, the structural basis of learning and memory at the molecular level remains to be fully elucidated, and the difficulty in pinpointing the biological structure of memory lies within the complex neuroanatomical circuitry. Engrams, proposed by Richard Semon (Semon, 1909), are subsets of neurons that form circuitry incorporating different brain regions underlying memory (Roy et al., 2022). They are modified upon

experiences, including in their connectivity, underlie physicochemical changes to codify and store information, and are reactivated by relevant cues to elicit memory recall and a behavioral response (Liu et al., 2012; Liu et al., 2014; Josselyn et al., 2015; Josselyn and Tonegawa, 2020; Ortega-De San Luis and Ryan, 2022). These neurons are wired together via communication junctions called synapses, which are modulated dynamically in response to activity and learning (Hebb, 1949; Bliss and Lømo, 1973). Indeed, modifications to synaptic wiring patterns caused by structural plasticity mechanisms are a plausible physical substrate for information (Lichtman and Colman, 2000; Chklovskii et al., 2004; Tonegawa et al., 2015), as explored next.



B

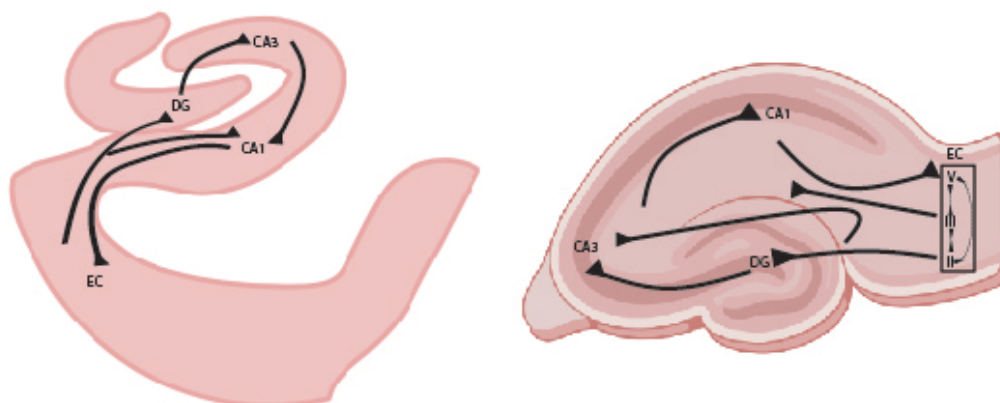


Figure 1.1.2: The neurological circuitry that underlies memory.

- A) *The neuroanatomy for distinct memory systems in the human brain.*
- B) *The detailed circuitry of the human hippocampus, left, and murine hippocampus, right, critical to declarative, episodic and semantic memories. CA1/CA3- Cornu Ammonis 1/3, DG- Dentate gyrus, EC- Entorhinal cortex. Both human and murine hippocampi have unidirectional circuitry, transferring information via two parallel circuits: the perforant tri-synaptic circuit and the monosynaptic temporo-anatomic circuit. In the perforant tri-synaptic circuit, EC layer II projects to the DG, which relays activity via the mossy fibres to the CA3. CA3 Schaffer collateral neurons then project to the CA1 region to synapse with CA1 pyramidal neurons, which re-enter the deep layers of the EC. In contrast, in the temporo-anatomic monosynaptic circuit, the CA1 neurons receive a direct projection from EC layer III.*

Based on (Chapi Mori, 2016; López-Madrona et al., 2017; Billig et al., 2022).

Created with BioRender.com

1.2. Synapses as Candidates for the Acquisition of Long-term Memory

Memory has temporal features that are encoded in milliseconds but can last a lifetime (Hebb, 1949). As postulated by Hebb, long-term memory must have a structural basis, as temporary silencing of neuronal activity or uncontrolled neuronal activity, such as violent cortical storms including *grand mal* epileptic seizures, occur without eliminating long-term memories (Hebb, 1949). Such observations infer that electrochemical activity alone does not account for long-term memory. Thus, memory is a structural property of neuronal circuits. Relationships between electrical activity, modulation of synaptic strength (synaptic plasticity) and structural modifications at synapses have since been observed, such as changes to connectivity patterns, synaptic head shape and size, and number of synapses (Bliss and Lømo, 1973; Lichtman and Colman, 2000; Chklovskii et al., 2004; Tonegawa et al., 2015), supporting Hebb's postulate and highlighting the key role of synapses in learning.

There are approximately 85 billion neurons in the brain (Herculano-Houzel, 2009), yet there are an estimated 100-500 trillion synapses (Drachman, 2005), indicating the

complexity of these circuits. Synapses enable many independently functioning input-specific connections to be made with an extensive combinatorial coding potential (Frey and Morris, 1997; Engert and Bonhoeffer, 1997; Lichtman and Colman, 2000), predicted to be necessary for information processing and memory storage. Synapse density varies by brain region, as demonstrated using focussed ion beam milling-scanning electron microscopy (FIB-SEM), in which all fluorescently labelled synapses within a known volume of brain were reconstructed from serial sections (Santuy et al., 2020), revealing that the more synapse-dense regions are found rostrally, including the neocortex. This suggests a great capacity for communication, information handling and memory storage. Furthermore, the synaptic connectivity between engram cells was evidenced to be updated with learning and recall (Redondo et al., 2014; Ryan et al., 2015; Vetere et al., 2017; Ryan et al., 2021; Ortega-de San Luis et al., 2023), implicating a synaptic mechanism of memory acquisition and recall.

In immature circuits of the mammalian brain, there are few synaptic connections and cognitive functions are limited. However, throughout post-natal development, wiring of the neuroanatomical circuits occurs, which increases the number of synaptic connections (Bourgeois et al., 1994; Huttenlocher and Dabholkar, 1997; Hsia et al., 1998), enabling both implicit and explicit cognitive functions (Greer and Greenberg, 2008). Such neuroanatomical development correlates to increased expression of synaptic proteins (Gonzalez-Lozano et al., 2016), including Psd95 (Frank et al., 2016), a protein activated in developmentally mature synapses. Psd95 is an integral component of the postsynaptic density in glutamatergic synapses, where it acts within a scaffold of proteins to anchors receptors at the postsynaptic membrane, notably ionotropic glutamate receptors, and interacts with intracellular proteins such as Ca^{2+} /calmodulin-dependent protein kinase II (CaMKII) (Broadhead et al., 2016; Frank et al., 2016). The application of western blotting demonstrated that Psd95 was expressed at detectable levels in forebrain homogenate once mice reached 8 days of age, and expression levels continued to increase over the following 69 days (Frank et al., 2016). Hence, synaptic density is modified in development as cognitive functions advance.

Thus, synapses present attractive candidates for the acquisition of long-term memory because they have great combinatorial coding potential (Drachman, 2005; Santuy et

al., 2020), and an increase in number of synaptic connections correlates positively with cognitive functions in development (Bourgeois et al., 1994; Huttenlocher and Dabholkar, 1997; Hsia et al., 1998; Frank et al., 2016) and the acquisition of memory in behavioural paradigms (Redondo et al., 2014; Choi et al., 2018; Ortega-de San Luis et al., 2023). Finally, synaptic plasticity is crucial to the electrophysiology of learning and memory (Kandel and Tauc, 1965; Bliss and Lømo, 1973), as explored in detail next.

1.3 Synaptic Plasticity in Learning and Memory

Changes to electrical, biochemical and structural neuronal properties via synaptic activity have mnemonic properties. The simple gill withdrawal reflex in *Aplysia Depilans* (sea slug) was investigated to map specific functions of the neuroanatomical circuitry with electrophysiology (Kandel and Tauc, 1965). A small excitatory post-synaptic potential (EPSP) was produced in response to a weak stimulus to one pathway, yet when the EPSP was paired several times with a strong stimulus to a second pathway, a prolonged facilitation was measured. These observations inferred that prolonged paired stimulation of a circuit strengthened the synaptic connection (Kandel and Tauc, 1965). Moreover, electrophysiology was performed on mammalian brain slices, leading to the observation of long-term potentiation (LTP) (Bliss and Lømo, 1973). LTP refers to the strengthening of a synapse and is expressed as a long-lasting output induced by an input of shorter duration. Potentiated responses were displayed in the dentate gyrus for periods of thirty minutes to ten hours after conditioned trains for ten to fifteen seconds (Bliss and Lømo, 1973). Together, these pioneering studies indicated that synapses are plastic and can be modified dynamically with activity.

Synaptic plasticity can be short-term or long-term, with long-term referring to mechanisms that underlie changes lasting more than thirty minutes (Poo et al., 2016). Increased use of a synapse strengthens the connection, whereas unused synapses are pruned (Chidambaram et al., 2019). Phagocytosing cells, particularly astrocytes, play a crucial role in the elimination of synapses for circuit homeostasis (Lee et al., 2020). Hence, synaptic connectivity is carefully regulated by supporting cells based on the use of individual connections.

The strengthening and weakening of synapses are known as potentiation and depression, respectively. LTP and long-term depression (LTD) are induced by distinct patterns of stimulation. LTP is induced by various protocols, including high frequency stimuli and paired-pulse stimuli in which the pre- and post- synaptic neurons are depolarised (Andrade-Talavera et al., 2016), whereas LTD is triggered by repeated low frequency stimuli (Hagena and Manahan-Vaughan, 2013). However, potentiation is not an all-or-nothing response; instead, the relative weight is critical. This is controlled by homeostatic scaling, the mechanisms by which individual neurons can reduce their overall firing rate in response to chronically elevated activity (Turrigiano, 2012). Thus, the strength of synapses can be modified dynamically on a continuous scale. Crucially, synaptic plasticity is a correlate of memory but does not directly measure memory itself.

Although synaptic plasticity has consistently been the most convincing suggested mechanism for memory acquisition, there was a lack of direct evidence linking plasticity and long-term memory due to the approaches not investigating the site of a specific engram *in vivo*. The development of optogenetics, referring to the introduction of light-gated ion channels into specific neurons to control their activity artificially using light (Liu et al., 2012; Liu et al., 2014; Ramirez et al., 2014), has bridged this gap. Channelrhodopsin genes are expressed downstream of activity-dependent promoters, enabling their expression specifically within active neurons within a memory task, thus enabling the labelling and light-gated activation of the subset of engram cells involved in the acquisition of a particular memory (Liu et al., 2012; Nabavi et al., 2014; Liu et al., 2014; Ryan et al., 2015). Accordingly, LTP and LTD induction *in vivo* using optogenetic stimuli have respectively induced or erased memories in mice (Nabavi et al., 2014; Liu et al., 2014), indicating that plasticity of synapses between engram cells is key to mnemonic functions. These engram circuits provide a stable configuration of neuronal ensembles, allowing for memory formation, recall and forgetting in a manner that is reversible and updatable, with the connectivity between engram cells being crucial to their mnemonic function (Redondo et al., 2014; Tonegawa et al., 2015; Autore et al., 2023; Ortega-de San Luis et al., 2023). Hence, the structural connectivity of engram circuits is key to memory.

Multiple mechanisms contribute towards the structural changes in memory circuits, including the dynamic modification of the number and shape of spines, referring to the dendritic regions on which synapses form (Engert and Bonhoeffer, 1999; Matsuo et al., 2008; Yang et al., 2009). Underlying these changes, synaptic strength is modified at the molecular level via ionotropic glutamate receptors (Collingridge et al., 1983; Park et al., 2019), calcium signalling (Augustine et al., 2003; Herring and Nicoll, 2016), and the synthesis of new proteins necessary for synaptic growth, such as cytoskeletal and transport proteins (Flood et al., 1975; Naghdi et al., 2003; Shrestha et al., 2020). The following sub-sections explore these processes in-depth.

1.4 Spine Dynamics in Learning and Memory

Dendritic spines are protrusions of the dendrite on which synapses are often located. These spines receive input from axon terminals at synapses. The shape of spines (Matsuo et al., 2008) and the number of spines per neuron (Engert and Bonhoeffer, 1997; Yang et al., 2009; Lai et al., 2012) are altered dynamically over time, demonstrating plasticity of the neuroanatomical circuitry in the brain. In mice, contextual learning resulted in a greater number of mushroom-shaped spines relative to stubby or thin spines in the hippocampus (Matsuo et al., 2008). This indicates that learning is associated with an increased surface area at a synapse, and therefore greater space for receptors, which is necessary to change the functional output of synapses. The number of spines can also be modified in learning, allowing for new synapses and multi-input synapses (Choi et al., 2018; Aziz et al., 2019).

The emergence of nascent spines occurs within 30 minutes of LTP induction *in vitro* and these spines take between several hours to four days to mature, according to time lapse imaging (Knott et al., 2006; Chidambaram et al., 2019). Increased spine number and density were evidenced using two-photon imaging of *in vitro* hippocampal CA1 neurons (Engert and Bonhoeffer, 1999) and of *in vivo* mouse cortex (Yu and Zuo, 2014). Two-photon transcranial imaging was used *in vivo* to visualise the cortex (Grutzendler et al., 2002; Yang et al., 2009; Lai et al., 2012). Such studies have monitored spine formation and elimination over time with motor (Yang et al., 2009), visual (Grutzendler et al., 2002) and fear (Lai et al., 2012) learning paradigms. For example, in the motor cortex, learning was associated with spine formation (Yang et al., 2009). Importantly, it was identified that spines were remodelled cue- and location-

specifically, dynamically modifying the same dendritic segment, inferring that different synapses are responsible for the storage of specific memories (Lai et al., 2012). However, the mechanisms of spine retraction and protrusion were not elucidated.

Dendritic spines have been suggested to be the locus of memory storage (Chidambaram et al., 2019) as these are the sites of synapse formation and are necessary for neuronal communication and for learning and memory. Interestingly, although memory was associated with strengthening of synapses at one synaptic input in young mice, memory in aged mice correlated to an increase in the number of synapses with multiple inputs (Aziz et al., 2019), suggesting that long-term memory storage and impairment of memory updating in older mice is dependent upon a distinct mechanism. Accordingly, *in vivo* imaging of the mouse somatosensory cortex inferred that many spines are unstable in young mice, with the fraction of persistent spines growing through development into adulthood (Holtmaat et al., 2005). Upon further study, although new spines formed rapidly with experience in the motor cortex, only select populations were maintained during persistent experience, indicating that these populations of spines (~0.04% daily new-formed spines and ~70% neonatally developed spines) are stable and survive a significant time (Yang et al., 2009). Similarly, in the adult mouse visual cortex, ~96% spines were reported to be stable (Grutzendler et al., 2002). In 6-month-old mice, spine turnover was higher in the somatosensory cortex compared to the visual cortex, suggesting that different levels of plasticity in the different areas of the cortex could be attributed to the stability of the spines in each area (Holtmaat et al., 2005). Interestingly, in contextual fear conditioning, in which mice are trained to associate a fear stimulus like a foot shock with a specific environmental cue, CA3 and CA1 engram cells demonstrated enhanced connectivity. This was observed as an increase in the number and size of spines on CA1 engram cells receiving CA3 engram cell input. However, these projections persisted in the absence of LTP induction, suggesting that enhanced stable structural connectivity between engram cells could underly this long-term memory (Choi et al., 2018). Therefore, populations of stable spines could be key to memory storage at synapses and the mechanisms of long-term memory acquisition could differ with age.

However, it is difficult to isolate dendritic spines from other protrusions which do not have synapses, such as filopodia, without a synaptic marker. Therefore, the number

of protrusions measured in some studies may not directly correlate to the number of synapses. Additionally, spontaneous and non-activity dependent remodelling of synapses was observed (Dvorkin and Ziv, 2016), inferring that synapses can be unstable and that other factors can contribute towards spine remodelling. The small populations of stable spines could be key to memory storage (Yang et al., 2009); further studies could identify a structural difference in these populations which explains their stability and their role in long-term memory storage. Therefore, although spine number and geometry are important in plasticity and memory, more evidence is required of the molecular mechanisms that underlie spine dynamics, spine stability and the structural changes at synapses associated with the acquisition of long-term memory.

1.5 Ionotropic Glutamate Receptors at Synapses

Electrophysiological and structural observations of mnemonic properties, including LTP and modified synapse number, were observed at synapses (Kandel and Tauc, 1965; Bliss and Lømo, 1973) and the molecular mechanisms linking the electrophysiological observations to the subsequent structural changes have since been probed, including investigations into ionotropic glutamate receptors.

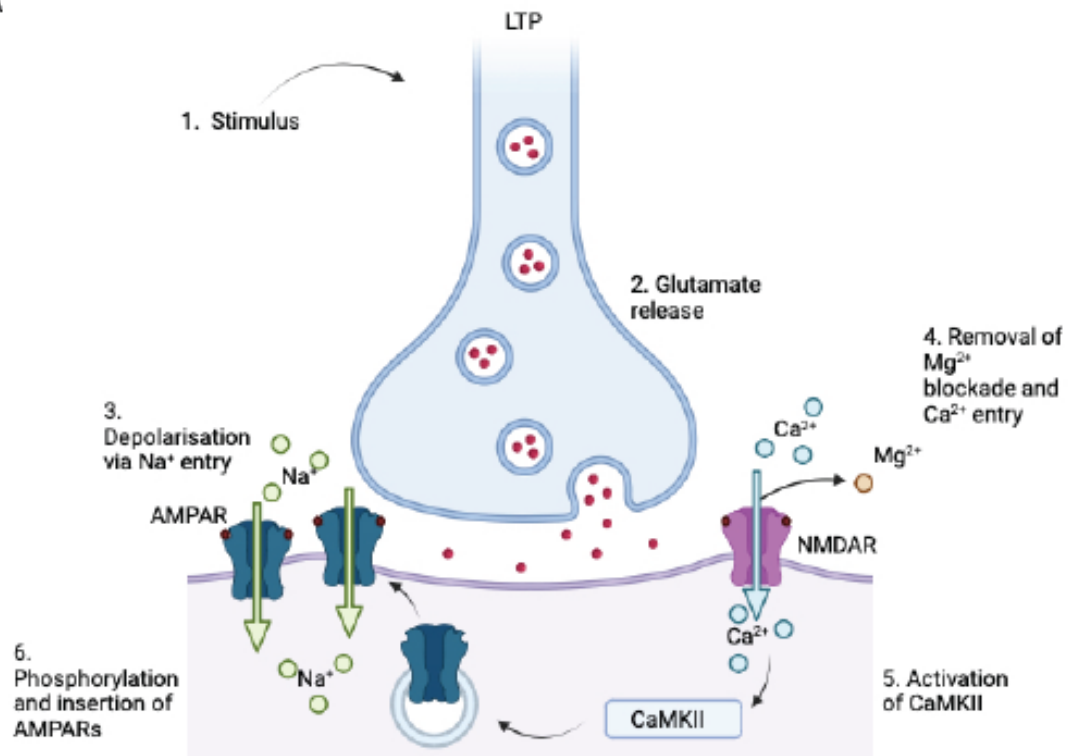
Glutamate is the predominant excitatory neurotransmitter in the mammalian central nervous system (CNS). Glutamate activates multiple receptors, including both metabotropic and ionotropic receptors (Meldrum, 2000). The ionotropic glutamate receptors found at synapses include α -amino-3-hydroxy-5-methyl-4-isoxazolepropionic acid receptors (AMPA), N-methyl-D-aspartate receptors (NMDAR) and kainate receptors (Sobolevsky et al., 2009; Lee et al., 2014). According to electron microscopy performed on conventional resin-embedded stained samples, most receptors are found on the postsynaptic density (PSD), a protein-dense specialisation of the post-synaptic neuron (Gray, 1959; Sheng and Kim, 2011).

At postsynaptic neurons, NMDARs interact with a variety of synaptic proteins, including cytoskeletal molecules and signalling proteins, such as Ca^{2+} /calmodulin-dependent protein kinase II (CaMKII) (Shen and Meyer, 1999; Husi et al., 2000; Frank et al., 2016). LTP is induced by high frequency stimulation, whereas LTD is induced by low frequency stimulation (Neyman and Manahan-Vaughan, 2008; Andrade-

Talavera et al., 2016); these are both dependent on calcium influx through NMDAR (Fig. 1.5), but the kinetic profile of calcium ions dictates whether the mechanisms for LTP or LTD are stimulated (Ismailov et al., 2004). The prevalent model of LTP (Fig. 1.5) involves NMDAR-mediated Ca^{2+} influx, leading to activation of CaMKII, phosphorylation of AMPARs and insertion of AMPARs into the plasma membrane, whereas the prevalent model of LTD involves the slow influx of calcium ions leading to the endocytosis of AMPARs (Ismailov et al., 2004; Hunt and Castillo, 2012).

Inhibition of NMDARs prevented LTP in brain slices (Collingridge et al., 1983), indicating that NMDARs have a key role in plasticity. Accordingly, this inhibition prevented spatial learning in mice (Davis et al., 1992), suggesting that NMDARs are critical to the induction of synaptic plasticity and the associated learning and memory. NMDARs have several attributes that make them suitable for their role in synaptic plasticity. NMDARs are known as “coincidence detectors”, referring to their ability to discriminate between correlated and un-correlated activity (Miyashita et al., 2012). Coincidence detectors act to link events, such as depolarisation and a back-propagation, or depolarisation and a second stimulation, decoding spike frequency and associating neuronal events, which is key to LTP (Miyashita et al., 2012; Tabone and Ramaswami, 2012). As indicated in Fig. 1.5, at resting membrane potential, NMDARs do not permeate ions, as they are blocked by Mg^{2+} . However, after post-synaptic depolarisation facilitated by other ion channels, such as AMPARs, the Mg^{2+} blockade is removed, allowing for calcium ion permeation via NMDARs (Mayer et al., 1984; Mayer and Westbrook, 1987; Miyashita et al., 2012). These unique activation properties (Miyashita et al., 2012), make NMDARs useful coincidence detectors for plasticity (Tabone and Ramaswami, 2012). Furthermore, NMDARs have a negative slope conductance, enabling signal amplification, which makes NMDAR-mediated plasticity a powerful mechanism for refinement of information encoding and storage (Hunt and Castillo, 2012).

A



B

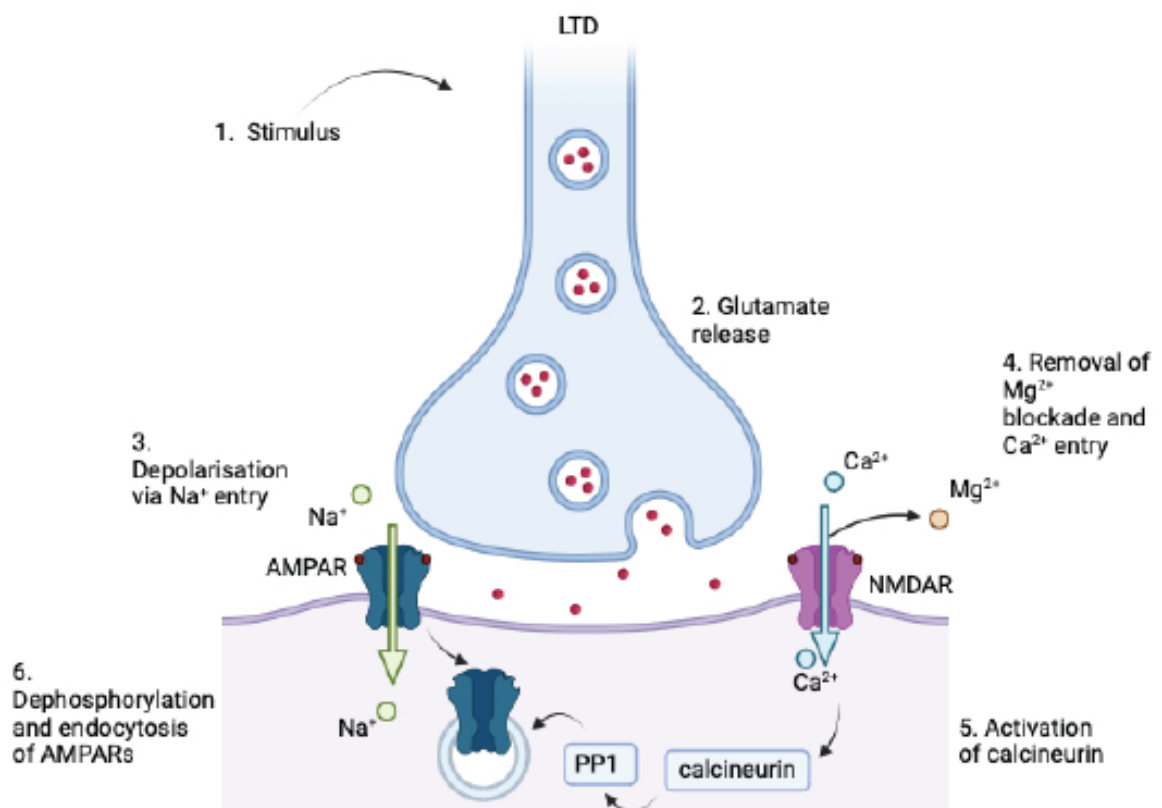


Figure 1.5: The molecular mechanisms of NMDAR-dependent plasticity

- A) *Long term potentiation (LTP): strong stimuli induce glutamate release from the presynaptic neuron. Glutamate binds to AMPA receptors (AMPA), inducing sodium ion (Na^+) influx and rapid depolarisation. Repetitive high frequency stimulation leads to the binding of glutamate to NMDA receptors (NMDARs), inducing NMDAR activation, removal of the magnesium ion (Mg^{2+}) blockade, and calcium ion (Ca^{2+}) influx. Ca^{2+} activate calcium/calmodulin dependent protein kinase II (CaMKII), phosphorylating AMPARs and promoting AMPAR insertion into the postsynaptic membrane for LTP.*
- B) *Long term depression (LTD): weaker stimuli induce glutamate release from the presynaptic neuron. Glutamate binds to AMPA receptors (AMPA), inducing sodium ion (Na^+) influx and depolarisation. Depolarisation promotes NMDAR activation, removal of the magnesium ion (Mg^{2+}) blockade, and calcium ion (Ca^{2+}) influx. The modest increase in Ca^{2+} activates calcineurin, which has a stronger affinity for Ca^{2+} than CaMKII, so accordingly responds to modest increases in Ca^{2+} . Calcineurin promotes the activation of protein phosphatase 1 (PP1), which promotes the dephosphorylation and endocytosis of AMPARs.*

Created with BioRender.com. Figure adapted from (Hyun et al., 2020)

A second important property of NMDARs for synaptic plasticity is calcium ion permeability, which acts as an intracellular second messenger to initiate structural changes to synapses. Calcium ions can act as intracellular second messengers to induce downstream cascades, including the activation of CaMKII, a calcium-sensitive kinase (Shen and Meyer, 1999; Husi et al., 2000). NMDARs are found in intra- and extra- synaptic pools (Harris and Pettit, 2007), although the role of these distinct compartments is presently unclear. Therefore, a structural approach is needed to explore the relevance of these pools, which could resolve their subunit composition and the architecture of complexes between NMDARs and CaMKII, from which the mechanisms of NMDAR activity could be further elucidated.

How does calcium ion influx via NMDARs promote the expression of LTP? LTP expression is associated with an increased number of AMPARs, whereas LTD correlates to a reduced number. Such changes are critical to plasticity, as AMPAR insertion is responsible for the increased EPSP activity measured in LTP. Calcium ion influx via NMDARs induces AMPAR insertion into the postsynaptic membrane via CaMKII-mediated activity during LTP (Herring and Nicoll, 2016). An increase in surface AMPAR number during contextual learning was observed via fluorescence microscopy through adding a green fluorescent protein (GFP) tag to AMPARs; the number of GFP-positive and mushroom-shaped spines in the hippocampus increased (Matsuo et al., 2008), correlating AMPAR insertion and the memory-associated structural changes at synapses. Similarly, an increased number of AMPARs was associated with mushroom-shaped spines, compared to thin spines, in electrophysiological quantal analysis (Matsuzaki et al., 2001).

Although NMDARs induce an increase in surface AMPARs, the importance of AMPARs to plasticity has been questioned. For example, LTP was established in the absence of the C-terminal region required for the trafficking of AMPARs (Granger et al., 2013), indicating that although a reserve pool of glutamate receptors is needed for plasticity *in vitro*, AMPARs are not critical. The role could instead be fulfilled by kainate receptors. However, a cell-specific cre-lox system was used to delete all major AMPAR subunits, followed by overexpression of a mutant form lacking the C-terminus, meaning observations may not have been physiologically comparable to the natural situation. Therefore, although LTP is associated with an increase in AMPAR number, the importance of this is controversial.

AMPAR subunits are suggested to be modified to permeate calcium ions (Plant et al., 2006; Zhang et al., 2023); at CA1 hippocampal pyramidal neurons, AMPAR subunits were shown to undergo a switch (Plant et al., 2006). AMPARs are composed of subunits termed GluA1 and GluA2, which can exist in heteromers and homomers. At resting membrane potential, electrophysiological investigations indicated that AMPARs contained calcium-permeable GluA1 and calcium-impermeable GluA2. However, upon LTP induction, there was an increase in GluA2-lacking AMPARs, allowing calcium ion entry via AMPARs (Plant et al., 2006). It is possible that NMDAR-plasticity induces an increased number of surface calcium-permeable AMPARs, which

could contribute towards subsequent calcium-induced activity. The raised level of GluA2-lacking AMPARs lasted for ~25 minutes after LTP induction, indicating that their presence was transient (Plant et al., 2006), inferring that calcium-permeable channels were recycled and replaced by calcium-impermeable channels. *In vivo*, GluA1 subunits were selectively recruited at mushroom-shaped synapses at hippocampal CA1 neurons 24 hours after fear conditioning (Matsuo et al., 2008), suggesting that calcium-permeable AMPAR-mediated enhancement of synaptic strength occurs at specific synapses. Upon further study, there was a reduction in spine density on learning-activated hippocampal CA1 neurons (Sanders et al., 2012); together, these studies infer that the acquisition of long-term memory involves synaptic refinement through strengthening of a sub-set of spines. This could link to the high structural stability of specific spines. However, the roles of different GluA subunits on structural plasticity, calcium ion dynamics and memory processes remain unclear.

Further research into the roles, spatial arrangement and structures of NMDARs and AMPARs at synapses is required. For example, what is the composition and spatial positioning of NMDARs and AMPARs at synapses? Moreover, structural studies could explore the NMDAR complex to identify the interactions and arrangements of proteins. NMDARs are known to have multiple protein-protein interactions (Frank, 2011; Frank et al., 2016). One such protein is CaMKII, which could be critical to coincidence detection by measuring the timing of stimulations (Shen and Meyer, 1999), and to structural LTP (Tullis et al., 2023). Knowledge on the molecular composition, protein-protein interactions, and spatial arrangement of NMDARs and AMPARs at engram synapses would enhance our understanding of synaptic mechanisms at the molecular level and would potentially unveil the structural basis of learning and memory in the mammalian brain.

1.6 Translational and Transcriptional Changes Associated with Long-term Memory

Long-term memories can persist for a lifetime, yet synaptic connectivity is dynamic and, on average, protein turnover in the brain has a rate of ~9 days (Price et al., 2010). This raises important questions, namely: How is the machinery for enhanced synaptic connectivity maintained at dynamic and stable synapses over the time-course of long-term memory, despite such high protein turnover? It is most likely that intracellular

feedback mechanisms across specific cellular compartments regulate signal transduction and translational and transcriptional programs within engram cells (Rao-Ruiz et al., 2021), enabling engram cells to maintain connectivity for long-term mnemonic functions. These feedback loops could involve NMDAR-mediated calcium signalling (Augustine et al., 2003), regulators of local translation at synapses, “synaptic tags” for directing protein products between synapses (Frey and Morris, 1997), transcription regulators (Bourtchuladze et al., 1994) and dynamic epigenetic modifications (Miller et al., 2010; Poo et al., 2016).

NMDARs are critical to synaptic plasticity and the associated learning and memory (Collingridge et al., 1983; Davis et al., 1992; Miyashita et al., 2012). Probing the signalling pathways of NMDAR-plasticity identified calcium ions as pivotal to such signalling. Calcium ion entry via NMDARs acts as a secondary messenger to activate various signalling cascades, translation and transcription (Augustine et al., 2003). These downstream cascades are essential to the maintenance of long-term plasticity.

Application of a protein synthesis inhibitor, anisomycin, or a transcription inhibitor, actinomycin D, prevented LTP (Frey et al., 1996; Hagena and Manahan-Vaughan, 2013), inferring that the synthesis of new proteins is required for long-term plasticity. Accordingly, anisomycin impaired spatial memory (Naghdi et al., 2003) and RNA polymerase II inhibitors impaired fear memory in rats (Igaz et al., 2002), suggesting that translation and transcription contribute towards the acquisition of long-term memory. Indeed, such observations are perhaps unsurprising, considering the requirement of ongoing protein turnover (Price et al., 2010; Dörrbaum et al., 2018) and the new proteins necessary for the growth of new spines after 20 minutes of LTP (Knott et al., 2006; Chidambaram et al., 2019).

Translation contributes to plasticity, hence anisomycin attenuates plasticity (Hagena and Manahan-Vaughan, 2013). Translation of proteins, including the cytoskeletal protein β -actin (Mitsushima et al., 2011; Yoon et al., 2016; Aziz et al., 2019), is required to enlarge the synaptic head, or to develop new spines. The evidenced molecular mechanisms of plasticity-related translation incorporate local protein synthesis and synaptic tagging.

Local protein synthesis has been directly evidenced *in vivo* using axon- translating ribosome affinity purification (axon-TRAP), a method by which the ribosome-bound mRNAs in the distal components of retinal ganglion cells were isolated in a CRE-reporter mouse setup. The local translation of mRNAs for cytoskeletal proteins and synaptic proteins was particularly high in axons, inferring that the proteins needed for synaptic remodelling were synthesised locally (Shigeoka et al., 2016). Moreover, translation has been evidenced in severed axons using various techniques (Kim and Jung, 2015). For example, in a study of retinal growth cones, soma-less axons were treated with an extrinsic cue or vehicle and the axonal abundance of the proteins netrin-1 and semaphorin-3A, necessary to attract or repel the growth of receptor-bearing axons, was compared. An increase in protein abundance was seen in response to extrinsic cues, which was blocked by translation inhibitors (Campbell and Holt, 2001), implying that proteins were translated locally. Local protein synthesis is regulated by calcium ions. The influx of calcium ions can induce kinases such as CaMKII to phosphorylate binding proteins and release initiation factors, which bind to ribosomes, increasing the rate of translation of mRNA at synapses (Klann et al., 2004; Panja et al., 2009). Therefore, calcium ion signalling controls local protein synthesis via initiation factors at dendrites, enabling structural changes and the development of new spines during LTP. However, the macromolecular machinery orchestrating local calcium ion signalling to translation is unknown; in-tissue structural studies could reveal this machinery.

However, after LTP at one synapse, anisomycin does not prevent LTP at a second synapse (Frey and Morris, 1997), suggesting that new protein synthesis does not contribute towards LTP if a nearby synapse has recently been activated. Therefore, a molecular tag could be added to direct proteins synthesised at the first active synapse to the second, enabling computation between the synapses (Frey and Morris, 1997). This process is entitled synaptic tagging, although the mechanism and the identity of the tag are not fully understood. The tag must be short-lived, as these effects did not persist after 3 hours (Frey and Morris, 1997). If structures of potentiated synapses could be obtained, revealing the macromolecular machinery, the mechanisms of synaptic tagging could be explored.

Transcription, regulated by transcription factors are suggested to be involved in late long-term memory functions (Bourtchuladze et al., 1994; Ghiani et al., 2007), inferring that transcription occurs post-translation. This observation suggests that local protein synthesis and synaptic tagging could be key to the early stages of long-term memory, utilising proteins formed at the synapses. However, a further mechanism could then stimulate transcriptional changes, as changes to gene expression are then required to sustain the protein production and metabolism of the active neuron and its synapses.

Gene expression in plasticity is regulated by transcription factors, which can be enhancing or suppressing. Transcription factors include cAMP-responsive element binding protein (CREB), an enhancing transcription factor known to regulate a multitude of genes. CREB was demonstrated to be crucial to long-term but not short-term memory, as mice containing inactivating CREB mutations had normal memory function for up to 1 hour, but impaired long-term memory in the Morris water maze and in fear conditioning (Bourtchuladze et al., 1994), inferring that CREB-regulated transcription is important in long-term memory functions.

CREB is phosphorylated by calcium-sensing kinases for activation (Sakamoto et al., 2011), suggesting that the rise in calcium ion concentration during plasticity could regulate CREB activity. The activation of NMDARs induced both plasticity, measured via immunostaining of synaptophysin, and CREB phosphorylation (Ghiani et al., 2007), directly linking NMDAR activity, CREB activity and synaptic plasticity. Transcription could produce proteins necessary for structural modification of synapses, including enlarging the postsynaptic head into a mushroom shape (Chidambaram et al., 2019), thus enhancing synaptic strength.

Although protein synthesis is critical to long-term plasticity and memory in mice (Flood et al., 1975), inhibition of protein synthesis during the consolidation phase of memory in mice did not impair retrieval (Ryan et al., 2015), inferring that augmentation of synaptic strength is important in early stages such as the acquisition and encoding of long-term memory, but not in retrieval. Furthermore, long-term memory in *Aplysia* was re-instated following erasure of its synaptic expression through forced retraction of spines or the blockade of re-consolidation (Chen et al., 2014). Together, these studies suggest that an alternative long-lasting mechanism accounts for the late stages of memory.

Epigenetics, which refers to the dynamic regulation of gene expression by chromatin modification over the timespan of many years in response to experience and environment, has been suggested as a potential mechanism for long-term memory storage (Poo et al., 2016). Epigenetic markers include acetylation and methylation, which can be added or removed from the genome based on experience, as indicated in twin studies in which young identical twins had few differences, whereas older identical twins had a variety of different epigenetic markers (Fraga et al., 2005).

Acetyl groups are reversibly added to histones by histone acetyl-transferases (HATs), making the histone structure more open to increase gene expression, or removed by histone deacetylases (HDACs). Reversible acetylation by HATs and HDACs was investigated in the context of memory in mouse models; neuron-specific overexpression of HDAC2 impaired memory, which was rescued by HDAC inhibition (Guan et al., 2009). Moreover, transgenic mice expressing CREB binding protein with a lack of HAT activity had unchanged acquisition of memory but impaired consolidation (Korzus et al., 2004).

Furthermore, methylases can methylate specific residues for site-specific activity. For example, methylation of lysine 4 on histone 3 increases gene expression, whereas methylation of lysine 9 represses expression (Stewart et al., 2005). Methylation in the brain is dynamic, yet neurons are not constantly dividing, so methylation cannot be accounted for in replication. Therefore, an active mechanism accounts for methylation. Epigenetic markers such as methylation can last for long periods of time, yet methylation in the hippocampus after learning was transient and lasted 24 hours (Miller et al., 2010). Memories last much longer, suggesting that hippocampal methylation cannot account for long-term memory. In contrast, methylation in the cortex after the same learning event lasted for 30 days (Miller et al., 2010), inferring that after approximately 24 hours, the trace of memory could be transferred via epigenetic mechanisms from the hippocampus to the cortex for storage. However, the mechanism of this transfer remains unexplained. Furthermore, the true lifespan of these dynamic epigenetic markers is unknown.

Therefore, epigenetics could contribute towards the consolidation, stabilisation, and retrieval of memories; these long-lived molecules could be key to the transfer of the mnemonic trace to the cortex for long-term memory storage (Miller et al., 2010),

although further investigation is required. It is possible that epigenetic mechanisms play a role in sustaining feedback loops to regulate the expression of persistent transcriptional signatures necessary for the retention of specific synaptic connections within the engram cell network (Rao-Ruiz et al., 2021), although the molecular mechanisms of these possible epigenetic feedback loops to support specific engram synapses remain to be explained.

1.7 The Current Outlook and Future Directions

Together, the discussed literature provides evidence of numerous molecular mechanisms that contribute towards long-term memory on a temporal scale. Synaptic plasticity and the associated structural remodelling of spines are important in memory acquisition, and specific populations of stable spines could be critical to long-term memory functions. Other non-synaptic processes, such as transcription and epigenetics, likely contribute to later stages.

Currently, a structural perspective on memory acquisition has not been provided. Through studying the molecular architecture, referring to the 3D organisation of the proteins, macromolecular complexes, organelles and membranes that constitute a cellular environment, the structural components underlying biological functions could be revealed. How could the architecture and arrangement of proteins, macromolecular complexes, and organelles supporting synapses between engram cells during memory acquisition be elucidated in their native environment? Such a workflow could be possible via cryogenic correlated light and electron microscopy (cryoCLEM) and cryogenic electron tomography (cryoET), which together enable in-tissue structural studies of fluorescently labelled biological components of interest within a cryopreserved, vitreous environment (Kukulski et al., 2011; Lovatt et al., 2022).

Fluorescence microscopy (FM) enables the labelling and identification of biomolecules of interest (Jensen, 2012; Fang et al., 2018; Tu et al., 2021), which is critical for localisation and analysis of proteins within biological samples. However, the ultrastructural localisation of the fluorescence is lacking. In contrast, electron microscopy (EM) enables the visualisation of cellular ultrastructure. Traditionally, conventional EM involves the use of a heavy metal stain on chemically fixed, dehydrated, resin-embedded samples (Gray, 1959; Harris and Weinberg, 2012), but

EM can also be applied to vitreous, cryopreserved cells and tissues prepared via cryo-sectioning or FIB-milling (Al-Amoudi et al., 2004; Lučić et al., 2013; Schaffer et al., 2019), termed cryogenic electron microscopy (cryoEM). These cryoEM images can be correlated with FM images using correlative techniques, enabling the localisation of fluorescent signals within a complex biological environment, and thus the mapping of biomolecules of interest (Kukulski et al., 2011; Carter et al., 2018; Peukes et al., 2021; Lovatt et al., 2022). However, the resolution of cryoCLEM is limited, so to provide molecular resolution (~ 2 nm) in a 3D environment (Vilas et al., 2020), cryogenic electron tomography (cryoET) is applied, in which images are collected of a specimen at different tilt increments (-60 to -60°) and computationally reconstructing into a 3D volume (Kaplan et al., 2021; Lovatt et al., 2022), called a tomogram.

EM enables the visualisation of structures on the scale of angstrom resolution (Henderson, 1995; Briggs, 2013; Kühlbrandt, 2014), and can be applied as single particle analysis (SPA) or as cryoET. SPA resolves the structures of purified proteins by imaging multiple copies of the protein plunge-frozen onto on a cryoEM grid. Images are classified based on orientation and are averaged to obtain a high-resolution structure (Bai et al., 2015; Glaeser, 2019; Lovestam and Scheres, 2022). In contrast, to obtain *in situ* high-resolution structures, proteins are cryopreserved within cells or tissues via high pressure freezing or plunge-freezing (Lučić et al., 2013; Asano et al., 2016; Beck and Baumeister, 2016; Plitzko et al., 2016). Thin sections are prepared via cryo-sectioning or FIB-milling and cryo-liftout (Al-Amoudi et al., 2004; Lučić et al., 2013; Schaffer et al., 2019). Subsequently, the sample is imaged with cryoET, in which the sample is tilted, enabling the imaging of the same specimen from a range of angles for subsequent reconstruction into a 3D volume (Lučić et al., 2013; Asano et al., 2016; Beck and Baumeister, 2016). Proteins can then be identified, aligned, and averaged using subtomogram averaging (STA) protocols for high-resolution structures (Briggs, 2013; Peukes et al., 2021; Gilbert et al., 2023).

The application of cryoCLEM and cryoET to memory circuits has the potential to unveil the proteins and macromolecular complexes that constitute an engram, which could elucidate the architectures underlying memory acquisition. Here, this thesis will focus on developing a novel workflow that can be applied to investigate the molecular architectures that underlie the acquisition of long-term memory at synapses between

engram cells. The workflow will incorporate engram labelling technology, cryoCLEM, and cryoET. Additionally, new methodologies to interrogate glutamatergic synapses in different brain regions will be developed, enabling architectural insight into excitatory synapses in different brain regions responsible for encoding different types of memory. Overall, this thesis will develop workflows and tools for further research in the memory field to provide structural insight for the biological observations.

1.8 Aims and Hypotheses

This project will investigate the architectural basis of dynamic synapses and long-term memory acquisition at the molecular level through addressing the following aims:

1. To establish a novel workflow to investigate the architecture of synapses between engram cells, enabling the resolution of macromolecules.
2. To determine the architecture of specific engram-engram synapses, such as synapse geometry, organelle content, and protein number, using a combination of engram labelling technology, cryoCLEM and cryoET.
3. To delineate architectural differences in excitatory glutamatergic synapses in different brain regions.
4. To obtain in-tissue structures of proteins within brain tissue, including at the synaptic cleft, via subtomogram averaging.
5. To develop a novel live-labelling approach to identify specific proteins in tomograms of synapses.

It is hypothesised that:

1. The workflow developed will enable the collection of tomograms of engram-labelled cells, including synapses.
2. Engram synapses will have input-specific differences in synaptic architecture.
3. Differences in synaptic architecture will exist between synapses from different brain regions.

4. Ionotropic glutamate receptors will be identified within glutamatergic synaptic clefts and within synaptic clefts between engram neurons.

5. Live-labelling will enable the identification of specific proteins and their surrounding subcellular architecture, including NMDARs, at synapses.

Ultimately, the workflows developed in this thesis aim to be applied to explore memory mechanisms with a structural approach, which could elucidate the changes to molecular architecture at synapses responsible for long-term memory acquisition through the comparison on non-activated and re-activated engram synapses, and the collection of architectural data at different timepoints after memory acquisition. This could include investigations into iGluR localisation, structure and macromolecular interactions, changes to synaptic geometry, and alterations to cytoskeletal machinery. Therefore, this thesis will establish the workflows necessary for preparing and collecting synaptic tomograms in an in-tissue cryoCLEM/cryoET workflow, and the methodologies for examining synaptic architectures within tomograms to create protocols for future studies.

Chapter 2. Materials and Methods

2.1 Buffers and solutions

Buffers and solutions were made in-house, as indicated in Table 2.1.

Table 2.1: Buffers made in-house.

Buffer	Components	Reference
NMDG cutting buffer	3 mM NMDG, 2.5 mM potassium chloride, 1.2 mM sodium hydrogen carbonate, 20 mM HEPES, 25 mM glucose, 5 mM sodium ascorbate, 2 mM thiourea, 3 mM sodium pyruvate, 10 mM magnesium sulphate heptahydrate, 0.5 mM calcium chloride dihydrate; pH 7.4, 300 - 315 mOsm/L	(Ting et al., 2018)
HEPES-buffered artificial cerebrospinal fluid (hACSF)	120 mM NaCl ₂ , 5 mM KCl, 1.2 mM MgCl ₂ .6H ₂ O, 2 mM CaCl ₂ .2H ₂ O, 25 mM HEPES, 30 mM glucose; pH 7.2-7.4	Modified from (Wakayama et al., 2017)
Artificial cerebrospinal fluid (ACSF)	125 mM NaCl, 25 mM KCl, 25 mM NHCO ₃ , 25 mM glucose, 2.5 mM KCl, 2 mM CaCl ₂ , 1.25 mM NaH ₂ PO ₄ , 1 mM MgCl ₂ ; pH 7.2-7.4, 310 mOsM/L	
Tris-Buffered Saline (TBS)	50 mM Tris, 150 mM NaCl; pH 7.6.	
Cryoprotectant	20 % dextran in NMDG cutting buffer	Adapted from (Zuber et al., 2005)

2.2 Sample preparation

Laboratory animals and stereotactic surgery

Glutamate is the most prevalent excitatory neurotransmitter in the brain (Meldrum, 2000), and therefore glutamatergic synapses are found abundantly in many brain regions. How do the architectures of these excitatory synapses differ in the hippocampus, used as a temporary locus of memory to collate sensory information, and the cortex, where long-term memories are stored for up to years? In order to identify architectural differences at excitatory glutamatergic synapses with different roles in memory stages, readily-available WT and knockin mice (Frank et al., 2016; Zhu et al., 2018) with GFP-tagged PSD95 and FLAG-tagged GluN1, the obligatory subunit of NMDARs, (*Psd95^{GFP/GFP} GluN1^{FLAG/FLAG}*) were utilised. These knockin mice had heritable labelling of endogenous PSD95 and GluN1, which does not affect their electrophysiological properties, endogenous protein levels, assembly into supercomplexes, or developmental timing of expression (Frank et al., 2016; Broadhead et al., 2016; Zhu et al., 2018). All mice were socially housed in groups of 2 to 5 at the clean-side animal facility at the University of Leeds (Leeds, England), where they had access to food and water *ad libitum*. All laboratory animals were housed and bred according to the British Home Office Regulations, local ethical approval, and NIH guidelines. Adult male mice (3-9 months) were used for experiments in chapter 3 to control for sex and age-related variability.

To label a specific memory circuit and therefore enable investigations into a specific, controllable memory circuit and the identification of the synapses within, engram-labelled mice were generated at Trinity College, Dublin. B6.Cg-Tg(Fos-tTA,Fos-EGFP*)1Mmay/J mice (Jackson Stock no: 018306) were housed at the Comparative Medicine Unit in the Trinity Biomedical Science Institute, Trinity College Dublin (Dublin, Ireland). The use of these mice enabled the generation of tetracycline trans-activator (tTA) in neurons expressing *cfos*, an immediate early gene expressed only by active neurons (Bullitt, 1990; Ryan et al., 2015; Chung, 2015; Roy et al., 2022). The use of tTA and *cfos* in combination can limit gene expression to a specific time window and to solely active neurons. Therefore, fluorescent genes of interest under tTA and *cfos* promoters can be cerebrally injected into the brain via stereotactic surgery, and

expression of these genes can be made doxycycline-conditional within active neurons, labelling solely active neurons during the time in which doxycycline is not present and a memory is made, thus labelling an engram (Fig.2.2.1). All procedures were performed under appropriate Project Authorization (AE19136/P081) granted by the Health Products Regulatory Authority, the Irish competent authority for scientific animal protection legislation. Mice had access to food and water *ad libitum* and were socially housed in numbers of 2 to 5. Adult male mice (7-14 weeks) were used for experiments in chapter 4 to control for sex and age-related variability during workflow development.

Stereotactic surgery was performed by Dr Clara Ortega-de San Luis at Trinity College, Dublin, under stereotactic guidance using standard mouse stereotactic frames. Adult B6.Cg-Tg(Fos-tTA,Fos-EGFP*)1Mmay/J mice (7-14 weeks old) were anaesthetised using 500 mg/kg avertin (Sigma). During the procedure, a bilateral craniotomy using a 0.5 mm diameter drill was carried out and viral cocktails (Fig. 2.2.1) were injected through a metal needle attached to a 10 μ L Hamilton microsyringe (701LT; Hamilton) and an automated microsyringe pump (WPI).

To identify synapses within a specific memory circuit, it was necessary to label engram cells originating in the CA3 and in the contralateral CA1 with two different fluorophores (Fig.2.2.1). These locations were chosen as the CA3-CA1 schaffer collaterals are well-documented (Ishizuka et al., 1990; Shepherd and Harris, 1998). Expression of fluorophores needed to be limited to a specific time window and to active neurons. Therefore, a combination of promoters was used. These included a tetracycline transactivator (TRE), a doxycycline-controlled promoter, meaning expression was limited to time windows where doxycycline was not present, as doxycycline is able to sequester tTA to prevent it binding to the TRE promoter for expression of the gene of interest. Additionally, a *cfos* promoter was used to limit expression to active neurons, as only active neurons express *cfos* (Bullitt, 1990; Ryan et al., 2015; Chung, 2015; Roy et al., 2022). Hence, fluorophores under the control of these promoters enabled the labelling of engram neurons within a specific training task. The CA3 neurons were labelled with channelrhodopsin (ChR2) conjugated to EYFP, enabling the reactivation of presynaptic engram neurons originating in the CA3 region via optogenetic stimuli. Reactivation was not utilised in the present thesis, as the purpose of this study was to

develop the workflow to target specific fluorescently labelled neurons. However, this addition will permit future reactivation studies, enabling comparisons to be made between active and inactive engram synapses at different stages of memory. The postsynaptic CA1 neurons were labelled with an mCherry fluorophore, a cytosolic marker. It was assumed that the overlapping signals of EYFP and mCherry would correlate to engram synapses via cryoCLEM.

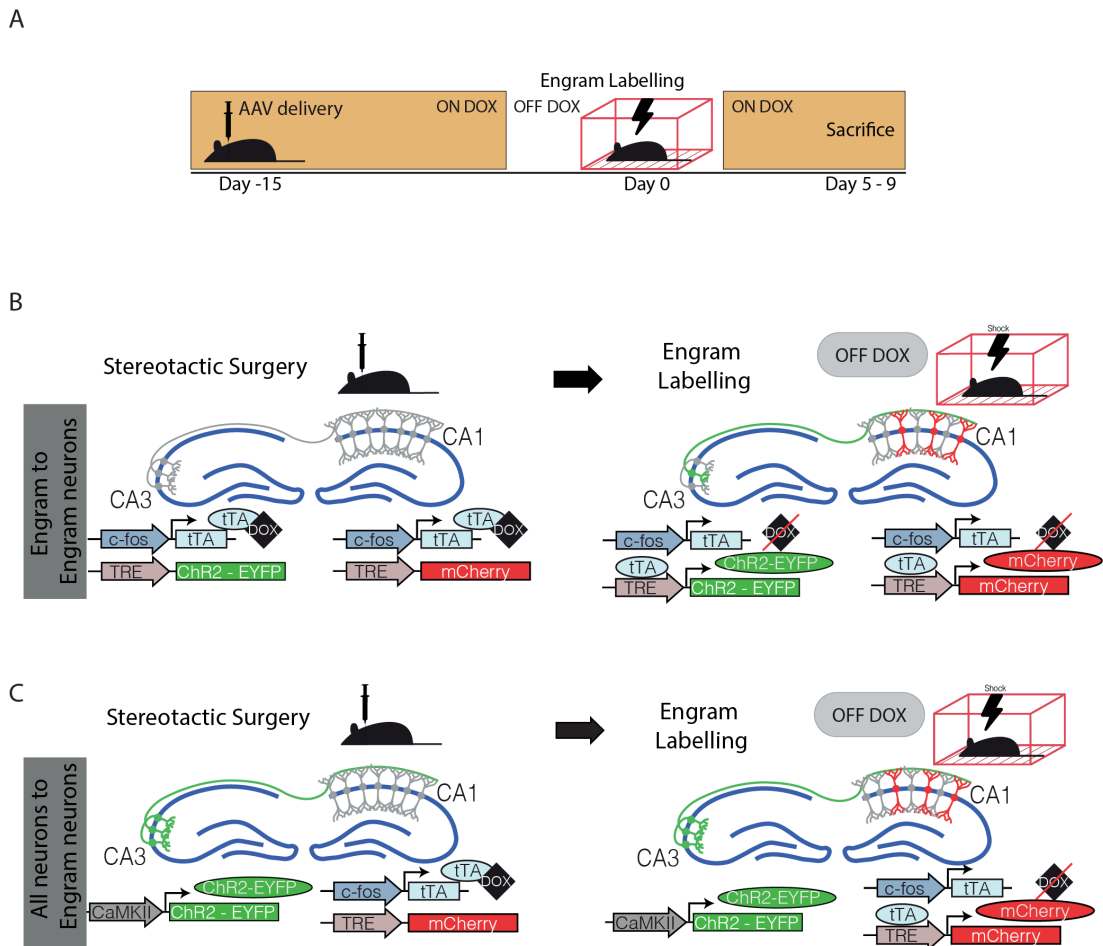


Figure 2.2.1: Schematic depicting the application of engram labelling technology.

A) *Experimental timeline.* Mice (B6.Cg-Tg(Fos-tTA,Fos-EGFP*)1Mmay/J) were used to enable the expression of tetracycline trans-activator (tTA), which permits the expression of genes of interest to be made doxycycline-dependent, and therefore controllable within a given timeframe. Mice were subject to two intracerebral injections of genes of interest via stereotactic surgery. At the CA3 region of the hippocampus, these were either plasmid Adeno-Associated Virus-

Tetracycline Response Element- Channelrhodopsin-Enhanced Yellow Fluorescent Protein (pAAV-TRE-ChR2-EYFP), to label engram neurons, or plasmid Adeno-Associated Virus- Calcium-calmodulin-dependent Kinase II- Channelrhodopsin-Enhanced Yellow Fluorescent Protein (pAAV-CaMKII-ChR2-EYFP), to label all neurons. At the contralateral CA1 region of the hippocampus, plasmid Adeno-Associated Virus- Tetracycline Response Element- mCherry (pAAV-TRE-mCherry) was intracerebrally injected to label postsynaptic engram neurons in the CA1 region. Mice were left to recover for 15 days whilst on a doxycycline diet to suppress the expression of genes of interest. Next, for engram labelling, mice were taken off the doxycycline diet to enable the expression of the genes of interest and were transported to an experimental room where they were allowed to explore a context for 3 minutes, followed by 3 successive 0.75 mA shocks of 2 s duration spaced by 1 minute. Contextual cues used were a triangular shape inset and Benzhaldehyde 0.25%. After training, mice were put back on a doxycycline diet to prevent further expression of the genes of interest. Mice were sacrificed 6 days after engram labelling for the cryoCLEM/cryoET workflow.

- B) Schematic depicting the constructs used for the labelling of engram-to-engram (EE) CA3-CA1 neurons using engram labelling technology. After stereotactic surgery to administer the genes of interest packaged in AAVs, mice consumed a doxycycline diet. This sequesters the tetracycline trans-activator (tTa) in the system so that the tetracycline response element (TRE) is not activated, thus preventing expression. However, once the mice are taken off the doxycycline diet, tTa binds to TRE, activating downstream expression. Additionally, the cfos promoter limits expression to neurons with high cfos levels, which corresponds to active neurons. Hence, only active neurons in the CA3 and contralateral CA1 during the time of the training episode are labelled, labelling an engram.*
- C) Schematic depicting the constructs used for the labelling of control non-engram-to-engram (NEE) CA3-CA1 neurons using engram labelling technology. To label all CA3 neurons, a pan-neuronal promoter was used (Calcium-calmodulin-dependent Kinase II; CaMKII), which labelled all CA3 neurons with an EYFP fluorophore. After stereotactic surgery to administer the*

genes of interest packaged in AAVs, mice consume a doxycycline diet. This sequesters the tetracycline trans-activator (tTa) in the system so that the tetracycline response element (TRE) is not activated in the CA1 neurons, thus preventing expression. However, once the mice are taken off the doxycycline diet, tTa binds to TRE, activating downstream expression. Additionally, the cfos promoter limits expression to neurons with high cfos levels, which corresponds to active neurons. Hence, only active CA1 neurons during the time of the training episode are labelled, labelling CA1 engram neurons.

Figure courtesy of Dr Clara Ortega-de San Luis

To label CA1 and CA3 engram cells, respectively, two plasmids were constructed and packaged. These were a plasmid adeno-associated virus vector containing an mCherry fluorophore under a tetracycline trans-activator promoter (pAAV-TRE-mCherry) and a plasmid adeno-associated virus vector containing channelrhodopsin (ChR2) conjugated to EYFP under a tetracycline trans-activator promoter (pAAV-TRE-ChR2-EYFP) (Fig. 2.2.1). Both plasmids were previously AAV9 serotyped and packed into viral particles by Vigene Bioscience (Maryland, USA). The needle was placed on appropriate stereotactic coordinates and remained for 5 min before the injection commenced. The coordinates used were: CA1 (-2.0 mm AP, +/- 1.5 mm ML, -1.5 mm DV) and CA3 (-2.0 mm AP, +2.3 mm ML, -2.2 mm DV); 300 nL of cocktail virus were injected at 60 nL/min speed. After the injection, the needle stayed for ten additional minutes before it was carefully withdrawn. The incision was closed with sutures. Mice were given 1.5 mg/kg metacam (Meloxicam) as an analgesic once per day for two days after surgery. Once returned to the home cage, animal health was assessed every two to three days. Mice were allowed to recover for ten days prior to engram labelling.

Mice were fed 40 mg kg⁻¹ doxycycline (DOX) for at least a week before surgery. Animals were individually handled for three min each day for three days immediately before the engram labelling. On the fourth day, the DOX diet was substituted for regular diet. After 36 hours, animals were subjected to Contextual Fear Conditioning (CFC). For CFC, animals were transported to an experimental room where they were allowed to explore a context for 3 minutes, followed by 3 successive 0.75 mA shocks

of 2 s duration spaced by one minute. Contextual cues used were a triangular shape inset and Benzaldehyde 0.25% (Med Associates Contextual Chambers). Immediately after CFC, animals were put back on DOX diet. Four to seven days after engram labelling, animals were sacrificed at the University of Leeds by an intraperitoneal injection of Sodium Pentobarbital at 100 mg/kg, followed by cardiac perfusion of NMDG cutting buffer (Table 2.1) and decapitation. Brains were dissected for experimentation.

Preparation of cryoEM grids via plunge-freezing

Whole hippocampi from two engram-labelled mice were homogenised in 500 μ L hACSF (Table 2.1) using a glass Teflon pestle and mortar (Cole-parmer). After optimisation of dilution and blotting parameters, homogenates were diluted 1:50 and combined with 10 nm diameter BSA-coated gold bead fiducials. Samples were loaded onto glow-discharged (Cressington Glow discharger; 60 s, 10^{-4} mV) 300 mesh Cu 1.2/1.3 grids (Quantifoil Microtools, Jena, Germany) pre-stained with tetraspecks (ThermoFisher) for alignment. Excess liquid was manually back-blotted for 8-10 s using filter paper (Whatman, grade 1). An FEI Vitrobot at 4°C and 95% humidity was used to plunge-freeze samples into liquid ethane at -180°C (Fig.2.2.2A) to vitrify tissue homogenate.

Preparation of acute slices

Mice underwent a schedule 1 intraperitoneal injection of pentobarbital before exsanguination and an intracardial perfusion of room temperature NMDG cutting buffer (Table 2.1). Coronal sections 100 μ m thick were prepared using a Leica vibratome (speed=0.26 mm/s) in ice-cold NMDG cutting buffer. The slices were recovered in hACSF at room temperature (Table 2.1) for 30-45 minutes. Samples used for cryoEM grid preparation were incubated in 1 μ M Hoechst 33342 solution (ThermoFisher, cat #62249) for at least 3 minutes to label cell bodies.

Live labelling and immunohistochemistry

For histological imaging of *Psd95^{GFP/GFP} GluN1^{FLAG/FLAG}* mouse brain regions, whole brains were fresh-frozen within optimal cutting temperature (OCT) compound by

submersion in isopentane surrounded by liquid nitrogen. OCT-embedded samples were mounted in a cryostat (Leica). At -18°C , $14\ \mu\text{m}$ thick brain sections were cut on a cryostat and attached to glass slides. Sections were fixed in ice-cold methanol for 7 minutes, washed in TBS (Table 2.1) and mounted in Vectashield mountant with DAPI (Vector Laboratories, Burlingame, CA).

For live-labelling of *Psd95^{GFP/GFP}GluN1^{FLAG/FLAG}* mouse brain, mice were subject to a cardiac perfusion of NMDG cutting buffer, before brains were dissected and $100\ \mu\text{m}$ thick acute coronal slices were cut in NMDG cutting buffer (Table 2.1) with a vibratome. Acute slices were incubated in 1:100 FLAG-CY3 antibody (Sigma, cat A9594) in ACSF buffer (Table 2.1) for 2 hours at room temperature with continued carbogen perfusion. For immunohistochemistry, free-floating coronal sections were fixed in 4 % PFA. After three washes in TBS (Table 2.1), slices were mounted in Vectashield mountant with DAPI (Vector laboratories, Burlingame, CA).

For immunohistochemistry of ChR2-EYFP-labelled and TRE-mCherry-labelled brains, whole brains were fresh-frozen within OCT compound by submersion in isopentane surrounded by liquid nitrogen. OCT-embedded samples were mounted in a cryostat (Leica). At -18°C , $14\ \mu\text{m}$ thick brain slices were cut and attached to glass slides. Slices were fixed in ice-cold methanol for 7 minutes and were stained with antibodies against Synapsin-1 (Invitrogen cat #A-6442, 1:200) or PSD-95 (Neuromab, cat #75-028, 1:200) at 4°C overnight. The next day, slides were washed in TBS. A secondary antibody was applied (ThermoFisher Goat Anti-Rabbit-AF 568, 1:1000, Goat Anti-Mouse-IgG2a-AF 594, 1:1000, or Goat Anti-Mouse-IgG1-AF 488) for 2 hours at room temperature. Tissue sections were washed 3 times for 5 minutes in TBS and mounted in Vectashield mountant with DAPI (Vector Laboratories, Burlingame, CA).

All images for analysis were captured using a confocal laser scanning microscope (Zeiss LSM 700) utilising a 63x oil objective lens with a 1.2 numerical aperture and frame size 1024×1024 pixels. For hippocampus overviews, 5×5 tilescans were collected using a 10x air objective lens with a 0.45 numerical aperture and frame size 1024×1024 pixels. Samples were obtained with a pixel size of $0.1\ \mu\text{m}$. Samples were imaged using 405 nm, 488 nm and 561 nm lasers to detect fluorophores (Table 2.2.1).

Colocalization was measured using the Coloc2 package in Fiji and the Pearson's correlation value was plotted.

Table 2.2.1: Excitation/emission spectra for each fluorophore used for immunohistochemistry.

Fluorophore	Excitation Wavelength (nm)	Emission Wavelength (nm)
DAPI	350	465
GFP	488	507
AF-488	488	496
EYFP	513	527
CY3	555	569
AF-568	578	603
AF-594	590	618

Conventional EM of fixed brain tissue

Samples were prepared by Dr Conny Leistner at the University of Leeds from adult (P65-P100) male *Psd95^{EGFP/EGFP}* knockin and wildtype mice. Fresh 2 mm diameter biopsy samples of the primary or secondary somatosensory cortex were collected from acute brain slices (prepared as previously described). Biopsies were fixed with chemi-fix buffer composed of 4% paraformaldehyde 2% glutaraldehyde in 50 mM phosphate (PB) pH 7.4 for 1 hour. Next, samples were washed three times in PB for 1 minute before post-fixation in 2% osmium tetroxide for 1 hour at room temperature. Subsequently, samples were washed three times in PB for 1 minute each, then once in 50% ethanol for 1 minute. Samples were stained with 4% w/v uranyl acetate in 70% ethanol for 1 hour at room temperature before dehydration with sequential washes in 70% ethanol, 90% ethanol, 100% ethanol, and 100% acetone for 5 minutes each. Samples were resin embedded by washing twice with propylene oxide for 20 minutes before incubation in 50% araldite epoxy resin in propylene oxide at room temperature overnight. Finally, samples were incubated twice in epoxy resin for 10-16 hours before the resin was polymerized in a mold at 60 °C for 3 days. Ultrathin (80-100 nm) sections

collected via room temperature ultramicrotomy by Martin Fuller at the University of Leeds were placed on 3.05-mm copper grids, stained with saturated uranyl acetate for 30 minutes, and then with Reynold's lead citrate for 5 minutes. Ultrathin specimens were imaged on a Technei F20 TEM at 5,000 and 29,000 magnification by Dr Conny Leistner at the University of Leeds.

High-pressure freezing

Acute slices (prepared as previously described) were incubated in 1 μ M Hoechst 33342 solution (ThermoFisher, cat #62249) to label the cell bodies for subsequent identification of the granular layer. For engram-labelled samples, acute slices were imaged on an EVOS Auto2 microscope with a 4x air objective (0.13 Ph LWD) and equipped with DAPI (Ex357/44, Em 447/60), GFP (Ex470/22, Em 510/42) and RFP (Ex531/40, Em 593/40) filter cubes (Invitrogen). Biopsy punches were taken from regions of interest using a 1 mm tissue puncher and were incubated in cryoprotectant (Table 2.1) for 30 mins at room temperature. 100 μ m deep wells inside 3 mm A-type gold carriers were filled with cryoprotectant and a single tissue punch. The A- and lipid-coated B- type carriers were loaded into the cartridge of the Leica EM ICE and were high-pressure frozen. Carriers were stored in liquid nitrogen.

Cryogenic fluorescence microscopy of carriers

Carriers were screened for fluorescence using a cryogenic fluorescence microscope (Leica cryo-CLEM with a HC PL APO 50x/0.9 NA cryo-objective, Orca Flash 4.0 V2 sCMOS camera (Hamamatsu Photonics), a Solar Light Engine (Lumencor) and DAPI (420-450 nm excitation; 420-450 nm emission), GFP (450-490 nm excitation; 500-550 nm emission) or YFP-ET (500/20 excitation, 535/30 emission), Rhodamine (375-407 nm excitation; 565-605 nm emission) and CY5 (608-648 nm excitation; 692-740 nm emission) filter sets. Regions of interest were identified based on the fluorescent signals and their location relative to cell bodies viewed in the DAPI channel. The CY5 channel was used to control for autofluorescence, such as ice contamination or microplastics. Tilescans of carriers were acquired using the LASX navigator and were used to direct cryo-ultramicrotomy.

Cryo-ultramicrotomy

High-pressure frozen carriers were mounted into the specimen holder of the Leica EM FC7 for cryo-sectioning (Al-Amoudi et al., 2004). Carriers were trimmed with a diamond knife (Diatome, Trim20) to expose a pyramid of tissue from the region of interest, based on screening. To generate ribbons, 70 nm to 150 nm thick cryo-sections were cut at -160 °C using a cutting knife (Diatome, cryo-immuo). The cryo-sections were pulled into ribbons with a gold eyelash using a micro-manipulator, then were transferred onto glow-discharged 300 mesh 3.5/1 Cu EM grids (Quantifoil Micro Tools, Jena, Germany).

Cryogenic fluorescence microscopy of grids

Tissue cryo-sections mounted on EM grids were screened for fluorescence using a cryogenic fluorescence microscope (Leica cryo-CLEM with a HC PL APO 50x/0.9 NA cryo-objective, Orca Flash 4.0 V2 sCMOS camera (Hamamatsu Photonics), a Solar Light Engine (Lumencor) and DAPI (420-450 nm excitation; 420-450 nm emission), GFP (450-490 nm excitation; 500-550 nm emission) or YFP-ET (500/20 excitation, 535/30 emission), Rhodamine (375-407 nm excitation; 565-605 nm emission) and CY5 (608-648 nm excitation; 692-740 nm emission) filter sets. An additional zoom factor of 5 was applied and images with frame size 2048x2048 pixels were obtained. Z-stacks of areas of interest were acquired with 30 % intensity and 0.2 s exposure time. Images were processed using Fiji ImageJ.

Cryogenic correlative light and electron microscopy and cryo-electron tomography

For the plunge-frozen samples, grid squares were selected for electron microscopy based on their fluorescent puncta and the thickness of the ice. Medium magnification images were collected of tissue sections with a pixel size of 6 nm. Ice and carbon foil holes were used as fiducials to estimate the locations of fluorescent regions. The high precision correlation between fluorescent images and electron micrographs was achieved using MatLab scripts and 10-15 fiducial markers (Kukulski et al., 2011; Schorb and Briggs, 2014). Tomograms were collected using an FEI Titan Krios G2, X-FEG and autoloader (camera: Energy-filtered Gatan K2 XP summit direct electron

1	Cortex	1	FEI Titan Krios, X- FEG, K2 XP	SerialEM	57	-6.33	3.42
1	Cortex	1	FEI Titan Krios, X- FEG, K2 XP	SerialEM	44	-6.70	3.42
1	Cortex	1	FEI Titan Krios, X- FEG, K2 XP	SerialEM	44	-6.70	3.42
1	Cortex	1	FEI Titan Krios, X- FEG, K2 XP	SerialEM	54	-5.81	3.42
1	Cortex	1	FEI Titan Krios, X- FEG, K2 XP	SerialEM	54	-6.60	3.42
1	Cortex	2	FEI Titan Krios, X- FEG, K2 XP	SerialEM	55	-6.70	3.42
1	Cortex	2	FEI Titan Krios, X- FEG, K2 XP	SerialEM	43	-6.10	3.42
2	Cortex	3	FEI Titan Krios, X- FEG, K2 XP	SerialEM	56	-6.28	3.42

3	Cortex	4	FEI Titan Krios, Falcon4- selectris	Tomo5	50	-4.14	3
4	CA3	5	FEI Titan Krios, Falcon4- selectris	Tomo5	55	-4.74	3
4	CA3	5	FEI Titan Krios, Falcon4- selectris	Tomo5	46	-4.30	3
4	CA3	5	FEI Titan Krios, Falcon4- selectris	Tomo5	59	-6.56	3
5	CA3	6	FEI Titan Krios, Falcon4- selectris	Tomo5	22	-5.55	3
5	CA3	6	FEI Titan Krios, Falcon4- selectris	Tomo5	41	-5.30	3
5	CA3	6	FEI Titan Krios, Falcon4- selectris	Tomo5	54	-5.14	3
5	CA3	6	FEI Titan Krios, Falcon4- selectris	Tomo5	43	-5.07	3

5	CA3	6	FEI Titan Krios, Falcon4- selectris	Tomo5	61	-4.31	3
5	CA3	6	FEI Titan Krios, Falcon4- selectris	Tomo5	40	-4.41	3
5	CA3	6	FEI Titan Krios, Falcon4- selectris	Tomo5	42	-3.98	3
5	CA3	6	FEI Titan Krios, Falcon4- selectris	Tomo5	61	-4.01	3
5	CA3	6	FEI Titan Krios, Falcon4- selectris	Tomo5	61	-3.65	3
5	CA3	6	FEI Titan Krios, Falcon4- selectris	Tomo5	56	-5.08	3
5	CA3	6	FEI Titan Krios, Falcon4- selectris	Tomo5	42	-5.23	3
5	CA3	6	FEI Titan Krios, Falcon4- selectris	Tomo5	42	-4.49	3

5	CA3	6	FEI Titan Krios, Falcon4- selectris	Tomo5	61	-4.31	3
5	CA3	6	FEI Titan Krios, Falcon4- selectris	Tomo5	55	-4.30	3
5	CA3	6	FEI Titan Krios, Falcon4- selectris	Tomo5	55	-5.30	3
5	CA3	6	FEI Titan Krios, Falcon4- selectris	Tomo5	50	-5.34	3
5	CA3	6	FEI Titan Krios, Falcon4- selectris	Tomo5	58	-6.04	3
5	CA3	6	FEI Titan Krios, Falcon4- selectris	Tomo5	55	-4.48	3
5	CA3	6	FEI Titan Krios, Falcon4- selectris	Tomo5	59	-4.01	3
5	CA3	6	FEI Titan Krios, Falcon4- selectris	Tomo5	42	-4.34	3

5	CA3	6	FEI Titan Krios, Falcon4- selectris	Tomo5	56	-5.07	3
5	CA3	6	FEI Titan Krios, Falcon4- selectris	Tomo5	59	-5.07	3
5	CA3	6	FEI Titan Krios, Falcon4- selectris	Tomo5	61	-5.08	3
5	CA3	6	FEI Titan Krios, Falcon4- selectris	Tomo5	61	-4.84	3
5	CA3	6	FEI Titan Krios, Falcon4- selectris	Tomo5	36	-4.56	3
5	CA3	6	FEI Titan Krios, Falcon4- selectris	Tomo5	51	-4.85	3
5	CA3	6	FEI Titan Krios, Falcon4- selectris	Tomo5	57	-4.41	3
5	CA3	6	FEI Titan Krios, Falcon4- selectris	Tomo5	52	-4.96	3

5	CA3	6	FEI Titan Krios, Falcon4- selectris	Tomo5	49	-5.23	3
5	CA3	6	FEI Titan Krios, Falcon4- selectris	Tomo5	61	-4.41	3
6	DG	7	FEI Titan Krios, Falcon4- selectris	Tomo5	59	-5.43	3
6	DG	7	FEI Titan Krios, Falcon4- selectris	Tomo5	47	-5.54	3
6	DG	7	FEI Titan Krios, Falcon4- selectris	Tomo5	57	-6.48	3
6	DG	7	FEI Titan Krios, Falcon4- selectris	Tomo5	51	-5.43	3
6	DG	7	FEI Titan Krios, Falcon4- selectris	Tomo5	61	-5.72	3
6	DG	7	FEI Titan Krios, Falcon4- selectris	Tomo5	58	-6.19	3

6	DG	7	FEI Titan Krios, Falcon4- selectris	Tomo5	46	-5.63	3
7	DG	8	FEI Titan Krios, Falcon4- selectris	Tomo5	61	-3.81	3
7	DG	8	FEI Titan Krios, Falcon4- selectris	Tomo5	46	-3.90	3
7	DG	8	FEI Titan Krios, Falcon4- selectris	Tomo5	55	-4.20	3
7	DG	8	FEI Titan Krios, Falcon4- selectris	Tomo5	42	-6.42	3
7	DG	8	FEI Titan Krios, Falcon4- selectris	Tomo5	45	-6.32	3
7	DG	8	FEI Titan Krios, Falcon4- selectris	Tomo5	61	-5.44	3

Table 2.2.3: Collection parameters for tomograms of engram synapses discussed in chapter 4. Defocus was estimated using Gctf.

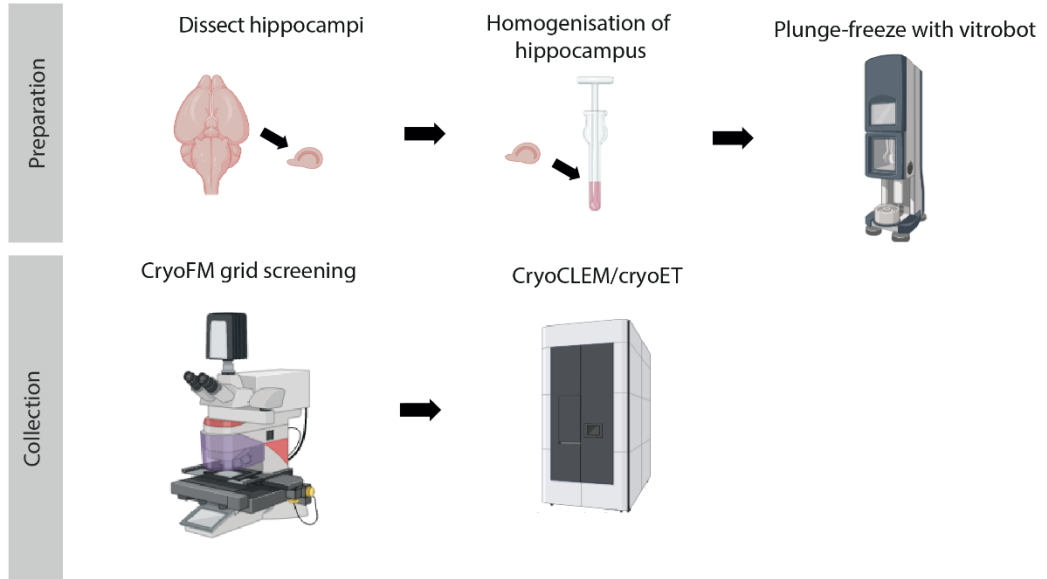
Mouse	Fluorophores	Dataset	Hardware	Software	Views	Defocus (μm)	Pixel size (\AA)
1	CaMKII- Chr2- EYFP/TRE- mCherry	1	FEI Titan Krios, Falcon4- selectris	Tomo5	53	-5.19	3.6
1	CaMKII- Chr2- EYFP/TRE- mCherry	2	FEI Titan Krios, Falcon4- selectris	Tomo5	42	-4.96	3
1	CaMKII- Chr2- EYFP/TRE- mCherry	2	FEI Titan Krios, Falcon4- selectris	Tomo5	56	-5.54	3
2	TRE-ChR2- EYFPP/TRE- mCherry	3	FEI Titan Krios, Falcon4- selectris	Tomo5	48	-3.84	3
3	TRE-ChR2- EYFPP/TRE- mCherry	4	FEI Titan Krios, Falcon4- selectris	Tomo5	61	-4.42	3
3	TRE-ChR2- EYFPP/TRE- mCherry	4	FEI Titan Krios, Falcon4- selectris	Tomo5	38	-4.78	3
3	TRE-ChR2- EYFPP/TRE- mCherry	4	FEI Titan Krios,	Tomo5	51	-5.40	3

			Falcon4-selectris				
3	TRE-ChR2-EYFPP/TRE-mCherry	4	FEI Titan Krios, Falcon4-selectris	Tomo5	45	-5.51	3
3	TRE-ChR2-EYFPP/TRE-mCherry	4	FEI Titan Krios, Falcon4-selectris	Tomo5	46	-5.50	3
3	TRE-ChR2-EYFPP/TRE-mCherry	4	FEI Titan Krios, Falcon4-selectris	Tomo5	61	-5.67	3
3	TRE-ChR2-EYFPP/TRE-mCherry	4	FEI Titan Krios, Falcon4-selectris	Tomo5	61	-5.55	3
3	TRE-ChR2-EYFPP/TRE-mCherry	4	FEI Titan Krios, Falcon4-selectris	Tomo5	61	-5.68	3
3	TRE-ChR2-EYFPP/TRE-mCherry	4	FEI Titan Krios, Falcon4-selectris	Tomo5	44	-3.26	3
3	TRE-ChR2-EYFPP/TRE-mCherry	4	FEI Titan Krios, Falcon4-selectris	Tomo5	55	-4.21	3
3	TRE-ChR2-EYFPP/TRE-mCherry	4	FEI Titan Krios,	Tomo5	61	-2.05	3

			Falcon4-selectris				
4	TRE-ChR2-EYFPP/TRE-mCherry	5	FEI Titan Krios, Falcon4-selectris	Tomo5	52	-4.60	3
4	TRE-ChR2-EYFPP/TRE-mCherry	5	FEI Titan Krios, Falcon4-selectris	Tomo5	54	-4.03	3
4	TRE-ChR2-EYFPP/TRE-mCherry	5	FEI Titan Krios, Falcon4-selectris	Tomo5	61	-4.09	3
4	TRE-ChR2-EYFPP/TRE-mCherry	5	FEI Titan Krios, Falcon4-selectris	Tomo5	38	-5.22	3
4	TRE-ChR2-EYFPP/TRE-mCherry	5	FEI Titan Krios, Falcon4-selectris	Tomo5	41	-4.53	3
4	TRE-ChR2-EYFPP/TRE-mCherry	5	FEI Titan Krios, Falcon4-selectris	Tomo5	49	-4.88	3
4	TRE-ChR2-EYFPP/TRE-mCherry	5	FEI Titan Krios, Falcon4-selectris	Tomo5	47	-3.40	3
4	TRE-ChR2-EYFPP/TRE-mCherry	5	FEI Titan Krios,	Tomo5	48	-4.03	3

			Falcon4-selectris				
4	TRE-ChR2-EYFPP/TRE-mCherry	5	FEI Titan Krios, Falcon4-selectris	Tomo5	60	-5.42	3
4	TRE-ChR2-EYFPP/TRE-mCherry	5	FEI Titan Krios, Falcon4-selectris	Tomo5	50	-4.88	3
4	TRE-ChR2-EYFPP/TRE-mCherry	5	FEI Titan Krios, Falcon4-selectris	Tomo5	61	-5.01	3
4	TRE-ChR2-EYFPP/TRE-mCherry	5	FEI Titan Krios, Falcon4-selectris	Tomo5	52	-3.14	3

A



B

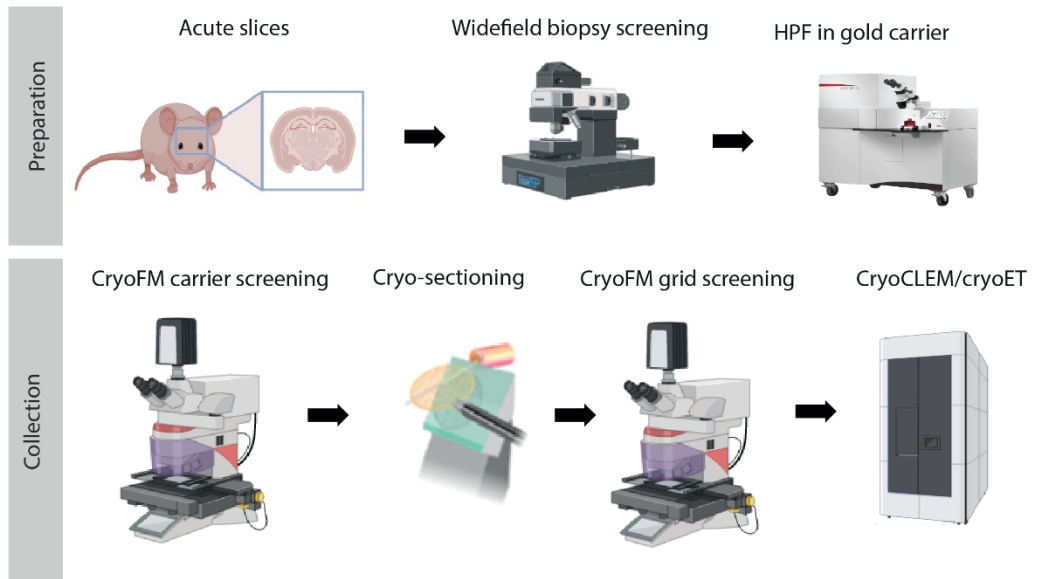


Figure 2.2.2: Schematic summary of in situ workflows

A) Hippocampi were dissected from murine brains and were homogenised in hACSF buffer, before being plunge-frozen onto cryoEM grids in liquid ethane with a vitrobot. CryoEM grids were screened using cryogenic fluorescence microscopy (cryoFM), before tilt series were collected using cryogenic correlated light and electron microscopy (cryoCLEM) and cryogenic electron tomography (cryoET).

B) Murine brains were dissected and cut into acute slices using a vibratome. A widefield microscope was used to direct biopsy collection from regions of interest. Tissue biopsies were high-pressure frozen into gold carriers. Carriers were screened with cryoFM to direct the collection of cryo-sections using cryo-ultramicrotomy. Cryo-sections were attached to cryoEM grids, which were screened using cryoFM to direct cryoCLEM and cryoET collections.

2.3 Data presentation and analysis

Ultrastructural analysis

Ultrastructural constituents of tomograms were identified based upon studies utilising conventional EM and cryoET (Table 2.3.1). All measurements were taken from bin4 tomograms (pixel size 12 Å).

Table 2.3.1: Criteria for the identification of ultrastructural constituents within cryo-tomograms.

Constituent	Description	Reference
Extracellular vesicle (including exosomes)	< 50 nm diameter membranous compartments found in	(Leistner et al., 2023)

	the extracellular space which close within the tomographic volume.	
F-Actin	~6 nm diameter branching filaments found intracellularly.	(Jung et al., 2020; Peukes et al., 2021)
Filopodium	< 60 nm diameter membrane-bound protrusions with a closed tip within the tomographic volume.	(Mattila and Lappalainen, 2008)
Ionotropic glutamate receptors (iGluRs)	Y-shaped densities found in the synaptic cleft of glutamatergic synapses. Each arm is 14 nm in length.	(Sobolevsky et al., 2009; Peukes et al., 2021)
Membrane lipid bilayer	5 nm diameter sheet-like density surrounding intracellular texture.	(Gold et al., 2014; Peukes et al., 2021; Leistner et al., 2023)
Mitochondrion	Membrane-bound organelle consisting of an outer membrane and a folded inner membrane composed of cristae.	(Wolf et al., 2017; Delgado et al., 2019)
Myelinated axon	Concentric rings of membrane lipid bilayer encapsulating a central compartment.	(Stassart et al., 2018; Gilbert et al., 2023; Creekmore et al., 2023)
Presynaptic vesicle	< 50 nm diameter intracellular	(Akert et al., 1964; Zuber and Lučić, 2019)

	compartments localised to a presynaptic compartment.	
Synapse	Comprised of presynaptic and postsynaptic compartments separated by a synaptic cleft containing cleft proteins. Presynaptic compartments are rich in presynaptic vesicles. Synaptic cryoCLEM labels correlate to these compartments.	(Schikorski and Stevens, 1997; Zuber et al., 2005; Tao et al., 2018; Peukes et al., 2021)

Molecular density was calculated using 31 voxel intensity line profiles from subvolumes of each synapse in Fiji Image J (Schindelin et al., 2012). Profiles were aligned to the lipid membranes, averaged, and background subtracted to calculate the relative density of molecular crowding within the compartments. Data were excluded if the postsynaptic compartment was obscured due to nearby ice or tissue damage from cryo-sectioning. Statistical analysis was performed in Microsoft excel, taking a Student's t-test per tomogram of all measurements between 5-30 nm from the postsynaptic membrane compared to those between 50-200 nm from the postsynaptic membrane. A Bonferroni correction was applied to the data. To analyse conventional EM data, one molecular density profile was collected from each 2D synapse. Profiles were aligned based on the lipid membrane, and regions 5-30 nm and 50-150 nm were compared via a Student's t-test.

Measurements of vesicle occupancy and diameter were collected and analysed using a combination of IMOD (Kremer et al., 1996) and a custom MatLab script (appendices). To measure diameter, pairs of model points were picked using IMOD at the central section of each vesicle. The first pair were placed at either end of the vesicle at its widest position. The second pair were placed perpendicular to the first, forming an overall cross shape with its centre at the centre of the vesicle. A new object was created for each vesicle. A custom MatLab script was used to measure between pairs, generating an information table indicating the distances between the points within each pair. Two measurements were used per vesicle to detect compression, which would be apparent if there was a consistent smaller measurement in one direction. To measure vesicle occupancy, the volume of space proximal (<45 nm from presynaptic membrane), intermediate (45-75 nm from presynaptic membrane) and distal (>75 nm from presynaptic membrane) occupied by vesicles was calculated (Radecke et al., 2023). Measurements refer to the position of the centre of the vesicle.

Distribution of cleft height was measured using dynamo software (Navarro et al., 2018) and MatLab scripts (Peukes et al., 2021). Points were placed along the pre- and post- synaptic membranes every 10 z-slices to create a model per membrane, which were exported as tables. A custom MatLab script (appendices) was used to measure the pairwise distance between the membrane points to calculate the distribution of distances. These distributions were plotted as kernel density plots.

Cluster analysis of cleft proteins was performed using PEET outputs of model points and a custom MatLab script (appendices), which calculated the number of receptors within a triangulation mesh.

F-Actin ultrastructural analysis was performed using an available MatLab toolkit (Dimchev et al., 2021). Briefly, model points were picked at either end of each filament using IMOD, before being exported into a Matlab table. Tables were

analysed using the lamellipodia analysis kit for multiple lamellipodia, giving outputs of number, volume fraction, angle, and length of filaments. The number of filaments was also plotted against database values for tomogram thickness, number of tilt angles and defocus. Slope analysis was performed in GraphPad Prism 10 software.

Segmentations of tomographic volumes were generated using a combination of IMOD (Kremer et al., 1996), dynamo (Navarro et al., 2018) and chimera-x 1.6 software (Pettersen et al., 2004). Graphs were produced and statistics were performed using GraphPad Prism 10 software. Figures were prepared in Adobe Illustrator. Schematics used content created with BioRender.com. Image processing workflows are summarised in Fig. 2.3.1.

Subtomogram averaging

For subtomogram averaging (STA) of synaptic cleft proteins in engram tomograms, a combination of Dynamo (Navarro et al., 2018), IMOD (Kremer et al., 1996), PEET (Nicastro et al., 2006; Heumann et al., 2011) and chimerax-1.6 (Pettersen et al., 2004) was used (Fig.2.3.2A). Membrane oversampling models were generated in Dynamo on 20 weighted back projected bin4 tomograms (pixel size 12 Å) from 2 mice (n=13 EE synapses, 7 ENE synapses). These were used for alignment and averaging in PEET (Nicastro et al., 2006; Heumann et al., 2011), using a 20x20x20 box, defined search parameters (Table 2.3.2), and the removal of duplicates. Classification was achieved with PCA analysis in PEET, producing 7 class averages, containing 70, 63, 43, 42, 38, 37 and 36 subvolumes, respectively. Chimera-x 1.6 (Pettersen et al., 2004) was used to dock published structures from PDB into subtomogram averaged maps.

Table 2.3.2: Search parameters for subtomogram averaging of synaptic proteins using membrane oversampling with duplicate removal.

Iteration	Angular Search Range						Search	Low-Pass		Ref
	Phi		Theta		Psi		Distance	Filter		
	Max	Step	Max	Step	Max	Step		CutOff	Sigma	Threshold
1	0	1	0	1	0	1	0	0.1	0.05	100
2	180	30	24	8	24	8	5	0.1	0.05	100
3	30	10	12	4	12	4	4	0.1	0.05	100
4	15	5	6	2	6	2	3	0.1	0.05	100
5	7.5	2.5	3	1	3	1	2	0.1	0.05	100
6	3.75	1.25	1.5	0.5	1.5	0.5	2	0.1	0.05	100

For STA of microtubules in engram and *Psd95^{GFP/GFP} GluN1^{FLAG/FLAG}* tomograms (Fig.2.3.2B), models were generated on bin4 (pixel size 12 Å) CTF-corrected tomograms in IMOD. Co-ordinates were picked as a two-point contour with the respective head and tail model points positioned at the poles of each axial microtubule. To improve alignment, model points were added every 3 voxels using AddModPoints. Averaging was performed in PEET with a 32x26x32 box and cylindrical mask (Nicastro et al., 2006; Heumann et al., 2011). For *Psd95^{GFP/GFP} GluN1^{FLAG/FLAG}* samples, 157 microtubules within 42 tomograms from 6 mice were used, generating 483 subvolumes for averaging. For engram samples, 81 microtubules within 19 tomograms from 2 mice were used, generating 997 subvolumes for averaging. For both projects, 4 search iterations were used with strict search limits (Table 2.3.3). Chimera-x 1.6 was used to dock published structures from PDB to validate the structures. Fourier shell correlation (FSC) plots were calculated in PEET.

Table 2.3.3: Search parameters for the subtomogram averaging of microtubules with duplicate removal.

Iteration	Angular Search Range						Search	Low-Pass		High-Pass		Ref
	Phi		Theta		Psi		Distance	Filter		Filter		
	Max	Step	Max	Step	Max	Step		CutOff	Sigma	CutOff	Sigma	Threshold
1	12	4	0	1	0	1	5	0.15	0.05	0.15	0.05	225
2	6	2	6	2	6	2	4	0.2	0.05	0.2	0.05	225
3	3	1	3	1	3	1	2	0.25	0.05	0.25	0.05	225
4	1.5	0.5	1.5	0.5	1.5	0.5	2	0.25	0.05	0.25	0.05	225

For STA of iGluRs in tomograms from *Psd95^{GFP/GFP} GluN1^{FLAG/FLAG}* mice, 137 two-point contours of Y-shaped synaptic cleft densities 14 nm in length were manually picked from 28 bin4 (pixel size 12 Å) CTF-corrected weighted back projection tomograms from 6 mice. Stalklnit was used to generate centroid models, initial motive lists and rotation axes files for alignment and averaging in PEET with a 20x20x14 box size and a custom binary mask (Fig.2.3.2C) using defined search parameters (Table 2.3.4). The fourier shell correlation (FSC) plot was calculated in PEET.

Table 2.3.4: Search parameters for the subtomogram averaging of putative ionotropic glutamate receptors with duplicate removal.

Iteration	Angular Search Range						Search	Low-Pass		Ref
	Phi		Theta		Psi		Distance	Filter		
	Max	Step	Max	Step	Max	Step		CutOff	Sigma	Threshold
1	0	1	0	1	0	1	0	0.1	0.05	100
2	180	30	24	8	24	8	5	0.1	0.05	100
3	30	10	12	4	12	4	4	0.1	0.05	100
4	15	5	6	2	6	2	3	0.1	0.05	100
5	7.5	2.5	3	1	3	1	2	0.1	0.05	100
6	3.75	1.25	1.5	0.5	1.5	0.5	2	0.1	0.05	100

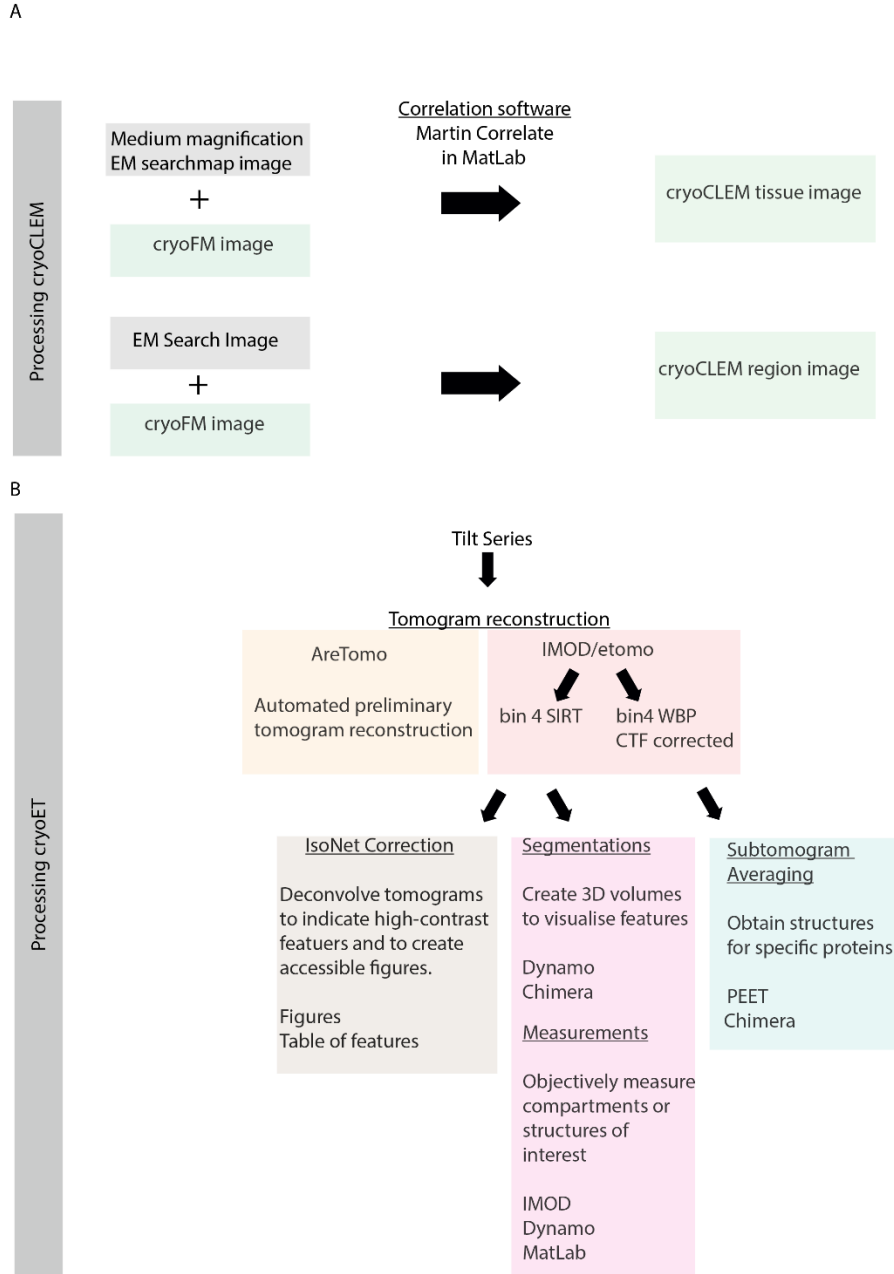


Figure 2.3.1: Flow diagrams showing processing workflows.

A) CryoCLEM correlation was achieved using the `martin_correlate` package on cryoFM and cryoEM images within MatLab, in which fiducials such as carbon holes or tissue edges were used to align FM and EM images with high precision.

B) CryoET processing incorporated multiple software including AreTomo, IMOD, IsoNet, Dynamo and ChimeraX-1.6.

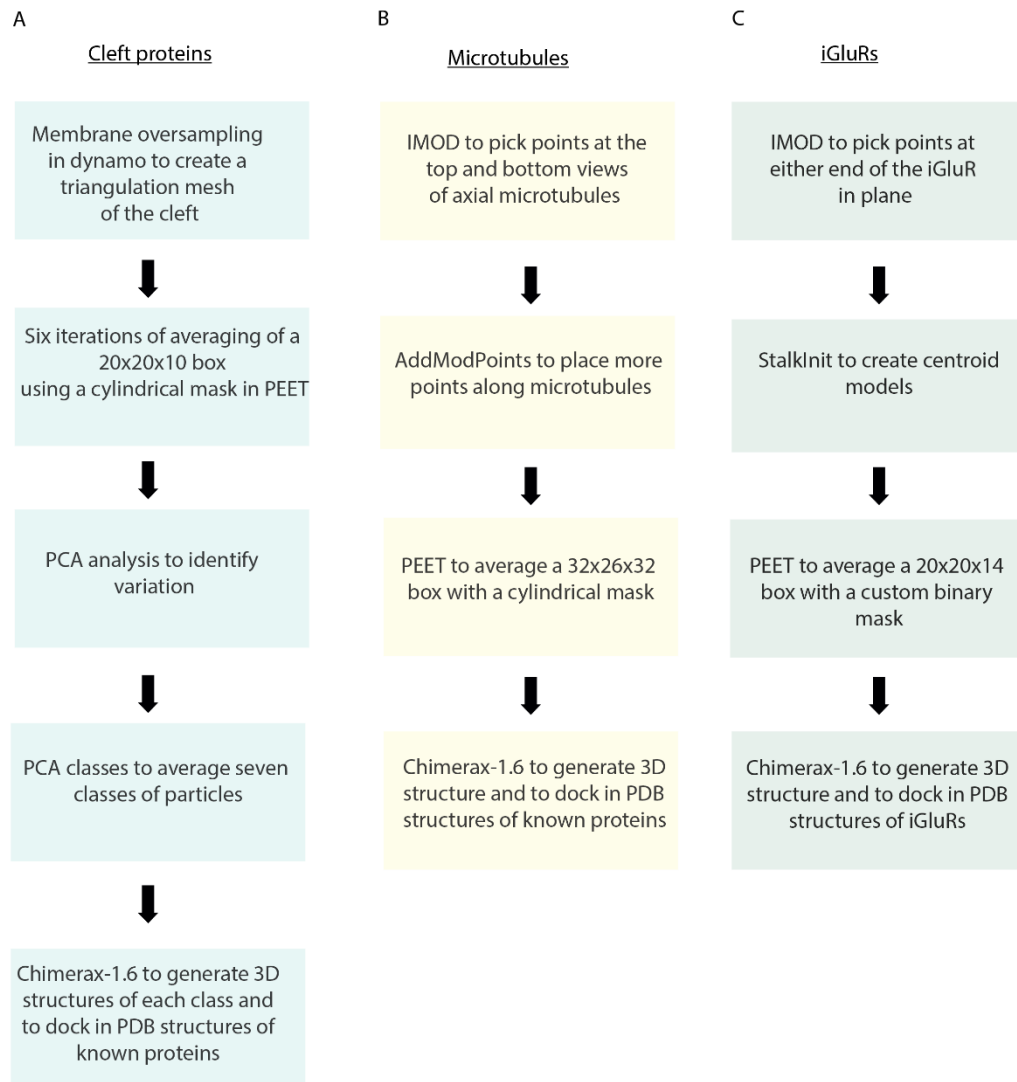


Figure 2.3.2: Flow diagrams depicting protocols used for subtomogram averaging.

A) Workflow to align, classify and class average synaptic cleft proteins.

B) Workflow to align, classify and average microtubules.

C) Workflow to align, classify and average ionotropic glutamate receptors (iGluRs).

Chapter 3: The *in-tissue* Molecular Architecture of Glutamatergic Synapses

Multiple brain regions contribute towards memory functions, with region-specific roles in distinct stages and types of memory (Squire, 2004). For example, the hippocampus is important for episodic memory acquisition and processing, utilizing sensory input from the cortex to collate information (Johnston and Amaral, 2004; Squire, 2004; Ramirez et al., 2014; Billig et al., 2022), whereas the cortex is important for sensory information and the storage of long-term memories for subsequent hippocampal retrieval (Chklovskii et al., 2004; Tanaka et al., 2014; Tonegawa et al., 2015). Underlying these properties are synapses, which are essential for communication within neuroanatomical circuits (Bliss and Lømo, 1973; Davis et al., 1992; Klann et al., 2004; Poo et al., 2016), and can be modified dynamically by plasticity mechanisms (Bliss and Lømo, 1973; Collingridge et al., 1983; Nabavi et al., 2014). Moreover, diversity in protein expression exists between synapses across the brain (Zhu et al., 2018; Bulovaite et al., 2022). Together, these observations suggest that synapses have variable molecular architectures, which could relate to their specific roles or location.

Neurotransmitters are essential for neurochemical communication at synapses, with glutamate, the predominant excitatory neurotransmitter in the brain, activating ionotropic and metabotropic receptors (Somogyi et al., 1998; Meldrum, 2000). In the hippocampus, excitatory glutamatergic neurons account for approximately 80% of neurons, whereas inhibitory GABAergic neurons are fewer in number (Klausberger and Somogyi, 2008; Basu and Siegelbaum, 2015). Most excitatory synapses in the cortex are also glutamatergic (Somogyi et al., 1998), indicating that glutamatergic synapses are particularly important for neuronal communication in the mammalian brain.

Accordingly, compositional and functional differences exist between synapses in different brain regions (Zhu et al., 2018; Bulovaite et al., 2022), reflecting the diverse roles in memory formation and storage (Johnston and Amaral, 2004;

Chklovskii et al., 2004; Squire, 2004; Tanaka et al., 2014; Billig et al., 2022). In the cortex, where long-term memories are stored (Chklovskii et al., 2004; Tonegawa et al., 2015), there is diversity in gene expression, morphological properties, and electrophysiological properties (Harris and Shepherd, 2015; Tremblay et al., 2016; Scala et al., 2020; Bulovaite et al., 2022). Excitatory glutamatergic synapses are critical for communication between cortical neurons and have variable responses to presynaptic release of neurotransmitter (Di Maio, 2021), including a 24% smaller probability of release at synapses with contralateral input compared to ipsilateral (Le Bé et al., 2007). Moreover, the cortex is associated with a longer protein half-life, with Psd95 protein, essential to mature glutamatergic synapses, exhibiting a 12.1-day half-life in the motor cortex compared to 5.5 days in the CA1 region and 3.0 days in the CA3 region (Bulovaite et al., 2022), which could relate to the more stable and less plastic synapses in the cortex, reflecting role of the cortex in memory storage as opposed to acquisition. Hence, functional and compositional variation exists in cortical neurons and synapses, and some of these features are region-specific, suiting the cortex to memory storage roles.

In contrast, the hippocampus is crucial for memory acquisition (Ramirez et al., 2014; Choi et al., 2018; Ryan et al., 2021), and involves distinct neuroanatomical pathways. There are two main neuronal pathways in the hippocampus (Fig.1.1.2B). In the tri-synaptic pathway (Entorhinal cortex Layer-II (EC LII) → Dentate Gyrus (DG) → Cornu Ammonis 3 (CA3) → Cornu Ammonis 1 (CA1)), the EC LII stellate cells excite the granule cells of the DG via the glutamatergic perforant path, inducing activation of the mossy fiber projections to excite CA3 pyramidal neurons, in turn exciting CA1 pyramidal cells through the Schaffer collateral pathway. In contrast, in the direct pathway (Entorhinal cortex Layer-III (EC LIII) → CA1), the CA1 pyramidal neurons are directly excited by the perforant path from EC LIII (Squire, 2004; Basu and Siegelbaum, 2015; López-Madrona et al., 2017). The excitatory drive from the tri-synaptic and direct pathways to the CA1 region differs due to the distinct dendritic locations of the indirect proximal

synapses in the *Stratum Radiatum* and the direct pathways in the *Stratum Lacunosum* (Squire, 2004; Basu and Siegelbaum, 2015). The indirect pathway provides strong excitation, compared to the weak excitation of the direct pathway, representing some diversity in glutamatergic neurons across the hippocampus.

Specifically, the DG has a largely unilateral nature, which could be functionally crucial to its role in the production of declarative memories (Amaral et al., 2007). Compositionally, the DG exhibits short Psd95 protein lifetime, indicative of high protein turnover (Bulovaite et al., 2022), relating to ongoing plasticity mechanisms. The CA3 is part of the hippocampus proper (Squire, 2004; Basu and Siegelbaum, 2015), exhibiting shorter Psd95 lifespan, and therefore synaptic protein turnover, compared to the CA1 and CA2, suggesting that here synaptic protein lifespan is determined by cell-wide mechanisms (Bulovaite et al., 2022). Within the CA3 region, mossy fibres form synapses with CA3 dendrites characterized by a presynaptic mechanism of LTP, with plasticity-dependent depotentiation evident (Vyleta et al., 2016). Finally, the CA3 has been evidenced to contain a sub-population of larger postsynaptic compartments (Harris and Weinberg, 2012; Broadhead et al., 2016; Cizeron et al., 2020), suggesting a structural difference at the dendrites.

Hence, functional and compositional differences exist within and between the cortex, DG and CA3 regions, relating to their roles in memory acquisition and storage. It is likely that architectural differences exist at these synapses, which remains to be explored in cryopreserved, unfixed tissue with cryoET.

Therefore, it was hypothesized that:

1. Region-dependent structural differences exist at excitatory glutamatergic synapses (Zhu et al., 2018; Böger et al., 2019; Bulovaite et al., 2022), reflecting the varying roles of synapses in long-term memory functions over time (Klausberger and Somogyi, 2008; Mayford et al., 2012).

2. Differences exist in synaptic architecture within each brain region, reflecting the variability in synaptic strength and dendritic location (Squire, 2004; Bourne and Harris, 2012; Basu and Siegelbaum, 2015).

Here, a workflow utilizing mouse genetics, high-pressure freezing, cryoCLEM and cryoET was developed to explore the molecular organization of glutamatergic synapses in the cortex, DG and CA3 within cryopreserved, unfixed, unstained tissue, enabling investigations into the various glutamatergic synapses in different brain regions.

3.1 The in-tissue architectures of glutamatergic cortical and hippocampal synapses in cryo-sections have variable postsynaptic density (PSD) distribution

To determine the structure of native cortical excitatory synapses, knockin mice (*Psd95^{GFP/GFP}*) with an in-frame C-terminal fusion of the fluorescent tag EGFP to the gene encoding Psd95 were used (Frank et al., 2016; Broadhead et al., 2016; Zhu et al., 2018). Psd95 is a cytoplasmic protein that concentrates within mature glutamatergic synapses and forms supercomplexes with ionotropic glutamate receptors residing on the postsynaptic membrane (Frank et al., 2016). The signal from *Psd95^{GFP/GFP}* knockin mice indicates the location of mature glutamatergic synapses without over-expression, detectible effect on electrophysiological function, synaptic function or ability for psd95 to form supercomplexes (Frank et al., 2016; Broadhead et al., 2016; Zhu et al., 2018). Therefore, glutamatergic synapses were identifiable with cryoCLEM (Supp.Fig.1).

To vitrify tissue, biopsies were taken from the cortex of acute coronal slices of anatomically intact adult *Psd95^{GFP/GFP}* brain and were cryopreserved by high-pressure freezing within cryoprotectant. Using cryo-ultramicrotomy, 70-150 nm thick vitreous brain tissue sections were collected (Fig. 3.1.2A). Glutamatergic synapses were identified within cryo-sections by cryoCLEM (Fig 3.1.2B), from which 9 cryo-electron tomograms were collected from 3 mice, revealing the cryopreserved in-tissue architecture of cortical glutamatergic synapses (Fig.3.1.1;

Fig. 3.1.2D, Supplementary Table 1). A great diversity of subcellular compartments and organelles existed in and around glutamatergic synapses, as demonstrated in tissue segmentations of glutamatergic synapses and their surrounding environment (Fig. 3.1.2C) and documented in Fig.3.1.1 and Supplementary Table 1. Hence, glutamatergic synapses were identified and analysed within vitreous tissue.

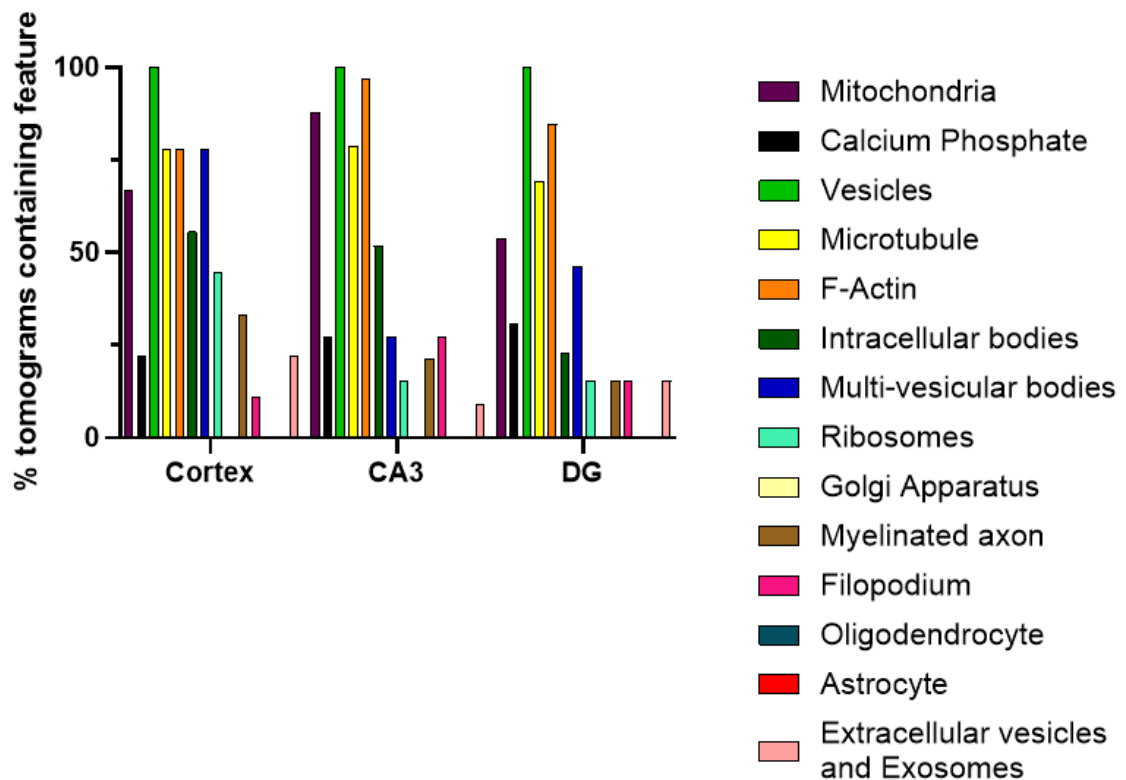


Figure 3.1.1: Graphical representation of constituents within tomograms of glutamatergic synapses from the cortex, CA3 and DG brain regions.

Variable numbers of organelles and vicinal features were identified across the cortex, CA3 and DG regions, indicating diversity in synaptic architecture in all brain regions. Data are presented as a percentage of tomograms containing each feature. Cortex, n=9 tomograms from 3 mice, CA3, n=33 tomograms from 2 mice, DG n=13 tomograms from 2 mi

The glutamatergic cortical synapses shared features with those previously reported via conventional EM (Gray, 1959; Harris and Weinberg, 2012), and in cryoET studies of synapses reported in ultra-fresh synaptosomes (Peukes et al., 2021) and cultured neurons (Tao et al., 2018). These features included a presynaptic compartment packed with presynaptic vesicles (Tao et al., 2018; Zuber and Lučić, 2019; Radecke et al., 2023), a postsynaptic compartment characterized by an extensive F-Actin cytoskeleton (Peukes et al., 2021), and a synaptic cleft separating the two containing numerous proteins (Martinez-Sanchez et al., 2021) (Fig.3.1.2C).

However, differences were observed when compared to conventional EM studies of synapses. Based on conventional EM of fixed, dehydrated, heavy-metal-stained tissue, glutamatergic synapses were indicated to have a conserved 30-50 nm layer of more densely packed proteins on the cytoplasmic side of the postsynaptic membrane called the postsynaptic density (PSD) (Gray, 1959; El-Din El-Husseini et al., 2000; Chen et al., 2000) (Fig.3.1.2E). However, within the fresh, cryopreserved cortical synapses reported here, this feature was not a conserved sheet-like component present in all synapses. Instead, the architecture was variable, suggesting that not all glutamatergic synapses are characterised by a dense PSD. Similar variability was previously reported in cryoET of cultured neurons (Tao et al., 2018) and homogenized glutamatergic synapse structures (Peukes et al., 2021). It is likely that the high-contrast sheet-like conserved PSD observed in conventional EM misrepresents the organization of synapses due to the chemical fixation, dehydration, heavy metal staining and projection involved. This treatment washes out some components that cannot be fixed, such as non-protein containing lipids, carbohydrates, leaving behind the membrane-bound structures, which have a high relative contrast when stained.

To confirm that the variable PSD was not caused by the *Psd95^{GFP/GFP}* knockin mutation or by sample preparation, conventional EM was performed (Fig 3.1.2E). These data indicated clear PSDs in *Psd95^{GFP/GFP}* comparable to those in wildtype mice (Fig. 3.1.2E) and in the literature (Gray, 1959).

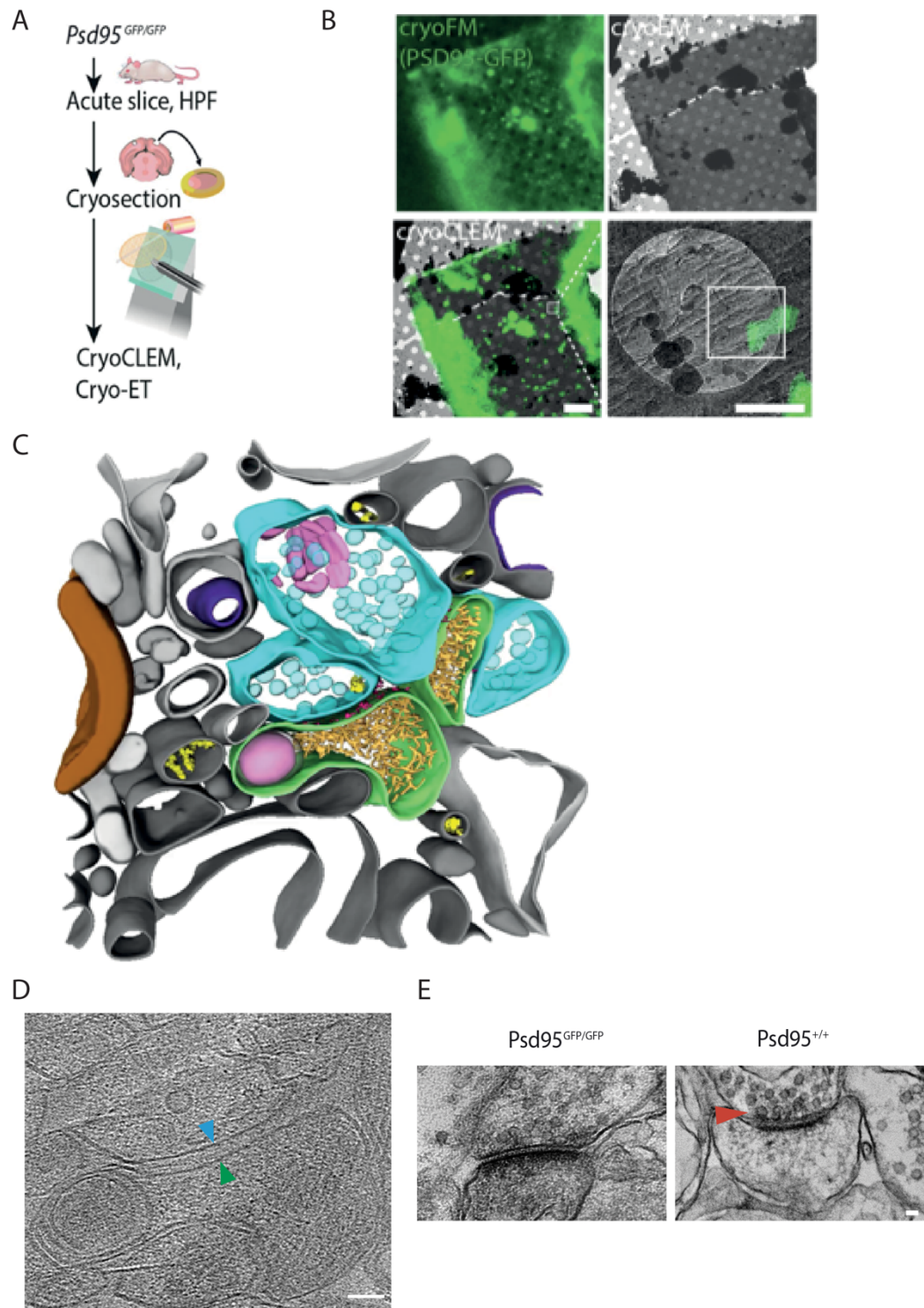


Figure 3.1.2: The in-tissue architecture of native glutamatergic cortical synapses in cryo-sections.

A) Schematic showing the cryoCLEM and cryoET workflow using thin vitreous sections from brains of adult $Psd95^{GFP/GFP}$ knockin mice to determine the in-tissue architecture of glutamatergic synapses in the cortex. Mice are culled and dissected. Acute slices 100 μm thick are collected, and 2 mm diameter biopsy of cortex are high-pressure frozen. Next, 150 nm thick cryo-sections are cut from vitrified tissue and attached to cryoEM grids for cryoCLEM and cryoET. Created with BioRender.com

B) CryoCLEM of cryoEM grid square containing 150 nm thick cryo-sections. Top left, cryoFM image of a holey carbon grid square. Top right, cryoEM image of the same grid square shown in top left. Bottom left, merged image of cryoFM and cryoEM images indicating location of $Psd95\text{-GFP}$ puncta. Scale bar, 5 μm . Black box indicates region enlarged in Bottom right, showing $Psd95\text{-GFP}$ associated with postsynaptic membrane (PoSM). White box indicates region where images for the tomogram shown in D were acquired. Scale bar, 500 nm.

C) 3D segmentation of membranes and macromolecules in a representative tomographic volume of a $Psd95$ -containing glutamatergic synapse within thin vitreous cryo-section of adult mouse cortex. The PoSM (green) was identified by $PSD\text{-GFP}$ cryoCLEM and the presynaptic membrane (PreSM) (cyan) was identified by its tethering to the PoSM and the prevalence of synaptic vesicles. Salient organelle and macromolecular constituents are indicated: Magenta, membrane proteins within synaptic cleft. Purple, mitochondrion. Yellow, microtubule. Pink, putative endosomal compartment. Brown, myelin. Gold, actin. Grey, vicinal membrane-bound subcellular compartments.

D) Tomographic slice through cryo-electron tomogram of $Psd95\text{-GFP}$ containing synapse within thin vitreous cryo-section of adult mouse cortex. Cyan arrowhead, presynaptic membrane. Green arrowhead, postsynaptic membrane. Scale bar = 50 nm.

E) Conventional negative-stain EM of synapses in chemically fixed, resin-embedded, heavy metal-stained acute brain slice biopsies from Psd95^{GFP/GFP} knockin (left) and wildtype (right), respectively. Red arrowhead, postsynaptic density. Scale bar = 50 nm. Conventional EM samples prepared by Martin Fuller and imaged by Conny Leistner.

B-D use one representative tomogram from one mouse. E uses two representative 2D EM images from two mice.

The hippocampus has a laminar anatomical architecture with the clustering of cell bodies marking distinct regions (Ramón y Cajal, 1909; Johnston and Amaral, 2004). To explore synapse diversity by anatomical region, the distribution of cell nuclei was marked with Hoechst indicator, enabling the identification of these distinct neuroanatomical layers within the hippocampus. Acute brain slices were incubated in Hoechst indicator before biopsy punches were taken from the cortex and hippocampus. The high-pressure frozen samples were imaged in gold carriers with cryoFM to identify the regions of interest (Fig. 3.1.3). This information was used to direct collection of cryo-sections for cryoCLEM and cryoET, specifically obtaining cryo-sections from the molecular layers (Johnston and Amaral, 2004), which are known to contain synapses.

Cryopreserved vitreous sections from the hippocampal CA3 and DG regions were collected and imaged with cryoCLEM and cryoET (Fig. 3.1.4A), resulting in 33 CA3 and 13 DG synaptic tomograms from a total of 4 mice. Psd95-GFP correlated to postsynaptic compartments (Fig.3.1.4A). Diverse architectures, including a range of organelles and macromolecular complexes, were observed within and between regions (Fig.3.1.1; Supplementary Table 1), similarly to the cortex. Noticeably, a distinct PSD was not observed in all synapses.

To explore the distribution of macromolecules within cortical synapses, the molecular density profiles of the pre- and post- synaptic compartments were analysed (Fig. 3.1.4B) by measuring the voxel intensity profiles in 31 subvolumes aligned to the lipid membranes (Fig.3.1.4B). No significant differences were observed between synapses via an ANOVA with Tukey's posthoc analysis, $p > 0.05$, from the cortex (Fig.3.1.4C), DG (Fig.3.1.4D) and CA3 (Fig.3.1.4E), with each group showing variability in the molecular density throughout the postsynaptic compartments. Therefore, data were compiled, indicating variability in molecular density in cryopreserved glutamatergic synapses, with 36% exhibiting a significantly more molecularly dense region ($n=22$, Student's t-tests, $p < 0.05$) proximal to the postsynaptic membrane (Fig.3.1.5A) in contrast to 100% ($n=5$, Student's t-test, $p < 0.05$) of synapses imaged by conventional EM (Fig.3.1.5B). Hence, a PSD is not a conserved and essential component of all glutamatergic synapses.

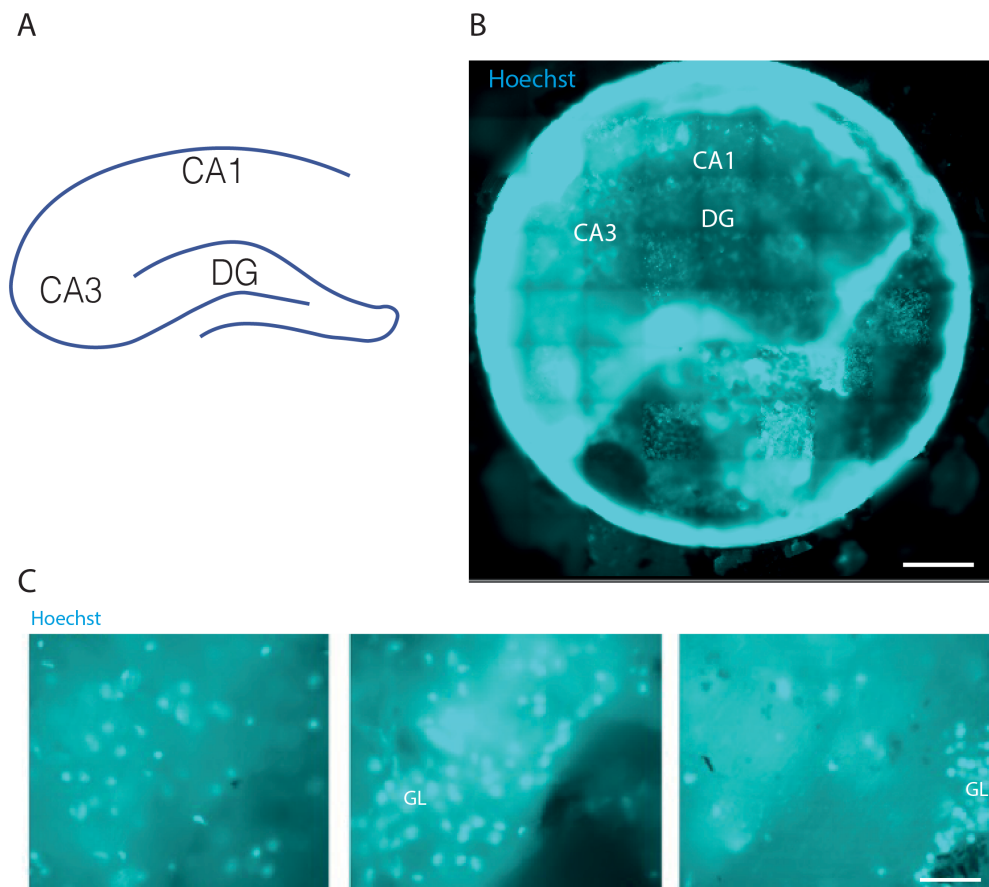


Figure 3.1.3: Identification of anatomical region in high-pressure frozen brain biopsies based on cell body labelling.

A) Schematic of the hippocampus in a coronal section. The granular layers are indicated in blue. CA1, Cornu Ammonis 1; CA3, Cornu Ammonis 3; DG, Dentate Gyrus.

B) Example tilescans of high pressure-frozen tissue within gold carriers with the same regions indicated. Scalebar = 250 μm .

C) Individual images from a carrier indicating the granular layer (GL), a region of densely packed cell bodies which was avoided in cryo-section collections to obtain tomograms of synapses from the molecular layer. Scalebar = 50 μm .

Example images are from one biopsy from one mouse.

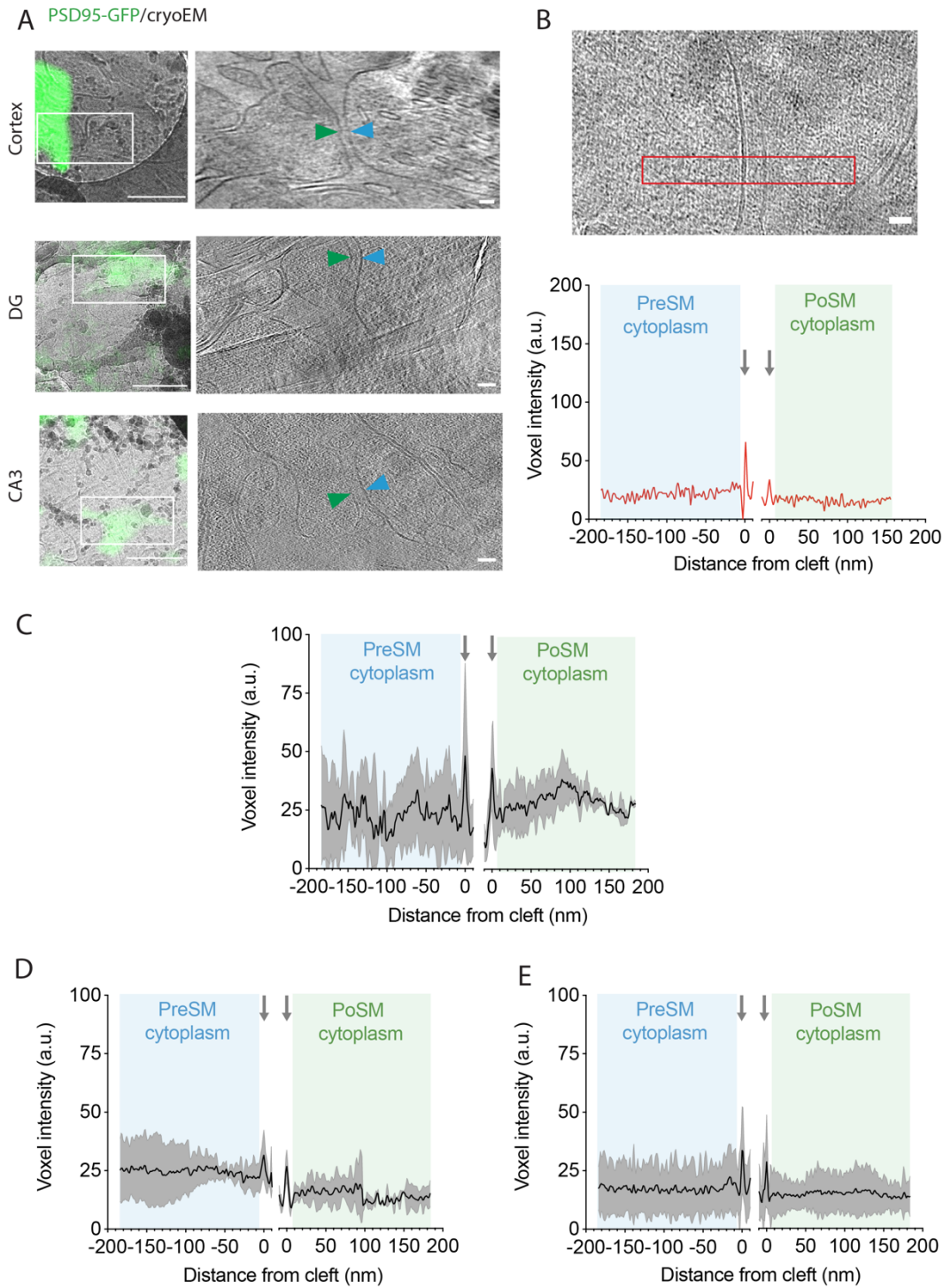


Figure 3.1.4: Cryo-preserved vitreous glutamatergic synapses had variable molecular crowding profiles independent of brain region.

A) Left, cryoCLEM of tissue cryo-sections from the cortex, DG and CA3 regions of the brain. White boxes indicate the regions depicted on right in tomographic slices. Green arrowhead, postsynaptic membrane (PoSM) and cyan arrowhead, presynaptic membrane (PreSM). Scalebars = 0.5 μ m, 20 nm.

B) Top, tomographic slice from the CA3 region with white box indicating the region from which molecular distribution was measured on this tomographic slice. Scalebar = 20 nm. Bottom, voxel intensity (a.u.) of presynaptic (cyan) and postsynaptic (green) cytoplasm from the same synapse as the example tomographic slice above. Profiles were taken from 31 subvolumes and were aligned to the presynaptic (PreSM) or postsynaptic membrane (PoSM) (grey arrows).

C) Voxel intensity (a.u.) of presynaptic (cyan) and postsynaptic (green) cytoplasm at 4 synapses measured from 31 subvolumes each collected from cortical cryo-sections from 2 mice. Data are represented as mean voxel intensity profile \pm SD. Profiles were aligned to the lipid membrane peak of the presynaptic (PreSM) or postsynaptic membrane (PoSM) (grey arrows).

D) Voxel intensity (a.u.) of presynaptic (cyan) and postsynaptic (green) cytoplasm at 3 synapses measured from 31 subvolumes each collected from DG cryo-sections from 2 mice. Data are represented as mean voxel intensity profile \pm SD. Profiles were aligned to the lipid membrane peak of the presynaptic (PreSM) or postsynaptic membrane (PoSM) (grey arrows).

E) Voxel intensity (a.u.) of presynaptic (cyan) and postsynaptic (green) cytoplasm at 15 synapses measured from 31 subvolumes each collected from CA3 cryo-sections from 2 mice. Data are represented as mean voxel intensity profile \pm SD. Profiles were aligned to the lipid membrane peak of the presynaptic (PreSM) or postsynaptic membrane (PoSM) (grey arrows).

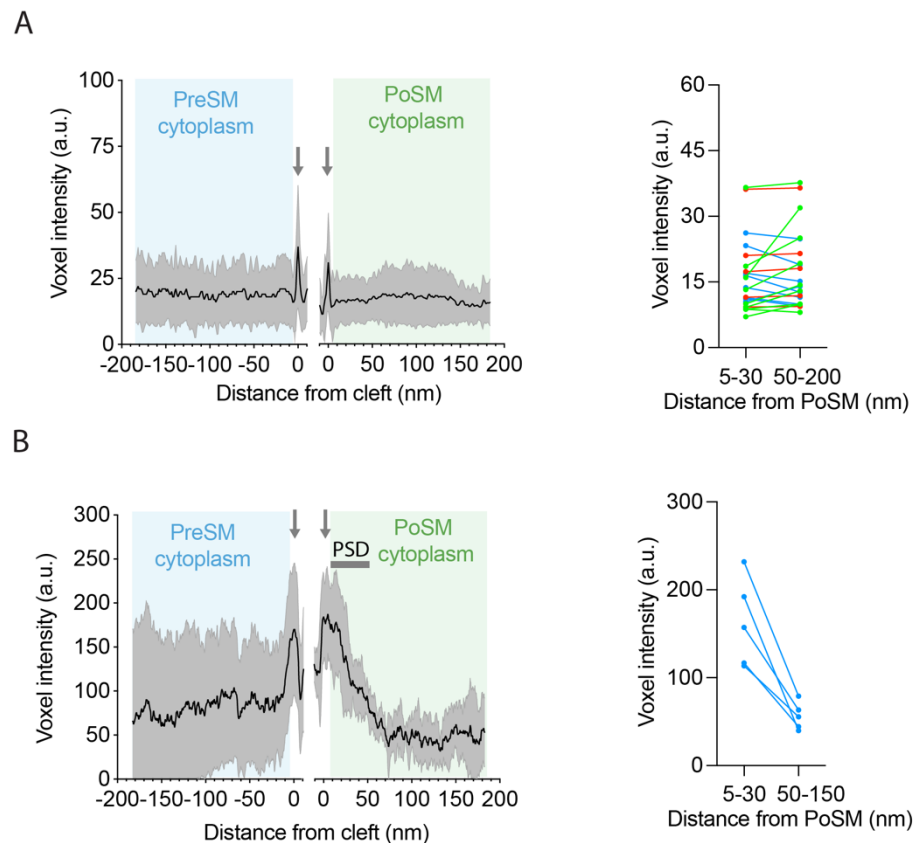


Figure 3.1.5: The PSD is not always significantly more molecularly dense than regions distal to the membrane in cryopreserved tissue.

A) Left, the voxel intensity (a.u.) of presynaptic (cyan) and postsynaptic (green) cytoplasm at 22 synapses measured from 31 tomographic subvolumes per tomogram collected from cortical and hippocampal cryo-sections from 6 mice. Data are represented as mean voxel intensity profile \pm SD. Profiles were aligned to the lipid membrane peak of the presynaptic (PreSM) or postsynaptic membrane (PoSM) (grey arrows). Right, the average voxel intensity in regions 5-30 nm from the PoSM and regions 50-150 nm from the PoSM. Blue indicates a significantly higher voxel intensity proximal to the PoSM; Green indicates a significantly higher voxel intensity distal to the PoSM; Red indicates no significance between the proximal and distal regions (via Student's *t*-tests).

B) Left, the voxel intensity (a.u.) of presynaptic (cyan) and postsynaptic (green) cytoplasm measured from 2D images of resin-embedded stained cortical sections. The average intensity is indicated in black. Profiles were aligned to the lipid membrane peak of the PreSM or PoSM (grey arrows). A clear, conserved PSD (red) was detected proximal to the postsynaptic membrane, with a higher molecular density than the rest of the postsynaptic compartment. Right, the average voxel intensity across 5-30 nm from the PoSM compared to that of 50-150 nm from the postsynaptic PoSM. Blue indicates a significantly higher voxel intensity proximal to the PoSM (via Student's t-tests).

3.2 The CA3 hippocampal region contains a sub-population of larger postsynaptic compartments

To investigate postsynaptic compartment size, fixed slices were imaged via confocal microscopy and cryo-sections were imaged via cryoFM, enabling measurements of Psd95-GFP puncta size. Analysis indicated that there was a sub-population of significantly larger Psd95 puncta in the CA3 region (Fig 3.2AB) in agreement with previous literature (Broadhead et al., 2016). In confocal image analysis, the CA3 region displayed a significantly larger mean punctum area compared to the DG and CA1 regions ($0.41 \mu\text{m}^2$, $n = 1119$ puncta in the CA3 compared to $0.20 \mu\text{m}^2$, $n = 818$ puncta in the DG and $0.22 \mu\text{m}^2$, $n = 908$ in the CA1; one-way ANOVA with Tukey's posthoc analysis, $p < 0.0001$). These observations were reflected in cryoFM image analysis (Fig.3.2C), in which the CA3 had a significantly larger mean punctum area compared to the DG and cortex ($0.44 \mu\text{m}^2$, $n = 169$ puncta in the CA3 compared to $0.35 \mu\text{m}^2$, $n = 1079$ puncta in the DG and $0.36 \mu\text{m}^2$, $n = 274$ in the cortex; one-way ANOVA with Tukey's posthoc analysis, $p < 0.0001$). These data infer that the CA3 region contains a sub-population of larger synapses or synapses which contain more Psd95 protein.

To investigate the volume of postsynaptic compartments in the cortex, DG and CA3, segmented tomographic volumes of GFP-positive postsynaptic compartments within tomograms were measured (Fig 3.2D), revealing a greater range of postsynaptic compartment volume in the CA3 region

compared to in the DG and cortex, without a significant region-specific difference in the mean volume. These data support that the CA3 region contains a subpopulation of larger postsynaptic compartments, although how this difference in size relates to their function remains to be explored.

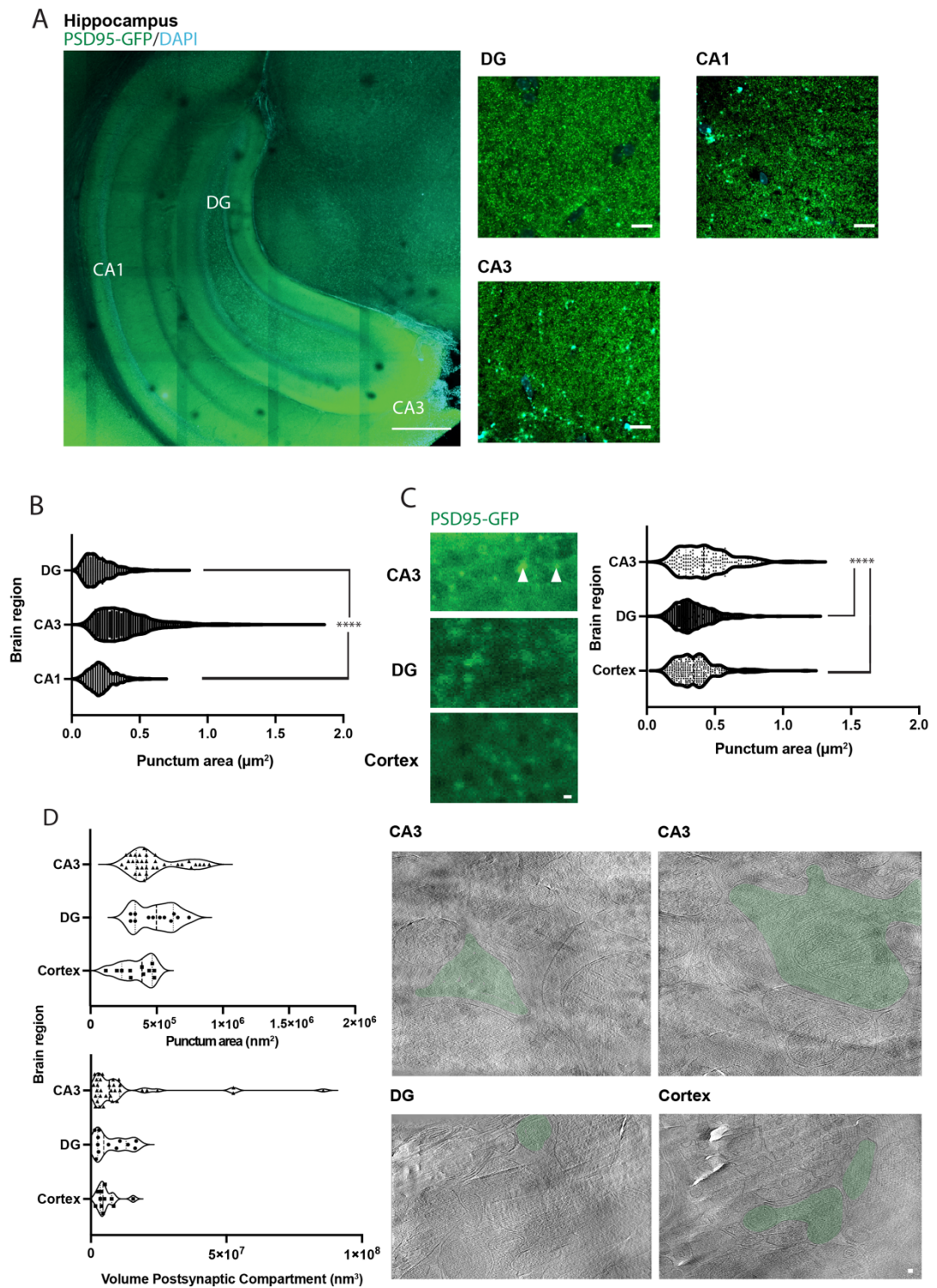


Figure 3.2: The diversity of post-synaptic compartment size in confocal microscopy of fixed acute slices, cryoFM of cryo-sections, and cryoET of cryo-sections.

A) Left Image of a Psd95-GFP labelled hippocampus with confocal microscopy. Indicated are the CA1, CA3 and DG regions, identified by the shape of the granular layers. Scalebar = 500 μ m. Right, Representative images of the DG, CA1 and CA3 regions. The CA3 region had visibly larger, brighter Psd95-GFP puncta near the granular layer. Scalebars 10 μ m.

*B) Violin plot depicting the individual punctum area by brain region. Punctum area was significantly higher (**** $p < 0.0001$) in the CA3 region, with a proportion of puncta much larger than those in the DG and cortex. $n = 3$ mice, 1119 puncta CA3, 818 puncta DG, 908 puncta CA1. The CA3 region had significantly larger puncta on average (* $p < 0.05$).*

*C) Left, Representative cryoFM images from Top, CA3; Middle, DG; Bottom, Cortex. Indicated by white arrows are examples of larger, moon-shaped puncta, which represent the proportion of larger post-synaptic compartments seen in the CA3 region. Scalebar = 1 μ m. Right, Violin plot depicting the individual punctum area by brain region. The CA3 region contained significantly larger puncta (**** $p < 0.0001$) by one-way ANOVA with Tukey's posthoc test. $n = 3$ mice/region, 169 puncta CA3, 1079 puncta DG, 274 puncta cortex.*

D) Top, violin plot of punctum area in cryoFM images. Bottom, violin plot of corresponding postsynaptic compartment volume in tomograms. Right, representative tomographic slices. Postsynaptic compartments pseudo-coloured in green. The CA3 region contained some larger postsynaptic compartments, as in top right. Scalebar = 20nm. CA3, 32 synapses from 2 mice, DG, 12 synapses from 2 mice, Cortex, 11 synapses from 3 mice.

Some of the larger synapses could represent glutamatergic shaft synapses rather than spine synapses, which are suggested to be more immature (Cotman and Nieto-Sampedro, 1984; Engert and Bonhoeffer, 1999; Yuste and Bonhoeffer, 2004; Bucher et al., 2020), with mature synapses taking ~30 minutes to form (Engert and Bonhoeffer, 1999; Chidambaram et al., 2019) and up to 4 days to become structurally and functionally mature spines (Knott et al., 2006; Chidambaram et al., 2019).

Additionally, some of the larger postsynaptic compartments could be necessary to form multi-input synapses, given their larger surface area rendering more space for synaptic clefts, although no significant differences were identified via an ANOVA and Tukey's posthoc analysis in number of multi-input synapses between region presently. Presently, 12% postsynaptic compartments in the CA3 dataset were separated from presynaptic at least 2 presynaptic compartments via clefts, compared to 0% in the DG and 9% in the cortex, suggesting that some regions could have a greater capacity for multi-input synapses (Sorra and Harris, 1993), which have been linked to hippocampal memory storage (Aziz et al., 2019).

However, these cryo-sections only represented a thin section of the complete volume of each synapse, rather than a reconstruction of the whole synaptic volume, meaning some clefts could have been outside of the tomographic volume or perpendicular to the beam and therefore not identified. To test this hypothesis, a volumetric cryoFIB-SEM imaging or serial cryo-liftout approach would be needed (Knott et al., 2008; Santuy et al., 2020; Cirelli and Tononi, 2020; Schiøtz et al., 2023), which would be powerful with unfixed, unstained, high-pressure frozen tissue when combined with the cryoCLEM labelling of synapses. Additionally, the presynaptic origin of the compartments within tomograms containing multiple clefts are unknown, so it is unclear whether these synapses are forming between more than two neurons or if there are two neurons forming multiple clefts with each other.

To summarise, the CA3 region had a sub-population of larger postsynaptic compartments, although their function was unidentified in the present study.

3.3 The hippocampus has greater incidence of postsynaptic mitochondria than the cortex

Mitochondria were identified within compartments based on the presence of an outer membrane and an inner membrane formed from cristae (Fig 3.3A). Some of these mitochondria contained exceptionally dense deposits (Fig 3.3A), which have previously been seen with cryoET in various cell types (Faas et al., 2012; Woodward et al., 2015; Wolf et al., 2017; Wu et al., 2023) and have been characterized by energy dispersive X-ray (EDX) analysis (Wolf et al., 2017), identifying them as calcium phosphate granules.

Calcium is an important messenger in synaptic communication, with calcium influx inducing downstream changes associated with LTP (Murphy et al., 1994; Berridge et al., 2003; Augustine et al., 2003; Ismailov et al., 2004; Park et al., 2016). Mitochondria act as a reservoir to buffer changes to intracellular calcium, storing calcium within calcium phosphate granules, which contributes towards normal mitochondrial function (Martin and Matthews, 1969; Lehninger, 1970; Mattson et al., 2008).

Mitochondria within pre- and post- synaptic compartments from different regions were compared, revealing that the CA3 region had a higher fraction of mitochondria-containing presynaptic compartments (0.29 in the CA3 compared to 0.15 in the DG and 0.14 in the cortex), whilst only hippocampal synapses contained postsynaptic mitochondria (Fig.3.3B). Interestingly, the percentage of postsynaptic mitochondria containing calcium phosphate deposits was higher than in presynaptic mitochondria, significantly in the CA3 region (Student's t-test $p < 0.05$; 0% in presynaptic $n=10$, 67% in postsynaptic $n=3$) (Fig.3.3B), which could be due to the sequestration of Ca^{2+} into mitochondria to buffer Ca^{2+} -dependent activity at postsynaptic compartments (Wolf et al., 2017). This could reflect the greater susceptibility of synaptic mitochondria to calcium overload, defined as more readily undergoing permeability transition, referring to a process by which mitochondria increase their membrane permeability in response to calcium, enabling the diffusion of larger molecules up to 1.5 kDa in size (Haworth and Hunter, 1979; Bernardi et

al., 2023). This transition is indicated by a loss of membrane potential, leading to mitochondrial-mediated calcium-induced neuronal death (Brown et al., 2006). Alternatively, this could reflect the critical role of postsynaptic mitochondria in the metabolic maintenance of dendritic spines and their synapses, which have a high metabolic demand due to ongoing plasticity mechanisms (Schuman and Chan, 2004).

Additionally, these cryoET data highlight that the hippocampus contains glutamatergic postsynaptic compartments that are large enough to house mitochondria. Previously, volumetric EM revealed diversity in mitochondria in pre- and post- synaptic compartments, with postsynaptic mitochondria typically found in the dendritic shaft and with a characteristically long morphology (Li et al., 2004; Delgado et al., 2019). This could infer the presence of more hippocampal shaft synapses in the dataset compared to cortical shaft synapses (Yuste and Bonhoeffer, 2004). Here, some mitochondria were found in shaft regions, with clear dendritic spines emerging to form a synapse, whereas other mitochondria were found in closer proximity to the cleft (Fig.3.3C). The presence of mitochondria proximal to the cleft in postsynaptic compartments could relate to the larger size of the compartments. The mitochondria were found in regions >50 nm away from the cleft, enabling space for scaffolding proteins, such as Psd95, to support cleft proteins (Nair et al., 2013; Broadhead et al., 2016; Frank et al., 2017). Hence, synapses in all brain regions can contain mitochondria, although here postsynaptic mitochondria were only identified in hippocampal synapses, inferring the presence of some glutamatergic shaft synapses within the dataset.

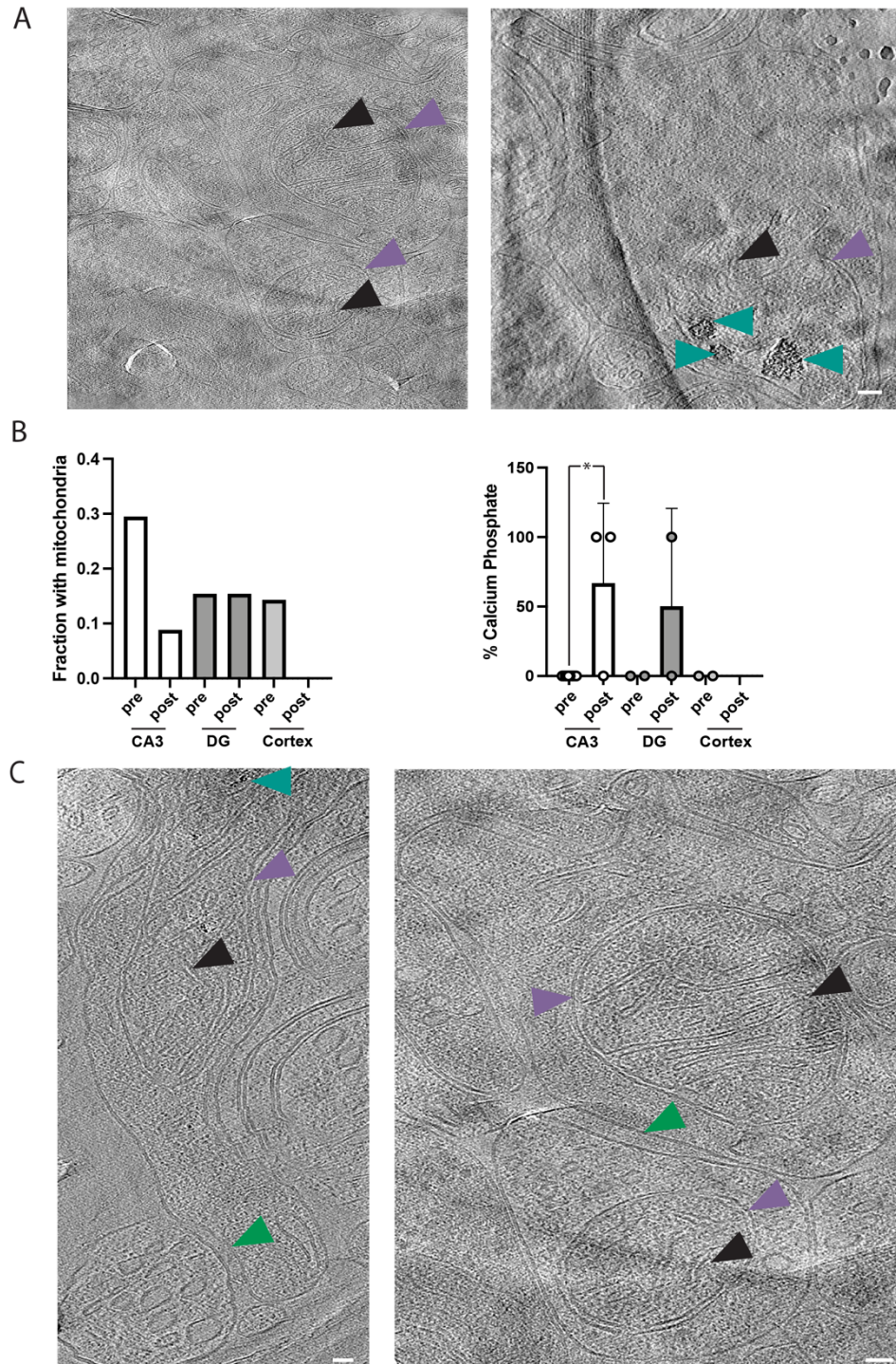


Figure 3.3: Postsynaptic mitochondria are more abundant in hippocampal synapses.

A) Mitochondria were present in some synapses. These were identified by being intracellular, having an outer membrane (purple arrowhead) and by

containing cristae (black arrowhead). Some mitochondria contained dense deposits (teal arrowhead) of calcium phosphate. Both tomographic slices are taken from the CA3 region. Scalebar = 20 nm.

B) Left, some presynaptic compartments in all regions contained mitochondria, but only hippocampal regions sometimes contained postsynaptic mitochondria. CA3, $n=33$ synapses from 2 mice, DG, $n=13$ synapses from 2 mice, Cortex, $n=9$ synapses from 3 mice.

Right, in the CA3 region, significantly more postsynaptic mitochondria contained calcium phosphate deposits compared to presynaptic CA3 mitochondria ($*p<0.05$) by Student's *t*-test. CA3, $n=14$ mitochondria from 2 mice, DG 4 mitochondria from 2 mice, Cortex, 2 mitochondria from 1 mouse. Data are presented as mean \pm SD.

C) Postsynaptic mitochondria were located within dendritic compartments either in the shaft (left) or in proximity to the cleft (right). Green arrowheads indicate the postsynaptic membrane. Scalebar = 20 nm.

3.4 The CA3 region has greater vesicle occupancy and vesicle tethering, inferring a presynaptic-mediated mechanism of activity

Conventional EM and tomography have characterized synaptic states based on the distribution and docking of presynaptic vesicles (Chicurel and Harris, 1992; Shepherd and Harris, 1998; Bourne and Harris, 2012; Imig et al., 2020). Briefly, presynaptic activity is indicated by a recruitment of vesicles in the active zone proximal to the presynaptic membrane, enabling tethering of presynaptic vesicles for subsequent docking and exocytosis of neurotransmitter (Szule et al., 2012; Imig et al., 2014). Therefore, the distribution of active zones correlates to synaptic release probabilities (Schikorski and Stevens, 1997). Such observations have been supported by cryoET studies of synaptosomes and primary neuronal cultures (Martinez-Sanchez et al., 2021; Radecke et al., 2023).

To investigate presynaptic activity at glutamatergic synapses in adult brain, vesicle diameter, occupancy and tethering were analyzed (Fig 3.4AB). The number of vesicles varied between synapses and had similar mean diameter in all regions of ~ 40 – 50 nm, as expected (Akert et al., 1964; Borges-Merjane et al., 2020; Peukes et al., 2021). Total vesicle occupancy, referring to the volume of space within the compartment occupied by vesicles, was significantly higher (one-way ANOVA with Tukey's posthoc analysis, $p < 0.01$) in the CA3 region compared to the cortex (Fig 3.4B), which could reflect the mossy fibre inputs onto CA3 neurons; these have previously been identified to have presynaptic mediated long-term potentiation with more vesicles primed for release (Suyama et al., 2007). Once subdivided into proximal (0-45 nm from PreSM), intermediate (45-75 nm from PreSM) and distal (>75 nm from PreSM) regions, vesicle occupancy was not significantly different in any region. Although CA3 presynaptic compartments have a greater proportion of their cytoplasm taken up by vesicles, this was not dependent on the distance from the PreSM, and vesicles were still distributed evenly throughout the compartment, inferring similar activity levels at the time of freezing.

The percentage of tethered proximal vesicles was calculated based on the number of vesicles attached to the presynaptic membrane via proteins. The CA3 and cortex had significantly more tethered vesicles than the DG region (Fig 3.4B), indicative of active zone recruitment (Imig et al., 2014). Further investigations could compare the occupancy, tethering and docking of vesicles in stimulated and unstimulated tissue as a measure of activity-dependent trafficking; this would be interesting when combined with a calcium indicator and imaged in a time-resolved manner (Kontziampasis et al., 2019; Radecke et al., 2023), enabling the assessment of synaptic architecture during communication, including the identification of molecular structures involved in docking and tethering, such as SNARES (Imig et al., 2014), within fresh, cryopreserved tissue.

Therefore, presynaptic compartments at glutamatergic synapses contain numerous vesicles for synaptic communication. In particular, the CA3 region has a high occupancy of evenly distributed vesicles in unstimulated tissue.

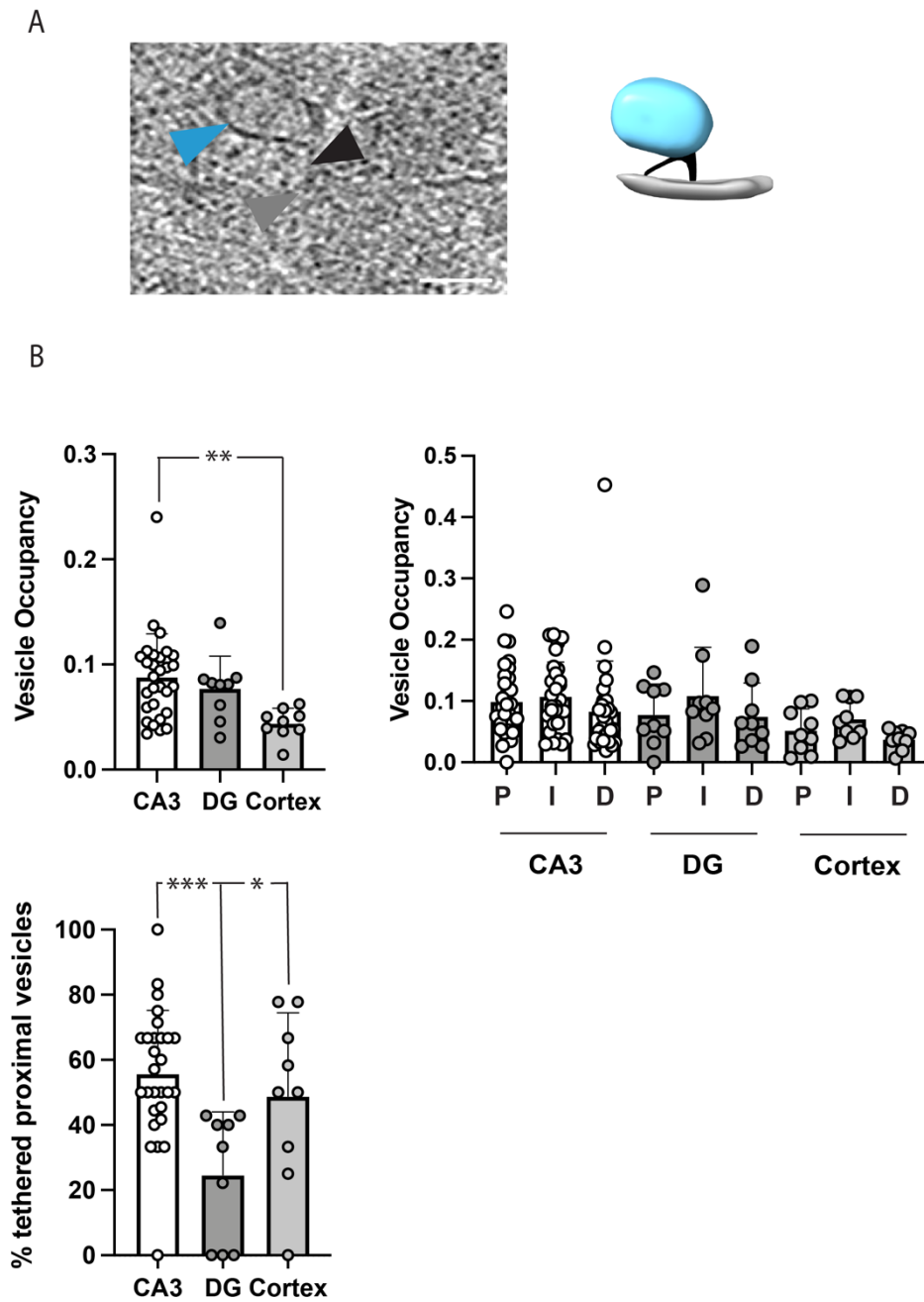


Figure 3.4: The CA3 region demonstrated signatures of presynaptic-mediated plasticity.

A) Left, tomographic slice indicating vesicles. Blue arrowhead, presynaptic vesicle in the active zone tethered to the presynaptic membrane. Black arrowhead, protein tethering a vesicle, Grey arrowhead, presynaptic membrane. Scalebar = 20 nm. Right, segmentation of vesicle (blue) tethered to a presynaptic membrane (grey) via a protein (black).

B) Total vesicle occupancy was significantly higher in CA3 compared to cortex (** $p < 0.01$). Vesicle occupancy was not significantly different between P, proximal (0-45 nm); I, intermediate (45-75 nm); or D, distal (>75 nm) regions of compartments. This indicates that vesicles were evenly distributed. The CA3 and cortex had a significantly higher percentage of tethered proximal vesicles compared to the DG (* $p < 0.05$, *** $p < 0.001$), suggesting that the DG region had fewer vesicles primed for release. Data are presented as mean \pm SD, with individual synapses marked as individual points. Statistical analysis used one-way ANOVAs with Tukey's posthoc test. CA3, $n=29$ synapses from 2 mice, DG $n=9$ synapses from 2 mice, Cortex, $n=9$ synapses from 3 mice.

3.5 Glutamatergic synapses have variable cleft height and distribution of iGluRs in the synaptic clefts across brain regions

Synaptic transmission is dependent upon multiple factors, including the concentration profile of neurotransmitter in the synaptic cleft and the electrophysiological resistance profiles of the cleft (Savtchenko and Rusakov, 2007). Whilst narrowing the synaptic cleft increases the concentration of neurotransmitter, promoting activity, this also increases the electrical resistance and therefore reduces local receptor currents (Savtchenko and Rusakov, 2007).

To measure the distribution of cleft height in synapses across different brain regions, segmented models of pre- and post- synaptic membranes were generated in dynamo and the pairwise distance was calculated with MatLab scripts. Pre- and post- synaptic compartments associated via synaptic clefts varied in height within and between synapses (Fig.3.5A), with some bimodal distributions inferring local modulation of cleft height by cleft adhesion

proteins. Mean cleft height ranged between ~ 10 nm – 33 nm, which was more variable than previously reported (Peters et al., 1970; Schikorski and Stevens, 1997), likely due to dehydration-mediated cleft shrinkage with conventional EM sample preparation methods (Zuber et al., 2005). Overall, no region-specific differences were detected in cleft height distribution (Fig.3.5A), which was instead variable within and between synapses.

Within the synaptic cleft exist numerous synaptic proteins, including cleft adhesion proteins and receptors (Honig and Shapiro, 2020; Martinez-Sanchez et al., 2021). Crucially, glutamatergic synapses express ionotropic glutamate receptors (iGluRs), including AMPARs and NMDARs, at the synaptic cleft, enabling synaptic transmission (Harris and Pettit, 2007; Peukes et al., 2021). NMDARs are critical to the induction of synaptic plasticity and the associated learning and memory (Collingridge et al., 1983; Davis et al., 1992; Hunt and Castillo, 2012; Miyashita et al., 2012), where they act as “coincidence detectors” to discriminate between correlated and uncorrelated activity (Miyashita et al., 2012), an essential component of plasticity. Synaptic plasticity, specifically LTP, has been linked to increased ratio of AMPAR:NMDAR-mediated currents (Matsuo et al., 2008; Park et al., 2016) and alterations in AMPAR subunit composition (Plant et al., 2006). Therefore, iGluRs have an important contribution to synaptic plasticity mechanisms at glutamatergic synapses, and thus their structures have been solved with X-ray crystallography (Sobolevsky et al., 2009; Karakas and Furukawa, 2014; Lee et al., 2014) and within ultra-fresh synaptosomes (Peukes et al., 2021). These structures indicate that iGluRs have a Y-shaped protrusion into the synaptic cleft with 14 nm long arms. Currently, the structures of iGluRs within intact tissue have not been investigated.

However, individual proteins within the synaptic cleft are difficult to identify within raw tomographic volumes of tissue sections due to the heterogeneity of synapses (Zhu et al., 2018; Bulovaite et al., 2022) and the crowded cellular molecular environment (Martinez-Sanchez et al., 2020; Martinez-Sanchez et al., 2021; Berger et al., 2023). To overcome this, STA (subtomogram averaging) can be applied, generating a high contrast, higher resolution

structure (Koning et al., 2008; Briggs, 2013; Grange et al., 2017; Kaplan et al., 2021; Erdmann et al., 2021; Gilbert et al., 2023). Since synaptic clefts exhibit variability in protein expression (Zhu et al., 2018; Bulovaite et al., 2022), and cryo-sections enable the reconstruction of a 70-150 nm thick section of the total synaptic volume, number of each cleft protein was low and therefore not suitable for the generation of high-resolution structures capable of resolving individual residues. To identify the maximum achievable resolution of structures within the dataset, STA was applied to microtubules, resulting in a structure consisting of 13 protofilaments surrounding a central tubule at ~3 nm resolution (Fig.3.5B), comparable to previous studies of microtubules in cells (Koning et al., 2008; Grange et al., 2017). This structure acted as a benchmark for averaging, indicating a maximum resolution obtainable in this dataset through STA of in-tissue molecular constituents, despite the low number and crowded in-tissue environment.

Putative iGluRs were identified within the synaptic cleft, where they protruded from the postsynaptic compartment as a Y-shaped density with 14 nm length arms (Sobolevsky et al., 2009; Peukes et al., 2021). An STA protocol was applied, producing an average structure of ~6 nm resolution from 137 proteins (Fig.3.5C). For a high-resolution 3D structure, a number in the range of thousands of the protein must be averaged, meaning this resolution was severely limited due to the low particle number. Furthermore, iGluRs likely exhibited conformational heterogeneity (Hansen et al., 2007; Frank, 2011; Dürr et al., 2014; Martinez-Sanchez et al., 2021; Zhang et al., 2023). The map bore resemblance to iGluRs, with the Y-shaped domain accommodating the atomic model for AMPAR reasonably well (Dürr et al., 2014), but the class likely contained a combination of AMPARs and NMDARs in different conformational states due to the resolution limitation. As expected, a high-resolution 3D structure was not obtained, but the localization (Fig.3.5D) and clustering of putative iGluRs (Fig.3.5EF) could be assessed. Putative iGluRs were detected in all regions with no significant differences in number (Fig.3.5D) and were found in clusters (defined as at least 3 receptors within 960 Å in a triangulation mesh) on the postsynaptic membrane as opposed to evenly spread (Fig.3.5EF). This was reflective of super-resolution microscopy (Nair et al.,

2013) and cryoET of ultra-fresh synaptosomes (Peukes et al., 2021), in which iGluRs were found in clustered nanodomains.

However, in the present study, whole synapses were not collected due to the use of thin cryo-sections. A much larger dataset or a serial cryo-sectioning approach would be required to fully understand the clustering of iGluRs and to obtain high-resolution in-tissue structures of these proteins.

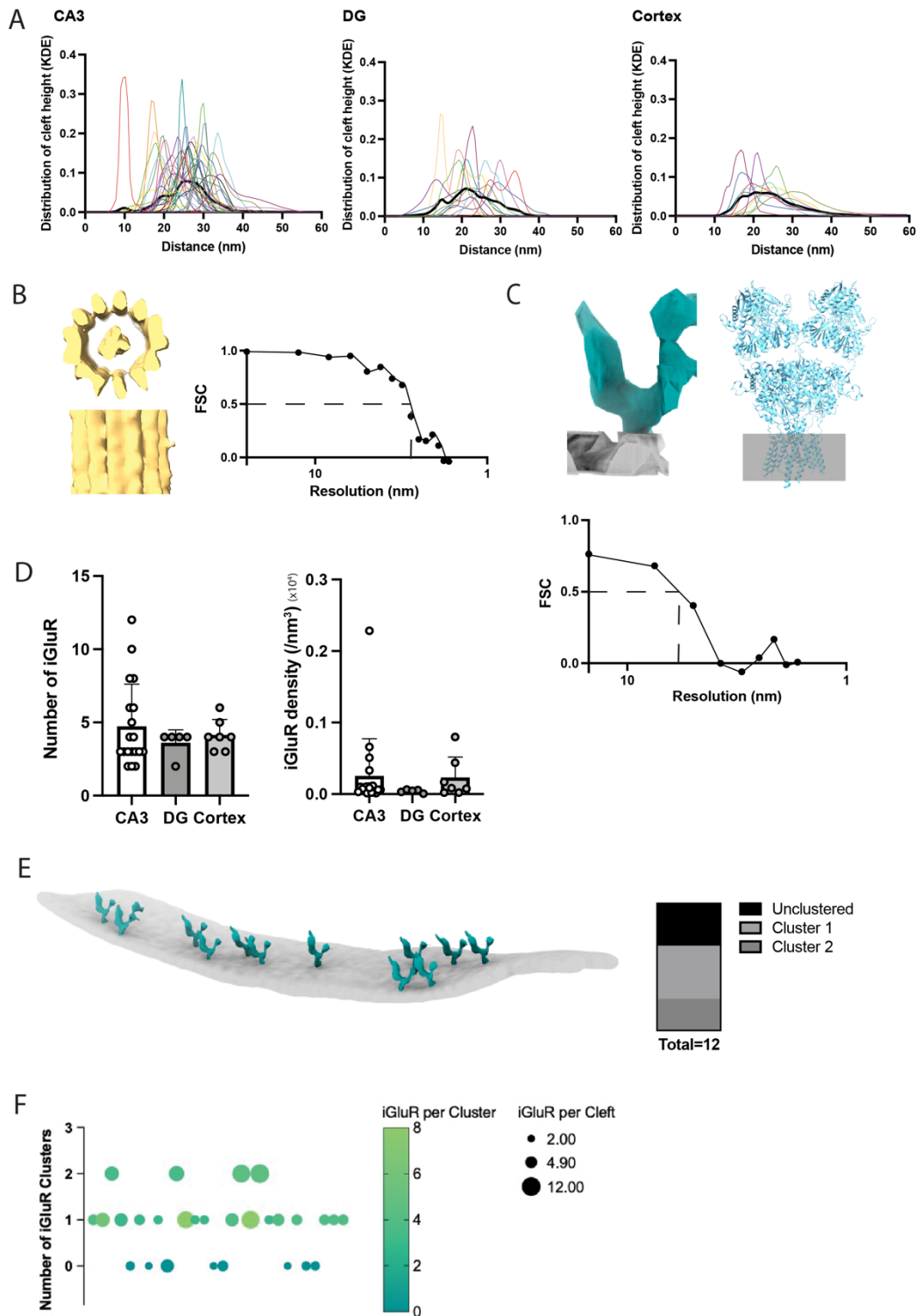


Figure 3.5: Molecular constituents of the synaptic cleft

A) Cleft height in the CA3, DG and cortex regions depicted as kde plots. All regions contained synapses with variable cleft height, reflecting the dynamic

remodelling cleft height by cleft adhesion proteins. There were no significant differences between mean cleft height by regions.

B) Subtomogram averaged structure of an in-tissue microtubule at ~3 nm resolution.

C) Left, subtomogram averaged structure of a putative iGluR (cyan) on a postsynaptic membrane (grey) at ~6 nm resolution. Right, AMPAR structure (cyan) (Dürr et al., 2014) with schematic “postsynaptic membrane” (grey). Both structures are Y-shaped with 14 nm long arms.

D) Left, Number of putative iGluRs within the synaptic clefts by region. Right, density of putative iGluRs in the synaptic cleft per region. CA3, n=16 synapses from 2 mice, DG, n=5 synapses from 2 mice, Cortex, n= 7 synapses from 2 mice. Data are presented as mean \pm SD.

E) Localization of putative iGluRs on a postsynaptic membrane from one tomogram. Two clusters of proteins were present, with the rest unclustered.

F) Multivariable graph depicting the number of putative iGluRs per cleft and per cluster and the number of clusters per cleft. Each bubble represents an individual synaptic cleft, with larger bubbles corresponding to a greater number of putative iGluRs within the cleft. The colour gradient reflects the mean number of receptors per cluster. n=28 synapses from 6 mice.

3.6 Glutamatergic postsynaptic compartments contained extensive actin-associated cytoskeletal networks, particularly in the CA3 region

The cytoskeleton is crucial for the trafficking of vesicles, movement of cargo and remodelling of compartment shape, which are critical components of learning and memory (Korobova and Svitkina, 2010; Basu and Lamprecht, 2018; Ortega-De San Luis and Ryan, 2022). Indeed, these networks were evidenced to remodel and sustain the geometry of compartments in response to activation of the neuron (Okamoto et al., 2004; Korobova and Svitkina,

2010; Basu and Lamprecht, 2018; Goto et al., 2021). Specifically, the cytoskeleton is composed predominantly of filamentous actin (F-Actin) (Landis and Reese, 1983; Korobova and Svitkina, 2010), which undergoes nucleation and polymerization dependent upon Arp2/3 (Goley and Welch, 2006; Hotulainen et al., 2009). Enhanced F-Actin at dendritic spines has been linked to LTP (Fukazawa et al., 2003).

To investigate the number and geometry of the filaments within the cytoskeletal network of postsynaptic compartments, an ultrastructural MatLab toolkit to detect and analyse parameters of filaments was applied (Dimchev et al., 2021). F-Actin was detected as ~6 nm diameter filaments within postsynaptic compartments (Fig.3.6A), where it formed extensive branched networks (Korobova and Svitkina, 2010; Jung et al., 2020). The number of F-Actin was compared across regions, indicating that postsynaptic compartments in the CA3 region had significantly more F-Actin than in the DG region (Fig.3.6B). Furthermore, postsynaptic compartments in the CA3 region were identified to have a higher volume fraction of F-Actin (Fig.3.6C). These observations support that an extensive F-Actin-associated cytoskeletal network underlies the postsynaptic compartment (Jung et al., 2020; Ortega-De San Luis and Ryan, 2022), particularly in the CA3 region.

Additionally, there were some expected shared features across all regions, including the average angle of filaments relative to the postsynaptic membrane (Fig.3.6D) and the average length of F-Actin (Fig.3.6E). These geometric features, consistent with Arp2/3 mediated F-Actin branching (Goley and Welch, 2006), could be critical for force generation and therefore the maintenance and modulation of postsynaptic shape in response to activity (Landis and Reese, 1983; Hotulainen et al., 2009; Korobova and Svitkina, 2010; Jung et al., 2020; Ortega-De San Luis and Ryan, 2022), so were expected to be similar in the present study due to the latent timepoint after engram labelling and absence of reactivation.

To ensure that F-Actin detection within tomograms was not significantly hindered by variability in tomogram quality, the number of F-Actin was

compared to the tomogram thickness, number of tilt images used for tomogram generation, and defocus values (Fig.3.6F). These factors can influence signal-to-noise and resolution, and therefore the ability to detect molecular features. No relationships were detected between F-Actin number and tomogram thickness or number of tilt images per tomogram. However, a significantly non-zero (simple linear regression, * $p < 0.05$, $R^2 = 0.2505$) positive correlation was detected between number of F-Actin and the respective defocus value (Fig.3.6F). Tomograms collected closer to focus had a greater number of F-Actin present, inferring that the detection of F-Actin was improved in these tomograms. Within this dataset, the average defocus for the CA3 region was -4.7 ± 0.5 , compared to -5.2 ± 1.3 in the DG and -6.4 ± 0.4 in the cortex, with a significant difference between CA3 and cortex (**** Student's t-test, $p < 0.0001$). This could have influenced the ability to detect F-Actin and therefore the observed increase in number and volume fraction of F-Actin in this workflow.

Overall, glutamatergic postsynaptic compartments contained F-Actin within branched networks (Landis and Reese, 1983; Goley and Welch, 2006; Hotulainen et al., 2009; Korobova and Svitkina, 2010; Ortega-De San Luis and Ryan, 2022). Presently, the number and occupancy of F-Actin appeared higher in postsynaptic compartments of the CA3 region compared to their counterparts in the DG and cortex, although this may have been influenced by the tomogram defocus.

A

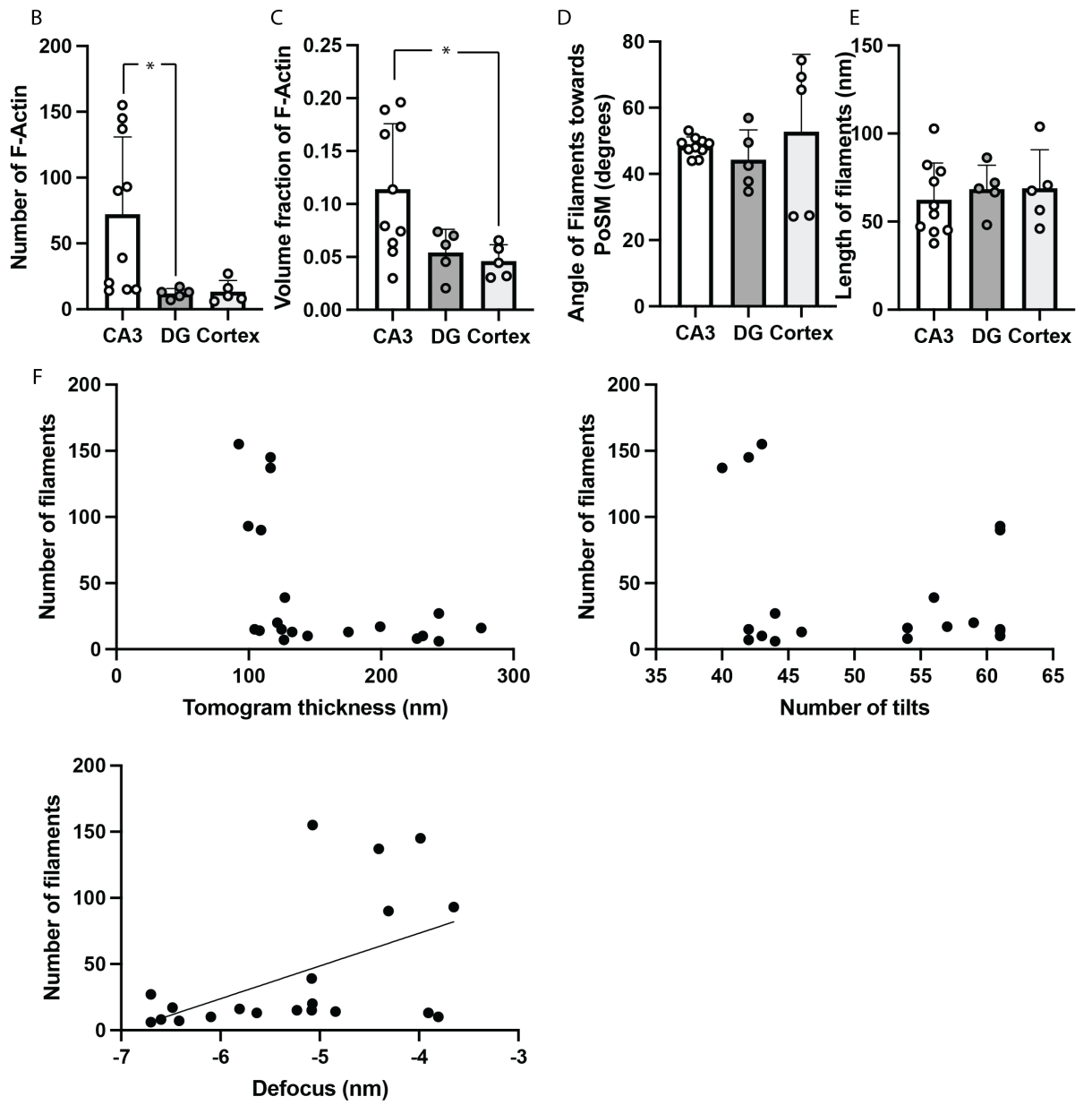
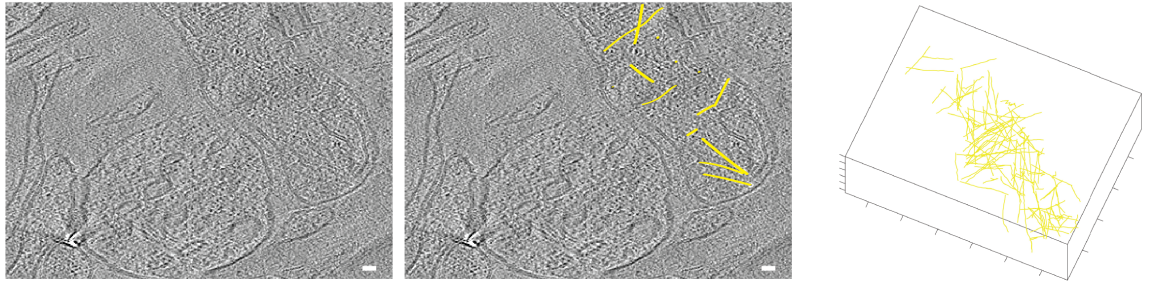


Figure 3.6: Postsynaptic compartments contained extensive cytoskeletal networks, with more F-Actin in the CA3 region

A) Left, a representative example of a synapse within a tomographic virtual slice. Middle, yellow overlay indicating F-Actin in a cross-section. Right, 3D model of F-Actin within the tomographic volume. Scalebar = 20 nm.

*B) Number of F-Actin per postsynaptic compartment in the CA3, DG and cortex regions. The CA3 region contained significantly more postsynaptic F-Actin than the DG region (ANOVA, * $p < 0.05$).*

C) The volume fraction of F-Actin in the CA3, DG and cortex regions. The CA3 region had a significantly higher volume fraction of F-Actin than the cortex (ANOVA, $p < 0.05$).

D) The angle of the filaments relative to the postsynaptic membrane (PoSM) in the CA3, DG and cortex regions. No significant differences were detected between groups (ANOVA).

E) The length of F-Actin filaments in the CA3, DG and cortex regions. No significant differences were detected between groups (ANOVA).

F) Quality control of F-Actin data. The number of F-Actin plotted against tomogram thickness, number of tilts and defocus. Relationships between tomogram thickness and number of tilts were not evident. Positive correlation (simple linear regression, $p < 0.05$, $R^2 = 0.2505$) was detected between the defocus value and the number of F-Actin, indicating that tomograms collected at closer to focus had a higher incidence of F-Actin detection.

All data are presented as mean per postsynaptic compartment \pm SD. In each group, $n = 2$ mice. 10 postsynaptic compartments from the CA3 region, 5 from the DG and 5 from the cortex were analysed.

3.7 Concluding comments

To summarise, a tomographic synaptic survey was carried out comparing glutamatergic synapses in the cortex with those from the DG and CA3 hippocampal regions. These data represent the first obtained in-tissue tomograms of glutamatergic synapses. Analysis revealed great variability of synapses, as expected (Zhu et al., 2018; Bulovaite et al., 2022), including in postsynaptic volume and organelles and proteins present.

Irrespective of brain region, glutamatergic synapses had shared features, similarly to previous cryoET studies using cultured neurons (Tao et al., 2018), organotypic slices (Fernández-Busnadiego et al., 2010), synaptosomes (Fernández-Busnadiego et al., 2010) and ultra-fresh synaptosomes (Peukes et al., 2021). These features included a presynaptic compartment rich in presynaptic vesicles, with similar distribution to reported unstimulated synapses (Radecke et al., 2023) and a synaptic cleft containing numerous proteins and complexes (Honig and Shapiro, 2020; Martinez-Sanchez et al., 2021). For example, iGluRs were found distributed in clusters within the synaptic cleft, reminiscent of nanodomains (Harris and Pettit, 2007; Broadhead et al., 2016; Peukes et al., 2021). Postsynaptic compartments exhibited branched F-Actin cytoskeletal networks similarly to reported dendritic spines (Landis and Reese, 1983; Hotulainen et al., 2009; Korobova and Svitkina, 2010; Jung et al., 2020).

Additionally, some region-specific differences were observed. Postsynaptic compartments and Psd95 puncta were variable in size, with the CA3 containing a sub-population of large postsynaptic compartments, reminiscent of fluorescent microscopy on glutamatergic synapses (Broadhead et al., 2016). Postsynaptic dendritic compartments contained F-Actin irrespective of brain region (Landis and Reese, 1983; Korobova and Svitkina, 2010), but the CA3 region was observed to contain a greater number and volume fraction of F-Actin compared to the DG and cortex. These observations suggest that more nucleation and polymerization of actin occurred (Hotulainen et al., 2009; Korobova and Svitkina, 2010; Spence and Soderling, 2015), which could be a

characteristic unique to the CA3 region or could be indicative of greater baseline activity in these tissue samples (Yang et al., 2023). However, this analysis may have been influenced by the CA3 region tomograms being collected closer to focus, improving the ability to detect F-Actin for the workflow.

Differences in mitochondrial distribution were also observed, with only the hippocampus exhibiting postsynaptic mitochondria, inferring a larger proportion of glutamatergic shaft synapses in the hippocampus compared to the cortex. This conflicted with the literature, as only a reported 10% mature glutamatergic hippocampal synapses were located on shaft regions, compared to up to 30% in the cortex (Bourne and Harris, 2011; Reilly et al., 2011). This difference could have arisen due to the relatively small sample size of synapses compared to within volume imaging. A greater proportion of postsynaptic mitochondria contained calcium phosphate deposits compared to presynaptic mitochondria, inferring the buffering of recent calcium activity in the postsynaptic compartment (Wolf et al., 2017), and reflecting the role of mitochondria in the maintenance of calcium levels (Martin and Matthews, 1969; Lehninger, 1970; Mattson et al., 2008; Delgado et al., 2019).

Analysis of the molecular distribution profiles of glutamatergic synapses revealed heterogeneity in protein distribution, as previously documented in cultured neurons (Tao et al., 2018) and tissue homogenate (Peukes et al., 2021). The voxel intensity profiles indicated proteins adjacent to the postsynaptic membranes, but these regions were not always of a higher molecular density than distal regions of the compartment. This contrasted with conventional EM studies, in which a sheet-like region of high molecular density termed the postsynaptic density (PSD) is a conserved feature proximal to the postsynaptic membrane (Gray, 1959; Chicurel and Harris, 1992; Petersen et al., 2003). The conserved sheet-like PSD may be a result of chemical fixation, dehydration and heavy metal staining (Gray, 1959; Scarff et al., 2018), which washes away components of the cytoplasm that cannot be fixed and preferentially labels the membrane-bound components with a heavy metal stain, resulting in heightened contrast between regions proximal and distal to

the postsynaptic membrane. Instead, it is proposed that postsynaptic proteins are distributed variably at the postsynaptic membrane, meaning that a more molecularly dense PSD is not always a detectable, essential feature. Moreover, the use of vitreous tissue sections preserved the architecture of the postsynaptic compartment, reducing the loss of other cytoplasmic features that provide molecular density throughout the compartment. Hence, the presence of a PSD alone should not be used to identify glutamatergic synapses with electron microscopy.

This thesis presents the first cryoET of glutamatergic synapses within intact brain tissue, revealing the variable molecular architectures that underlie learning and memory, reflecting the diversity of synapses in the mammalian brain. However, some questions remain unanswered. For example, high-resolution in-tissue structures of iGluRs were not obtained, but this could be possible with larger datasets to increase the particle number for STA. Another labelling method could be implemented, such as DNA origami tags (Silvester et al., 2021), to identify iGluRs more precisely within tomographic volumes. Larger datasets would also be advantageous to account for the heterogeneity of synapses (Zhu et al., 2018; Bulovaite et al., 2022), enabling the detection of region-specific differences.

This thesis utilized cryo-sections to generate samples for cryoCLEM/cryoET (Al-Amoudi et al., 2004), enabling the maintenance of an in-tissue environment and avoiding the use of homogenization or purification steps. However, cryo-sectioning can induce knife-related damage and compression, hindering the quality of samples. For future research into glutamatergic synapses, samples could be prepared using the cryo-liftout technique (Marko et al., 2007; Schaffer et al., 2019; Schiøtz et al., 2023) to avoid such sample compression.

Overall, glutamatergic synapses in the cortex and hippocampus were variable within and between regions, including in molecular distribution, cleft geometry, and organelle composition. Most of these observations were in accordance with the literature (Landis and Reese, 1983; Zuber et al., 2005; Korobova and Svitkina, 2010; Broadhead et al., 2016; Zhu et al., 2018; Tao et al., 2018;

Delgado et al., 2019; Peukes et al., 2021; Bulovaite et al., 2022), although the observed differences in molecular distribution challenge how we identify synapses in cryoET and highlight how sample preparation is key to understanding unperturbed synaptic architecture in such investigations.

Chapter 4: The *in-tissue* Architecture of Engram-labelled Synapses

Memory refers to the process by which the brain encodes, retains and recalls information to accordingly alter behaviour. Richard Semon pioneered the *engram*, referring to the biological substrate in the brain responsible for the acquisition and storage of memory (Semon, 1909). Hence, the specific set of changes in the brain that account for a given memory can be referred to as an *engram* (Josselyn and Tonegawa, 2020; Ortega-De San Luis and Ryan, 2022). Defining the mechanism of engram formation is crucial to understanding how the brain computes information to adapt to changing environments (Ryan and Frankland, 2022).

Within the brain, neurons are wired into complex neuroanatomical circuitry via electrochemical junctions called synapses, the strength of which can be modified dynamically via the action of synaptic plasticity (Hebb, 1949; Frey and Morris, 1997; Chowdhury and Hell, 2018). Relationships between electrical activity, synaptic plasticity and structural modifications at synapses have been observed (Kandel and Tauc, 1965; Bliss and Lømo, 1973), and an increase in the number of synaptic connections between engram cells correlates positively with the acquisition of memory in learning paradigms (Ryan et al., 2015; Choi et al., 2018; Lee et al., 2022; Ortega-de San Luis et al., 2023), highlighting the importance of synapses. Indeed, modifications in synaptic wiring patterns caused by structural plasticity mechanisms are a plausible physical substrate for information (Lichtman and Colman, 2000; Chklovskii et al., 2004; Tonegawa et al., 2015).

When labelled with optogenetics, engram cells can be observed and manipulated *in vivo* and *ex vivo* (Liu et al., 2012; Nabavi et al., 2014; Liu et al., 2014; Ryan et al., 2015), providing a *bona fide* link between plasticity and memory. Structurally, connectivity patterns between engram cells distributed across different brain areas are modified by learning (Redondo et al., 2014; Vetere et al., 2017; Roy et al., 2022). However, the structural basis of behavioural properties remains to be explored at the synaptic level.

Various sample preparations for cryoET have been developed to investigate cryopreserved synapses, such as with synaptosomes (Végh et al., 2014), ultra-fresh synaptosomes from tissue homogenate (Peukes et al., 2021), neurons grown on grids (Tao et al., 2018), and within intact tissue (Al-Amoudi et al., 2004; Peukes et al., 2021). However, the architectures of synaptic junctions between engram neurons have not yet been reported by cryoET in any preparation.

Here, a workflow was developed combining engram labelling technology (Liu et al., 2012; Liu et al., 2014; Ramirez et al., 2014; Ryan et al., 2015) with cryogenic correlated light and electron microscopy (cryoCLEM) and cryoET (Kukulski et al., 2011; Harapin et al., 2015; Peukes et al., 2021) to elucidate the molecular architecture of synapses between engram cells. A vast array of organelles, macromolecular complexes and molecular constituents were identified, highlighting the heterogeneity of synapses in engram circuits. The workflow presented here allows the inspection of native structural properties of engram cells.

The work presented in this chapter was carried out at a latent timepoint of 6 days post-engram labelling for the purpose of workflow development. Hence, the data presented here constitute this latent timepoint for future comparisons and show the types of data and observations that can be made through the application of this workflow. It is envisaged that in future studies, the workflow will be applied at earlier intervals to study earlier stages of memory acquisition, in addition to utilising the channelrhodopsin tag for optogenetic reactivation of a memory engram, enabling comparisons to be made between active and inactive engram synapses. These further studies will investigate plasticity mechanisms that underlie memory encoding, storage and recall through the application of the workflow and analysis of the organelles and proteins as presented here.

4.1 Engram cell labelling in mice

To detect engram synapses for cryoET, a fluorescent labelling approach was applied based on an established method (Liu et al., 2012; Ryan et al., 2015), to label the commissural fibres projecting contralaterally from the CA3 to the CA1 (Tao et al., 2021). AAV constructs encoding TRE-ChR2-EYFP and TRE-mCherry were intracerebrally injected in the CA3 and contralateral CA1, respectively, thus labelling presynaptic engram CA3 neurons with ChR2-EYFP and postsynaptic engram CA1 neurons with mCherry (Fig.4.1.1). Mice were subject to contextual fear conditioning (Fig.4.1.1), during which the corresponding engram cells were labelled (see methods section 2.2).

To confirm expression of ChR2-EYFP at presynaptic terminals, CaMKII-ChR2-EYFP was injected into the CA3 region of mice and immunofluorescence using postsynaptic Psd95 (Frank et al., 2016) and presynaptic synapsin-1 (Ryan et al., 1996) antibodies was detected at the contralateral CA1 region with confocal microscopy (Fig.4.1.2ABC). This data verified that ChR2-EYFP injected into CA3 neurons was expressed at presynaptic terminals that synapsed in the contralateral CA1 region. Similarly, in immunofluorescence of acute slices from mice subject to TRE-mCherry injection in the CA1 region, sparse engram labelling with mCherry puncta was detected both within the cell bodies and colocalised with Psd95 puncta (Fig.4.1.2D). Hence, the labelling methodology was sufficient for the detection of CA3-CA1 synapses.

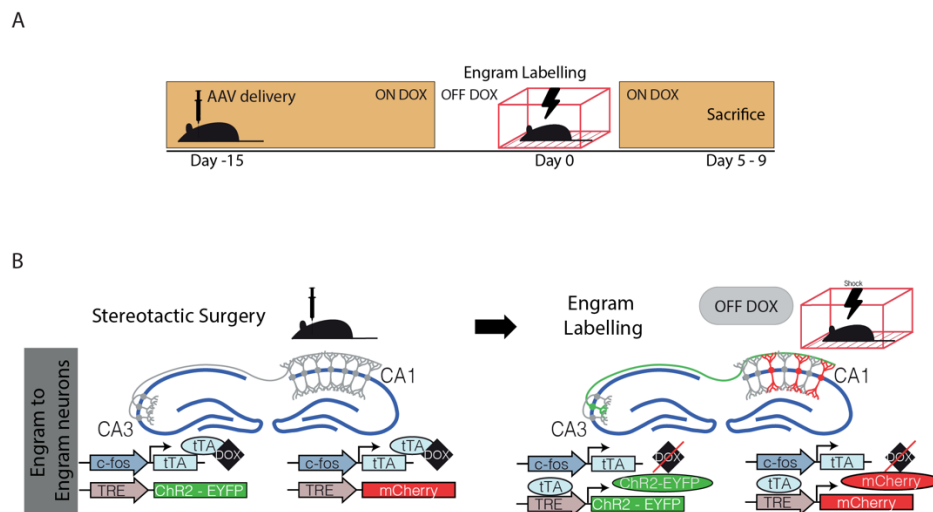


Figure 4.1.1: Schematic depicting the application of engram labelling technology.

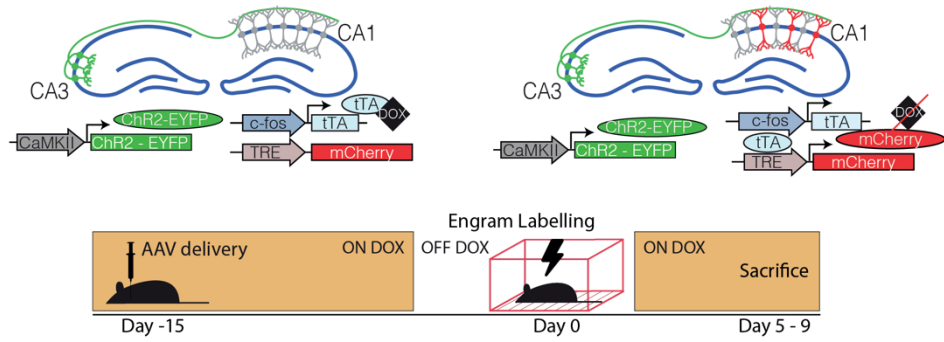
A) *Experimental timeline.* Mice (B6.Cg-Tg(Fos-tTA,Fos-EGFP*)1Mmay/J) were used to enable the expression of tetracycline trans-activator (tTA), which enables the expression of genes of interest to be made doxycycline-dependent, and therefore controllable within a given timeframe. Mice were subject to two intracerebral injections of genes of interest via stereotactic surgery. At the CA3 region of the hippocampus, these were either plasmid Adeno-Associated Virus- Tetracycline Response Element- Channelrhodopsin-Enhanced Yellow Fluorescent Protein (pAAV-TRE-ChR2-EYFP), to label engram neurons, or plasmid Adeno-Associated Virus- Calcium-calmodulin-dependent Kinase II-Channelrhodopsin-Enhanced Yellow Fluorescent Protein (pAAV-CaMKII-ChR2-EYFP), to label all neurons. At the contralateral CA1 region of the hippocampus, plasmid Adeno-Associated Virus-Tetracycline Response Element- mCherry (pAAV-TRE-mCherry) was intracerebrally injected to label postsynaptic engram neurons in the CA1 region. Mice were left to recover for 15 days whilst on a doxycycline diet to suppress the expression of genes of interest. Next,

for engram labelling, mice were taken off the doxycycline diet to enable the expression of the genes of interest and were transported to an experimental room where they were allowed to explore a context for 3 minutes, followed by 3 successive 0.75 mA shocks of 2 s duration spaced by 1 minute. Contextual cues used were a triangular shape inset and Benzaldehyde 0.25%. After training, mice were put back on a doxycycline diet to prevent further expression of the genes of interest. Mice were sacrificed 6 days after engram labelling for the cryoCLEM/cryoET workflow.

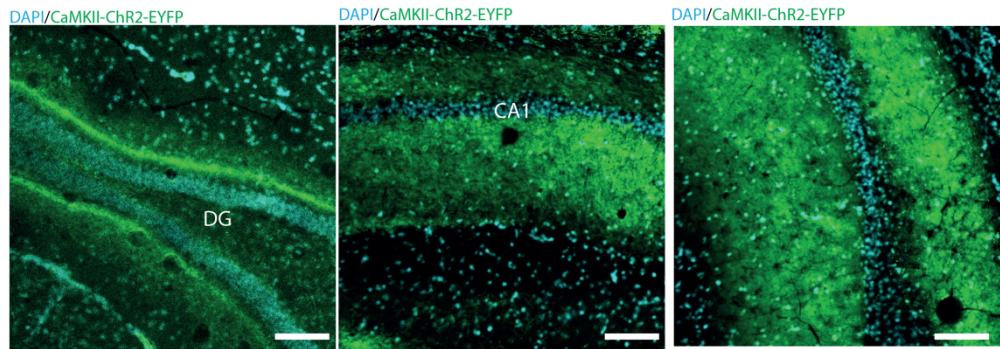
*B) Schematic depicting the constructs used for the labelling of engram-to-
engram (EE) CA3-CA1 neurons using engram labelling technology. After stereotactic surgery to administer the genes of interest packaged in AAVs, mice consume a doxycycline diet. This sequesters the tetracycline trans-activator (tTa) in the system so that the tetracycline response element (TRE) is not activated, thus preventing expression. However, once the mice are taken off the doxycycline diet, tTa binds to TRE, activating downstream expression. Additionally, the cfos promoter limits expression to neurons with high cfos levels, which corresponds to active neurons. Hence, only active neurons in the CA3 and contralateral CA1 during the time of the training episode are labelled, labelling an engram.*

Figure courtesy of Clara Ortega-de San Luis.

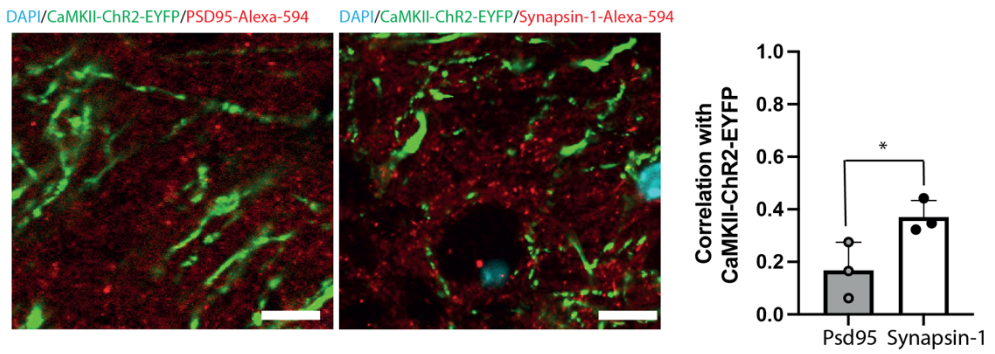
A



B



C



D

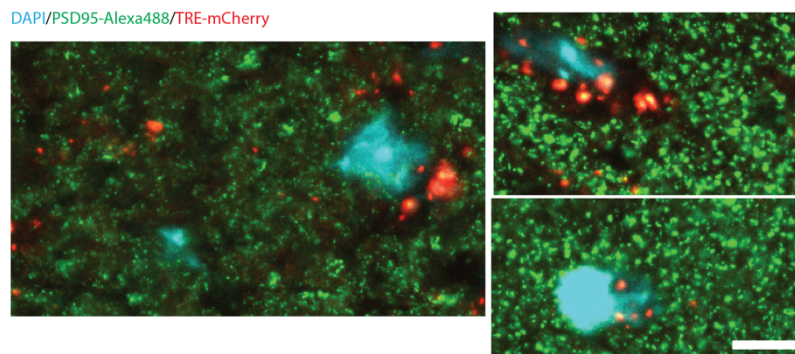


Figure 4.1.2: Confocal microscopy of engram-labelled cells in the hippocampal dorsal CA1 region.

A) Labelling of non-engram to engram synapses. Constructs were delivered into contralateral CA3 and CA1 hippocampal regions to allow simultaneous labeling of presynaptic and postsynaptic components respectively. Projections into CA1 were labelled by contralateral CA3 injection of AAV-CaMKII-ChR2-EYFP, whereas engram-specific labelling was achieved with the doxycycline (DOX)-controlled AAV cocktail AAV-cFos-tTA; AAV-TRE-mCherry. In the absence of DOX, engram neurons encoding for an episodic memory (contextual fear conditioning) became tagged with mCherry. Lightning symbol represents foot-shock delivery.

B) Cryostat sections of CaMKII-ChR2-EYFP-injected brain tissue from the contralateral side, indicating the DG, CA1 and CA3 regions. Scalebar = 100 μ m.

*C) Left, Cryostat sections of CaMKII-CAM-ChR2-EYFP-injected brain tissue from the contralateral CA1 region labelled with antibodies against Psd95 (left) and Synapsin-1 (right). Scalebar = 10 μ m. Right, correlation analysis using Pearson's correlation coefficient indicating negligible correlation of CaMKII-ChR2-EYFP and Psd95 and low-moderate correlation of CaMKII-ChR2-EYFP and synapsin-1-alexa-594. * $p < 0.05$ via two-tailed Student's t-test. Data presented as mean per acute slice \pm SEM, with at least 3 images taken per slice. $n = 3$ mice.*

D) Cryostat sections of TRE-mCherry-injected brain tissue from the CA1 region labelled with an antibody against Psd95. Scalebar = 10 μ m.

4.2 Developing and optimising the engram preparation for cryoCLEM and cryoET

To vitrify brain tissue, hippocampi dissected from engram-labelled mice were homogenised and plunge-frozen in liquid ethane onto cryoEM grids using a vitrobot (Fig.4.2A). To collect tomograms of engram synapses, cryoCLEM and cryoET were performed (Fig.4.2A). CryoFM indicated discrete ChR2-EYFP- and mCherry- positive puncta in the plunge-frozen hippocampal homogenate. The signals of mCherry-positive puncta were variable in intensity (Fig.4.2.1BC). For cryoCLEM correlation, medium magnification images of grid squares were collected and correlated to their respective cryoFM images.

Tilt series were collected from holes in the cryoEM grids containing puncta of ChR2-EYFP and mCherry, based on the cryoCLEM correlation. Together, cryoCLEM and cryoET enabled the identification of engram-labelled compartments *in situ*. For example, the ChR2-EYFP signal localised to a compartment characterized by containing numerous macromolecules and vesicles (mean vesicle diameter of 38 nm; n=20) (Fig.4.2.1B). This compartment had noticeable contacts with unlabelled membranes, reminiscent of synaptic architecture (Fig.4.2.1B). The mCherry puncta had varying degrees of intensity; high intensity mCherry signals correlated to tomograms of non-synaptic material. For example, in part of an mCherry-positive region, a cluster of macromolecular tubules, which ranged in diameter from 10-17 nm (n=20), was identified (Fig.4.2.1B). The shape of the mCherry signal did not clearly localise to a corresponding compartment, suggesting that the homogenisation process may have released the cytosolic mCherry from the labelled neuron. Alternatively, the macromolecular structure may have been auto fluorescent endogenous biological material within the mCherry range, which was already present in the brain, or may have been a result of overexpression of mCherry in the labelling strategy. Hence, the bright mCherry puncta detected did not correlate to engram-labelled postsynaptic compartments.

Conversely, 1 out of 18 tomograms collected from weak mCherry areas (Fig.4.2.1C) contained features consistent with being a synaptic junction, including a putative synaptic contact, a multitude of vesicles and numerous cleft proteins (Fig.4.2.1C). The ChR2-EYFP-positive neuron contained vesicles ranging in diameter from 26-31 nm (n=2) (Fig.4.2.1C). These measurements were consistent with plunge-frozen glutamatergic synapses (Peukes et al., 2021), suggesting that engram-labelled neurons can be detected using cryoFM, with weak mCherry signals indicating architecture resembling synapses.

However, the approach was low fidelity, prohibiting the acquisition of large numbers of engram synapse tomograms. In the plunge-frozen tomograms, intracellular features, such as vesicles and actin, were often absent or seen in the extracellular space (Fig.4.2.1BC), inferring that the approach was causing some damage to the architecture. These observations indicated that the sample preparation method was affecting the data quality, likely due to the freeze-thawing of brains and the homogenisation. Therefore, a different sample preparation method was required to improve the fidelity, preserve the fluorescent labels, and maintain the molecular architecture of engram synapses.

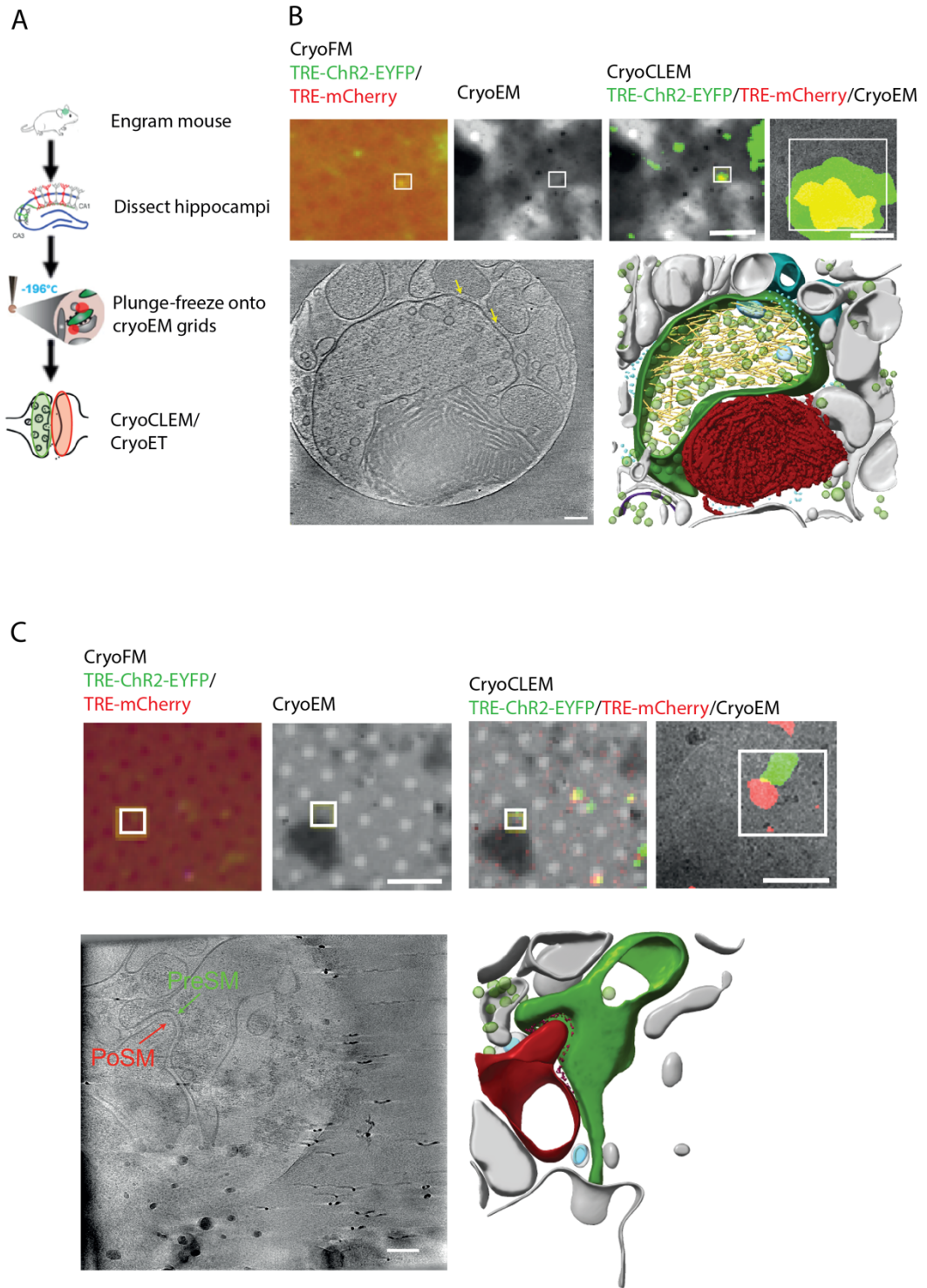


Figure 4.2.1: In situ molecular architecture of plunge-frozen engram-labelled neurons.

A) Workflow schematic using plunge-frozen hippocampus homogenate to determine the architecture of engram-labelled synapses. Mice were culled and brains were dissected. Hippocampi were homogenised in hACSF and plunge-

frozen in liquid ethane onto cryoEM grids using a vitrobot for cryoCLEM and cryoET. Created with BioRender.com

B) Left, Cryogenic correlated light and electron microscopy (cryoCLEM) localisation of engram subcellular structures. Top left, cryogenic fluorescence microscopy detection of TRE-ChR2-EYFP (green) and TRE-mCherry (red). Top right, cryo-electron micrograph. Bottom left, merge. Scale bar 5 μ m. Bottom right, enlarged merge. Scale bar 500 nm. White box indicates collection region.

Right, Tomography of engram-labelled subcellular structures. Top, Virtual slice through a reconstructed tomogram of TRE-ChR2-EYFP/TRE-mCherry – labelled subcellular structures. Potential clefts are indicated by yellow arrows. Scale bar 50 nm. Bottom, Segmentation from reconstructed tomogram in C. Green, ChR2-EYFP-positive pre-synaptic compartment. Red, mCherry-positive macromolecular features. Teal, neighbouring compartments with contacts. Grey, other neighbouring compartments. Translucent green, vesicles. Cyan, ribosomes. Gold, cytoskeletal network. Translucent blue, intracellular membranes.

C) Left, Cryogenic correlated light and electron microscopy (cryoCLEM) localisation of engram subcellular structures. Top left, cryogenic fluorescence microscopy detection of TRE-ChR2-EYFP (green) and TRE-mCherry (red). Top right, cryo-electron micrograph of engram subcellular structures. Bottom left, merge. Scale bar 5 μ m. Bottom right, enlarged merge. Scale bar 500 nm. White box indicates collection region.

Middle, Virtual slice through a reconstructed tomogram of TRE-ChR2-EYFP/TRE-mCherry –labelled putative engram synapse. Pre- and post-synaptic membranes are indicated with green and red arrows, respectively. Scale bar 50 nm.

Right, Segmentation from reconstructed tomogram in C. Green, ChR2-EYFP-positive pre-synaptic compartment. Red, mCherry-positive post-synaptic compartment. Grey, neighbouring compartments. Translucent green, vesicles. Translucent blue, intracellular membranes. Claret, cleft proteins.

To identify engram synapses with a higher-fidelity approach, optimisation of the workflow was required to preserve cytosolic mCherry signal, improving the detection rate of engram synapses. Cryo-sectioning was applied (Al-Amoudi et al., 2004), aiming to preserve the native cellular features of the sample and maintain the fluorescent labels. Moreover, brains were processed rapidly post-mortem without flash-freezing, minimising tissue damage and sample degradation.

To improve the fidelity, the workflow was optimised including the use of cell body labels and further screening steps (Fig.4.2.2A). To improve localisation of the neuroanatomical region, acute brain slices were incubated in Hoechst stain to indicate the cell bodies and therefore the granular layers of the hippocampus (Ramón y Cajal, 1909; Johnston and Amaral, 2004). This enabled collection specifically from the molecular layers, where numerous synapses are located (Johnston and Amaral, 2004). Acute slices were screened with an EVOS microscope and the CA1 molecular region was targeted with a 1 mm biopsy punch (Fig.4.2.2AB).

To vitrify the tissue, biopsies were incubated in cryoprotectant and were high-pressure frozen into gold carriers. The carriers were screened on the cryoFM for EYFP and mCherry signals, as well as to direct trimming to the *Stratum Oriens* and *Stratum Lacunosum* based on neuroanatomical layers (Fig.4.2.2B). The region of interest within the carrier was mapped and a pyramid of tissue was trimmed for cryo-sectioning, with cryoCLEM-directed cryoET being performed on the cryo-sectioned tissue ribbons. Discrete, sparse EYFP and mCherry puncta were identified with higher signal to noise than with the previous homogenization approach. Through application of cryo-sectioning, tomograms were collected of engram to engram (EE), non-engram to engram (NEE) and engram to non-engram (ENE) synapses in their in-tissue environment. Hence, the cryo-sectioning approach maintained the in-tissue architecture of the engram cells for a higher fidelity cryoCLEM workflow.

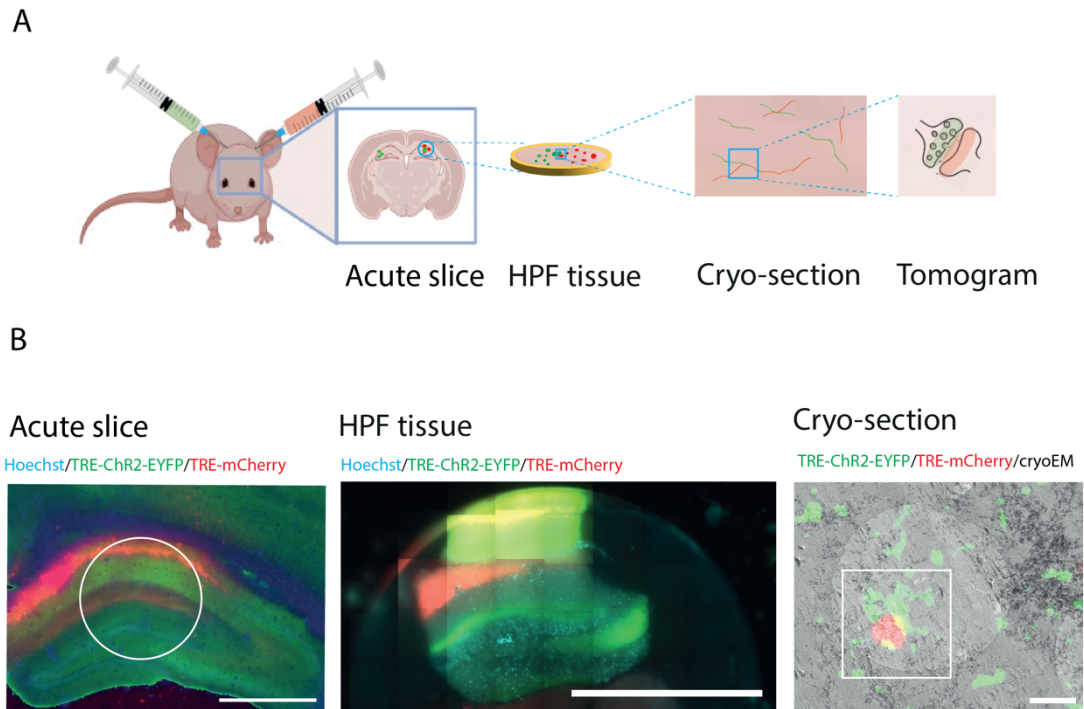


Figure 4.2.2: A workflow to detect engram synapses within cryopreserved tissue for cryoCLEM and cryoET

A) Schematic depicting the labelling and detection of engram neurons within the mouse, acute brain slice, high -pressure frozen (HPF) tissue and cryo-sections. These fluorescent puncta were used to direct cryoET collections of synapses. Created with BioRender.com

B) Engram labels in acute slice, high-pressure frozen (HPF) tissue and cryo-section. Scale bars 1 mm, 1 mm and 0.5 μ m.

4.3 Compositional analysis of engram-labelled synapses

A cryoCLEM-guided cryoET of an engram synapse (3 Å pixel size, ~110 e/Å² dose, field of view 1.2 μm²) was collected. Computationally reconstructing the tomographic volume revealed the circuit-specific in-tissue molecular architecture of an engram synapse (Fig.4.3.2A). ChR2-EYFP puncta were localized to three presynaptic membrane compartments each containing numerous presynaptic vesicles. These terminals were organized around a single CA1 mCherry-positive postsynaptic compartment, reminiscent of multibouton synapses that have been shown by *in vivo* fluorescence imaging to be upregulated in mice following hippocampal memory acquisition (Aziz et al., 2019), and within serial EM studies of the hippocampus (Sorra and Harris, 1993). This cryoET volume resolved macromolecular assemblies, including a branched F-actin cytoskeleton in the postsynaptic compartment and microtubules within the several pre-synaptic compartments (Fig.4.3.2A). Individual protein complexes were observed protruding from the postsynaptic membrane, as well as macromolecular complexes that tethered the pre- to the post- synaptic membrane (Fig.4.3.2A).

Next, analysis was expanded to account for heterogeneity (Bulovaite et al., 2022), collecting 87 engram-labelled in-tissue tomograms from a total of 4 mice, including 27 tomograms containing synapses. These included engram to engram (EE), non-engram to engram (NEE) and engram to non-engram (ENE) synapses, based on the presence of fluorophores in cryoFM imaging (Supp.Fig.2). A total of 15 EE synapses were obtained from 3 mice. These synapses contained a range of cellular organelles, (Fig.4.3.1; Supplementary Table 2), macromolecular complexes and proteins. Additionally, 9 control ENE synapses were collected from 2 of these engram-labelled mice, representing connections outside of the engram-labelled circuit. These synapses also had vast heterogeneity, with a variety of organelles and structures present in the cytoplasm and surrounding compartments (Fig.4.3.1; Supplementary Table 2). In an example ENE synapse (Fig. 4.3B), the EYFP-positive presynaptic terminal contained many vesicles and a mitochondrion.

To obtain additional control non-engram cryoET datasets, NEE synapses were labelled with a pan-neuronal ChR2-YFP at CA3 neurons and TRE-mCherry at CA1 neurons (CaMKII-ChR2-EYFP/TRE-mCherry) (Fig.4.3.1; Fig.4.3.2C; Supplementary Table 2). This yielded 3 NEE synapses from 2 mice.

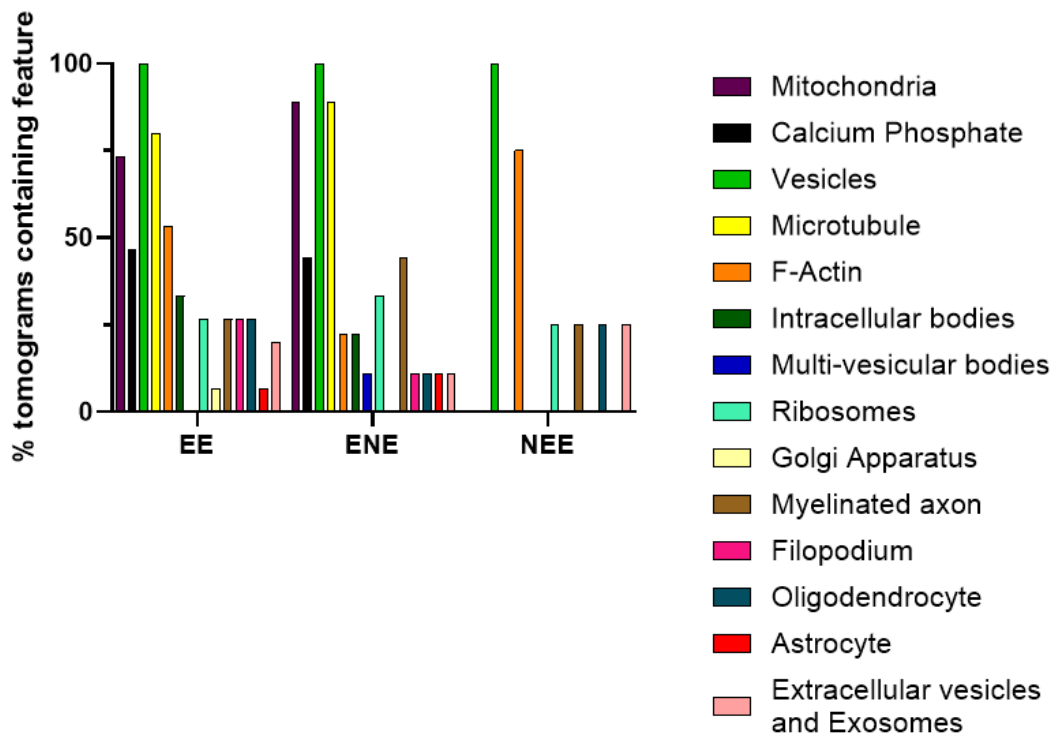


Figure 4.3.1: Constituents of tomograms containing engram-labelled synapses.

Variability was observed in tomograms containing EE, ENE and NEE synapses regarding the organelles and vicinal features.

Data are presented as a percentage of tomograms containing features. EE, n=15 tomograms from 3 mice, ENE, n=9 tomograms from 2 mice, NEE, n=3 tomograms from 2 mice

EE synapses shared many of same features as ENE and NEE synapses (Fig.4.3.1; Supplementary Table 2). All synapses contained presynaptic vesicles and an extensive postsynaptic cytoskeleton, with a synaptic cleft of variable height between the compartments (Fig.4.3.2). However, only 41% of synapses contained mitochondria, 26% microtubules and 36% membranous organelles. Overall, some structural and compositional features were shared between synapses, including presynaptic vesicles and cytoskeletal filaments, but not all synapses contained identical organelles and macromolecular constituents.

The subcellular compartments surrounding each synapse gave in-tissue contextual information, showing membrane enclosed processes (ranging 17-627 nm diameter) forming an elaborate cellular environment. The origin for most of these structures could not be definitively determined. Nonetheless, within tomographic volumes containing a synapse, 33% also contained a myelinated axon, 15% a filopodium, and 19% extracellular vesicles and exosomes. Compartments were surrounded by interstitial space, with the interstitial space occupying ~24% of the tomographic volume (n = 14 tomograms from 3 mice). These data were in-keeping with diffusion studies (Syková and Nicholson, 2008) and measurements from freeze-substituted tissue (Van Harreveld et al., 1965; Van Harreveld and Steiner, 1970), but larger than previously reported interstitial space in chemically-fixed tissue (Korogod et al., 2015). A sparse distribution of exosomes (0-5 per tomogram) was observed within interstitial space, as previously reported (Leistner et al., 2023).

Overall, these in-tissue cryoET data indicate that engram synapses and their surrounding environments were variable, consistent with the reported diversity of synapses (Cizeron et al., 2020; Zhu et al., 2021; Bulovaite et al., 2022).

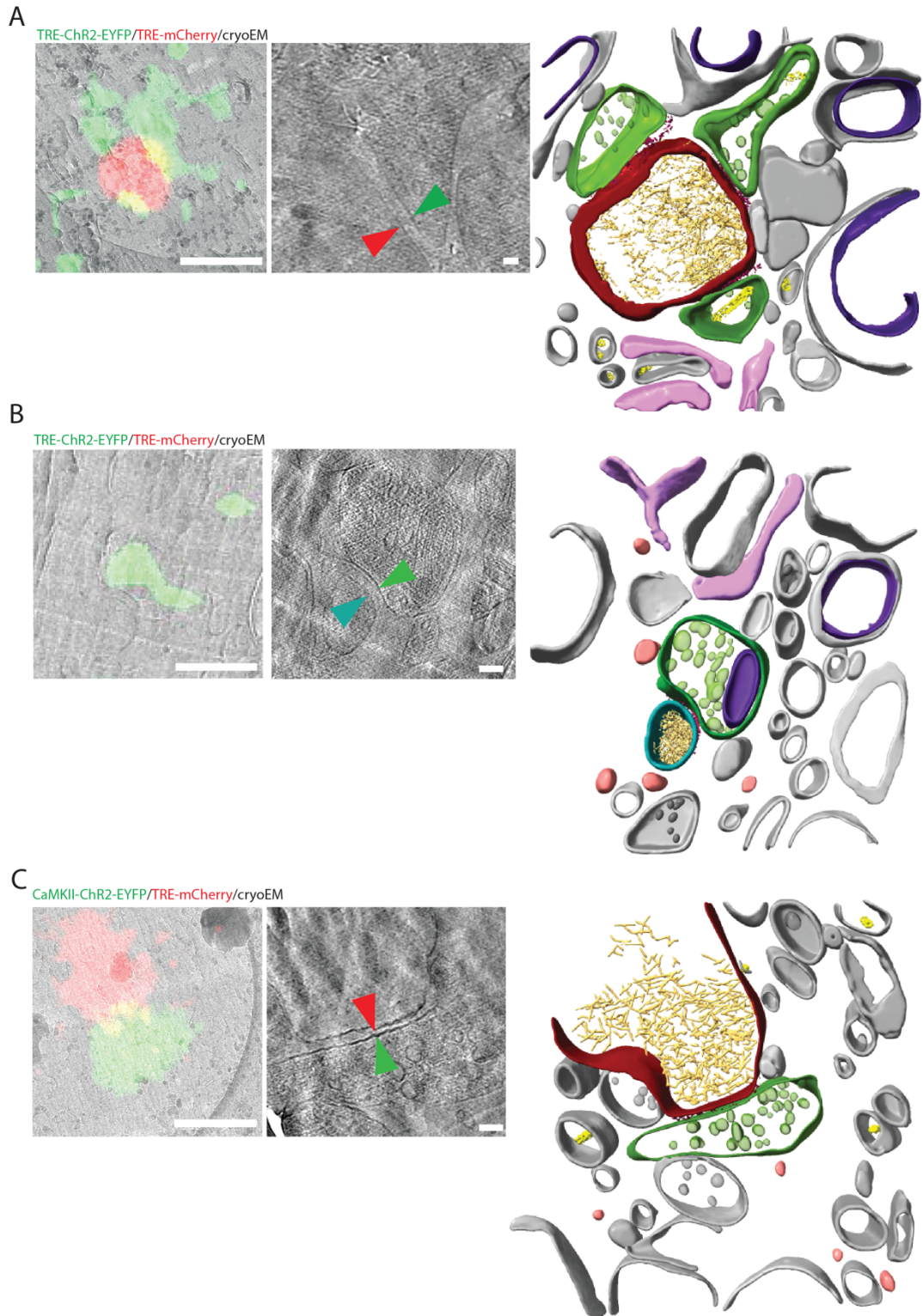


Figure 4.3.2: CryoCLEM and cryoET of engram-labelled synapses within cryo-sections.

A) An engram to engram labelled synapse from a TRE-ChR2-EYFP/TRE-mCherry-labelled mouse brain. Top left, cryoCLEM correlation of cryoFM and medium magnification cryoEM image. Scalebar = 0.5 μ m.

Bottom left, virtual tomographic slice indicating presynaptic (green) and postsynaptic (red) membranes. Scalebar = 20 nm.

Right, segmentation from tomogram on left. Key: Green, EYFP-positive presynaptic membrane; Red, mCherry-positive postsynaptic membrane; Claret, cleft proteins; Translucent green, presynaptic vesicles; Gold, actin-associated cytoskeletal filaments; Yellow, microtubules; Purple, mitochondria; Salmon, extracellular vesicles including exosomes; Light grey, other membranes.

B) An engram to non-engram labelled synapse from a TRE-ChR2-EYFP/TRE-mCherry-labelled mouse brain. Top left, cryoCLEM correlation of cryoFM and medium magnification cryoEM image. Scalebar = 0.5 μ m.

Bottom left, virtual tomographic slice indicating presynaptic (green) and postsynaptic (teal) membranes. Scalebar = 20 nm.

Right, segmentation from tomogram on left. Key: Green, EYFP-positive presynaptic membrane; Teal, unlabelled postsynaptic membrane; Claret, cleft proteins; Translucent green, presynaptic vesicles; Gold, actin-associated cytoskeletal filaments; Yellow, microtubules; Dark grey, non-synaptic vesicles; Salmon, extracellular vesicles including exosomes; Pink, filopodia; Purple, mitochondria; Light grey, other membranes.

C) A non-engram to engram labelled synapse from a CaMKII-ChR2-EYFP/TRE-mCherry-labelled mouse brain.

Top left, cryoCLEM correlation of cryoFM and medium magnification cryoEM image. Scalebar = 0.5 μ m.

Bottom left, virtual tomographic slice indicating presynaptic (green) and postsynaptic (red) membranes. Scalebar = 20 nm.

Right, segmentation from tomogram on left. Key: Green, EYFP-positive presynaptic membrane; Red, mCherry-positive postsynaptic membrane; Claret, cleft proteins; Translucent green, presynaptic vesicles; Gold, actin-associated cytoskeletal filaments; Yellow, microtubules; Dark grey, non-synaptic vesicles; Salmon, extracellular vesicles including exosomes; Light grey, other membranes.

4.4 Quantitative analysis of engram synaptic architecture revealed diverse features

Extensive diversity in organelle constituents existed within populations of EE, ENE, and NEE synapses (Fig.4.3.1; Supplementary Table 2), including the presence of cellular organelles. Mitochondria were identified based on the presence of an outer membrane and inner membrane composed of cristae (Fig.4.4A). Overall, 7 presynaptic compartments and 7 postsynaptic compartments contained mitochondria, and there were no significant differences in the prevalence of mitochondria between EE, ENE, and NEE synapses (Fig.4.4A). Some mitochondria were found within postsynaptic compartments, which could relate to the observed larger postsynaptic/dendritic mitochondria within the CA1 region (Delgado et al., 2019; Yao et al., 2020). Since dendritic spines do not contain mitochondria (Knott et al., 2002; Tamada et al., 2020), it is possible that some of these synapses with postsynaptic mitochondria could correspond to immature excitatory synapses, excitatory synapses onto inhibitory neurons, or inhibitory synapses (Yuste and Bonhoeffer, 2004; Chiu et al., 2013; Konietzny et al., 2019; Bucher et al., 2020).

Mitochondria store intracellular calcium (Mattson et al., 2008), forming calcium phosphate deposits (Faas et al., 2012; Woodward et al., 2015; Wolf et al., 2017; Wu et al., 2023). To assess sequestered calcium stores, calcium phosphate deposits were quantified. Only one presynaptic compartment, which belonged to an ENE synapse, contained dense deposits. Conversely, these deposits were readily identified in 71% of all postsynaptic mitochondria, which was significantly greater than in presynaptic compartments ($p \leq 0.05$)

(Fig.4.4A). This could be indicative of recent calcium activity at CA1 dendrites, resulting in calcium sequestration into mitochondria (Mattson et al., 2008). There were no significant differences between EE and ENE synapses, indicating that without recall before sacrificing, EE and ENE synapses have similar prevalence of mitochondrial calcium phosphate stores. There were no mitochondria present at NEE synapses for comparison (Fig.4.4B). Hence, calcium phosphate stores are prevalent in the postsynaptic compartments of engram synapses, perhaps indicative of recent calcium activity in the CA1 region.

Presynaptic vesicles were present in all synapses (Fig.4.3.1; Supplementary Table 2), reflecting their critical role in action potential-evoked neurotransmission involving vesicle coupling and distribution in the active zone (Südhof, 2012). Vesicles are distributed throughout presynaptic compartments and are trafficked to the active zone to become release-competent (Zuber and Lučić, 2019; Borges-Merjane et al., 2020; Radecke et al., 2023).

To assess presynaptic activity, the vesicle diameter, distribution, and tethering were measured using a combination of IMOD and MatLab scripts (Fig.4.4CD). It was expected that more active synapses would have a greater proportion of release-competent vesicles, which would be reflected in a greater proportion in the active zone and tethered to the presynaptic membrane. The mean vesicle diameter was 33 ± 1.22 nm, as expected (Akert et al., 1964; Zuber et al., 2005; Borges-Merjane et al., 2020; Peukes et al., 2021). The percentage of vesicles within the proximal (0-45 nm from presynaptic membrane), intermediate (45-75 nm from presynaptic membrane) and distal (>75nm from presynaptic membrane) regions were calculated. No significant differences were found between the groups of synapse type, although ENE synapses showed a significantly larger proportion of vesicles in the distal region compared to the proximal ($p < 0.05$), inferring a larger population of vesicles in distal pools and therefore reduced activity.

However, the volume of the postsynaptic compartments was variable, suggesting that the increase in percentage of distal vesicles in ENE synapses could have been influenced by the total volume of the distal region within the cryo-section. Hence, the vesicle occupancy based on the volume of each region occupied by vesicles was calculated (Fig.4.4D). No significant differences were detected, inferring that vesicles were evenly distributed across groups. These values were within a similar range to previously published WT samples (Radecke et al., 2023).

Finally, the percentage of tethered proximal vesicles was calculated, inferring variability in recent activity in all groups (Fig.4.4D). Together, these data reflect the heterogeneity of synapses and indicate that in the absence of reactivation induced by natural or artificial recall, EE synapses have comparable presynaptic activity to controls.

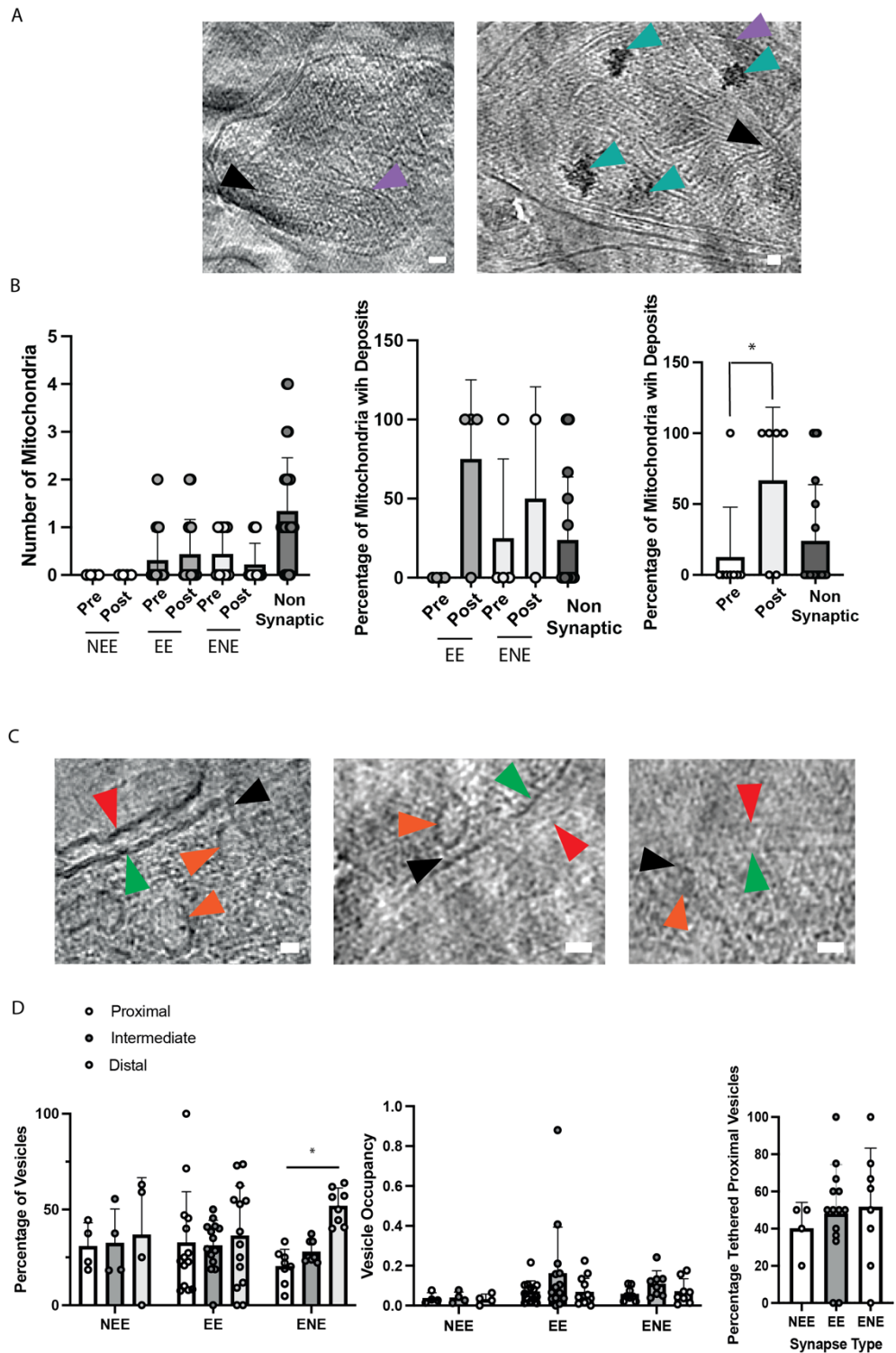


Figure 4.4: Variability in prevalence of cellular organelles in engram-labelled synapses

A) Virtual tomographic slices depicting mitochondria found at engram-labelled synapses. Purple, mitochondrial outer membranes, black, cristae, and teal, calcium phosphate deposits Scalebars = 20 nm.

B) Left, the number of mitochondria in presynaptic and postsynaptic compartments from EE (engram to engram), NEE (non-engram to engram) and ENE (engram to non-engram) synapses, and from non-synaptic compartments. Presented as mean number of mitochondria per tomogram \pm SD. Middle, graph depicting the percentage of mitochondria with calcium phosphate deposits in EE synapses, ENE synapses and non-synaptic compartments. Presented as mean number of mitochondria per tomogram \pm SD. No significant differences were detected between EE and ENE presynaptic and postsynaptic compartments using a one-way ANOVA with Tukey's post-hoc test. Right, graph depicting the percentage of mitochondria with calcium phosphate deposits in presynaptic, postsynaptic, and non-synaptic compartments. Presented as mean number of mitochondria per tomogram \pm SD. * $p \leq 0.05$ using one-way ANOVA with Tukey's post-hoc test. More calcium phosphate deposits were detected in postsynaptic compartments compared to presynaptic compartments.

C) Virtual tomographic slices depicting vesicles found at engram-labelled synapses. Green arrowhead, presynaptic membrane; Red arrowhead, postsynaptic membrane; Orange arrowhead presynaptic vesicle; Black arrowhead, tethering protein. Scalebars = 20 nm.

D) Left, The percentage of vesicles in the proximal, intermediate, and distal regions in NEE, EE and ENE synapses. * $p < 0.05$ using a one-way ANOVA and Tukey's post-hoc test. Significantly more vesicles were found in the distal compared to proximal regions of ENE synapses. No significant differences were found between groups. Middle, vesicle occupancy based on the volume of the proximal, intermediate, and distal regions occupied by vesicles. No significant differences were detected between EE, ENE and NEE synapses according to one-way ANOVA with Tukey's post-hoc test. Right, the percentage of docked vesicles found in the proximal region. No significant differences were found.

Data presented as mean number per tomogram \pm SD. $n=3$ mice for EE and $n=2$ mice for NEE and ENE.

4.5 Macromolecular constituents of the synaptic cleft demonstrated vast heterogeneity

Synaptic transmission is dependent upon multiple factors, including the concentration profile of neurotransmitter in the synaptic cleft and the electrophysiological resistance profiles of the cleft (Savtchenko and Rusakov, 2007). Whilst narrowing the synaptic cleft increases the concentration of neurotransmitter, promoting activity, this also increases the electrical resistance and therefore reduces local receptor currents (Savtchenko and Rusakov, 2007).

To quantify the distance between synaptic contacts, synaptic cleft height was measured using MatLab scripts, revealing variable mean cleft height between 10-35 nm (Fig.4.5.1A). This range was larger than previously reported (Peters et al., 1970; Savtchenko and Rusakov, 2007), due to the present cryopreservation approach avoiding the use of fixatives and cross-linking chemicals which could shrink and dehydrate the cleft (Zuber et al., 2005). However, cleft height distribution was comparable to Psd95-EGFP-labelled glutamatergic synapses in homogenized tissue and cryo-sections (Peukes et al., 2021) (chapter 3). Some clefts had bimodal distributions, inferring that there were two distinct sub-populations of cleft height. The length of cleft adhesion proteins supported the range of cleft heights, suggesting that these structural features could be involved in local modulation of the cleft height (Fig.4.5.1B).

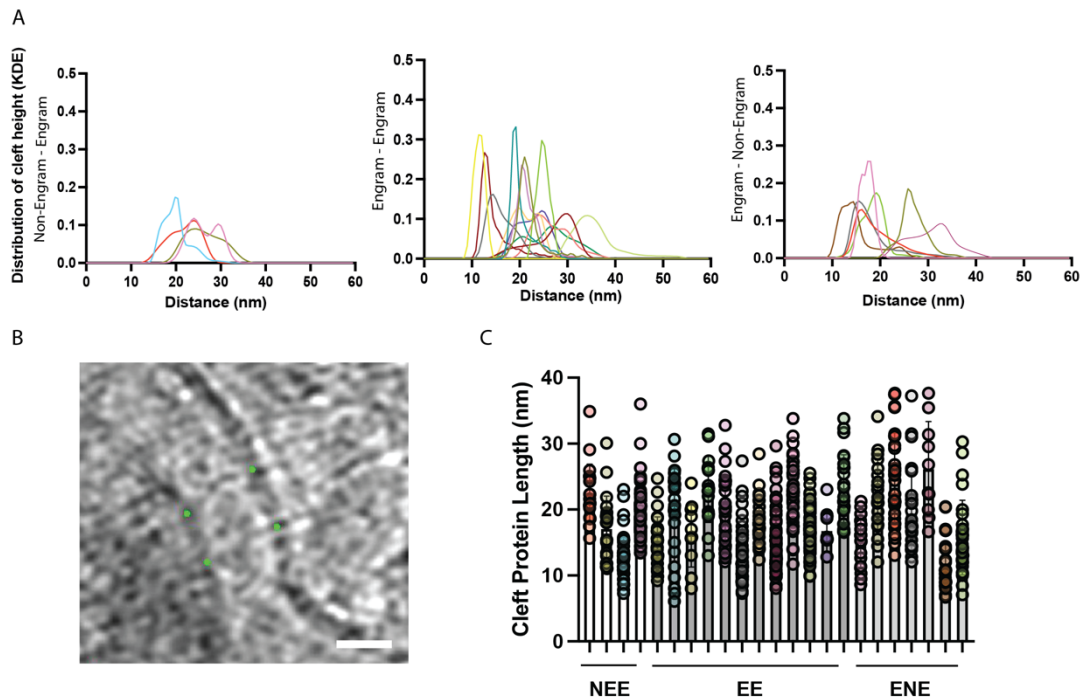


Figure 4.5.1: Engram-labelled synapses demonstrated variable distribution of synaptic cleft height.

A) Kde plots of cleft height from non-engram to engram, engram to non-engram and engram to engram -labelled synapses. Each trace represents an individual synaptic cleft. All groups had variable cleft height distribution, representing synaptic heterogeneity and dynamic remodelling.

B) Tomographic slice indicating two cleft adhesion proteins spanning presynaptic to postsynaptic membrane, with green model points placed at each membrane contact. Measurements were taken between pairs of model points. Scalebar = 20 nm.

C) Graph depicting the length of cleft adhesion proteins in EE (engram to engram), ENE (engram to non-engram) and NEE (non-engram to engram) synapses. Each colour describes the cleft adhesion proteins within the matching colour cleft height trace in A. Data are plotted as individual protein length and mean \pm SD. $n=3$ mice for EE and $n=2$ mice for NEE and ENE.

To quantify molecular features, subtomogram averaging was performed to sort molecular constituents into classes based on their dimensions. As a resolution benchmark, microtubules were averaged to estimate maximal resolution of *in-tissue* features within bin4 tomograms. Subtomogram averaging of microtubules generated a structure at ~3.12 nm resolution (Fig.4.5.2A), comparable to previous studies which identified microtubules in cells (Koning et al., 2008; Grange et al., 2017), indicating the achievable resolution from the *in-tissue* tomograms. A tubulin alpha/beta dimer (PDB: 1TUB (Nogales et al., 1998)) was docked to verify the structure (Fig.4.5.2A). The microtubules consisted of 13 protofilaments surrounding a central tubule. Interestingly, the averaged microtubules had a central density similarly structured to decorated cofilactin (PDB 8OH4; Fig.4.5.2A) previously reported in insect microtubules (Santos et al., 2023). Therefore, the achievable resolution of a high contrast feature through this methodology in the cryo-sections was ~3.12 nm.

Next, subtomogram averaging was applied to the synaptic cleft using a membrane oversampling method, resulting in the generation of seven class averages via PCA analysis (Fig.4.5.2BC). The density of these classes was highly variable within and between groups, with no statistically significant difference between EE and ENE synapses, reflecting synaptic heterogeneity in engram circuits. Class averages were compared to published structures to putatively identify the molecular constituents (Shapiro and Weis, 2009; Honig and Shapiro, 2020).

Class 1 was a horizontal density identified running through the centre of the synaptic cleft parallel to the plasma membranes (Fig.4.5.2D), reminiscent of previous reports (Zuber et al., 2005; Peukes et al., 2021). Numerous adhesion proteins interdigitated this density (Fig.4.5.2D), connecting it to the synaptic membranes. A variety of cleft adhesion proteins have been reported in the literature forming these lattices (Shapiro and Weis, 2009; Harrison et al., 2011; Brasch et al., 2019), including at neuronal synapses relating to dynamic activity (Martinez-Sanchez et al., 2021).

Class 2 proteins were found in almost all synapses, including ENE synapses, often in clusters (Fig.4.5.2E), bridging the synaptic cleft to engage with numerous postsynaptic proteins. Cluster analysis was performed, in which a cluster was defined as a minimum of 3 proteins within 720 Å in a triangulation mesh. Here, 7 tomograms contained enough class 2 proteins for this analysis; 3 tomograms contained a cluster of 4 proteins, 1 tomogram had a cluster of 4 and a cluster of 5, and the remaining 3 tomograms were unclustered. These data highlight that class 2 is commonly found in groups at the synaptic cleft. These features were reminiscent of super-resolution microscopy of neurexins, critical presynaptic adhesion molecules distributed in clusters (Trotter et al., 2019). Furthermore, similarly to class 2 proteins which engaged postsynaptic proteins, neurexins are known to interact with postsynaptic membrane proteins such as neuroligins, LRRTM1/2 and α/β -Dystroglycan to recruit iGluRs or GABARs at opposing postsynaptic membranes (Südhof, 2017; Gomez et al., 2021). Since neurexin-1a is an important presynaptic cleft adhesion protein in synapse maturation and organisation, promoting interactions with a variety of other proteins such as neuroligins (Leone et al., 2010), it was a good candidate for the identity of class 2 proteins. An available atomic model of neurexin-1a was well-accommodated in the presynaptic half of the map (Chen et al., 2011) (Fig.4.5.2E).

Class 3 proteins were putatively identified as ionotropic glutamate receptors (iGluRs), due to their distinctive Y-shape, postsynaptic location and clustering (Broadhead et al., 2016; Peukes et al., 2021) (Fig.4.5.2F). Without high-resolution tomographic structures with identifiable residues, differentiation between AMPAR, desensitized AMPAR and NMDAR was not possible based on published structures (PDB 4u2p (Dürr et al., 2014), PDB 4u4f (Yelshanskaya et al., 2014), PDB 5iou (Zhu et al., 2016)), suggesting that class 3 contained ionotropic glutamate receptors in a mix of conformational states, similarly to previous studies (Martinez-Sanchez et al., 2021).

Although not statistically significant (Student's t-test, $p > 0.05$), a greater mean number of ionotropic glutamate receptors were observed at glutamatergic spine EE synapses compared to ENE synapses (Fig.4.5.2F), suggesting that

EE synapses could have a trend for AMPAR insertion. Cluster analysis of class 3 proteins was performed, in which a cluster was defined as a minimum of 3 proteins within 720 Å in a triangulation mesh. Presently, 3 EE tomograms contained enough class 3 proteins for this analysis, in which 2 tomograms contained 1 cluster and the remaining tomogram was unclustered, suggesting that ionotropic glutamate receptors tend to be found in groups. This is reminiscent of super-resolution microscopy studies which identified nanodomains (Broadhead et al., 2016; Tang et al., 2016), and of previous cryoET studies utilising brain homogenate (Peukes et al., 2021). However, it is important to consider that with 70 nm thick samples, only a subsample through the synapse could be reconstructed rather than the whole synapse. Therefore, the exact number of AMPARs could not be counted per synapse, especially with the known clustering of iGluRs (Harris and Pettit, 2007; Peukes et al., 2021), so a larger dataset would be needed to accurately assess AMPAR numbers, AMPAR distribution and to obtain high-resolution structures.

The remaining 4 classes could not be identified due to the resolution limitation and heterogeneity within the class (Fig.4.5G).

Overall, molecular constituents could be detected within the synaptic clefts in engram circuits, enabling assessment of number and distribution of classes, although heterogeneity and low number limited the achievable resolution obtainable through subtomogram averaging, meaning high resolution in-tissue structures were not solved.

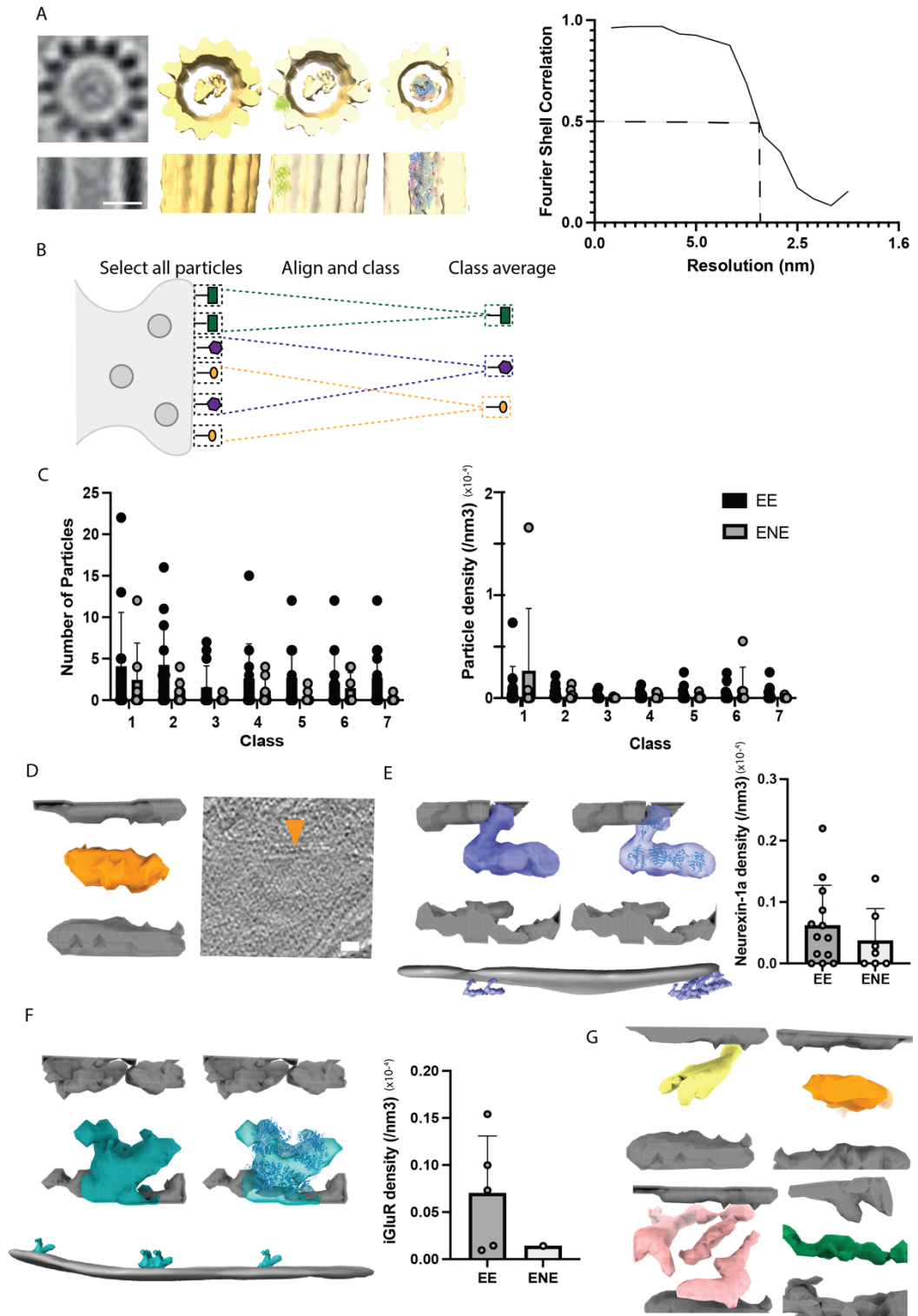


Figure 4.5.2: Classification of molecular features in synaptic clefts revealed variability.

A) Left, Subtomogram averaged structure of a microtubule. Middle left, microtubule volume. Middle right, structure with beta-tubulin (PDB 1TUB) docked into a protofilament, scalebar 10 nm. Right, structure with cofilactin (PDB 8OH4) docked into central density of filament. Bottom, FSC plot of subtomogram averaged microtubule, indicating a resolution of ~3.12 nm.

B) Schematic representation of the selection of particles through membrane oversampling and the averaging of these particles to generate class averages of molecular features. These class averages were used to quantify the density of each class within the cleft.

C) Left, the number of each class of protein present per tomogram, based on the output of PEET and PCA analysis from EE and ENE synapses. Right, the density of each class within the synaptic cleft. Data are plotted as mean per tomogram \pm SD. $n=2$ mice for both groups.

D) Left, class 1 average. Right, a virtual tomographic slice of a synaptic cleft with a central density corresponding to class 1 average indicated by orange arrowhead. Scalebar = 20 nm.

E) Left, class 2 average. Middle, class 2 average with neurexin-1a (PDB ID 3qcw) docked. Right, Density of putative neurexin-1a in the synaptic cleft. Bottom, localisation of class 2 proteins on a presynaptic membrane. Data are plotted as mean per tomogram \pm SD. $n=2$ mice for both groups.

F) Left, class 3 average. Middle, class 3 average with desensitised AMPAR structure docked (PDB ID 4u2p). Right, graph depicting the density of putative iGluRs in the synaptic cleft of identified glutamatergic spine synapses. Data are plotted as mean per tomogram \pm SD. $n=2$ mice for both groups.

G) Averages for classes 4-7, clockwise from top left. These classes were not identified due to low number, variability and resolution limitations.

4.6 Postsynaptic compartments exhibit F-Actin-associated cytoskeletal networks

In the postsynaptic compartments of EE, ENE and NEE synapses, extensive cytoskeletal networks were observed (Supplementary Table 2, Fig.4.6). These networks are composed predominantly of filamentous actin (F-Actin) (Landis and Reese, 1983; Korobova and Svitkina, 2010), and remodel and sustain the geometry of a compartment in response to neuronal activation (Okamoto et al., 2004; Korobova and Svitkina, 2010; Basu and Lamprecht, 2018; Goto et al., 2021). Such activity underlies LTP at dendritic spines (Fukazawa et al., 2003). Accordingly, the dynamics of the F-Actin-associated cytoskeleton are critical to learning and memory consolidation in engram cells (Lv et al., 2019; Ortega-De San Luis and Ryan, 2022).

To investigate the F-Actin number and geometry of the cytoskeletal network within postsynaptic compartments, an ultrastructural analysis toolkit was applied, which calculates the number, distance and angle of filaments within a 3D network (Dimchev et al., 2021). F-Actin was detected within postsynaptic compartments based on its ~6 nm diameter (Fig.4.6A), where it formed extensive branched networks (Korobova and Svitkina, 2010; Jung et al., 2020). The number of F-Actin filaments was not significantly higher at EE synapses (Fig.4.6B), indicating that cytoskeletal remodelling was not a unique feature of engram synapses at this latent timepoint. Similarly, the volume fraction of F-Actin and the average filament angle relative to the postsynaptic membrane were unchanged at engram synapses (Fig.4.6CD). In contrast, filament length was significantly higher in NEE synapses compared to EE and ENE synapses (Fig.4.6E), taken together with the similar volume fractions, these data infer that the non-engram control synapses contained longer filaments, rather than densely packed shorter filaments, which could relate to the greater branching of F-Actin in engram cells (Lv et al., 2019).

The number of F-Actin detected was not significantly affected by tomogram thickness, number of tilt images per tomogram, or defocus (Fig.4.6F), indicating that the data were of a consistent quality for F-Actin detection.

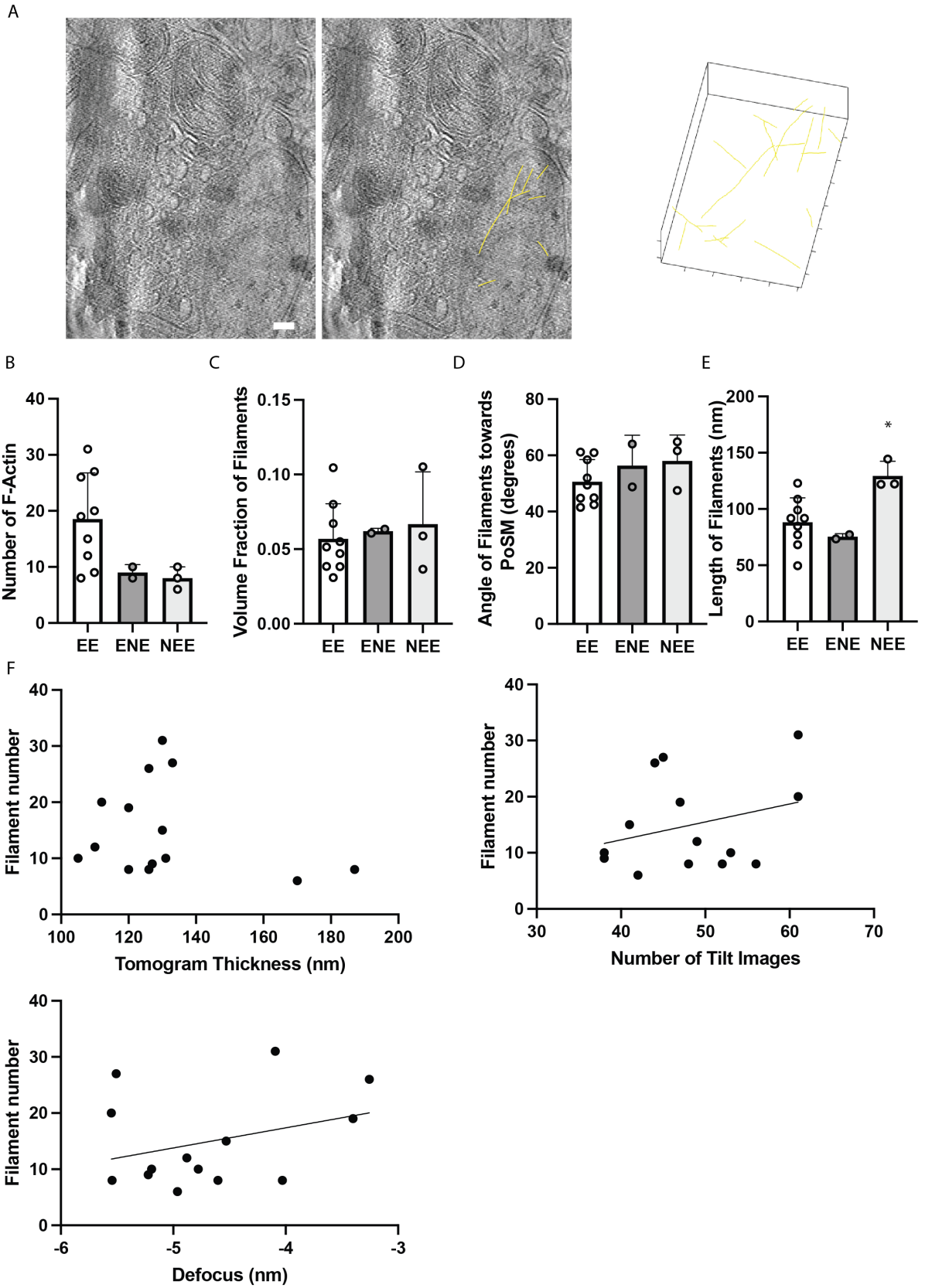


Figure 4.6: Ultrastructural analysis of F-Actin in engram-labelled cells revealed variability.

A) Left, virtual tomographic slice containing an engram-engram synapse. Middle, the same cross-sectional tomographic slice with F-Actin indicated in yellow. Right, 3D model of F-Actin within the tomographic volume. Scalebar = 20 nm.

B) The mean number of F-Actin per postsynaptic compartment in EE, ENE and NEE synapses. No significant differences were detected (ANOVA, $p=0.05$).

C) The volume fraction of F-Actin within postsynaptic compartments in EE, ENE and NEE synapses. No significant differences were detected (ANOVA, $p=0.05$).

D) The angle of F-Actin relative to the postsynaptic membrane in EE, ENE and NEE synapses. No significant differences were detected (ANOVA, $p=0.05$).

E) The length of F-Actin filaments in EE, ENE and NEE postsynaptic compartments. The NEE postsynaptic compartments evidenced significantly longer F-Actin compared to EE and ENE (ANOVA, * $p<0.05$).

F) The number of F-Actin detected was not significantly influenced by tomogram thickness, number of tilt images, or defocus (simple linear regression).

EE, $n=9$ synapses from 2 mice, ENE, $n=2$ synapses from 2 mice, NEE, $n=3$ synapses from 2 mice. Synapses were excluded if F-Actin could not be unambiguously detected.

4.7 Vicinal engram-labelled features

The workflow also enabled the collection of tomograms from vicinal subcellular regions of engram-labelled cells, due to the use of cell-wide labels (Supplementary Table 2, Fig.4.7). ChR2-EYFP signals could be broadly classified into 3 groups:

i) 16% extrasynaptic ChR2-YFP mapped to filopodia (Fig.4.7A), with average diameter ranging from 18-46 nm. These likely relate to the nascent early stages of synaptogenesis (Chang and De Camilli, 2001; Menna et al., 2009; Ketschek and Gallo, 2010).

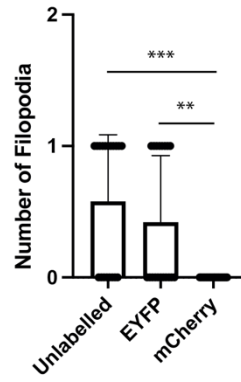
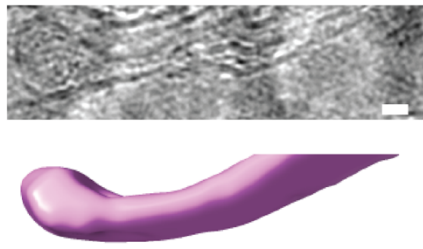
ii) 14 % extrasynaptic ChR2-YFP were myelinated axons (Fig.4.7B). Myelin was identified based on its similarity to myelin within negative-stained tissue samples (Stassart et al., 2018), and myelinated axons were defined by having five or more layers of 6-8 nm thick membrane lipid bilayers enclosing a subcellular compartment (Caspar and Kirschner, 1971; Gilbert et al., 2023). This was consistent with CA3 (presynaptic) targeting of ChR2-EYFP expression (Nickel and Gu, 2018). Accordingly, mCherry was not correlated to myelinated axons in these CA1 molecular layer tomograms.

iii) The remaining 70% of extrasynaptic ChR2-YFP likely correspond to unmyelinated axonal processes.

Vicinal regions contained a range of organelles and extracellular features including vesicles, ribosomes and membranous bodies (Fig.4.7C).

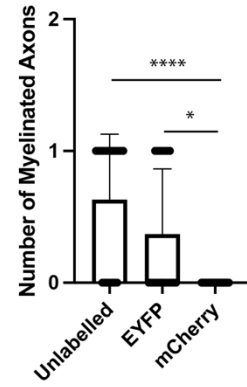
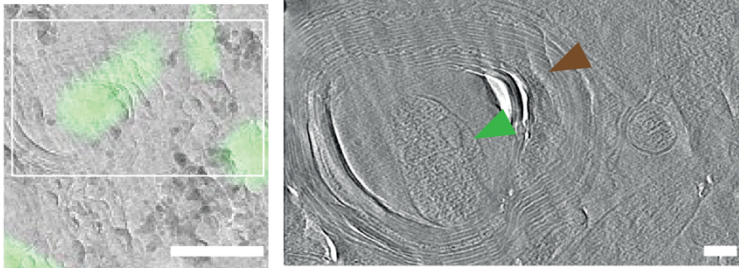
All extrasynaptic mCherry labelled cellular regions (n = 38 tomograms containing non-synaptic mCherry-positive regions) likely corresponded to somato-dendritic regions of CA1 cells (Fig.4.7D).

A

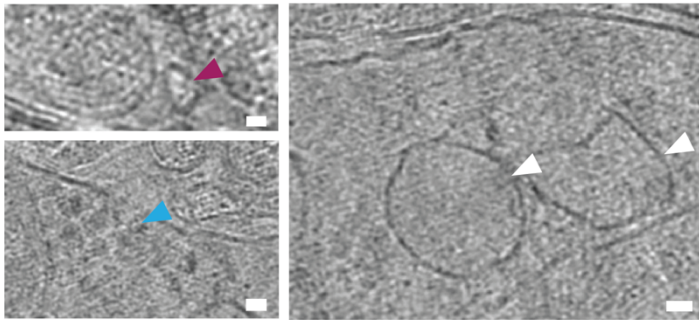


B

TRE-ChR2-EYFP/TRE-mCherry/cryoEM



C



D TRE-ChR2-EYFP/TRE-mCherry/cryoEM

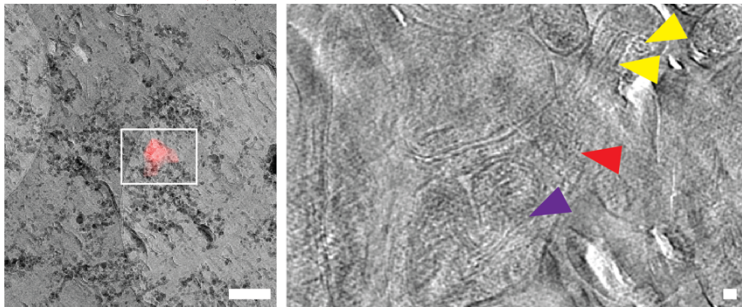


Figure 4.7: CryoCLEM of extracellular non-synaptic engram-labelled constituents.

*A) Left, a filopodium within a tomographic virtual slice and a segmentation from the same reconstruction. Scalebar = 20 nm. Right, graph depicting the number of putative filopodia per tomogram in engram-labelled brain tissue. There were significantly fewer mCherry-positive filopodia than unlabelled or EYFP-positive according to a one-way ANOVA with Tukey's post-hoc test. ** $p < 0.01$, *** $p < 0.001$. $n = 19$ tomograms from 2 mice.*

*B) Left, cryoCLEM depicting EYFP signal correlating to a myelinated axon. Middle, virtual tomographic slice from area indicated by white box in left. Green arrowhead indicates a compartment of vesicles within a myelinated axon. Brown arrowhead indicates myelin. Right, graph depicting the number of myelinated axons per tomogram in engram-labelled tissue. Significantly fewer myelinated axons were mCherry-positive compared to EYFP-positive or unlabelled according to a one-way ANOVA with Tukey's post-hoc test. * $p < 0.05$, **** $p < 0.0001$. $n = 19$ tomograms from 2 mice. Scalebars = $0.5 \mu\text{m}$ and 50 nm.*

C) Top left, an extracellular vesicle in a synaptic cleft. Pink arrowhead, extracellular vesicle. On average, tomograms of EE synapses contained 0.33 exosomes, whereas NEE synapses were associated with 0.75, and ENE synapses had 0.635. $n = 27$ synapses from 4 mice. These differences were not significant by synapse group (one-way ANOVA and Tukey's post-hoc test). Bottom left, ribosomes in an engram-labelled compartment. Cyan arrowhead, ribosome. Right, intracellular membranes within an engram-labelled compartment. White arrowheads, intracellular membrane. Scalebars = 20 nm.

D) Left, cryoCLEM depicting mCherry signal correlated to a non-synaptic dendritic region. Right, virtual tomographic slice from area indicated by white box in left. Red arrowhead indicates mCherry-positive dendritic region. Yellow arrowheads indicate microtubules. Purple arrowhead indicates mitochondrion. Scalebars $0.5 \mu\text{m}$ and 20 nm.

4.8 Concluding comments

To summarise, a novel workflow was developed to bridge from mouse behaviour in a memory task to the ensemble of macromolecules and proteins at synapses underlying this memory. Variable architectures were detected at engram and control synapses, highlighting the heterogeneity of in-tissue synapses. Although a feature unique to engram synapses was not detected in this study due to synaptic heterogeneity and the time after encoding, in future studies, the workflow could be applied to different timepoints, enabling investigations into memory stages such as recall, consolidation, and information storage. Furthermore, a larger dataset could mitigate synaptic heterogeneity and distinguish engram-specific architectures.

In agreement with the literature, all synapses were diverse in their organelle composition (Sorra and Harris, 1993; Shepherd and Harris, 1998; Delgado et al., 2019; Peukes et al., 2021), molecular constituents of the synaptic cleft (Zhu et al., 2018; Bulovaite et al., 2022), and number of cellular components, such as F-Actin (Korobova and Svitkina, 2010; Jung et al., 2020). Equally, some features were consistently shared by all synapses, including numerous vesicles within the presynaptic compartment (Zuber and Lučić, 2019; Martinez-Sanchez et al., 2021; Radecke et al., 2023) and an extensive F-Actin-associated cytoskeletal network in the postsynaptic compartment (Spence and Soderling, 2015; Jung et al., 2020; Peukes et al., 2021).

A range of organelles were observed in presynaptic and postsynaptic compartments, including mitochondria, which have previously been identified in the CA1 region (Delgado et al., 2019). No significant differences were detected relating to the engram, although an enrichment of mitochondrial calcium phosphate granules (Wolf et al., 2017; Wu et al., 2023) was observed postsynaptically, inferring the sequestration of calcium to buffer recent calcium-dependent events (Martin and Matthews, 1969; Lehninger, 1970; Brown et al., 2006; Mattson et al., 2008). However, this analysis was limited as the NEE synapses within the dataset did not have any mitochondria to compare, and therefore whether this is a feature relating to synapses from presynaptic CA3 engram cells remains to be fully elucidated.

Other organelles analysed included presynaptic vesicles, which had variable occupancy comparable to unstimulated synapses (Radecke et al., 2023). Engram synapses did not have any significant differences in vesicle occupancy or tethering, suggesting that, as expected without natural or artificial recall (Liu et al., 2012; Liu et al., 2014), these synapses did not have significantly different presynaptic activity to controls.

Additionally, the F-Actin-associated postsynaptic cytoskeleton was analysed to indicate number, volume fraction, angle and length of F-Actin (Dimchev et al., 2021). F-Actin was not significantly upregulated in engram synapses, conflicting with the literature (Okamoto et al., 2004; Lv et al., 2019; Goto et al., 2021), although this was likely due to the latent timepoint of 6 days after engram labelling that was observed in this study. Although here it was shown that F-Actin number was not significantly altered in engram synapses 6 days after labelling, an important future study should establish how cytoskeleton is modified at earlier intervals, starting from immediately after engram labelling. Furthermore, it is likely that not all synapses within this study were excitatory synapses onto dendritic spines, which could account for some of the variability, as dendritic spines are known to be enriched in F-Actin (Landis and Reese, 1983; Hotulainen et al., 2009; Korobova and Svitkina, 2010).

The synaptic cleft was analysed to determine the distribution of cleft height, relating to neurotransmitter concentration and resistance profiles (Savtchenko and Rusakov, 2007). These data agreed with other cryoET studies of synapses using alternative preparations (Zuber et al., 2005; Peukes et al., 2021), but conflicted with conventional EM studies of the synaptic cleft (Schikorski and Stevens, 1997), likely due to the cryopreserving approach avoiding the use of chemical fixatives that shrink and dehydrate the cleft (Zuber et al., 2005). Moreover, the dataset could have included some synapses which were not excitatory synapses onto dendritic spines, which could account for some of the heterogeneity observed here (Linsalata et al., 2014; High et al., 2015; Tao et al., 2018).

Finally, molecular constituents of the synaptic cleft were aligned and averaged into classes, permitting the putative identification of neurexins (Südhof, 2017; Trotter et al., 2019) and iGluRs (Hansen et al., 2007; Sobolevsky et al., 2009; Peukes et al., 2021; Zhang et al., 2023), despite the low number. The variable nature of the crowded synaptic cleft (Zhu et al., 2018; Bulovaite et al., 2022) limited the number of each cleft constituent obtainable within this dataset, and therefore limited the achievable resolution. High-resolution structures were not obtained in this study, but with a larger number of high-quality tomograms, this could be achievable in the future. Other ways to address the low number could include using a quantum dot label (Masich et al., 2006) for the protein of interest, such as to indicate AMPARs, directing collections towards excitatory synapses with *bona fide* AMPARs for averaging. Finally, cryoET could be combined with mass spectrometry, such as MALDI-TOF (O'Rourke et al., 2019; Kaya et al., 2021), enabling a read-out of the proteins present within the thin tissue sample after tomography collection.

Hence, this thesis describes the generation of a novel workflow to investigate engram synapses within tissue with advanced microscopy techniques. However, a feature unique to engram synapses was not identified in this study, possibly due to the 6-day interval between engram labelling and cryopreservation of tissue. Therefore, future studies should apply the same protocol at different timepoints to identify any engram-specific architectural features which may be more apparent at different stages of memory. Indeed, it would be interesting to reactivate the memory naturally or artificially (Liu et al., 2012; Nabavi et al., 2014; Liu et al., 2014; Ramirez et al., 2014), either within the mouse model or at the high-pressure freezer immediately before cryopreservation (Watanabe, 2016). Furthermore, activity could be investigated by incorporating a synapse-specific calcium indicator (Perez-Alvarez et al., 2020).

Other future changes to the workflow to improve tomogram quality include the use of FIB/SEM and cryo-liftout (Marko et al., 2007; Schaffer et al., 2019), reducing the damage and compression associated with cryo-sectioning (Lovatt et al., 2022). Furthermore, a volumetric FIB-SEM or serial cryo-liftout

approach could be applied (Dumoux et al., 2023; Berger et al., 2023; Schiøtz et al., 2023) to trace whole neurons, enabling investigations into multi-input synapses and engram connectivity with cryopreserved tissue.

Overall, this workflow enables a voyage of exploration into engram cells and input specificity, unveiling engram synapses within their cryopreserved native environment.

Chapter 5: CryoCLEM and CryoET Workflow Development

In this chapter, considerations for developing a new cryoCLEM and cryoET workflow will be described, including choosing fluorescent labels, sample preparation method, and optimising imaging. The approaches are generalisable and are therefore adaptable to look at different biomolecules of interest, but here the NMDA receptor at synapses will be used as an example.

Together, cryogenic correlated light and electron microscopy (cryoCLEM) and cryogenic electron tomography (cryoET) use fluorescently labelled cells or proteins of interest to gain knowledge on the architecture and arrangement of molecular structures *in situ*. Crucially, cryoCLEM applies fluorescence microscopy to map the location of the labelled molecules of interest (Kukulski et al., 2011; Carter et al., 2018; Peukes et al., 2021; Lovatt et al., 2022). Alone, fluorescence microscopy cannot answer all biological questions, as the in-tissue context for the fluorescent signal is lacking, preventing structural analysis. When combined with cryoET, ultrastructural analysis is permitted (Kukulski et al., 2011; Peukes et al., 2021), providing positional context for the labelled molecule.

By correlating fluorescence microscopy with cryoET, the labelled molecules or compartments can be identified *in situ* within 3D volumes, and therefore within the context of their biological environment (Kukulski et al., 2011; Peukes et al., 2021; Lovatt et al., 2022). Hence, a successful cryoCLEM and cryoET workflow will vitrify cells or tissues in their native state, so that the molecular architecture remains intact, and imaging is unaffected by crystalline ice. Moreover, it will use accurate and reliable fluorescent labels for localisation of biomolecules in cryogenic conditions. This information can direct STA analysis of proteins of interest.

This chapter will describe considerations for developing a successful cryoCLEM and cryoET *in situ* workflow to identify biomolecules for structural analysis. Three main considerations will be described:

1. How will molecules be fluorescently labelled?
2. How will tissue sections be prepared for cryoCLEM/cryoET?
3. How can samples be screened for optimal signal and vitrification?

5.1. Choosing a method for fluorescently labelling molecular targets for cryoCLEM and cryoET

For a successful cryoCLEM/cryoET workflow, biomolecules must be reliably labelled with a detectable fluorophore. Therefore, tagging targets should be considered. Biomolecules can be labelled with genetic, immunological or pharmacological tags (Jensen, 2012; Fang et al., 2018; Tu et al., 2021). Genetic fluorescent tags are a gold-standard reliable way of labelling proteins for fluorescence imaging, as they are not associated with non-specific labelling and can be used for both intracellular and extracellular proteins (Jensen, 2012). However, genetic tags take time to engineer and have a possibility of interfering with normal cellular functions. Immunological or pharmacological labels are simple, rapid, and applicable to many cell types, although are associated with some non-specific binding and can only reach extracellular epitopes (Jensen, 2012; Tu et al., 2021). Commonly, immunostaining protocols using fluorescent antibodies utilise chemical fixation of the tissue (Fang et al., 2018; Tu et al., 2021), but tissue must be unfixed for accurate *in situ* structural biology via cryoET. Here, a protocol to live-label biomolecules in fresh tissue is described, using NMDARs at synapses as an example. It is adaptable to other biomolecules.

Firstly, a way to identify synapses for cryoCLEM was needed. The Psd95^{GFP/GFP}GluN1^{FLAG/FLAG} mouse is well-characterised (Frank et al., 2016; Broadhead et al., 2016; Zhu et al., 2018), and detection of the GFP (Green Fluorescent Protein) tag has correlated directly to postsynaptic compartments (Frank et al., 2016; Peukes et al., 2021). Therefore, this mouse was used to detect glutamatergic synapses. To label alternative cell types or subcellular compartments for cryoCLEM, the GFP tag could be expressed conjugated to a different relevant gene.

The GFP tag directed cryoET collections to synapses (chapter 3, Peukes et al., 2021). However, these *in situ* cryoET volumes contain numerous macromolecular complexes and proteins within a crowded cellular environment (Beck and Baumeister, 2016; Peukes et al., 2021). Therefore, identifying specific molecules *in situ* is challenging. To unambiguously identify biomolecules, additional labels are necessary.

Here, NMDA receptors were investigated, as they are critical to synaptic plasticity and memory (Collingridge et al., 1983; Davis et al., 1992), and identifying them within *in situ* tomograms could enable exploration into unanswered questions regarding their location in intra- and extra- synaptic pools (Harris and Pettit, 2007), and their association with signalling complexes such as CaMKII for synaptic maturation and plasticity mechanisms (Frank, 2011; Frank et al., 2016). However, it is difficult to identify NMDARs without an additional label, as they are one of a related family of glutamate receptors found at synapses that includes AMPARs, which share a similar Y-shaped structure (Hansen et al., 2007; Sobolevsky et al., 2009; Lee et al., 2014; Karakas and Furukawa, 2014; Zhu et al., 2016; Peukes et al., 2021), rendering it challenging to differentiate between NMDARs and AMPARs at synapses with *in situ* cryoET. NMDARs were suitable candidates for the live-labelling approach as they present extracellular epitopes that are accessible to antibodies. The Psd95^{GFP/GFP}GluN1^{FLAG/FLAG} knockin mice has a FLAG-tagged GluN1 NMDAR subunit at the N-terminal domain (Zhu et al., 2016), so an anti-FLAG-CY3 antibody was chosen to label NMDARs. Therefore, live-labelling with an anti-FLAG-CY3 antibody could help resolve NMDARs from AMPARs to investigate the localisation and signalling complexes of NMDARs.

To prepare tissue for the live-labelling workflow, Psd95^{GFP/GFP}GluN1^{FLAG/FLAG} knockin mice were subject to cardiac perfusion of NMDG cutting buffer. Brains were dissected and imaged with a blue light to confirm the expression of GFP (Fig.3.1B), before being cut into 100 µm thick acute slices in NMDG cutting buffer with a vibratome under carbogen perfusion. Acute slices were transferred to individual well plates containing ACSF, where they were suspended on custom-built gauze shelves with controlled perfusion of

carbogen (Dorris et al., 2014). To live-label NMDARs, slices were incubated in a 1:100 antibody dilution in ACSF for two hours (Fig.5.1A) and were then washed in ACSF three times. Antibody labelling was specific to $\text{Psd95}^{\text{GFP/GFP}}\text{NMDAR}^{\text{FLAG/FLAG}}$ mice within live-stained slices imaged with confocal microscopy (Fig. 5.1C). A small amount of FLAG-CY3 signal was detectable in the WT sample, indicating some non-specific binding (Fig.5.1C). There was a moderate-strong colocalization of NMDAR and Psd95 (Pearson's R Value = 0.59) in $\text{Psd95}^{\text{GFP/GFP}}\text{NMDAR}^{\text{FLAG/FLAG}}$ mice samples, indicating successful labelling of NMDARs in live acute slices.

Cortical biopsies were taken from unfixed live-labelled acute slices for high-pressure freezing and cryo-sectioning. Both GFP and FLAG-CY3 puncta were detectable at cryogenic temperatures (Fig. 5.1D), so were suitable for cryo-fluorescence microscopy. This approach could be adapted to look at other proteins by changing the antibody target, or by utilising alternative knockin mice with FLAG tagged biomolecules of interest.

However, incubating the acute slices for 2 hours could impair the health of the tissue. To quantify this, an indicator of cell death, such as propidium iodide or annexin-V could be used to assess the health of the tissue (Crowley et al., 2016). Crucially, antibodies are large molecules of ~10 nm (Reth, 2013), posing a difficulty in delivering them to narrow spaces, such as synaptic clefts of ~25 nm in height (Savtchenko and Rusakov, 2007; Peukes et al., 2021). To circumvent this issue, smaller molecules such as aptamers, nanobodies, fab fragments, DNA origami or quantum dots could be used (Masich et al., 2006; Gold et al., 2014; Fang et al., 2018; Silvester et al., 2021). Quantum dots have the advantage of being highly electron dense, meaning they could also be identified in cryo-tomograms (Masich et al., 2006; Gold et al., 2014), but may have accessibility issues. The approach described here is only suitable for biomolecules with an extracellular epitope; for intracellular proteins a genetic fluorescent label (Jensen, 2012) would be recommended.

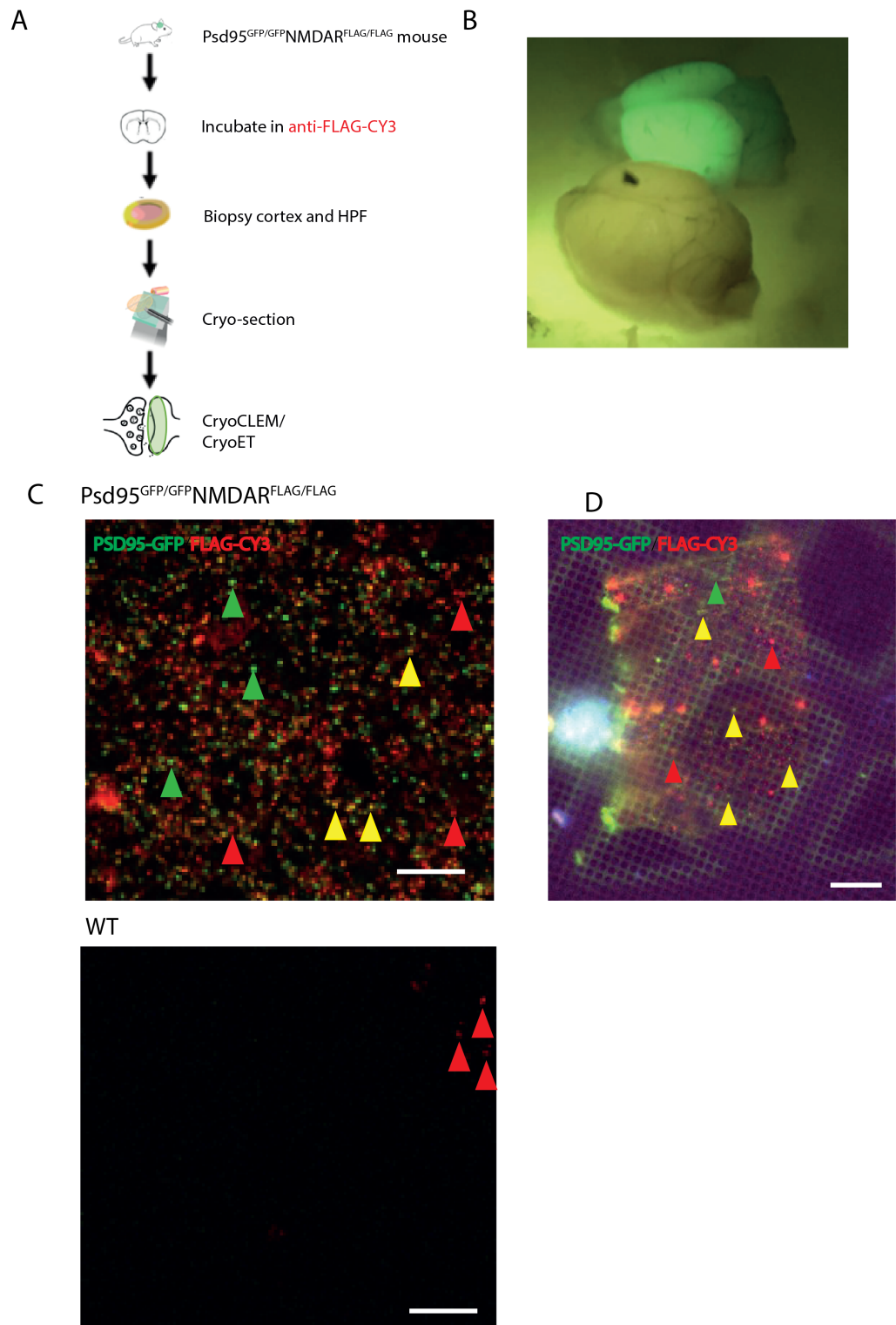


Figure 5.1: Developing a live-labelling workflow to detect NMDA receptors within cryopreserved synapses.

A) Workflow to live-label FLAG-tagged NMDAR for cryoCLEM and tomography. Brains were dissected from knockin mice and cut into acute slices, which were incubated in anti-FLAG antibody for 2 hours with carbogen

perfusion. Biopsy punches were taken from the cortex and high-pressure frozen (HPF) into gold carriers. Tissue was cryo-sectioned on a cryo-ultramicrotome before being imaged on cryo-fluorescence and cryo-electron microscopes for cryo- correlated light and electron microscopy (cryoCLEM) and cryo- electron tomography (cryoET). Created with BioRender.com

B) Front, wild-type (WT) brain and back, brain from Psd95^{GFP/GFP}NMDAR^{FLAG/FLAG} knockin mouse imaged under a blue lamp.

C) Confocal microscopy of fixed brain tissue from Psd95^{GFP/GFP}NMDAR^{FLAG/FLAG} knockin and WT mouse brain live-labelled with the antiFLAG-CY3 antibody. Distinct puncta were seen in the knockin mouse brain. A small amount of non-specific binding of FLAG-CY3 occurred in the WT mouse. Example puncta are indicated by arrowheads. Yellow arrowheads, colocalization of GFP and FLAG-CY3; green arrowheads, GFP alone; red arrowheads, FLAG-CY3 alone. Scale bar = 10 μ m.

D) FLAG-CY3 and Psd95-GFP puncta were detectable in vitreous brain tissue sections viewed by cryo-fluorescence microscopy, including some colocalization. Example puncta are indicated by arrowheads. Yellow arrowheads, colocalization of GFP and FLAG-CY3; green arrowheads, GFP alone; red arrowheads, FLAG-CY3 alone. Scale bar = 50 μ m.

5.2. Preparing tissue sections for cryoCLEM and cryoET

Once samples are fluorescently labelled, either genetically, immunologically or pharmacologically, a suitable tissue sectioning method should be chosen. There are multiple options for this, including conventional EM of resin-embedded samples (Gray, 1959), cryo-sectioning with a diamond knife (Al-Amoudi et al., 2004), FIB milling and cryo-liftout (Schaffer et al., 2019), or non-intact sample preparations, such as plunge-freezing (Dubochet et al., 1982) of tissue homogenate (Peukes et al., 2021). This section will discuss the benefits, drawbacks and applications of each.

Traditionally, there are two main methods for conventional electron microscopy of tissue sections. The first method involves chemically fixing tissue before applying a heavy-metal stain to improve the contrast (Gray, 1959). Although with EM it is possible to resolve the ultrastructure of sub-synaptic compartments, the contrast is enhanced by staining, meaning that the stain is resolved, which acts as a proxy for the molecules to which it binds (Gray, 1959; Rall et al., 1966; Korogod et al., 2015). The tissue is resin-embedded and cut at room temperature on a microtome. The second method incorporates high-pressure freezing, followed by freeze substitution (Van Harreveld et al., 1965; Hunziker and Schenk, 1984), including the use of organic solvents, before resin-embedding. The treatments in both methods disrupt and damage tissue, meaning that it is not preserved in its native state, leading to shrinkage, embedding artefacts (Rastogi et al., 2013), and the cross-linking of proteins with chemical fixatives (Hopwood, 1969). Therefore, new methods have been developed which aim to preserve tissue in its native state for subsequent cryoEM. Such methods include CEMOVIS (cryogenic electron microscopy of vitreous intact sections) (Al-Amoudi et al., 2004), also termed cryo-sectioning, and cryo-lift-out (Schaffer et al., 2019).

The CEMOVIS technique, or cryo-sectioning, involves attaching thin vitreous cryo-sections of tissue to a grid. This avoids the need for chemical fixation via cross-linking, dehydrating, and staining, retaining the native structures. Samples can be cut at a range of thicknesses, meaning thin sections can be

obtained with low background in imaging, which is crucial for cryoCLEM and cryoET for good contrast. Moreover, it is possible to collect multiple tomograms from one long ribbon of sections (Fig.5.2A), rendering a high throughput and enabling a serial approach for repeating subcellular structures (Lovatt et al., 2022). However, cryo-sectioning is associated with knife and compression damage (Richter, 1994; Lovatt et al., 2022), which can impair the sample quality.

Alternatively, a FIB-milling and cryo-liftout approach can be applied (Schaffer et al., 2019), which has the capacity for serial sampling of suitable whole organisms (Schjøtz et al., 2023) but not of serial sampling on the scale of subcellular compartments. This technique involves filing chunks of tissue using plasma into useable lamellae that are thin enough (< 200 nm) for cryoET (Fig.5.2B), avoiding the use of diamond knives and therefore the associated knife and compression damage. A greater electron dose is required to collect from thicker regions of the lamella (Fig.5.2B), which is potentially damaging. Cryo-liftout has been a low throughput technique due to difficulty in attaching lamellae, material-dependent vitrification quality, and surface ice contamination, with a success rate of ~20% (Schaffer et al., 2019). However, recent developments improving the automation and protocols, thus reducing the heavy ice contamination, improving the sample stability, and increasing the collection speed, have improved this success rate (Dumoux et al., 2023; Dung et al., 2023; Berger et al., 2023; Schjøtz et al., 2023). However, samples are affected by a surface layer of amorphous damage and curtaining of samples (Fig.5.2B), which can be optimised with an argon plasma source to improve the quality for imaging (Dumoux et al., 2023). Notably, tomograms obtained from cryo-sectioning and cryo-liftout have not been compared directly in terms of quality and achievable resolution, although recently the in-tissue structures of amyloids were resolved via STA using tomograms from each technique, and a similar resolution was obtained with both techniques (Gilbert et al., 2023).

Other cryogenic methodologies can be used to prepare samples for cryoCLEM which do not involve tissue sections, such as the use of plunge-frozen brain homogenate (Fig.5.2C) forming ultra-fresh synaptosomes (Peukes et al.,

2021). Although this method is faster and less technically challenging, the synapses are not always kept in their native environment due to the mechanical stress of homogenisation. This approach is therefore suitable for applications such as structural analysis of individual membrane-bound proteins, but not for the assessment of whole tissue architecture including analysis of neighbouring cells.

To summarise, sample preparation should be fit for purpose. For example, to analyse the cellular context, in-tissue approaches such as cryo-sectioning or cryo-liftout are more appropriate than a plunge-frozen homogenate approach, as they better preserve the native context and architecture. High-resolution in-tissue structural biology is achievable with both cryo-sectioning and cryo-liftout. For serial approaches of subcellular compartments or projects which require the generation of larger datasets, cryo-sectioning would be most suitable. In contrast, for compression-free tomograms, cryo-liftout would be recommended, which would be particularly suitable for quantitative measurements. For serial sampling of a whole organism, cryo-liftout would be more suitable. Alternatively, for fast, less technical production of tomograms where the in-tissue context does not need to be maintained, a plunge-frozen homogenate approach could be applied.

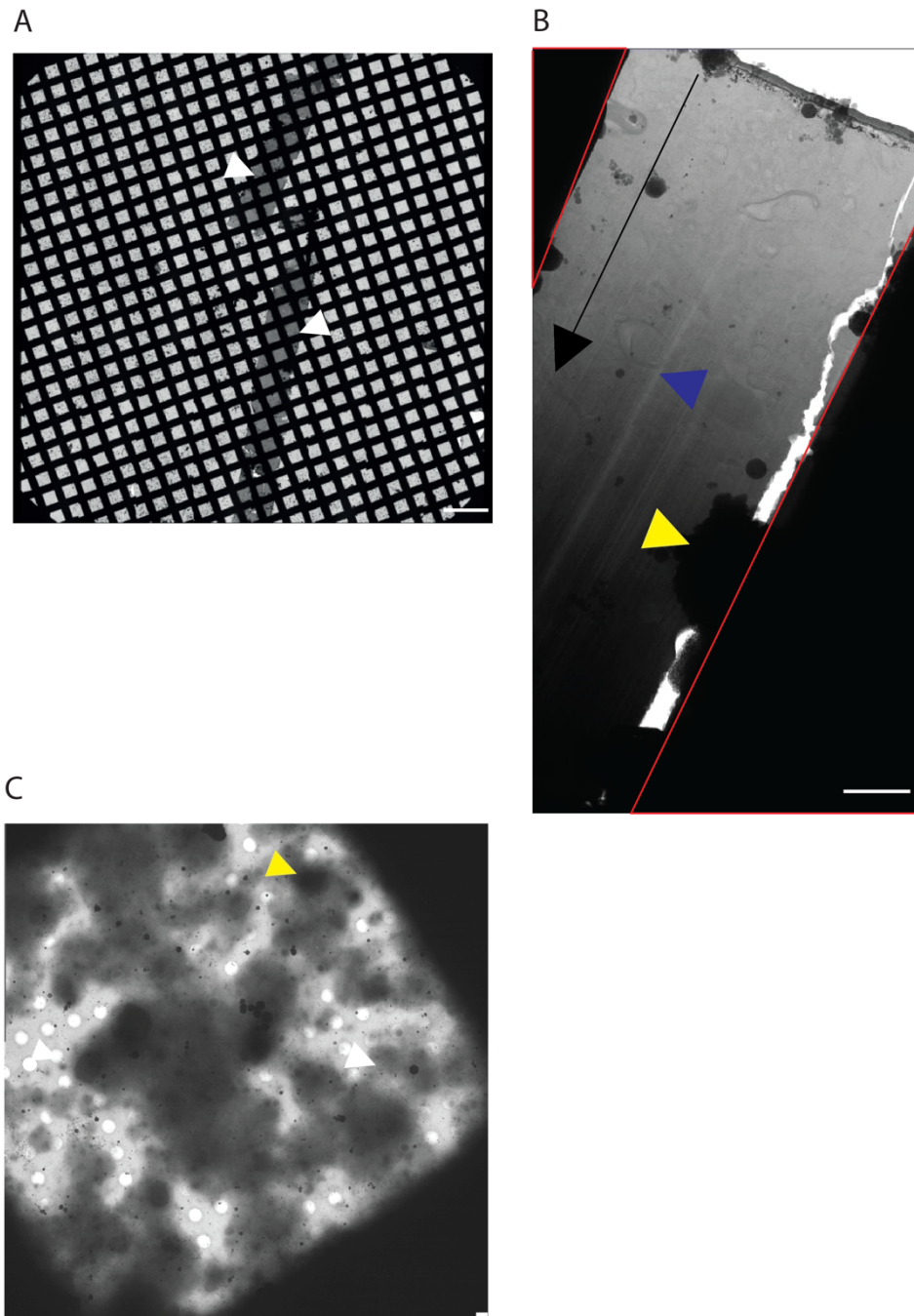


Figure 5.2: Sample preparation methods for in situ cryoET.

A) cryoEM of cryo-sections (white arrowheads) of vitreous brain tissue attached to a cryoEM grid. Individual cryo-sections are combined into cryo-section ribbons, enabling the collection of numerous tomograms from each grid, including serial studies. Scalebar = 200 μm . (Lovatt et al., 2022).

B) cryoEM of a lamella produced via cryo-liftout. Red triangular areas indicate regions of non-thinned tissue chunk that are too thick for cryoEM. Yellow arrowhead indicates ice contamination. Blue arrowhead indicates curtaining artefact. Black arrow indicates gradient of lamella thickness, with increasing thickness corresponding to arrow direction. Scalebar = 200 μm .

Sample was prepared by Nayab Fatima, cryo-liftout was performed by Andreas Schertel, and sample was imaged by Madeleine Gilbert and Yehuda Halfon (Gilbert et al., 2023).

C) cryoEM of plunge-frozen brain homogenate in one grid square of a cryoEM grid. White arrowheads indicate suitable collection regions, which contain thin specimen within the holes of the carbon film. Yellow arrowhead indicates a region that is too thick for cryoET. Scalebar = 1 μm .

5.3. Optimising and screening signal detection, ice thickness and vitrification

To confirm fluorescent signals and target cryo-section or lamella preparation, high-pressure frozen tissue within carriers can first be screened on the cryoFM to identify regions with high signal to noise (Leistner et al., 2023). This step is crucial for detecting localised fluorescence, such as amyloid plaques (Leistner et al., 2023), or specific subsets of cells, such as labelled engram cells (Fig.5.3.1A), but is not necessary for widespread signals, such as Psd95 (Fig.5.3.1B). Psd95 puncta are found throughout the tissue biopsy and are indistinguishable from neighbouring signals due to resolution limitations of the cryoFM (Fig.5.3.1B). To improve localisation, a confocal or super-resolution cryo-fluorescence microscope could be used (Liu et al., 2015; Tuijtel et al., 2019; Gilbert et al., 2023). Higher resolution imaging would be appropriate in the imaging of high-pressure frozen tissue within carriers for accurate targeting of proteins that form distinct shapes or localisations, such as tau tangles or β -amyloid plaques labelled with a fluorescent amyloid dye (Gilbert et al., 2023). Thus, cryoFM screening of high-pressure frozen tissue in carriers can direct preparation of cryo-sections and lamellae, improving the fidelity of hitting the labelled target within tissue.

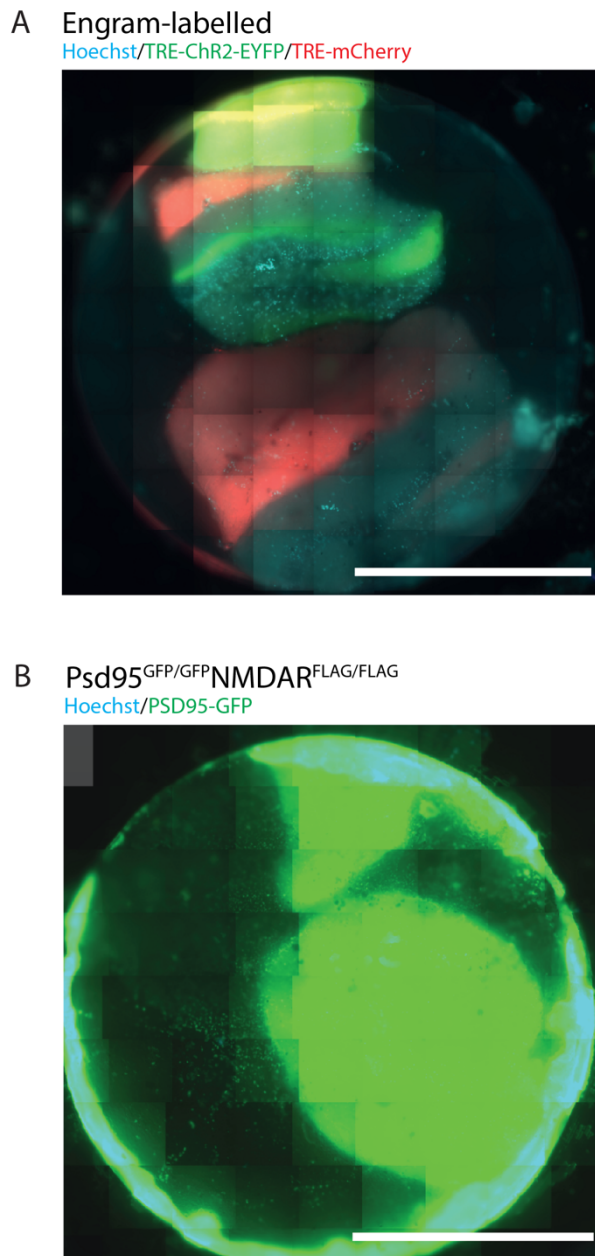


Figure 5.3.1: Detecting fluorescent signals in high-pressure frozen tissue within gold carriers via cryoFM.

A) High-pressure frozen brain tissue from an engram-labelled mouse brain, where EYFP and mCherry indicate engram cells originating from the CA3 and contralateral CA1 regions of the hippocampus, respectively. Hoechst labelling was used to indicate the cell bodies.

B) High-pressure frozen tissue from $Psd95^{GFP/GFP}NMDAR^{FLAG/FLAG}$ knockin mouse brain. The resolution of cryoFM imaging was not capable of resolving individual Psd95-GFP puncta, due to the multitude of Psd95-GFP signals throughout the 100 μm thick tissue sample.

Scalebars = 1 mm

Sample thickness is important to cryoEM. In cryo-sectioning, the thickness of the sample can be controlled using the input settings of the cryo-ultramicrotome, preparing sections at ~70-150 nm thick. In contrast, plunge-frozen samples, including tissue homogenate, have variable ice thickness due to factors such as sample viscosity, humidity and blotting parameters (Glaeser et al., 2016). If samples are too thick, resolution is impaired; if samples are too thin, the air-water interface can damage the sample (Glaeser et al., 2016; Noble et al., 2018). Selecting regions of optimum ice thickness for cryoET can be achieved using cryoFM (Fig.5.3.2). Screening with the brightfield and fluorescent channels enables the identification of very thick regions of non-vitreous ice, characterised by cracks in the ice (Fig.5.3.2A) and a higher background of fluorescent signal (Fig.5.3.2B). Additionally, screening with multiple fluorescent channels can identify autofluorescent material, such as contamination from surface ice or microplastics (Fig.5.3.2C), which tend to fluoresce in all channels (Carter et al., 2018). Ideal puncta for cryoET collections are situated within holes in the carbon foil in regions of thin ice, with low background fluorescence and a lack of ice cracks (Fig.5.3.2BC). Therefore, cryoFM screening enables the selection of optimum plunge-frozen sample grids for cryoET.

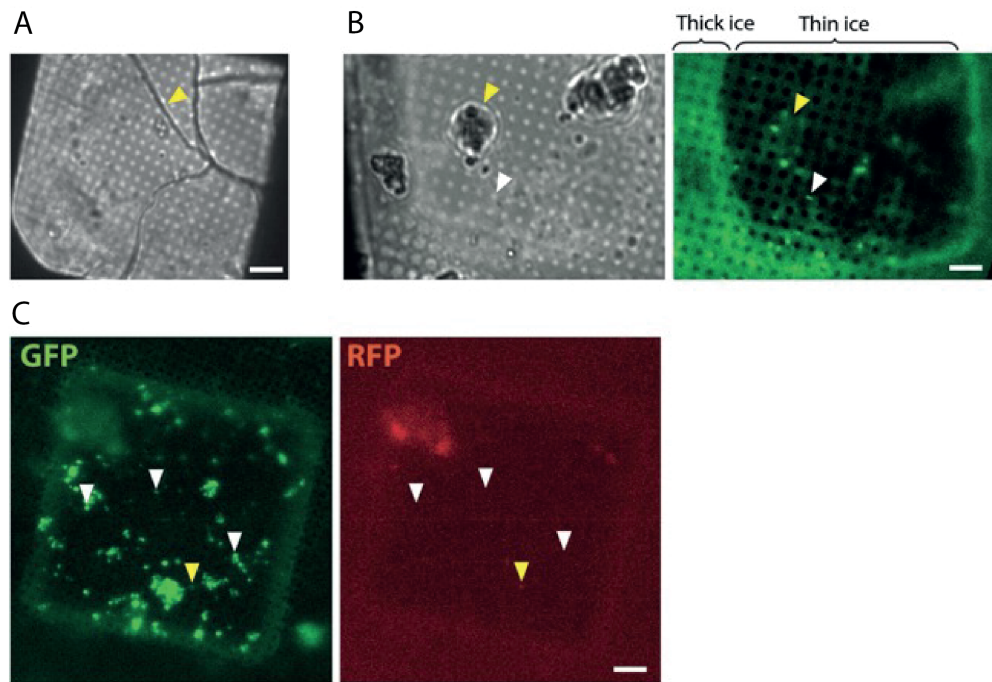


Figure 5.3.2: Optimising ice thickness and fluorescence detection in cryo-samples.

A) Brightfield image of grid square from plunge-frozen homogenate sample demonstrating thick ice, yellow arrowhead indicates crack in ice.

B) Left, Brightfield and Right, GFP imaging with cryo-fluorescence microscopy. Yellow arrowheads indicate ice contamination and white arrowheads indicate punctum suitable for collection.

C) Left, GFP and Right, RFP imaging of a grid square. Yellow arrowhead indicates region of auto-fluorescence, white arrowheads indicate regions suitable for collection. Scalebars = 6 μm .

(Lovatt et al., 2022).

Crucially, samples must be vitrified to avoid the formation of crystalline ice, which diffracts the electron beam and prevents transmission EM imaging (Thompson et al., 2016). Furthermore, vitrified samples are important to make physiologically relevant observations and to ensure that the structures and architectures are preserved in their native, undamaged state, as crystals withdraw water molecules from the hydrated specimen and compromise its structural integrity (Thompson et al., 2016). In this thesis, vitrification was achieved using a Leica ICE high-pressure freezer in combination with a cryoprotectant (20% dextran) (Zuber et al., 2005) for cryo-sections, or with a Leica vitrobot for plunge-frozen homogenate (Peukes et al., 2021). An NMDG cutting buffer was used as the base for the cryoprotectant (Ting et al., 2018; Peukes et al., 2021; Leistner et al., 2023), preventing the tissue from undergoing excitotoxic deterioration (Ting et al., 2018). The pH (pH 7.3-7.4) and osmolarity (305-315 mOsm/L) (Moyer and Brown, 1998; Ting et al., 2018) were controlled to mimic *in vivo* conditions, and a carbogen perfusion was supplied whilst recovering from the mechanical stress of vibratome slicing (Moyer and Brown, 1998).

Devitrification negatively impacts cryoET imaging due to crystalline ice formation (Fig.5.3.3). Therefore, we cannot reliably take measurements from these damaged samples, as we do not know the extent of the damage on molecular arrangement and interactions, or of the negative impact on imaging. Vitrification can be thoroughly tested by electron diffraction with a selective area aperture (Liu et al., 2015), or can be quickly tested by collecting images of tissue at several tilt angles on the cryo-electron microscope (Lovatt et al., 2022). If devitrified, this will reveal ice reflections that appear or disappear as the tilt angle increases (Fig 5.3.3), giving the appearance of “blinking”. Tilting can also ensure that the cryo-section is flat and in the same focal plane as the carbon foil. This is essential as areas of the grid often on carbon are used for focusing. If the sample is not flat, the defocus of the acquisition will differ from the target defocus and the lack of eucentricity will cause a tracking failure (Lovatt et al., 2022). Hence, devitrification and flatness of cryo-sections can be screened with cryoEM.

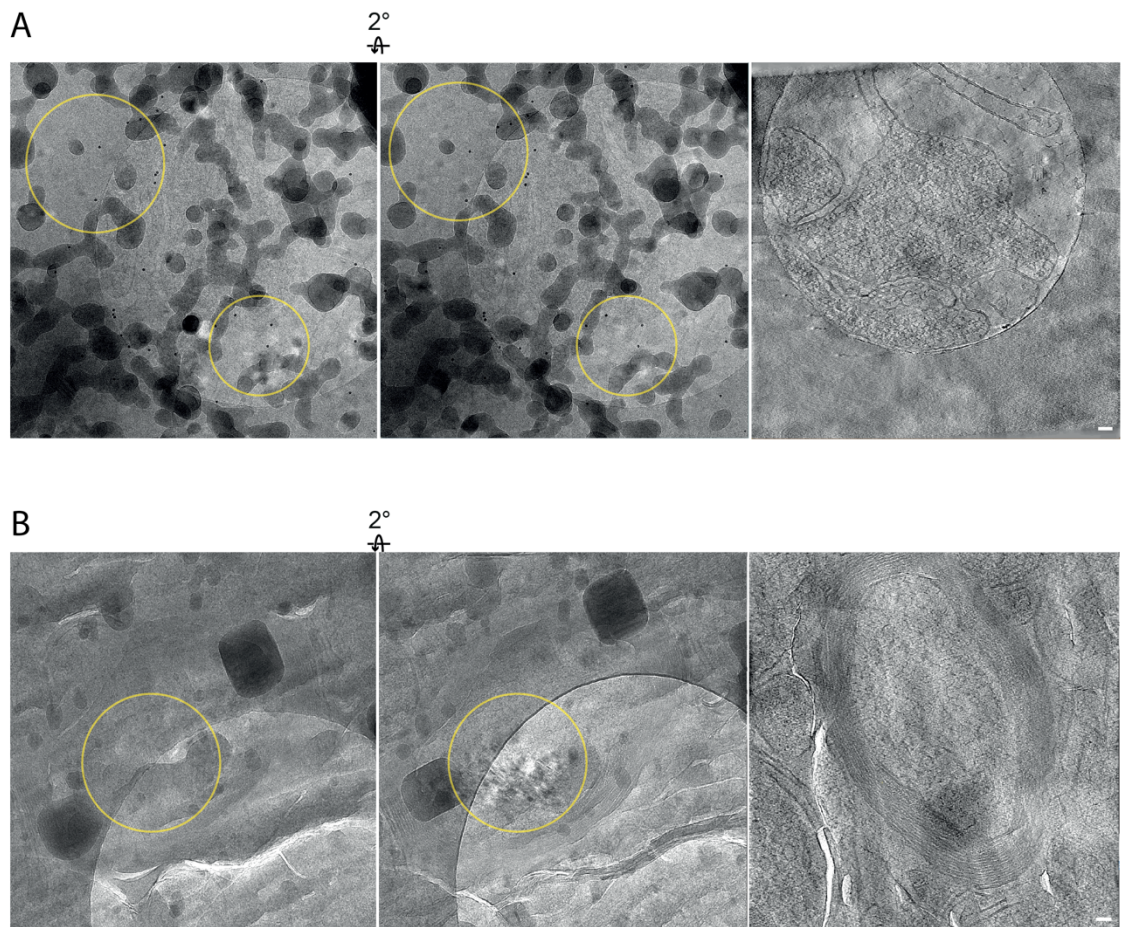


Figure 5.3.3: Testing for devitrification in cryo- samples.

A) Devitrification in a plunge-frozen homogenate preparation. Left and middle, two different tilts showing different ice patterns or “blinking”. Right, virtual slice from reconstructed tomogram with evident devitrification. Scale bar = 50 nm.

B) Devitrification in a cryo-section. Left and middle two different tilts showing different ice patterns due to the reflections of crystalline ice. Right, virtual slice from reconstructed tomogram. Devitrification is seen evident in the tomogram. Scale bar = 50 nm.

5.4. Concluding Comments

To summarise, there are many considerations for developing a new cryoCLEM and cryoET workflow, including the choice of fluorophore, the quality of the sample based on ice thickness and vitrification, and the method of tissue preparation. These considerations were applied during the development of the workflows in this thesis and offer recommendations for further development of cryoCLEM and cryoET workflows.

The use of a fluorescent antibody to label proteins within perfused acute tissue slices was trialed, representing the first protocol for live-labelling proteins within fresh, unfixed brain tissue for cryoCLEM and cryoET. Live-labelling was shown to be successful with room temperature confocal microscopy and with cryoFM, indicating the specific labelling of NMDA receptors in a way which survives cryogenic temperatures. However, antibodies are large molecules (Reth, 2013), hindering their ability to reach some NMDA receptors within the narrow synaptic cleft. Moreover, they are flexible, hindering localization within a tomographic volume and the ability to align and average proteins for higher resolution structures via STA (Briggs, 2013). Finally, the long periods of incubation time may have a negative impact on tissue health, which remains to be determined. Therefore, this line of investigation was not continued in the present study. Instead, smaller molecules which can be detected with cryoFM and within cryoET are recommended (Masich et al., 2006; Gold et al., 2014; Silvester et al., 2021).

A non-trivial aspect of cryoCLEM and cryoET workflows is the cryopreservation of tissues in a native, vitreous state (Al-Amoudi et al., 2004; Zuber and Lučić, 2019; Lovatt et al., 2022). Here, tissue slices were cut in a physiological buffer (Ting et al., 2018), with careful monitoring of the concentration of ions, pH, osmolarity and oxygenation of the solutions (Moyer and Brown, 1998; Ting et al., 2018). These steps were taken to keep brain slices as near to *in vivo* conditions as possible, aiming to keep slices as recommended for electrophysiological studies (Moyer and Brown, 1998). Physiological buffers were supplemented with 20% dextran as a

cryoprotectant (Zuber et al., 2005; Leistner et al., 2023) to avoid the formation of crystalline ice in high-pressure frozen tissue.

To conclude, when developing a new cryoCLEM/cryoET workflow, firstly the fluorophore, genetic, immunological or pharmacological, should be considered. Next, a sample-dependent assessment should be used to identify the most appropriate method of sample preparation, which could be plunge-frozen homogenate, cryo-sections or lamellae. Screening can be carried out using cryoFM and cryoEM to direct cryoET collections to optimum locations.

Chapter 6: General Discussion and Conclusions

Memory involves communication between neurons wired into complex neuroanatomical circuitry via synapses (Hebb, 1949; Bliss and Lømo, 1973; Frey and Morris, 1997; Drachman, 2005; Santuy et al., 2020). However, the architectural changes at synapses in memory processes are currently unknown. Here, workflows were developed to bridge from mouse behaviour in memory paradigms to the synaptic architecture underlying these functions. These workflows integrated mouse genetics, cryoCLEM and cryoET to label and detect synapses for the acquisition of high-resolution tomography, analysing synaptic architecture in 3D within a cryopreserved in-tissue environment. Architectures were reported for glutamatergic synapses in multiple brain regions (chapter 3) and for synapses between engram cells in the dorsal CA1 (Cornu Ammonis 1) region of the hippocampus (chapter 4). Moreover, the challenges and considerations for developing such cryoCLEM/cryoET workflows were summarised (chapter 5).

This thesis had five testable hypotheses:

1. The workflow developed will enable the collection of tomograms of engram-labelled cells, including synapses.
2. Engram synapses will have input-specific differences in synaptic architecture.
3. Differences in synapse architecture will exist in synapses from different brain regions.
4. Ionotropic glutamate receptors will be identified within glutamatergic synaptic clefts and within synaptic clefts between engram neurons.
5. Live labelling will enable the identification of specific proteins and their surrounding subcellular architecture, including NMDAR, at synapses.

The extent to which hypotheses were met will be discussed in the following subsections.

6.1 A workflow was developed, enabling the collection of tomograms of engram-labelled cells, including synapses

To investigate the site encoding a specific memory, a workflow was developed to explore the architecture of synapses between engram cells with engram-labelling technology (Liu et al., 2012; Ryan et al., 2015), cryoCLEM (Kukulski et al., 2011; Leistner et al., 2023) and cryoET (Harapin et al., 2015; Peukes et al., 2021; Leistner et al., 2023). These data unveiled the first in-tissue tomograms of engram-labelled cells within their native environment, achieving the first aim. Approximately ~31% of tomograms contained synapses, permitting molecular-resolution architectural insights into both synaptic connections and vicinal regions of engram cells.

To develop the workflow technically, alternatives to cryo-sectioning could be applied, improving the quality of the samples, such as FIB/SEM and cryo-lift out (Schaffer et al., 2019; Dumoux et al., 2023; Berger et al., 2023; Schiøtz et al., 2023). A volume imaging approach could be applied (Dumoux et al., 2023; Berger et al., 2023), enabling lower resolution reconstructions of whole synapses between engram cells. The neurons could be traced within the volume to quantify the number of multi-input synapses (Aziz et al., 2019) and to map engram connectivity (Ortega-de San Luis et al., 2023). Furthermore, cryo-liftout (Schaffer et al., 2019) could be applied to generate lamellae containing synapses. Tomograms obtained from these lamellae would be free from compression associated with cryo-sectioning. Other technical amendments could adapt the labelling to include a synapse-specific fluorescent tag (Masch et al., 2018; Perez-Alvarez et al., 2020), or DNA origami label (Silvester et al., 2021), improving detection fidelity of synapses.

6.2 Engram-specific differences were not detected in synaptic architecture

In this thesis, variability was detected with respect to synaptic organelles, geometry and protein content. Although engram synapses exhibited a larger number of F-Actin filaments within the postsynaptic volume, this was not significantly different from control synapses. Similarly, properties such as number of mitochondria, cleft height distribution and presynaptic vesicle occupancy were within the same range as control synapses. These observations indicate that at the latent timepoint of 6 days after engram labelling, significant differences were not detected between engram and control synapses. Instead, each group demonstrated heterogeneity in synaptic architecture, suggesting that regarding the parameters measured in this thesis, synapses show vast variation which is not engram-specific.

It is possible that differences were not detected because of the time period between labelling the engram and processing the brains for the cryoCLEM/cryoET workflow. Modifications to synapses, such as changes in receptor number, actin dynamics, and spine dynamics are crucial at earlier stages of learning and memory (Okamoto et al., 2004; Matsuo et al., 2008; Korobova and Svitkina, 2010; Chidambaram et al., 2019), suggesting that an engram-specific detectable difference at synapses may exist at an earlier timepoint post-engram labelling, but may be transient and therefore not detectable 6 days post-labelling. To test this hypothesis, the workflow should be applied at different intervals in memory acquisition to ascertain if any synaptic architectural features are engram-specific at earlier timepoints.

Furthermore, the hippocampus contains diverse cell types (Ramón y Cajal, 1909; Johnston and Amaral, 2004), including excitatory and inhibitory neurons (Johnston and Amaral, 2004; Almog et al., 2021), and diverse synapse types (Zhu et al., 2018; Bulovaite et al., 2022). Therefore, to mitigate this diversity, a larger dataset would be needed, including datasets using additional cryoCLEM labels to differentiate synapse types, such as excitatory glutamatergic synapses and inhibitory GABAergic synapses (Tao et al., 2018; Peukes et al., 2021).

6.3 Glutamatergic synapses obtained from different neuroanatomical brain regions exhibited variability in synaptic architecture, with some region-specific observations indicated for further studies

Investigation of glutamatergic synapses in the mammalian brain revealed great diversity in architecture, including in the composition of synapses and the surrounding compartments, irrespective of neuroanatomical brain region. Contrary to previous literature using conventional EM (Gray, 1959), the molecular density profiles of postsynaptic compartments were variable without a conserved higher density adjacent to the postsynaptic membrane. This difference likely arose from the chemical fixation, cross-linking and dehydration applied in conventional EM of resin-embedded samples, which caused a loss of cytoplasmic protein. Furthermore, the stain acted as a proxy for molecular density in lieu of observing molecules directly. In contrast, the methodology applied in this thesis maintained non-membrane bound constituents within the cytoplasm, meaning that although proteins were present proximal to the postsynaptic membrane, this region was not always more molecularly dense than other distal regions. Additionally, molecules were viewed directly instead of using stain as a proxy. This variability in synaptic composition was in-keeping with the known diversity of the synaptome (Zhu et al., 2018; Bulovaite et al., 2022), and with cryoET on ultra-fresh synaptosomes (Peukes et al., 2021) and cultured neurons (Tao et al., 2018).

Synapses varied in organelle content, geometry and molecular composition within and between regions, with the some of the hippocampal synapses containing postsynaptic mitochondria, unlike the cortex, and the CA3 (Cornu Ammonis layer 3) region having a subset of larger postsynaptic compartments. These observations suggest that synapses are heterogenous and vary by region and by circuitry. However, relative to the number and diversity of synapses within the brain (Lichtman and Colman, 2000; Drachman, 2005; Zhu et al., 2018; Bulovaite et al., 2022), the dataset for this analysis was small, which could have hindered the ability to detect significant differences due to the inherent variability (Zhu et al., 2018; Bulovaite et al., 2022). Additionally, the origin of the presynaptic compartments was unknown, as a specific circuit

was not labelled. Therefore, subtypes of synaptic input within a neuroanatomical region could not be compared (Johnston and Amaral, 2004; Squire, 2004; Cherubini and Miles, 2015; López-Madrona et al., 2017), such as the specific comparison of mossy fibre and commissural synapses in the CA3 region (Suyama et al., 2007; Hagena and Manahan-Vaughan, 2013).

6.4 Ionotropic glutamate receptors were detected within glutamatergic synapses and engram-labelled synapses

Ionotropic glutamate receptors (iGluRs) were observed via subtomogram averaging as Y-shaped proteins protruding from the postsynaptic membrane at some glutamatergic synapses within cryo-sections obtained from $\text{Psd95}^{\text{EGFP/EGFP}}\text{NMDAR}^{\text{FLAG/FLAG}}$ mouse brains, and at some synapses obtained from engram-labelled mouse brains. Not all glutamatergic synapses contained iGluRs, likely because the entire volume of the synapse could not be reconstructed within the thin (70-150 nm thick) cryo-sections. Additionally, in the engram preparation, synapses which were likely not excitatory synapses onto glutamatergic spines were also included in the dataset.

Through the application of subtomogram averaging, iGluRs were averaged for structural analysis and to ascertain the distribution and clustering of iGluRs within the synaptic cleft. However, due to low endogenous protein copy number within the thin cryo-sections and conformational heterogeneity, high resolution structures were not obtained in this thesis. To obtain high resolution structures, much larger datasets would be needed to increase the particle number at least ten-fold, due to the twin challenges of low endogenous copy number and compositional heterogeneity that is limiting in tissues. Alternatively, a labelling strategy for NMDA receptors, as described in chapter 5, could be applied, accounting for compositional heterogeneity, as NMDA receptors could be distinguished from similarly structured receptors in the glutamatergic receptor family, such as AMPA receptors, which are also found at synapses.

Although cluster analysis indicated clusters of iGluRs in-keeping with super-resolution microscopy (Nair et al., 2013) and cryoET of plunge-frozen homogenate (Peukes et al., 2021), a complete description of clustering by in-tissue cryoET was not possible because cryo-sections are necessarily thinner than the volume of a whole synapse (70 nm thick cryo-section versus 300-1000 nm thick synapse). To address this in the future, if serial cryo-sections could be registered, larger in-tissue volumes encompassing an entire synapse could be obtained.

6.5 Live labelling enabled the identification of proteins with cryoCLEM but was not suitable for a cryoCLEM/cryoET workflow

A protocol was developed to pinpoint NMDA receptors within tissue cryo-sections for cryoCLEM and cryoET. An antibody was applied to live-label NMDA receptors in acute brain slices. Detection was possible with cryoFM, enabling correlation of the signal to membranes with NMDA receptors in cryoEM imaging. Therefore, this approach was suitable for in-tissue cryoCLEM.

Ideally, these antibodies would be detectable based on electron density within tomograms for a cryoET workflow. However, due to antibodies being large, access to narrow regions such as the synaptic cleft was limited (Reth, 2013), meaning not all NMDA receptors could be labelled. Moreover, antibodies are flexible, making it difficult to identify NMDA receptors bound to antibodies within tomograms based on shape, rendering this a sub-optimal approach for subtomogram averaging. It is instead recommended to use a smaller, electron dense label to indicate a protein within tomograms, such as quantum dots (Gold et al., 2014), although this is non-trivial.

6.6 Concluding comments

Using these in-issue cryoCLEM/cryoET workflows, the ensembles of organelles, macromolecular complexes and proteins underlying memory functions were revealed. Vast synaptic heterogeneity was unveiled between engram cells in the CA1 region and at glutamatergic synapses in the cortex and hippocampus. Strikingly, synaptic organisation included organelles, complexes and proteins with variability in molecular density profiles, cytoskeletal network branching, cleft geometry and cleft proteins. This study initiates a voyage of discovery into neuronal connectivity, synaptic architecture and input specificity.

Appendices

Ethics statement

All work at the University of Leeds was ethically approved by the University of Leeds (BIOSCI21-005) and carried out in accordance with the UK Animals (Scientific Procedures) Act (1986) and NIH guidelines. All mice procedures at Trinity college Dublin were performed under appropriate Project Authorization (AE19136/P081) granted by the Health Products Regulatory Authority, the Irish competent authority for scientific animal protection legislation.

Supplementary Tables

Supplementary Table 1: Constituents of tomograms containing glutamatergic synapses.

Table is a binary table, where 1 indicates the presence of at least 1 incidence of the named constituent, 0 indicates an absence of the named constituent, and - indicates an observation that is not applicable to the tomogram.

Mouse	Region	Tomogram	Features						
			Pre-synaptic						
			Vesicles	MVB	Microtubules	Mitochondria	Granules in Mitochondria	Ribosomes	Cytoskeleton
1	Cortex	1	1	0	0	0	-	0	0
1	Cortex	2	1	0	1	0	-	0	0
1	Cortex	3	1	1	1	0	-	0	0
1	Cortex	4	1	0	0	0	-	0	0
1	Cortex	5	1	0	0	0	-	0	1
1	Cortex	1	1	1	0	1	1	0	0
1	Cortex	2	1	1	0	0	-	0	0
2	Cortex	1	1	0	0	0	-	0	0
3	Cortex	1	1	0	0	0	-	0	0

4	CA3	1	1	0	1	1	0	0	0
4	CA3	2	1	0	0	0	-	0	1
4	CA3	3	1	0	1	0	-	0	0
5	CA3	1	1	0	0	0	-	0	0
5	CA3	2	1	0	0	0	-	0	0
5	CA3	3	1	0	0	0	-	0	0
5	CA3	4	1	0	0	0	-	0	0
5	CA3	5	1	0	0	0	-	0	1
5	CA3	6	1	0	0	0	-	0	1
5	CA3	7	1	0	0	0	-	0	0
5	CA3	8	1	0	0	0	-	0	0
5	CA3	9	1	0	0	1	0	0	0
5	CA3	10	1	0	0	1	0	0	1
5	CA3	11	1	0	0	1	0	0	1
5	CA3	12	1	0	0	1	0	0	0
5	CA3	13	1	0	0	0	-	0	0
5	CA3	14	1	0	0	1	0	0	0
5	CA3	15	1	0	0	0	-	0	0
5	CA3	16	1	0	0	0	-	1	1
5	CA3	17	1	0	0	0	-	0	0
5	CA3	18	1	0	0	0	-	0	0
5	CA3	19	1	0	0	0	-	0	1
5	CA3	20	1	0	1	0	-	0	1
5	CA3	21	1	0	0	1	0	0	0
5	CA3	22	1	0	0	0	-	0	0
5	CA3	23	1	0	0	1	0	0	1

5	CA3	24	1	1	0	0	-	0	0
5	CA3	25	1	0	0	1	0	0	0
5	CA3	26	1	1	1	0	-	0	1
5	CA3	27	1	0	0	0	-	0	1
5	CA3	28	1	0	0	1	1	0	0
5	CA3	29	1	0	0	1	0	0	0
5	CA3	30	1	0	0	0	-	0	0
6	DG	1	1	0	0	1	1	0	0
6	DG	2	1	0	0	0	-	0	1
6	DG	3	1	0	0	0	-	0	1
6	DG	4	1	0	0	0	-	0	0
6	DG	5	1	0	0	0	-	0	0
6	DG	6	1	0	1	0	-	0	1
6	DG	7	1	0	0	0	-	0	0
7		1	1	1	0	0	-	0	1
	DG								
7	DG	2	1	0	0	0	-	0	0
7	DG	3	1	0	1	0	-	0	0
7	DG	4	1	0	0	1	0	0	1
7	DG	5	1	0	0	0	-	0	0
7	DG	6	1	0	0	0	-	0	0

Post-synaptic							Cleft		
Vesicles	MVB	Microtubules	Mitochondria	Granules in mitochondria	Ribosomes	Cytoskeleton	Cleft	Cleft proteins	Vesicles
0	1	1	0	-	0	1	1	1	0
0	1	0	0	-	1	1	1	1	0
0	0	0	0	-	0	1	1	1	0
0	0	0	0	-	1	1	1	1	0
0	0	0	0	-	0	1	1	1	0
0	0	0	0	-	0	0	1	1	0
0	1	0	0	-	1	1	1	1	0
0	0	0	0	-	0	0	1	1	0
0	0	0	0	-	0	1	1	1	0
0	0	1	0	-	0	1	1	1	0
0	0	0	0	-	0	0	0	0	0
1	0	1	0	-	0	1	1	1	0
0	0	0	0	-	0	1	1	1	0
1	0	1	0	-	0	1	1	1	0
0	0	0	0	-	0	0	1	0	0
1	0	0	0	-	0	1	1	1	1
0	0	0	0	-	0	1	1	1	0
0	0	0	1	1	0	1	1	1	0

1	0	0	1	1	0	1	1	1	0
0	0	0	0	-	0	1	1	1	0
0	0	0	0	-	0	1	1	1	0
0	0	0	0	-	0	1	1	0	0
0	0	0	0	-	0	1	1	1	0
0	0	0	0	-	0	1	0	0	0
0	0	0	0	-	0	1	1	1	0
0	0	0	0	-	0	1	0	0	0
0	0	0	0	-	0	1	1	1	0
0	0	0	0	-	0	1	1	1	0
0	0	0	0	-	0	1	1	1	0
1	0	0	0	-	0	1	1	1	0
0	0	0	0	-	0	1	1	1	0
0	0	0	0	-	0	1	1	1	0
0	0	0	0	-	0	1	1	1	0
0	0	0	0	-	0	1	1	1	0
0	0	0	0	-	0	1	1	1	0
0	0	0	0	-	0	1	1	1	0
0	0	0	1	0	0	1	1	1	0
0	0	0	0	-	0	1	1	1	0
0	0	0	0	-	0	1	1	1	0
0	0	0	0	-	0	1	1	1	0
0	0	0	0	-	0	1	1	1	0
0	0	0	0	-	0	1	1	1	0
0	0	0	0	-	0	1	1	1	0
1	0	0	0	-	0	1	1	1	0
0	0	0	0	-	0	1	1	0	0
0	0	0	0	-	0	1	1	1	0

0	0	0	0	-	0	1	1	1	0
0	0	0	0	-	0	1	1	1	0
0	0	0	0	-	0	1	1	1	0
0	0	1	1	1	0	1	1	1	0
0	0	0	0	-	0	1	1	1	0
0	0	0	0	-	0	1	1	1	0
0	0	0	0	-	0	0	1	1	0
0	0	0	0	-	0	1	1	0	0
0	0	0	1	1	0	1	1	1	1
0	0	0	0	-	0	0	1	1	0
0	0	0	0	-	0	0	1	0	0

Surrounding compartments									
Vesicles	MVB	Microtubules	Mitochondria	Granules in mitochondria	Ribosomes	Cytoskeleton	Filopodia	Extracellular vesicles	Myelin
0	1	0	1	1	1	0	0	0	0
1	1	1	1	0	0	0	0	0	1
1	1	1	1	0	0	0	0	0	1
1	1	1	1	0	1	0	0	0	1
0	1	1	1	0	0	0	1	1	0

0	0	1	1	0	0	0	0	0	0
1	1	1	0	-	0	0	0	0	0
1	1	0	0	-	0	0	0	1	0
1	0	0	0	-	0	0	0	0	0
1	0	0	1	0	0	0	0	0	1
1	1	0	1	0	0	0	0	0	0
1	1	1	0	-	1	1	0	0	0
1	0	1	0	-	0	1	0	0	0
1	1	1	1	0	0	1	1	0	0
1	0	1	1	0	0	0	1	0	0
1	0	1	1	0	1	1	0	1	0
1	1	1	1	0	1	1	0	0	0
1	1	1	0	-	0	1	1	0	1
1	0	1	1	0	0	1	0	0	1
1	0	1	1	0	0	0	1	0	0
1	1	0	1	0	0	0	0	0	1
1	0	0	1	1	0	0	1	0	0
0	0	1	0	-	0	0	1	0	0
1	0	1	1	0	0	0	0	0	1
1	0	1	1	1	0	0	0	0	0
1	0	1	0	-	0	0	0	0	0
1	0	1	1	0	0	0	0	0	0
0	0	1	1	1	0	0	0	0	0
1	0	0	1	0	0	0	0	0	0
1	0	1	1	0	0	0	1	0	1
1	0	1	1	0	0	0	0	0	1

1	0	1	1	0	0	0	0	0	0
1	0	0	1	0	0	0	0	0	0
1	0	0	1	1	0	0	0	0	0
1	0	1	1	0	0	0	0	1	0
1	0	1	0	-	0	0	1	0	0
1	0	0	1	1	0	1	0	0	0
1	1	1	0	-	0	0	0	0	0
1	0	1	1	0	0	1	1	1	0
1	0	1	1	1	0	1	0	0	0
0	1	1	1	1	1	0	0	0	0
1	0	1	1	0	0	0	0	0	0
1	0	0	1	0	0	0	0	0	0
1	0	0	1	1	0	1	0	0	0
1	1	1	0	-	0	0	0	0	1
0	1	1	0	-	0	0	0	0	0
1	0	0	0	-	0	0	0	0	0
1	1	1	1	0	0	0	0	0	0
1	0	1	0	-	0	0	1	0	1
0	0	1	1	0	1	0	0	1	0
1	0	1	0	-	0	0	0	0	1
1	1	1	1	0	0	0	0	0	0
1	0	1	1	0	0	1	1	1	0
1	1	1	1	0	1	1	0	0	0
1	0	0	0	-	0	0	0	0	0

Supplementary Table 2: Constituents of tomograms containing engram-labelled synapses.

Table is a binary table, where 1 indicates the presence of at least 1 incidence of the named constituent, 0 indicates an absence of the named constituent, and - indicates an observation that is not applicable to the tomogram.

Sample				
Mouse Number	Fluorophores	Dataset	Tomogram Number	Number of Views
1	CamKii-ChR2-EYFP/TRE-mCherry	1	1	53
1	CamKii-ChR2-EYFP/TRE-mCherry	2	1	42
1	CamKii-ChR2-EYFP/TRE-mCherry	2	2	56
2	TRE-ChR2-EYFP/TRE-mCherry	3	1	48
3	TRE-ChR2-EYFP/TRE-mCherry	4	1	61
3	TRE-ChR2-EYFP/TRE-mCherry	4	2	38
3	TRE-ChR2-EYFP/TRE-mCherry	4	3	51
3	TRE-ChR2-EYFP/TRE-mCherry	4	4	45
3	TRE-ChR2-EYFP/TRE-mCherry	4	5	46
3	TRE-ChR2-EYFP/TRE-mCherry	4	6	61
3	TRE-ChR2-EYFP/TRE-mCherry	4	7	61
3	TRE-ChR2-EYFP/TRE-mCherry	4	8	61
3	TRE-ChR2-EYFP/TRE-mCherry	4	9	44
3	TRE-ChR2-EYFP/TRE-mCherry	4	10	55
3	TRE-ChR2-EYFP/TRE-mCherry	4	11	61
4	TRE-ChR2-EYFP/TRE-mCherry	5	1	52

4	TRE-ChR2-EYFP/TRE-mCherry	5	2	54
4	TRE-ChR2-EYFP/TRE-mCherry	5	3	61
4	TRE-ChR2-EYFP/TRE-mCherry	5	4	38
4	TRE-ChR2-EYFP/TRE-mCherry	5	5	41
4	TRE-ChR2-EYFP/TRE-mCherry	5	6	49
4	TRE-ChR2-EYFP/TRE-mCherry	5	7	47
4	TRE-ChR2-EYFP/TRE-mCherry	5	8	48
4	TRE-ChR2-EYFP/TRE-mCherry	5	9	60
4	TRE-ChR2-EYFP/TRE-mCherry	5	10	50
4	TRE-ChR2-EYFP/TRE-mCherry	5	11	61
4	TRE-ChR2-EYFP/TRE-mCherry	5	12	52

Synapses		
Engram-Engram	Engram-Non-engram	Non-Engram-Engram
0	0	1
0	0	1
0	0	1
1	0	0
0	1	0
0	1	0
0	1	0
1	0	0
0	0	1

0	1	0
1	0	0
1	0	0
1	0	0
1	0	0
1	0	0
0	1	0
0	1	0
1	0	0
1	0	0
1	1	0
1	0	0
1	0	0
1	0	0
0	1	0
1	0	0
0	1	0
1	0	0

Cellular organelles								
Mitochondria	Calcium Phosphate	Vesicles	Microtubule	F-Actin	Intracellular bodies	Multi-vesicular bodies	Ribosomes	Golgi
0	0	1	0	1	0	0	0	0
0	0	1	0	1	0	0	0	0
0	0	1	0	1	0	0	0	0
1	0	1	0	1	0	0	0	0
1	0	1	1	0	0	0	0	0
1	0	1	1	0	0	0	0	0
1	0	1	1	1	0	0	0	0
1	0	1	1	1	0	0	0	0
0	0	1	0	0	0	0	1	0
0	0	1	1	0	0	1	0	0
0	0	1	1	0	0	0	0	0
0	0	1	1	1	0	0	0	0
0	0	1	1	0	0	0	0	0
0	0	1	1	0	0	0	0	0
1	0	1	1	1	0	0	0	0
1	1	1	1	0	0	0	0	0
1	1	1	0	0	0	0	0	0
1	1	1	1	1	1	0	1	0
1	1	1	0	0	0	0	0	0
1	1	1	1	0	1	0	1	0
1	0	1	1	1	1	0	0	0
1	1	1	0	0	1	0	1	0
1	1	1	1	0	1	0	0	0

1	1	1	1	0	0	0	1	0
1	1	1	1	1	0	0	0	1
1	0	1	1	1	1	0	1	0
1	1	1	1	1	0	0	1	0

Myelinated axon	Filopodium	Oligodendrocyte	Astrocyte	Extracellular vesicles
0	0	0	0	1
0	0	0	0	0
1	0	0	0	0
0	0	0	0	0
1	0	0	0	0
0	0	1	0	0
1	0	0	0	0
0	1	0	0	1
0	0	1	0	0
1	0	0	0	0
0	1	1	0	0
0	0	1	0	0
0	0	0	0	0
0	0	1	0	0
0	1	0	0	1

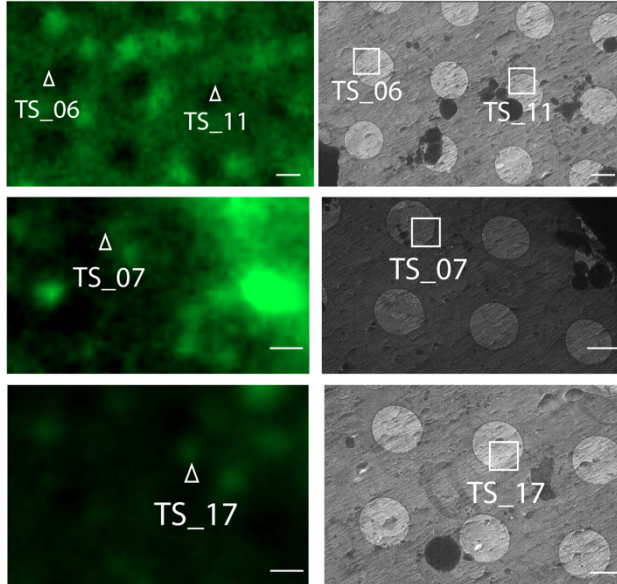
0	0	0	0	0
0	1	0	0	1
1	1	1	0	0
1	0	0	0	0
0	0	0	1	0
0	0	0	0	0
0	0	0	0	0
1	0	0	0	0
1	0	0	0	0
1	0	0	0	0
0	0	0	0	0
0	0	0	0	1

Supplementary figures

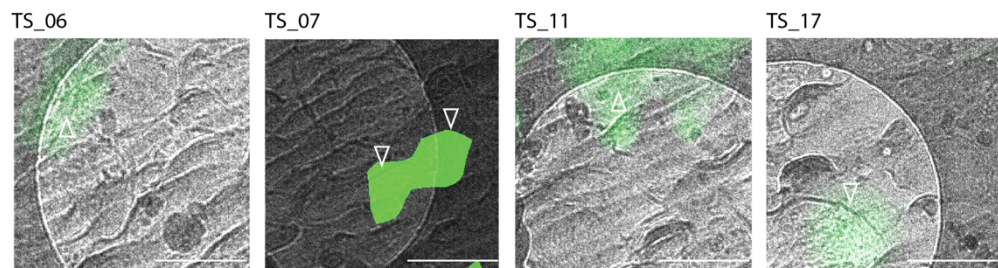
Cortex
Dataset1

CryoFM
PSD95-EGFP

CryoEM
cryoEM

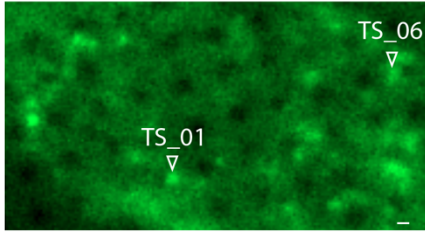


CryoCLEM
PSD95-EGFP/cryoEM

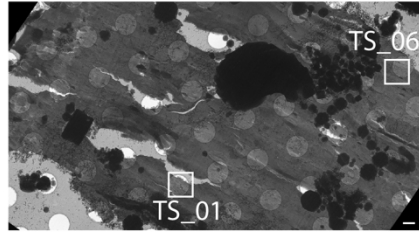


Cortex
Dataset 2

CryoFM
PSD95-EGFP

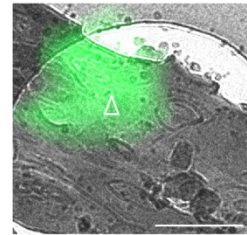


CryoEM
cryoEM

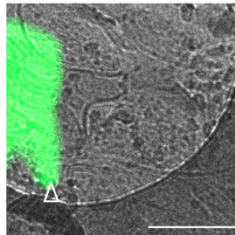


CryoCLEM
PSD95-EGFP/cryoEM

TS_01

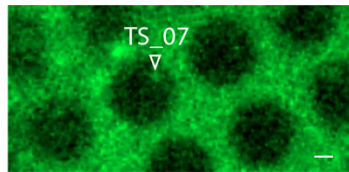


TS_06

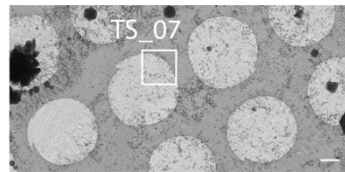


Cortex
Dataset 3

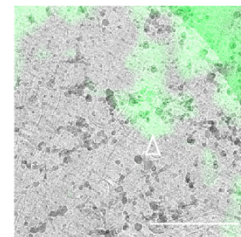
CryoFM
PSD95-EGFP



CryoEM
cryoEM

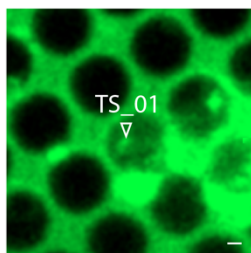


CryoCLEM
PSD95-EGFP/cryoEM
TS_07

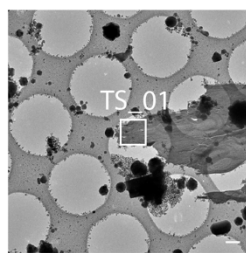


Cortex
Dataset 4

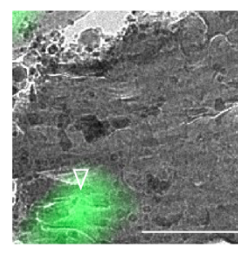
CryoFM
PSD95-EGFP



CryoEM
cryoEM



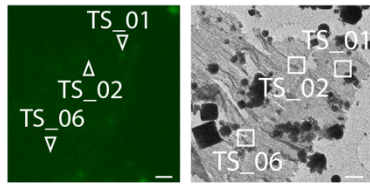
CryoCLEM
PSD95-EGFP/cryoEM
TS_01



CA3
Dataset 5

CryoFM
PSD95-EGFP

CryoEM
cryoEM

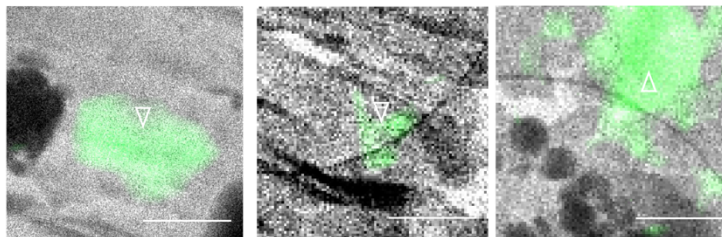


CryoCLEM
PSD95-EGFP/cryoEM

TS_01

TS_02

TS_06



CA3
Dataset 6

CryoFM
PSD95-EGFP

CryoEM
cryoEM

CryoFM
PSD95-EGFP

CryoEM
cryoEM



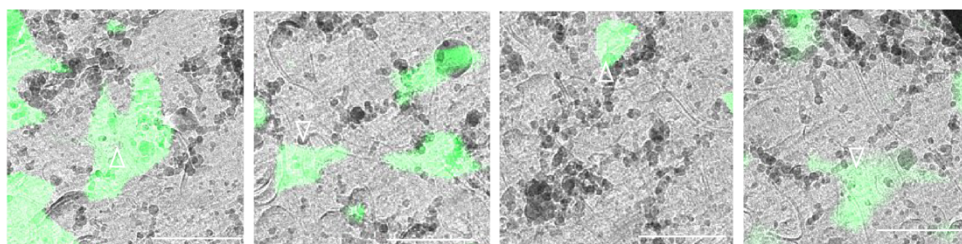
CryoCLEM
PSD95-EGFP/cryoEM

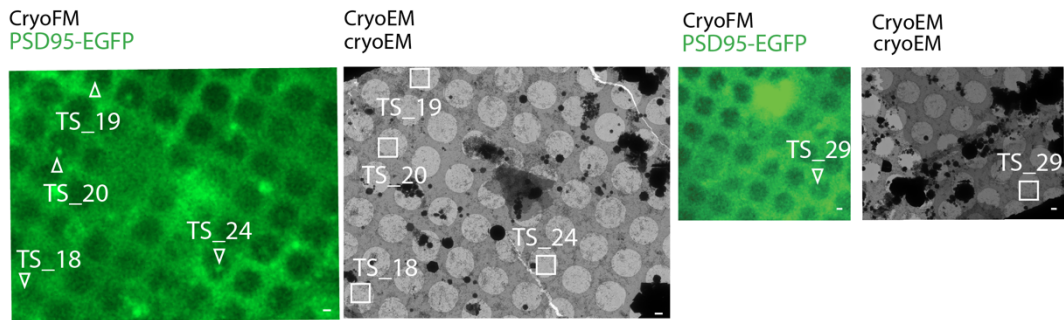
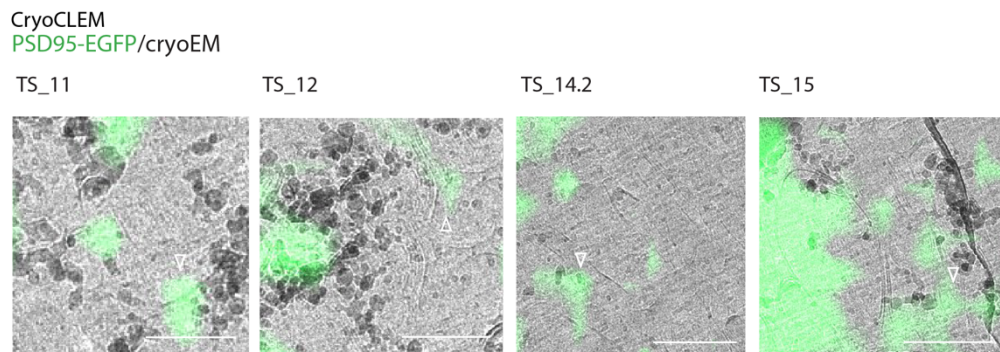
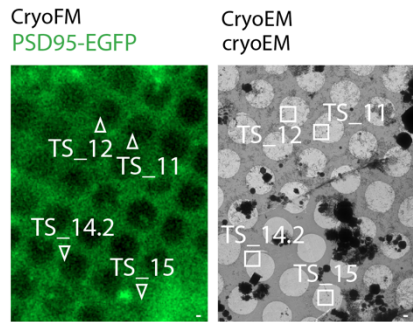
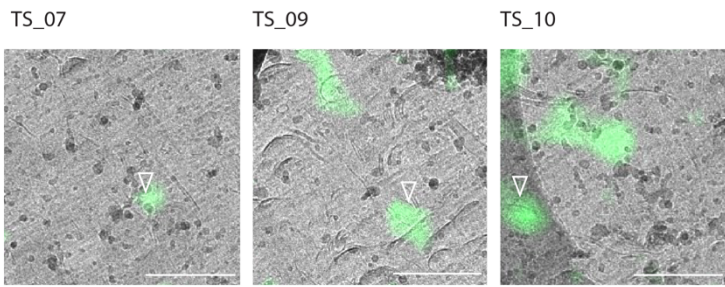
TS_01

TS_02

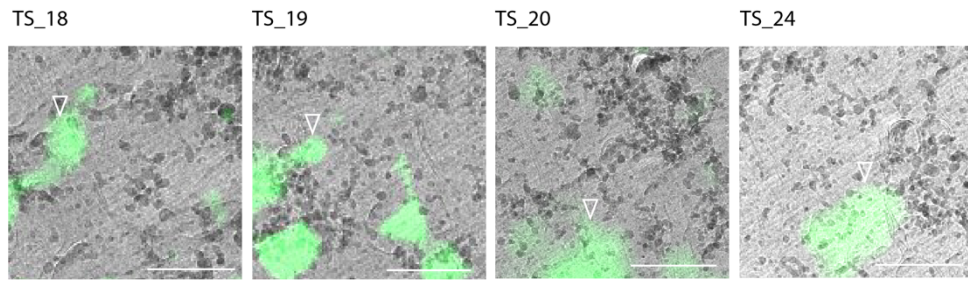
TS_03

TS_04

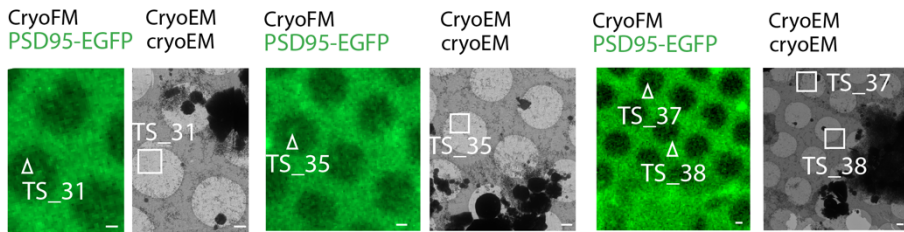
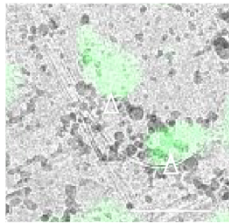




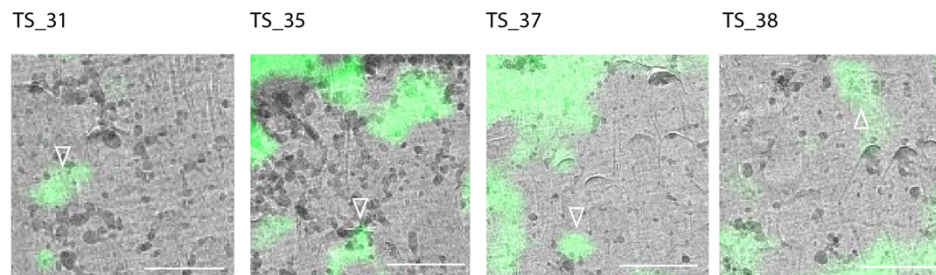
CryoCLEM
PSD95-EGFP/cryoEM



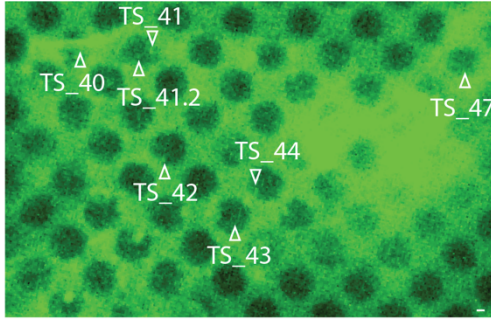
TS_29



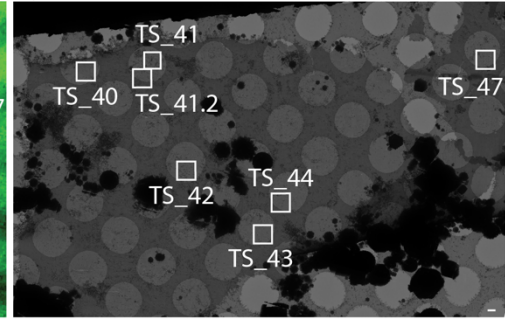
CryoCLEM
PSD95-EGFP/cryoEM



CryoFM
PSD95-EGFP

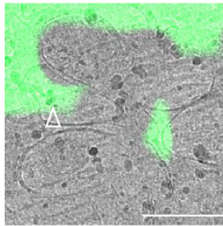


CryoEM
cryoEM

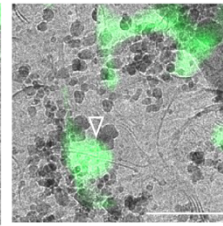


CryoCLEM
PSD95-EGFP/cryoEM

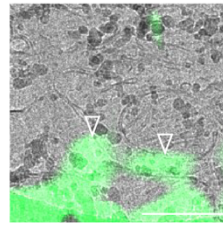
TS_40



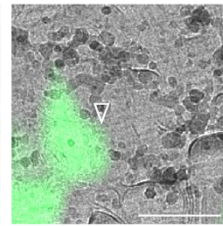
TS_41



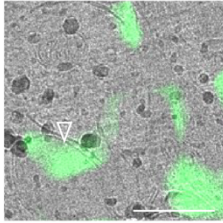
TS_41.2



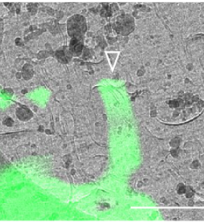
TS_42



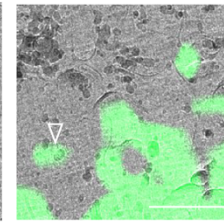
TS_43



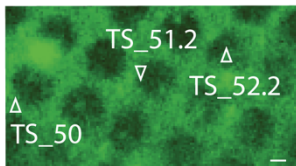
TS_44



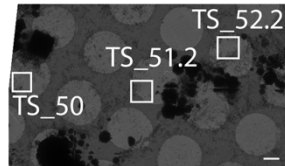
TS_47



CryoFM
PSD95-EGFP



CryoEM
cryoEM

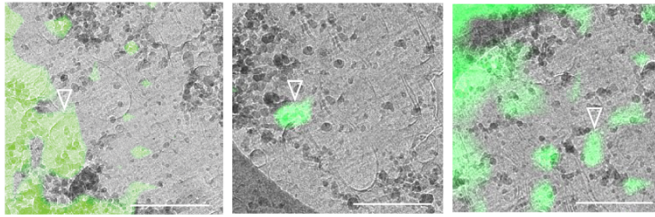


CryoCLEM
PSD95-EGFP/cryoEM

TS_50

TS_51.2

TS_52.2

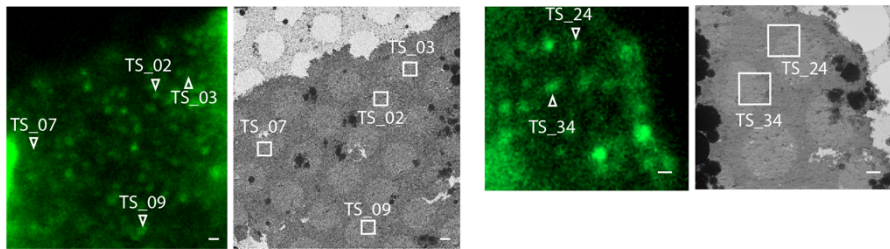


DG

Dataset 7

CryoFM
PSD95-EGFP

CryoEM
cryoEM



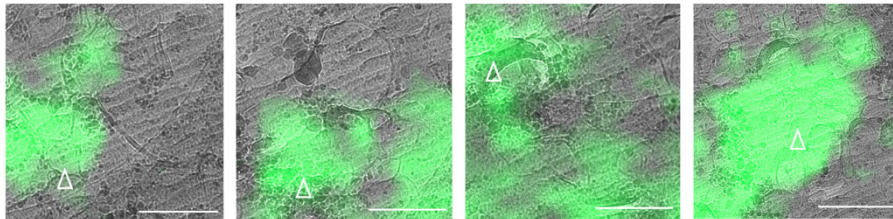
CryoCLEM
PSD95-EGFP/cryoEM

TS_02

TS_03

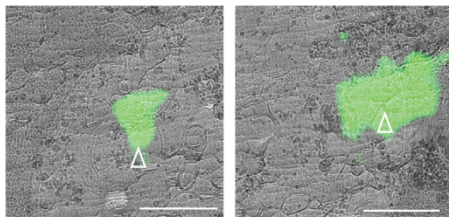
TS_07

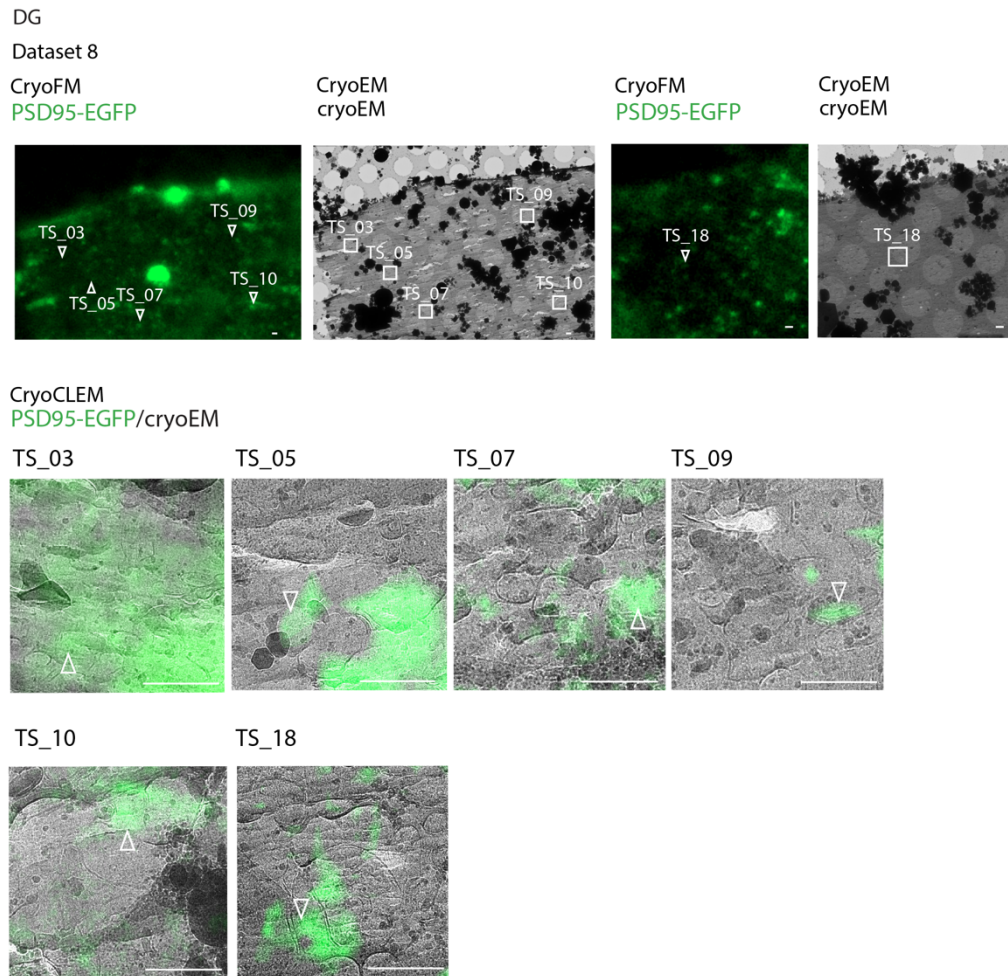
TS_09



TS_24

TS_34





Supplementary figure 1: All cryoFM, cryoEM and cryoCLEM of Psd95-EGFP-labelled glutamatergic synapses discussed in chapter 3.

Data are divided into cortex, CA3, and DG, with dataset collection number (as in Supplementary Table 1) indicated. CryoFM and cryoEM images depict tissue cryosections, with white arrowheads and boxes indicating regions for correlation. Scalebars = 1 μ m.

CryoCLEM images depict the tomogram collection regions, as indicated by white boxes on the associated tissue cryosections. Scalebars = 0.5 μ m.

GFP puncta corresponded to the postsynaptic compartments of glutamatergic synapses. White arrowheads on cryoCLEM images indicate the GFP-positive postsynaptic compartments used for analysis. Other GFP puncta

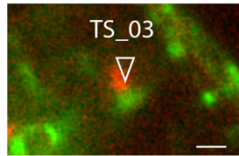
corresponded to either postsynaptic compartments which were not included in the analysis due to not having a visible cleft and associated presynaptic compartment within the tomographic volume, or artefacts such as autofluorescent ice contamination, crevasses within the cryosection, or out of focus unattached tissue.

Dataset 1

Non-Engram to Engram (CaMKII-ChR2-EYFP/TRE-mCherry)

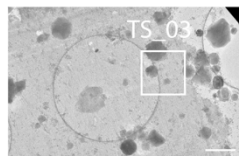
CryoFM

CaMKII-ChR2-EYFP/TRE-mCherry



CryoEM

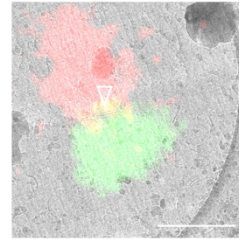
cryoEM



CryoCLEM

CaMKII-ChR2-EYFP/TRE-mCherry/cryoEM

TS_03

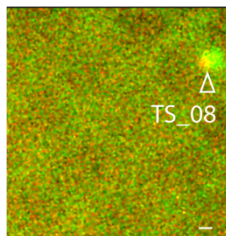


Dataset 2

Non-Engram to Engram (CaMKII-ChR2-EYFP/TRE-mCherry)

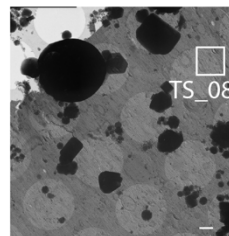
CryoFM

CaMKII-ChR2-EYFP/TRE-mCherry



CryoEM

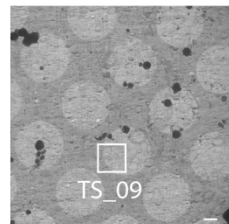
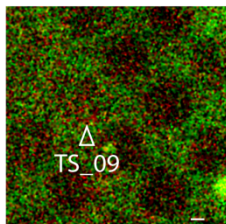
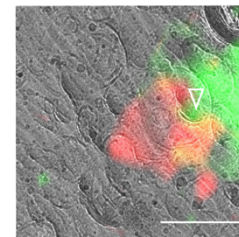
cryoEM



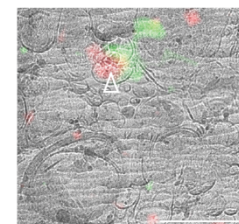
CryoCLEM

CaMKII-ChR2-EYFP/TRE-mCherry/cryoEM

TS_08



TS_09



Dataset 3

Engram to Engram (TRE-ChR2-EYFP/TRE-mCherry)

CryoFM

TRE-ChR2-EYFP/TRE-mCherry

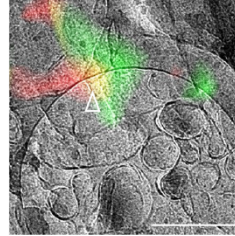
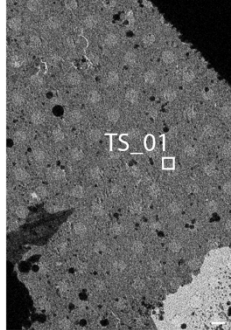
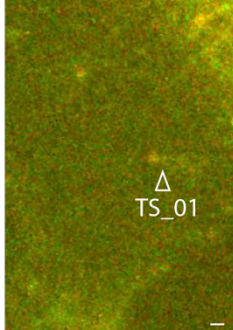
CryoEM

cryoEM

CryoCLEM

TRE-ChR2-EYFP/TRE-mCherry/cryoEM

TS_01



Dataset 4

Engram to Engram (TRE-ChR2-EYFP/TRE-mCherry)

CryoFM

TRE-ChR2-EYFP/TRE-mCherry

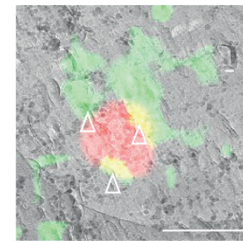
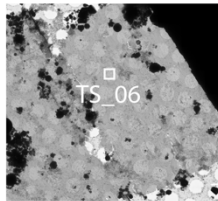
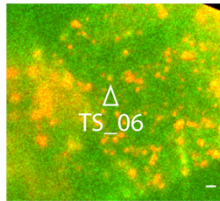
CryoEM

cryoEM

CryoCLEM

TRE-ChR2-EYFP/TRE-mCherry/cryoEM

TS_06



CryoFM

TRE-ChR2-EYFP/TRE-mCherry

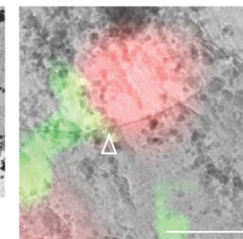
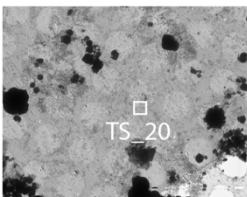
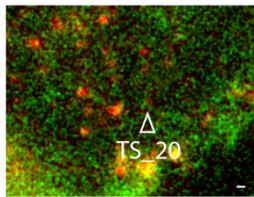
CryoEM

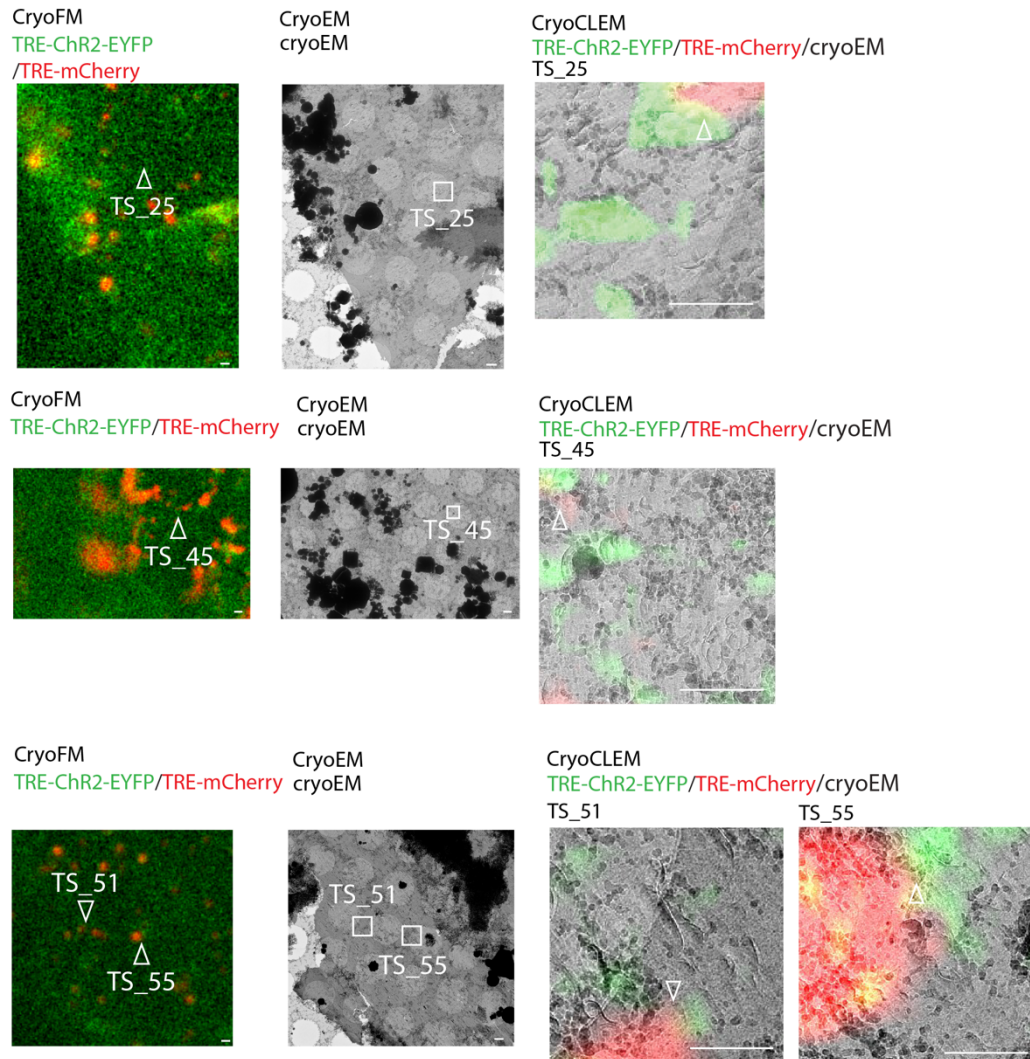
cryoEM

CryoCLEM

TRE-ChR2-EYFP/TRE-mCherry/cryoEM

TS_20





Engram to Non-Engram (TRE-ChR2-EYFP/TRE-mCherry)

CryoFM

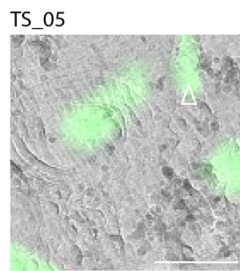
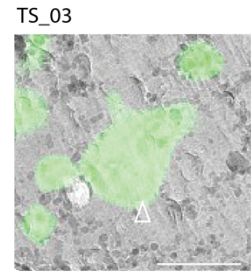
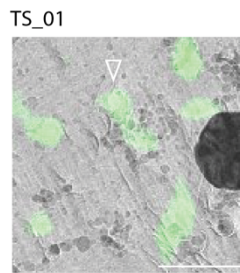
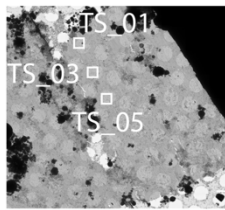
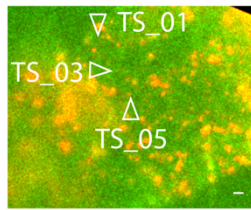
TRE-ChR2-EYFP/TRE-mCherry

CryoEM

cryoEM

CryoCLEM

TRE-ChR2-EYFP/TRE-mCherry/cryoEM



CryoFM

TRE-ChR2-EYFP/TRE-mCherry

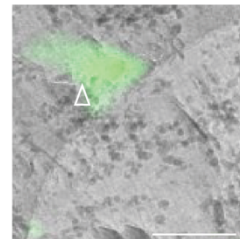
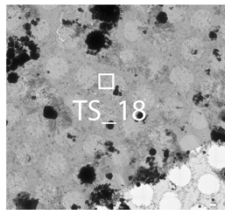
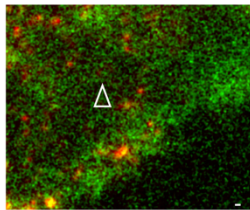
CryoEM

cryoEM

CryoCLEM

TRE-ChR2-EYFP/TRE-mCherry/cryoEM

TS_18



Non-Engram to Engram (TRE-ChR2-EYFP/TRE-mCherry)

CryoFM

TRE-ChR2-EYFP/TRE-mCherry

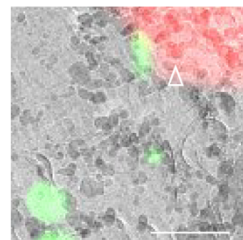
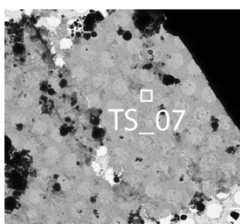
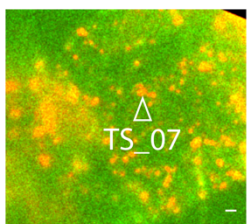
CryoEM

cryoEM

CryoCLEM

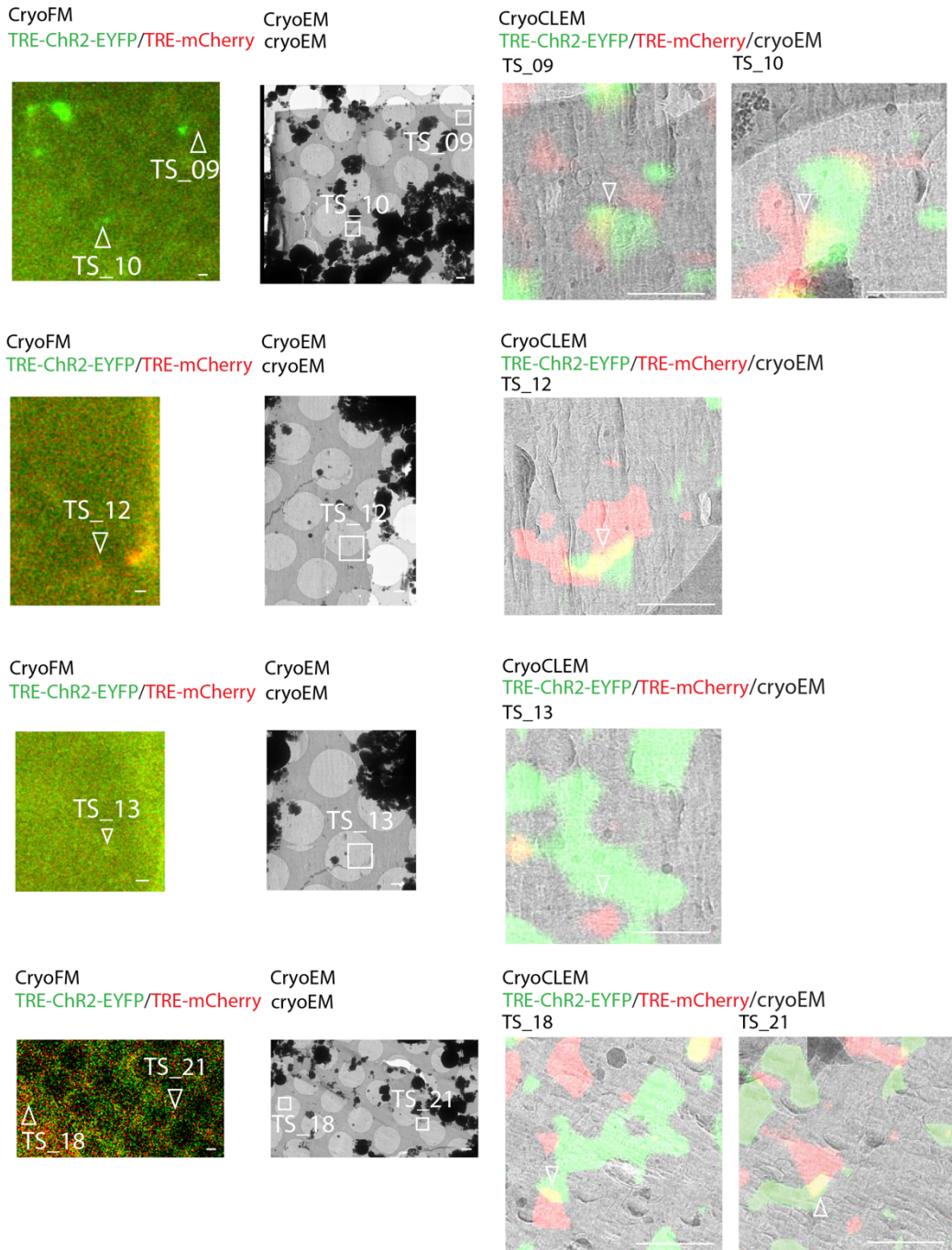
TRE-ChR2-EYFP/TRE-mCherry/cryoEM

TS_07



Dataset 5

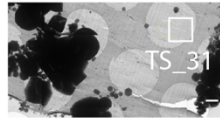
Engram to Engram (TRE-ChR2-EYFP/TRE-mCherry)



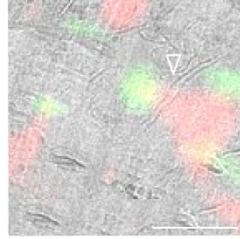
CryoFM
TRE-ChR2-EYFP/TRE-mCherry



CryoEM
cryoEM

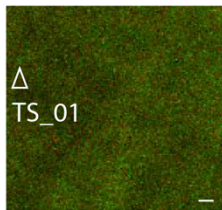


CryoCLEM
TRE-ChR2-EYFP/TRE-mCherry/cryoEM
TS_31

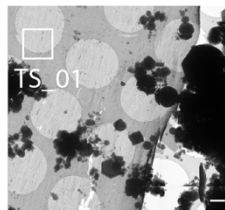


Engram to Non-Engram (TRE-ChR2-EYFP/TRE-mCherry)

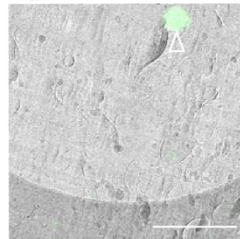
CryoFM
TRE-ChR2-EYFP/TRE-mCherry



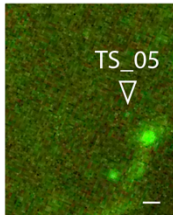
CryoEM
cryoEM



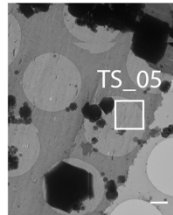
CryoCLEM
TRE-ChR2-EYFP/TRE-mCherry/cryoEM
TS_01



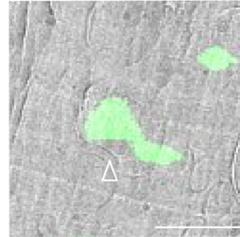
CryoFM
TRE-ChR2-EYFP/TRE-mCherry



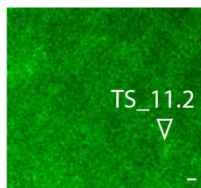
CryoEM
cryoEM



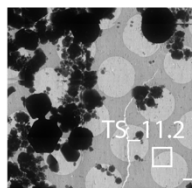
CryoCLEM
TRE-ChR2-EYFP/TRE-mCherry/cryoEM
TS_05



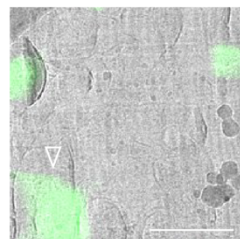
CryoFM
TRE-ChR2-EYFP/TRE-mCherry

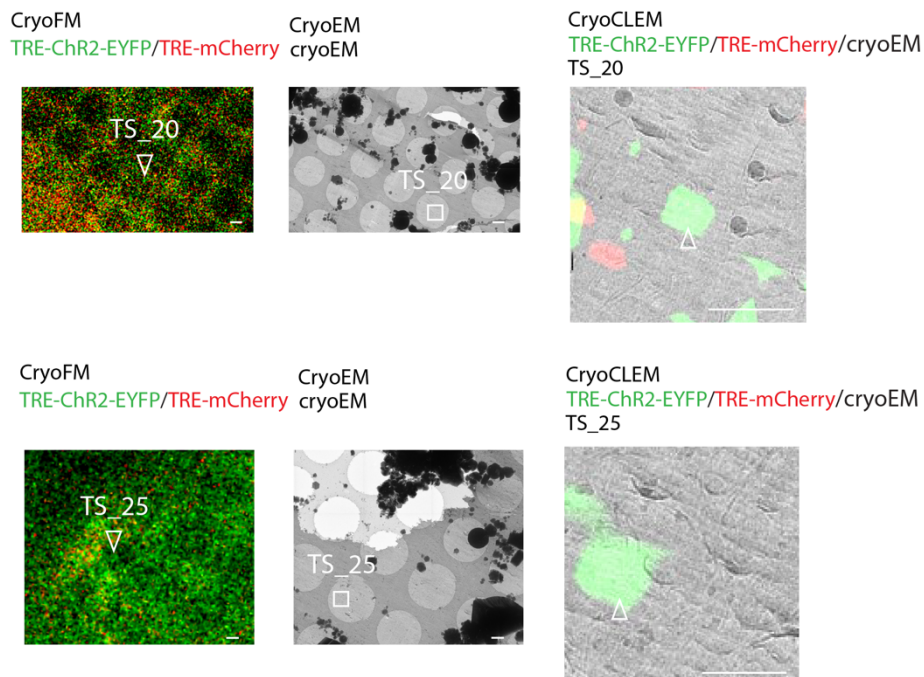


CryoEM
cryoEM



CryoCLEM
TRE-ChR2-EYFP/TRE-mCherry/cryoEM
TS_11.2





Supplementary figure 2: All cryoCLEM of engram-labelled synapses discussed in chapter 4. Data are divided into engram to engram, engram to non-engram and non-engram to engram synapses, with dataset (as indicated in Supplementary Table 2) and tomogram number indicated per group. CryoFM and cryoEM images depict tissue cryosections, with white arrowheads and boxes indicating regions for correlation. Scalebars = 1 μ m.

CryoCLEM images depict the tomogram collection regions, as indicated by white boxes on the associated tissue cryosections. Scalebars = 0.5 μ m.

EYFP puncta corresponded to the presynaptic compartments originating from the CA3 region, whilst mCherry corresponded to postsynaptic compartments of synapses in the CA1 region. White arrowheads on cryoCLEM images indicate the EYFP and mCherry used to direct cryoET collections. Other puncta corresponded to either non-synaptic regions of engram-labelled neurons, or artefacts such as autofluorescent ice contamination, crevasses within the cryosection, or out of focus unattached tissue.

Bibliography

- Akert, K., Sandri, C., Pfenninger, K. and Forel-Strasse, A. 1964. A NEW METHOD FOR STAINING SYNAPTIC VESICLES AT PERIPHERAL AND CENTRAL SYNAPSES. *Brain Res.* **26**, pp.286–295.
- Al-Amoudi, A., Chang, J.J., Leforestier, A., McDowall, A., Salamin, L.M., Norlén, L.P.O., Richter, K., Blanc, N.S., Studer, D. and Dubochet, J. 2004. Cryo-electron microscopy of vitreous sections. *EMBO Journal.* **23**(18), pp.3583–3588.
- Almog, Y., Fadila, S., Brusel, M., Mavashov, A., Anderson, K. and Rubinstein, M. 2021. Developmental alterations in firing properties of hippocampal CA1 inhibitory and excitatory neurons in a mouse model of Dravet syndrome. *Neurobiology of Disease.* **148**, p.105209.
- Amaral, D.G., Scharfman, H.E. and Lavenex, P. 2007. The dentate gyrus: fundamental neuroanatomical organization (dentate gyrus for dummies). *Progress in brain research.* **163**, p.3.
- Andrade-Talavera, Y., Duque-Feria, P., Paulsen, O. and Rodríguez-Moreno, A. 2016. Presynaptic Spike Timing-Dependent Long-Term Depression in the Mouse Hippocampus. *Cerebral Cortex.* **26**(8), pp.3637–3654.
- Asano, S., Engel, B.D. and Baumeister, W. 2016. In Situ Cryo-Electron Tomography: A Post-Reductionist Approach to Structural Biology. *Journal of molecular biology.* **428**(2 Pt A), pp.332–343.
- Augustine, G.J., Santamaria, F. and Tanaka, K. 2003. Local calcium signaling in neurons. *Neuron.* **40**(2), pp.331–346.
- Autore, L., O’leary, J.D., Ortega-De, C., Luis, S. and Ryan, J. 2023. Adaptive expression of engrams by retroactive interference. *CellReports.* **42**, p.112999.
- Aziz, W., Kraev, I., Mizuno, K., Kirby, A., Fang, T., Rupawala, H., Kasbi, K., Rothe, S., Jozsa, F., Rosenblum, K., Stewart, M.G. and Giese, K.P. 2019. Multi-input Synapses, but Not LTP-Strengthened Synapses, Correlate with Hippocampal Memory Storage in Aged Mice. *Current Biology.* **29**, pp.1–11.

- Bai, X. chen, McMullan, G. and Scheres, S.H.W. 2015. How cryo-EM is revolutionizing structural biology. *Trends in biochemical sciences*. **40**(1), pp.49–57.
- Basu, J. and Siegelbaum, S.A. 2015. The Corticohippocampal Circuit, Synaptic Plasticity, and Memory. *Cold Spring Harbor Perspectives in Biology*. **7**(11), p.a021733.
- Basu, S. and Lamprecht, R. 2018. The Role of Actin Cytoskeleton in Dendritic Spines in the Maintenance of Long-Term Memory. *Frontiers in Molecular Neuroscience*. **11**, p.143.
- Le Bé, J.V., Silberberg, G., Wang, Y. and Markram, H. 2007. Morphological, Electrophysiological, and Synaptic Properties of Corticocallosal Pyramidal Cells in the Neonatal Rat Neocortex. *Cerebral Cortex*. **17**(9), pp.2204–2213.
- Beck, M. and Baumeister, W. 2016. Cryo-Electron Tomography: Can it Reveal the Molecular Sociology of Cells in Atomic Detail? *Trends in cell biology*. **26**(11), pp.825–837.
- De Benedictis, A., Duffau, H., Paradiso, B., Grandi, E., Balbi, S., Granieri, E., Colarusso, E., Chioffi, F., Marras, C.E. and Sarubbo, S. 2014. Anatomico-functional study of the temporo-parieto-occipital region: Dissection, tractographic and brain mapping evidence from a neurosurgical perspective. *Journal of Anatomy*. **225**(2), pp.132–151.
- Berger, C., Dumoux, M., Glen, T., Yee, N.B. y., Mitchels, J.M., Patáková, Z., Darrow, M.C., Naismith, J.H. and Grange, M. 2023. Plasma FIB milling for the determination of structures in situ. *Nature Communications*. **14**(1).
- Bernardi, P., Gerle, C., Halestrap, A.P., Jonas, E.A., Karch, J., Mnatsakanyan, N., Pavlov, E., Sheu, S.S. and Soukas, A.A. 2023. Identity, structure, and function of the mitochondrial permeability transition pore: controversies, consensus, recent advances, and future directions. *Cell Death & Differentiation* 2023 30:8. **30**(8), pp.1869–1885.
- Berridge, M.J., Bootman, M.D. and Roderick, H.L. 2003. Calcium signalling: dynamics, homeostasis and remodelling. *Nature Reviews Molecular Cell Biology*. **4**(7), pp.517–529.

- Billig, A.J., Lad, M., Sedley, W. and Griffiths, T.D. 2022. The hearing hippocampus. *Progress in Neurobiology*. **218**, p.102326.
- Bliss, T.V.P. and Lømo, T. 1973. Long-lasting potentiation of synaptic transmission in the dentate area of the anaesthetized rabbit following stimulation of the perforant path. *The Journal of Physiology*. **232**(2), pp.331–356.
- Böger, C., Hafner, A.-S., Schlichthärle, T., Strauss, M.T., Malkusch, S., Endesfelder, U., Jungmann, R., Schuman, E.M. and Heilemann, M. 2019. Super-resolution imaging and estimation of protein copy numbers at single synapses with DNA-point accumulation for imaging in nanoscale topography. *Neurophotonics*. **6**(03), p.1.
- Borges-Merjane, C., Kim, O. and Jonas, P. 2020. Functional Electron Microscopy, “Flash and Freeze,” of Identified Cortical Synapses in Acute Brain Slices. *Neuron*. **105**(6), pp.992-1006.e6.
- Bourgeois, J.P., Goldman-Rakic, P.S. and Rakic, P. 1994. Synaptogenesis in the prefrontal cortex of rhesus monkeys. *Cerebral Cortex*. **4**(1), pp.78–96.
- Bourne, J.N. and Harris, K.M. 2011. Coordination of size and number of excitatory and inhibitory synapses results in a balanced structural plasticity along mature hippocampal CA1 dendrites during LTP. *Hippocampus*. **21**(4), pp.354–373.
- Bourne, J.N. and Harris, K.M. 2012. Nanoscale analysis of structural synaptic plasticity. *Current Opinion in Neurobiology*. **22**(3), p.372.
- Bourtchuladze, R., Frenguelli, B., Blendy, J., Cioffi, D., Schutz, G. and Silva, A.J. 1994. Deficient long-term memory in mice with a targeted mutation of the cAMP-responsive element-binding protein. *Cell*. **79**(1), pp.59–68.
- Brasch, J., Goodman, K.M., Noble, A.J., Rapp, M., Mannepalli, S., Bahna, F., Dandey, V.P., Bepler, T., Berger, B., Maniatis, T., Potter, C.S., Carragher, B., Honig, B. and Shapiro, L. 2019. Visualization of clustered protocadherin neuronal self-recognition complexes. *Nature*. **569**(7755), pp.280–283.
- Briggs, J.A.G. 2013. Structural biology in situ--the potential of subtomogram averaging. *Current opinion in structural biology*. **23**(2), pp.261–267.

- Broadhead, M.J., Horrocks, M.H., Zhu, F., Muresan, L., Benavides-Piccione, R., DeFelipe, J., Fricker, D., Kopanitsa, M. V., Duncan, R.R., Klenerman, D., Komiyama, N.H., Lee, S.F. and Grant, Seth G.N. 2016. PSD95 nanoclusters are postsynaptic building blocks in hippocampus circuits. *Scientific Reports*. **6**.
- Brown, M.R., Sullivan, P.G. and Geddes, J.W. 2006. Synaptic Mitochondria Are More Susceptible to Ca²⁺Overload than Nonsynaptic Mitochondria. *Journal of Biological Chemistry*. **281**(17), pp.11658–11668.
- Bucher, M., Fanutza, T. and Mikhaylova, M. 2020. Cytoskeletal makeup of the synapse: Shaft versus spine. *Cytoskeleton*. **77**(3–4), pp.55–64.
- Bullitt, E. 1990. Expression of c-fos-like protein as a marker for neuronal activity following noxious stimulation in the rat. *The Journal of comparative neurology*. **296**(4), pp.517–530.
- Bulovaite, E., Qiu, Z., Kratschke, M., Zgraj, A., Fricker, D.G., Tuck, E.J., Gokhale, R., Koniaris, B., Jami, S.A., Merino-Serrais, P., Husi, E., Mendive-Tapia, L., Vendrell, M., O'Dell, T.J., DeFelipe, J., Komiyama, N.H., Holtmaat, A., Fransén, E. and Grant, S.G.N. 2022. A brain atlas of synapse protein lifetime across the mouse lifespan. *Neuron*. **110**(24), pp.4057-4073.e8.
- Campbell, D.S. and Holt, C.E. 2001. Chemotropic responses of retinal growth cones mediated by rapid local protein synthesis and degradation. *Neuron*. **32**(6), pp.1013–1026.
- Carter, S.D., Mageswaran, S.K., Farino, Z.J., Mamede, J.I., Oikonomou, C.M., Hope, T.J., Freyberg, Z. and Jensen, G.J. 2018. Distinguishing signal from autofluorescence in cryogenic correlated light and electron microscopy of mammalian cells. *Journal of Structural Biology*. **201**(1), pp.15–25.
- Caspar, D.L.D. and Kirschner, D.A. 1971. Myelin membrane structure at 10 Å resolution. *Nature: New biology*. **231**(19), pp.46–52.
- Chang, S. and De Camilli, P. 2001. Glutamate regulates actin-based motility in axonal filopodia. *Nature Neuroscience* 2001 4:8. **4**(8), pp.787–793.
- Chapi Mori, J.L. 2016. Desarrollo Histórico Del Estudio Neuropsicológico De La Memoria. *Revista de Psicología (Trujillo)*. **18**(1), pp.87–100.

- Chen, F., Venugopal, V., Murray, B. and Rudenko, G. 2011. The structure of neurexin 1 α reveals features promoting a role as synaptic organizer. *Structure*. **19**(6), pp.779–789.
- Chen, L., Chetkovich, D.M., Petralia, R.S., Sweeney, N.T., Kawasaki, Y., Wenthold, R.J., Brecht, D.S. and Nicoll, R.A. 2000. Stargazin regulates synaptic targeting of AMPA receptors by two distinct mechanisms. *Nature*. **408**(6815), pp.936–943.
- Chen, S., Cai, D., Pearce, K., Sun, P.Y.W., Roberts, A.C. and Glanzman, D.L. 2014. Reinstatement of long-term memory following erasure of its behavioral and synaptic expression in *Aplysia*. *eLife*. **3**, p.e03896.
- Cherubini, E. and Miles, R. 2015. The CA3 region of the hippocampus: How is it? What is it for? How does it do it? *Frontiers in Cellular Neuroscience*. **9**(FEB), p.19.
- Chicurel, M.E. and Harris, K.M. 1992. Three-dimensional analysis of the structure and composition of CA3 branched dendritic spines and their synaptic relationships with mossy fiber boutons in the rat hippocampus. *The Journal of comparative neurology*. **325**(2), pp.169–182.
- Chidambaram, S.B., Rathipriya, A.G., Bolla, S.R., Bhat, A., Ray, B., Mahalakshmi, A.M., Manivasagam, T., Thenmozhi, A.J., Essa, M.M., Guillemain, G.J., Chandra, R. and Sakharkar, M.K. 2019. Dendritic spines: Revisiting the physiological role. *Progress in Neuro-Psychopharmacology and Biological Psychiatry*. **92**, pp.161–193.
- Chiu, C.Q., Lur, G., Morse, T.M., Carnevale, N.T., Ellis-Davies, G.C.R. and Higley, M.J. 2013. Compartmentalization of GABAergic inhibition by dendritic spines. *Science (New York, N.Y.)*. **340**(6133), pp.759–762.
- Chklovskii, D.B., Mel, B.W. and Svoboda, K. 2004. Cortical rewiring and information storage. *Nature 2004 431:7010*. **431**(7010), pp.782–788.
- Choi, J.H., Sim, S.E., Kim, J. il, Choi, D.I.I., Oh, J., Ye, S., Lee, J., Kim, T.H., Ko, H.G., Lim, C.S. and Kaang, B.K. 2018. Interregional synaptic maps among engram cells underlie memory formation. *Science*. **360**(6387), pp.430–435.
- Chowdhury, D. and Hell, J.W. 2018. Homeostatic synaptic scaling: Molecular regulators of synaptic AMPA-type glutamate receptors. *F1000Research*. **7**.

- Chung, L. 2015. A Brief Introduction to the Transduction of Neural Activity into Fos Signal. *Development & Reproduction*. **19**(2), p.61.
- Cirelli, C. and Tononi, G. 2020. Effects of sleep and waking on the synaptic ultrastructure. *Philosophical Transactions of the Royal Society B: Biological Sciences*. **375**(1799).
- Cizeron, M., Qiu, Z., Koniaris, B., Gokhale, R., Komiyama, N.H., Fransén, E. and Grant, S.G.N. 2020. A brainwide atlas of synapses across the mouse life span. *Science (New York, N.Y.)*. **369**(6501).
- Collingridge, G.L., Kehl, S.J. and McLennan, H. 1983. Excitatory amino acids in synaptic transmission in the Schaffer collateral-commissural pathway of the rat hippocampus. *The Journal of physiology*. **334**, pp.33–46.
- Cotman, C.W. and Nieto-Sampedro, M. 1984. Cell biology of synaptic plasticity. *Science (New York, N.Y.)*. **225**(4668), pp.1287–1294.
- Creekmore, B.C., Kixmoeller, K., Black, B.E., Lee, E.B. and Chang, Y.-W. 2023. Native ultrastructure of fresh human brain vitrified directly from autopsy revealed by cryo-electron tomography with cryo-plasma focused ion beam milling. *bioRxiv.*, 2023.09.13.557623.
- Crowley, L.C., Marfell, B.J., Scott, A.P. and Waterhouse, N.J. 2016. Quantitation of Apoptosis and Necrosis by Annexin V Binding, Propidium Iodide Uptake, and Flow Cytometry. *Cold Spring Harbor Protocols*. **2016**(11), pdb.prot087288.
- Davis, S., Butcher, S.P. and Morris, R.G.M. 1992. The NMDA receptor antagonist D-2-amino-5-phosphonopentanoate (D-AP5) impairs spatial learning and LTP in vivo at intracerebral concentrations comparable to those that block LTP in vitro. *Journal of Neuroscience*. **12**(1), pp.21–34.
- Delgado, T., Petralia, R.S., Freeman, D.W., Sedlacek, M., Wang, Y.X., Brenowitz, S.D., Sheu, S.H., W Gu, J., Kapogiannis, D., Mattson, M.P. and Yao, P.J. 2019. Comparing 3D ultrastructure of presynaptic and postsynaptic mitochondria. *Biology Open*. **8**(8).
- Dimchev, G., Amiri, B., Fäßler, F., Falcke, M. and Schur, F.K. 2021. Computational toolbox for ultrastructural quantitative analysis of filament networks in cryo-ET data. *Journal of Structural Biology*. **213**(4), p.107808.

- Dörrbaum, A.R., Kochen, L., Langer, J.D. and Schuman, E.M. 2018. Local and global influences on protein turnover in neurons and glia. *eLife*. **7**, p.e34202.
- Dorris, D.M., Hauser, C.A., Minnehan, C.E. and Meitzen, J. 2014. An aerator for brain slice experiments in individual cell culture plate wells. *Journal of Neuroscience Methods*. **238**, pp.1–10.
- Drachman, D.A. 2005. Do we have brain to spare? *Neurology*. **64**(12), pp.2004–5.
- Dubochet, J., Lepault, J., Freeman, R., Berriman, J.A. and Homo, J.-C. 1982. Electron microscopy of frozen water and aqueous solutions. *Journal of Microscopy*. **128**(3), pp.219–237.
- Dumoux, M., Glen, T., Smith, J.L.R., Ho, E.M.L., Perdigão, L.M.A., Pennington, A., Klumpe, S., Yee, N.B.Y., Farmer, D., Lai, P.Y.A., Bowles, W., Kelley, R., Plitzko, J.M., Wu, L., Basham, M., Clare, D.K., Siebert, C.A., Darrow, M.C., Naismith, J.H. and Grange, M. 2023. Cryo-plasma fib/sem volume imaging of biological specimens. *eLife*. **12**.
- Dürr, K.L., Chen, L., Stein, R.A., De Zorzi, R., Folea, I.M., Walz, T., McHaourab, H.S. and Gouaux, E. 2014. Structure and Dynamics of AMPA Receptor GluA2 in Resting, Pre-Open, and Desensitized States. *Cell*. **158**(4), pp.778–792.
- Dvorkin, R. and Ziv, N.E. 2016. Relative Contributions of Specific Activity Histories and Spontaneous Processes to Size Remodeling of Glutamatergic Synapses. *PLoS Biology*. **14**(10), p.e1002572.
- El-Din El-Husseini, A., Schnell, E., Chetkovich, D.M., Nicoll, R.A. and Brecht, D.S. 2000. PSD-95 Involvement in Maturation of Excitatory Synapses. *Science*. **290**(5495), pp.1364–1368.
- Engert, F. and Bonhoeffer, T. 1999. Dendritic spine changes associated with hippocampal long-term synaptic plasticity. *Nature*. **399**(6731), pp.66–70.
- Engert, F. and Bonhoeffer, T. 1997. Synapse specificity of long-term potentiation breaks down at short distances. *Nature*. **388**(6639), pp.279–284.
- Erdmann, P.S., Hou, Z., Klumpe, S., Khavnekar, S., Beck, F., Wilfling, F., Plitzko, J.M. and Baumeister, W. 2021. In situ cryo-electron tomography

- reveals gradient organization of ribosome biogenesis in intact nucleoli. *Nature Communications*. **12**(1).
- Faas, F.G.A., Cristina Avramut, M., van den Berg, B.M., Mieke Mommaas, A., Koster, A.J. and Ravelli, R.B.G. 2012. Virtual nanoscopy: Generation of ultra-large high resolution electron microscopy maps. *Journal of Cell Biology*. **198**(3), pp.457–469.
- Fang, T., Lu, X., Berger, D., Gmeiner, C., Cho, J., Schalek, R., Ploegh, H. and Lichtman, J. 2018. Nanobody immunostaining for correlated light and electron microscopy with preservation of ultrastructure. *Nature methods*. **15**(12), pp.1029–1032.
- Fastenrath, M., Coynel, D., Spalek, K., Milnik, A., Gschwind, L., Roozendaal, B., Papassotiropoulos, A. and de Quervain, D.J.F. 2014. Dynamic modulation of amygdala-hippocampal connectivity by emotional arousal. *The Journal of neuroscience : the official journal of the Society for Neuroscience*. **34**(42), pp.13935–47.
- Fernández-Busnadiego, R., Zuber, B., Maurer, U.E., Cyrklaff, M., Baumeister, W. and Lučić, V. 2010. Quantitative analysis of the native presynaptic cytomatrix by cryoelectron tomography. *The Journal of Cell Biology*. **188**(1), p.145.
- Flood, J.F., Bennett, E.L., Orme, A.E. and Rosenzweig, M.R. 1975. Effects of protein synthesis inhibition on memory for active avoidance training. *Physiology and Behavior*. **14**(2), pp.177–184.
- Fraga, M.F., Ballestar, E., Paz, M.F., Ropero, S., Setien, F., Ballestar, M.L., Heine-Suñer, D., Cigudosa, J.C., Urioste, M., Benitez, J., Boix-Chornet, M., Sanchez-Aguilera, A., Ling, C., Carlsson, E., Poulsen, P., Vaag, A., Stephan, Z., Spector, T.D., Wu, Y.-Z., Plass, C. and Esteller, M. 2005. Epigenetic differences arise during the lifetime of monozygotic twins. *Proceedings of the National Academy of Sciences of the United States of America*. **102**(30), pp.10604–9.
- Frank, R.A.W. 2011. Endogenous ion channel complexes: The NMDA receptor. *Biochemical Society Transactions*. **39**(3), pp.707–718.
- Frank, R.A.W., Komiyama, N.H., Ryan, T.J., Zhu, F., O'Dell, T.J. and Grant, S.G.N. 2016. NMDA receptors are selectively partitioned into complexes

- and supercomplexes during synapse maturation. *Nature Communications*. **7**, p.11264.
- Frank, R.A.W., Zhu, F., Komiyama, N.H. and Grant, S.G.N. 2017. Hierarchical organization and genetically separable subfamilies of PSD95 postsynaptic supercomplexes. *Journal of Neurochemistry*. **142**(4), pp.504–511.
- Frey, U., Frey, S., Schollmeier, F. and Krug, M. 1996. Influence of actinomycin D, a RNA synthesis inhibitor, on long-term potentiation in rat hippocampal neurons in vivo and in vitro. *Journal of Physiology*. **490**(3), pp.703–711.
- Frey, U. and Morris, R.G.M. 1997. Synaptic tagging and long-term potentiation. *Nature*. **385**(6616), pp.533–536.
- Fukazawa, Y., Saitoh, Y., Ozawa, F., Ohta, Y., Mizuno, K. and Inokuchi, K. 2003. Hippocampal LTP is accompanied by enhanced F-actin content within the dendritic spine that is essential for late LTP maintenance in vivo. *Neuron*. **38**(3), pp.447–460.
- Ghiani, C.A., Beltran-Parrazal, L., Sforza, D.M., Malvar, J.S., Seksenyan, A., Cole, R., Smith, D.J., Charles, A., Ferchmin, P.A. and De Vellis, J. 2007. Genetic program of neuronal differentiation and growth induced by specific activation of NMDA receptors. *Neurochemical Research*. **32**(2), pp.363–376.
- Gilbert, M.A.G., Fatima, N., Jenkins, J., O’Sullivan, T.J., Schertel, A., Halfon, Y., Morrema, T.H.J., Geibel, M., Radford, S.E., Hoozemans, J.J.M. and Frank, R.A.W. 2023. In situ cryo-electron tomography of β -amyloid and tau in post-mortem Alzheimer’s disease brain. *bioRxiv*, 2023.07.17.549278.
- Glaeser, R.M. 2019. How Good Can Single-Particle Cryo-EM Become? What Remains Before It Approaches Its Physical Limits? *Annual review of biophysics*. **48**, pp.45–61.
- Glaeser, R.M., Han, B.G., Csencsits, R., Killilea, A., Pulk, A. and Cate, J.H.D. 2016. Factors that Influence the Formation and Stability of Thin, Cryo-EM Specimens. *Biophysical Journal*. **110**(4), pp.749–755.

- Gold, V.A.M., Ieva, R., Walter, A., Pfanner, N., Van Der Laan, M. and Kühlbrandt, W. 2014. Visualizing active membrane protein complexes by electron cryotomography. *Nature Communications*. **5**.
- Goley, E.D. and Welch, M.D. 2006. The ARP2/3 complex: an actin nucleator comes of age. *Nature reviews. Molecular cell biology*. **7**(10), pp.713–726.
- Gomez, A.M., Traunmüller, L. and Scheiffele, P. 2021. Neurexins: molecular codes for shaping neuronal synapses. *Nature Reviews Neuroscience*. **22**(3), pp.137–151.
- Gonzalez-Lozano, M.A., Klemmer, P., Gebuis, T., Hassan, C., Van Nierop, P., Van Kesteren, R.E., Smit, A.B. and Li, K.W. 2016. Dynamics of the mouse brain cortical synaptic proteome during postnatal brain development. *Scientific Reports*. **6**, p.35456.
- Goto, A., Bota, A., Miya, K., Wang, J., Tsukamoto, S., Jiang, X., Hirai, D., Murayama, M., Matsuda, T., McHugh, T.J., Nagai, T. and Hayashi, Y. 2021. Stepwise synaptic plasticity events drive the early phase of memory consolidation. *Science*. **374**(6569), pp.857–863.
- Grange, M., Vasishtan, D. and Grünewald, K. 2017. Cellular electron cryo tomography and in situ sub-volume averaging reveal the context of microtubule-based processes. *Journal of Structural Biology*. **197**(2), p.181.
- Granger, A.J., Shi, Y., Lu, W., Cerpas, M. and Nicoll, R.A. 2013. LTP requires a reserve pool of glutamate receptors independent of subunit type. *Nature*. **493**(7433), pp.495–500.
- Gray, E.G. 1959. Axo-somatic and axo-dendritic synapses of the cerebral cortex: an electron microscope study. *Journal of anatomy*. **93**(Pt 4), pp.420–33.
- Greer, P.L. and Greenberg, M.E. 2008. From Synapse to Nucleus: Calcium-Dependent Gene Transcription in the Control of Synapse Development and Function. *Neuron*. **59**(6), pp.846–860.
- Grutzendler, J., Kasthuri, N. and Gan, W.B. 2002. Long-term dendritic spine stability in the adult cortex. *Nature*. **420**(6917), pp.812–816.
- Guan, J.S., Haggarty, S.J., Giacometti, E., Dannenberg, J.H., Joseph, N., Gao, J., Nieland, T.J.F., Zhou, Y., Wang, X., Mazitschek, R., Bradner,

- J.E., DePinho, R.A., Jaenisch, R. and Tsai, L.H. 2009. HDAC2 negatively regulates memory formation and synaptic plasticity. *Nature*. **459**(7243), pp.55–60.
- Hagena, H. and Manahan-Vaughan, D. 2013. Differentiation in the protein synthesis-dependency of persistent synaptic plasticity in mossy fiber and associational/commissural CA3 synapses in vivo. *Frontiers in Integrative Neuroscience*. **7**, p.10.
- Hansen, K.B., Yuan, H. and Traynelis, S.F. 2007. Structural aspects of AMPA receptor activation, desensitization and deactivation. *Current opinion in neurobiology*. **17**(3), pp.281–8.
- Harapin, J., Börmel, M., Sapra, K.T., Brunner, D., Kaech, A. and Medalia, O. 2015. Structural analysis of multicellular organisms with cryo-electron tomography. *Nature Methods*. **12**(7), pp.634–636.
- Van Harrevelde, A., Crowell, J. and Malhotra, S.K. 1965. A Study Of Extracellular Space In Central Nervous Tissue By Freeze-substitution. *The Journal of cell biology*. **25**(1), pp.117–137.
- Van Harrevelde, A. and Steiner, J. 1970. The magnitude of the extracellular space in electron micrographs of superficial and deep regions of the cerebral cortex. *Journal of Cell Science*. **6**(3), pp.793–805.
- Harris, A.Z. and Pettit, D.L. 2007. Extrasynaptic and synaptic NMDA receptors form stable and uniform pools in rat hippocampal slices. *Journal of Physiology*. **584**(2), pp.509–519.
- Harris, K.D. and Shepherd, G.M.G. 2015. The neocortical circuit: themes and variations. *Nat. Neurosci*. **18**(2), pp.170–181.
- Harris, K.M. and Weinberg, R.J. 2012. Ultrastructure of Synapses in the Mammalian Brain. *Cold Spring Harbor Perspectives in Biology*. **4**(5), p.7.
- Harrison, O.J., Jin, X., Hong, S., Bahna, F., Ahlsen, G., Brasch, J., Wu, Y., Vendome, J., Felsovalyi, K., Hampton, C.M., Troyanovsky, R.B., Ben-Shaul, A., Frank, J., Troyanovsky, S.M., Shapiro, L. and Honig, B. 2011. The extracellular architecture of adherens junctions revealed by crystal structures of type i cadherins. *Structure*. **19**(2), pp.244–256.
- Haworth, R.A. and Hunter, D.R. 1979. The Ca²⁺-induced membrane transition in mitochondria. II. Nature of the Ca²⁺ trigger site. *Archives of biochemistry and biophysics*. **195**(2), pp.460–467.

- Hebb, D.O. 1949. *The Organization of Behavior: A Neuropsychological Theory* [Online]. Wiley. [Accessed 23 August 2019]. Available from: <https://pdfs.semanticscholar.org/efee/3a0d3e8b34e45188dca4e19c15e6b6029edd.pdf>.
- Henderson, R. 1995. The potential and limitations of neutrons, electrons and X-rays for atomic resolution microscopy of unstained biological molecules. *Quarterly Reviews of Biophysics*. **28**(2), pp.171–193.
- Herculano-Houzel, S. 2009. The human brain in numbers: A linearly scaled-up primate brain. *Frontiers in Human Neuroscience*. **3**, p.31.
- Herring, B.E. and Nicoll, R.A. 2016. Long-Term Potentiation: From CaMKII to AMPA Receptor Trafficking. *Annual Review of Physiology*. **78**(1), pp.351–365.
- Heumann, J.M., Hoenger, A. and Mastronarde, D.N. 2011. Clustering and variance maps for cryo-electron tomography using wedge-masked differences. *Journal of Structural Biology*. **175**(3), pp.288–299.
- High, B., Cole, A.A., Chen, X. and Reese, T.S. 2015. Electron microscopic tomography reveals discrete transleft elements at excitatory and inhibitory synapses. *Frontiers in Synaptic Neuroscience*. **7**(JUN).
- Holtmaat, A.J.G.D., Trachtenberg, J.T., Wilbrecht, L., Shepherd, G.M., Zhang, X., Knott, G.W. and Svoboda, K. 2005. Transient and persistent dendritic spines in the neocortex in vivo. *Neuron*. **45**(2), pp.279–291.
- Honig, B. and Shapiro, L. 2020. Adhesion protein structure, molecular affinities, and principles of cell-cell recognition. *Cell*. **181**(3), p.520.
- Hopwood, D. 1969. Fixatives and fixation: a review. *The Histochemical journal*. **1**(4), pp.323–360.
- Hotulainen, P., Llano, O., Smirnov, S., Tanhuanpää, K., Faix, J., Rivera, C. and Lappalainen, P. 2009. Defining mechanisms of actin polymerization and depolymerization during dendritic spine morphogenesis. *The Journal of cell biology*. **185**(2), pp.323–339.
- Hsia, A.Y., Malenka, R.C. and Nicoll, R.A. 1998. Development of excitatory circuitry in the hippocampus. *Journal of Neurophysiology*. **79**(4), pp.2013–2024.

- Hunt, D.L. and Castillo, P.E. 2012. Synaptic plasticity of NMDA receptors: Mechanisms and functional implications. *Current Opinion in Neurobiology*. **22**(3), pp.496–508.
- Hunziker, E. and Schenk, R. 1984. Cartilage ultrastructure after high pressure freezing, freeze substitution, and low temperature embedding. II. Intercellular matrix ultrastructure - preservation of proteoglycans in their native state. *The Journal of cell biology*. **98**(1), pp.277–282.
- Husi, H., Ward, M.A., Choudhary, J.S., Blackstock, W.P. and Grant, S.G.N. 2000. Proteomic analysis of NMDA receptor-adhesion protein signaling complexes. *Nature Neuroscience*. **3**(7), pp.661–669.
- Huttenlocher, P.R. and Dabholkar, A.S. 1997. Regional differences in synaptogenesis in human cerebral cortex. *Journal of Comparative Neurology*. **387**(2), pp.167–178.
- Hyun, J.S., Inoue, T. and Hayashi-Takagi, A. 2020. Multi-Scale Understanding of NMDA Receptor Function in Schizophrenia. *Biomolecules 2020, Vol. 10, Page 1172*. **10**(8), p.1172.
- Igarashi, K.M., Lu, L., Colgin, L.L., Moser, M.B. and Moser, E.I. 2014. Coordination of entorhinal–hippocampal ensemble activity during associative learning. *Nature 2014 510:7503*. **510**(7503), pp.143–147.
- Igaz, L.M., Vianna, M.R.M., Medina, J.H. and Izquierdo, I. 2002. Two time periods of hippocampal mRNA synthesis are required for memory consolidation of fear-motivated learning. *Journal of Neuroscience*. **22**(15), pp.6781–6789.
- Imig, C., López-Murcia, F.J., Maus, L., García-Plaza, I.H., Mortensen, L.S., Schwark, M., Schwarze, V., Angibaud, J., Nägerl, U.V., Taschenberger, H., Brose, N. and Cooper, B.H. 2020. Ultrastructural Imaging of Activity-Dependent Synaptic Membrane-Trafficking Events in Cultured Brain Slices. *Neuron*. **108**(5), pp.843-860.e8.
- Imig, C., Min, S.W., Krinner, S., Arancillo, M., Rosenmund, C., Südhof, T.C., Rhee, J.S., Brose, N. and Cooper, B.H. 2014. The morphological and molecular nature of synaptic vesicle priming at presynaptic active zones. *Neuron*. **84**(2), pp.416–431.

- Ishizuka, N., Weber, J. and Amaral, D.G. 1990. Organization of intrahippocampal projections originating from CA3 pyramidal cells in the rat. *The Journal of comparative neurology*. **295**(4), pp.580–623.
- Ismailov, I., Kalikulov, D., Inoue, T. and Friedlander, M.J. 2004. The kinetic profile of intracellular calcium predicts long-term potentiation and long-term depression. *Journal of Neuroscience*. **24**(44), pp.9847–9861.
- Itskov, P.M., Vinnik, E. and Diamond, M.E. 2011. Hippocampal Representation of Touch-Guided Behavior in Rats: Persistent and Independent Traces of Stimulus and Reward Location. *PLOS ONE*. **6**(1), p.e16462.
- Itskov, P.M., Vinnik, E., Honey, C., Schnupp, J. and Diamond, M.E. 2012. Sound sensitivity of neurons in rat hippocampus during performance of a sound-guided task. *Journal of Neurophysiology*. **107**(7), pp.1822–1834.
- Jensen, E.C. 2012. Use of Fluorescent Probes: Their Effect on Cell Biology and Limitations. *The Anatomical Record: Advances in Integrative Anatomy and Evolutionary Biology*. **295**(12), pp.2031–2036.
- Johnston, D. and Amaral, D.G. 2004. Hippocampus. *The Synaptic Organization of the Brain*.
- Josselyn, S.A., Köhler, S. and Frankland, P.W. 2015. Finding the engram. *Nature Reviews Neuroscience* 2015 16:9. **16**(9), pp.521–534.
- Josselyn, S.A., Köhler, S. and Frankland, P.W. 2017. Heroes of the engram. *Journal of Neuroscience*. **37**(18), pp.4647–4657.
- Josselyn, S.A. and Tonegawa, S. 2020. Memory engrams: Recalling the past and imagining the future. *Science*. **367**(6473).
- Jung, M., Kim, D. and Mun, J.Y. 2020. Direct Visualization of Actin Filaments and Actin-Binding Proteins in Neuronal Cells. *Frontiers in Cell and Developmental Biology*. **8**, p.588556.
- Kandel, E.R. and Tauc, L. 1965. Mechanism of heterosynaptic facilitation in the giant cell of the abdominal ganglion of *Aplysia depilans*. *The Journal of physiology*. **181**(1), pp.28–47.
- Kaplan, M., Nicolas, W.J., Zhao, W., Carter, S.D., Metskas, L.A., Chreifi, G., Ghosal, D. and Jensen, G.J. 2021. In Situ Imaging and Structure Determination of Biomolecular Complexes Using Electron Cryo-

- Tomography. *Methods in molecular biology (Clifton, N.J.)*. **2215**, pp.83–111.
- Karakas, E. and Furukawa, H. 2014. Crystal structure of a heterotetrameric NMDA receptor ion channel. *Science (New York, N.Y.)*. **344**(6187), pp.992–997.
- Kaya, I., Jennische, E., Lange, S. and Malmberg, P. 2021. Multimodal chemical imaging of a single brain tissue section using ToF-SIMS, MALDI-ToF and immuno/histochemical staining. *Analyst*. **146**(4), pp.1169–1177.
- Ketschek, A. and Gallo, G. 2010. Nerve Growth Factor Induces Axonal Filopodia through Localized Microdomains of Phosphoinositide 3-Kinase Activity That Drive the Formation of Cytoskeletal Precursors to Filopodia. *The Journal of Neuroscience*. **30**(36), p.12185.
- Kim, E. and Jung, H. 2015. Local protein synthesis in neuronal axons: Why and how we study. *BMB Reports*. **48**(3), pp.139–146.
- Klann, E., Antion, M.D., Banko, J.L. and Hou, L. 2004. Synaptic plasticity and translation initiation. *Learning and Memory*. **11**(4), pp.365–372.
- Klausberger, T. and Somogyi, P. 2008. Neuronal Diversity and Temporal Dynamics: The Unity of Hippocampal Circuit Operations. *Science (New York, N.Y.)*. **321**(5885), p.53.
- Klinzing, J.G., Niethard, N. and Born, J. 2019. Mechanisms of systems memory consolidation during sleep. *Nature Neuroscience*. **22**(October).
- Knott, G., Marchman, H., Wall, D. and Lich, B. 2008. Serial Section Scanning Electron Microscopy of Adult Brain Tissue Using Focused Ion Beam Milling. *The Journal of Neuroscience*. **28**(12), p.2959.
- Knott, G.W., Holtmaat, A., Wilbrecht, L., Welker, E. and Svoboda, K. 2006. Spine growth precedes synapse formation in the adult neocortex in vivo. *Nature Neuroscience*. **9**(9), pp.1117–1124.
- Knott, G.W., Quairiaux, C., Genoud, C. and Welker, E. 2002. Formation of Dendritic Spines with GABAergic Synapses Induced by Whisker Stimulation in Adult Mice. *Neuron*. **34**(2), pp.265–273.
- Konietzny, A., González-Gallego, J., Bär, J., Perez-Alvarez, A., Drakew, A., Demmers, J.A.A., Dekkers, D.H.W., Hammer, J.A., Frotscher, M., Oertner, T.G., Wagner, W., Kneussel, M. and Mikhaylova, M. 2019.

- Myosin V regulates synaptopodin clustering and localization in the dendrites of hippocampal neurons. *Journal of Cell Science*. **132**(16).
- Koning, R.I., Zovko, S., Bárcena, M., Oostergetel, G.T., Koerten, H.K., Galjart, N., Koster, A.J. and Mieke Mommaas, A. 2008. Cryo electron tomography of vitrified fibroblasts: Microtubule plus ends in situ. *Journal of Structural Biology*. **161**(3), pp.459–468.
- Kontziampasis, D., Klebl, D.P., Iadanza, M.G., Scarff, C.A., Kopf, F., Sobott, F., Monteiro, D.C.F., Trebbin, M., Muench, S.P. and White, H.D. 2019. A cryo-EM grid preparation device for time-resolved structural studies. *IUCrJ*. **6**, pp.1024–1031.
- Korobova, F. and Svitkina, T.M. 2010. Molecular Architecture of Synaptic Actin Cytoskeleton in Hippocampal Neurons Reveals a Mechanism of Dendritic Spine Morphogenesis. *Molecular Biology of the Cell*. **21**(1), p.165.
- Korogod, N., Petersen, C.C.H. and Knott, G.W. 2015. Ultrastructural analysis of adult mouse neocortex comparing aldehyde perfusion with cryo fixation. *eLife*. **4**(AUGUST2015).
- Korzus, E., Rosenfeld, M.G. and Mayford, M. 2004. CBP histone acetyltransferase activity is a critical component of memory consolidation. *Neuron*. **42**(6), pp.961–72.
- Kremer, J.R., Mastronarde, D.N. and McIntosh, J.R. 1996. Computer visualization of three-dimensional image data using IMOD. *Journal of Structural Biology*. **116**(1), pp.71–6.
- Kühlbrandt, W. 2014. The resolution revolution. *Science*. **343**(6178), pp.1443–1444.
- Kukulski, W., Schorb, M., Welsch, S., Picco, A., Kaksonen, M. and Briggs, J.A.G. 2011. Correlated fluorescence and 3D electron microscopy with high sensitivity and spatial precision. *Journal of Cell Biology*. **192**(1), pp.111–119.
- Lai, C.S.W., Franke, T.F. and Gan, W.B. 2012. Opposite effects of fear conditioning and extinction on dendritic spine remodelling. *Nature*. **483**(7387), pp.87–92.
- Landis, D.M.D. and Reese, T.S. 1983. Cytoplasmic organization in cerebellar dendritic spines. *The Journal of cell biology*. **97**(4), pp.1169–1178.

- Lee, C., Lee, B.H., Jung, H., Choi, D. II, Park, H.Y. and Kaang
Correspondence, B.-K. 2022. Hippocampal engram networks for fear
memory recruit new synapses and modify pre-existing synapses in vivo
Spatial distribution of new E-E synapses induces clustering of engram
synapses. *Current Biology*.
- Lee, C.H., Lü, W., Michel, J.C., Goehring, A., Du, J., Song, X. and Gouaux,
E. 2014. NMDA receptor structures reveal subunit arrangement and
pore architecture. *Nature*. **511**(7508), pp.191–197.
- Lee, J.H., Kim, J. young, Noh, S., Lee, H., Lee, S.Y., Mun, J.Y., Park, H. and
Chung, W.S. 2020. Astrocytes phagocytose adult hippocampal synapses
for circuit homeostasis. *Nature*. **590**(7847), p.612.
- Lehninger, A.L. 1970. Mitochondria and calcium ion transport. *Biochemical
Journal*. **119**(2), pp.129–138.
- Leistner, C., Wilkinson, M., Burgess, A., Lovatt, M., Goodbody, S., Xu, Y.,
Deuchars, S., Radford, S.E., Ranson, N.A. and Frank, R.A.W. 2023. The
in-tissue molecular architecture of β -amyloid pathology in the
mammalian brain. *Nature Communications*. **14**(1), p.2833.
- Leone, P., Comoletti, D., Ferracci, G., Conrod, S., Garcia, S.U., Taylor, P.,
Bourne, Y. and Marchot, P. 2010. Structural insights into the exquisite
selectivity of neurexin/neuroligin synaptic interactions. *The EMBO
Journal*. **29**(14), p.2461.
- Li, Z., Okamoto, K.-I., Hayashi, Y. and Sheng, M. 2004. The Importance of
Dendritic Mitochondria in the Morphogenesis and Plasticity of Spines
and Synapses. *Cell*. **119**, pp.873–887.
- Lichtman, J.W. and Colman, H. 2000. Synapse elimination and indelible
memory. *Neuron*. **25**(2), pp.269–278.
- Linsalata, A.E., Chen, X., Winters, C.A. and Reese, T.S. 2014. Electron
tomography on γ -aminobutyric acid-ergic synapses reveals a
discontinuous postsynaptic network of filaments. *Journal of Comparative
Neurology*. **522**(4), pp.921–936.
- Liu, B., Xue, Y., Zhao, W., Chen, Y., Fan, C., Gu, L., Zhang, Y., Zhang, X.,
Sun, L., Huang, X., Ding, W., Sun, F., Ji, W. and Xu, T. 2015. Three-
dimensional super-resolution protein localization correlated with vitrified
cellular context. *Scientific Reports 2015 5:1*. **5**(1), pp.1–11.

- Liu, X., Ramirez, S., Pang, P.T., Puryear, C.B., Govindarajan, A., Deisseroth, K. and Tonegawa, S. 2012. Optogenetic stimulation of a hippocampal engram activates fear memory recall. . **484**(7394), pp.381–385.
- Liu, X., Ramirez, S. and Tonegawa, S. 2014. Inception of a false memory by optogenetic manipulation of a hippocampal memory engram. *Philosophical Transactions of the Royal Society B: Biological Sciences*. **369**(1633), p.20130142.
- López-Madróna, V.J., Matias, F.S., Pereda, E., Canals, S. and Mirasso, C.R. 2017. On the role of the entorhinal cortex in the effective connectivity of the hippocampal formation. *Chaos*. **27**(4), p.047401.
- Lovatt, M., Leistner, C. and Frank, R.A.W. 2022. Bridging length scales from molecules to the whole organism by cryoCLEM and cryoET. *Faraday discussions*.
- Lovestam, S. and Scheres, S.H.W. 2022. High-throughput cryo-EM structure determination of amyloids.
- Lučić, V., Rigort, A. and Baumeister, W. 2013. Cryo-electron tomography: The challenge of doing structural biology in situ. *Journal of Cell Biology*. **202**(3), pp.407–419.
- Lv, L., Liu, Y., Xie, J., Wu, Y., Zhao, J., Li, Q. and Zhong, Y. 2019. Interplay between α 2-chimaerin and Rac1 activity determines dynamic maintenance of long-term memory. *Nature Communications*. **10**(1).
- Di Maio, V. 2021. The glutamatergic synapse: a complex machinery for information processing. *Cognitive Neurodynamics*. **15**(5), p.757.
- Marko, M., Hsieh, C., Schalek, R., Frank, J. and Mannella, C. 2007. Focused-ion-beam thinning of frozen-hydrated biological specimens for cryo-electron microscopy. *Nature methods*. **4**(3), pp.215–217.
- Martin, J.H. and Matthews, J.L. 1969. Mitochondrial granules in chondrocytes. *Calcified Tissue Research*. **3**(1), pp.184–193.
- Martinez-Sanchez, A., Kochovski, Z., Laugks, U., Meyer zum Alten Borgloh, J., Chakraborty, S., Pfeffer, S., Baumeister, W. and Lučić, V. 2020. Template-free detection and classification of membrane-bound complexes in cryo-electron tomograms. *Nature Methods*. **17**(2), pp.209–216.

- Martinez-Sanchez, A., Laugks, U., Kochovski, Z., Papantoniou, C., Zinzula, L., Baumeister, W. and Lučić, V. 2021. Trans-synaptic assemblies link synaptic vesicles and neuroreceptors. *Science Advances*. **7**(10), pp.1–14.
- Martin-Ordas, G., Atance, C.M. and Caza, J.S. 2014. How do episodic and semantic memory contribute to episodic foresight in young children? *Frontiers in Psychology*. **5**, p.732.
- Masch, J.-M., Steffens, H., Fischer, J., Engelhardt, J., Hubrich, J., Keller-Findeisen, J., D'Este, E., Urban, N.T., Grant, S.G.N., Sahl, S.J., Kamin, D. and Hell, S.W. 2018. Robust nanoscopy of a synaptic protein in living mice by organic-fluorophore labeling. *Proceedings of the National Academy of Sciences*. **115**(34), pp.E8047–E8056.
- Masich, S., Östberg, T., Norlén, L., Shupliakov, O. and Daneholt, B. 2006. A procedure to deposit fiducial markers on vitreous cryo-sections for cellular tomography. *Journal of Structural Biology*. **156**(3), pp.461–468.
- Matsuo, N., Reijmers, L. and Mayford, M. 2008. Spine-type-specific recruitment of newly synthesized AMPA receptors with learning. *Science*. **319**(5866), pp.1104–1107.
- Matsuzaki, M., Ellis-Davies, G.C.R., Nemoto, T., Miyashita, Y., Iino, M. and Kasai, H. 2001. Dendritic spine geometry is critical for AMPA receptor expression in hippocampal CA1 pyramidal neurons. *Nature Neuroscience*. **4**(11), pp.1086–1092.
- Mattila, P.K. and Lappalainen, P. 2008. Filopodia: molecular architecture and cellular functions. *Nature Reviews Molecular Cell Biology* 2008 9:6. **9**(6), pp.446–454.
- Mattson, M.P., Gleichmann, M. and Cheng, A. 2008. Mitochondria in Neuroplasticity and Neurological Disorders. *Neuron*. **60**(5), p.748.
- Mayer, M.L. and Westbrook, G.L. 1987. Permeation and block of N-methyl-D-aspartic acid receptor channels by divalent cations in mouse cultured central neurones. *The Journal of physiology*. **394**(1), pp.501–527.
- Mayer, M.L., Westbrook, G.L. and Guthrie, P.B. 1984. Voltage-dependent block by Mg²⁺ of NMDA responses in spinal cord neurones. *Nature*. **309**(5965), pp.261–263.

- Mayford, M., Siegelbaum, S.A. and Kandel, E.R. 2012. Synapses and memory storage. *Cold Spring Harbor perspectives in biology*. **4**(6).
- Meldrum, B.S. 2000. Glutamate and Glutamine in the Brain Glutamate as a Neurotransmitter in the Brain: Review of Physiology and Pathology 1. *The Journal of Nutrition*. **130**(4), pp.1007S-1015S.
- Menna, E., Disanza, A., Cagnoli, C., Schenk, U., Gelsomino, G., Frittoli, E., Hertzog, M., Offenhauser, N., Sawallisch, C., Kreienkamp, H.J., Gertler, F.B., Di Fiore, P.P., Scita, G. and Matteoli, M. 2009. Eps8 Regulates Axonal Filopodia in Hippocampal Neurons in Response to Brain-Derived Neurotrophic Factor (BDNF). *PLoS Biology*. **7**(6), p.e1000138.
- Miller, C.A., Gavin, C.F., White, J.A., Parrish, R.R., Honasoge, A., Yancey, C.R., Rivera, I.M., Rubio, M.D., Rumbaugh, G. and Sweatt, J.D. 2010. Cortical DNA methylation maintains remote memory. *Nature Neuroscience*. **13**(6), pp.664–666.
- Mitsushima, D., Ishihara, K., Sano, A., Kessels, H.W. and Takahashi, T. 2011. Contextual learning requires synaptic AMPA receptor delivery in the hippocampus. *Proceedings of the National Academy of Sciences of the United States of America*. **108**(30), pp.12503–12508.
- Miyashita, T., Oda, Y., Horiuchi, J., Yin, J.C.P., Morimoto, T. and Saitoe, M. 2012. Mg²⁺ Block of Drosophila NMDA Receptors Is Required for Long-Term Memory Formation and CREB-Dependent Gene Expression. *Neuron*. **74**(5), pp.887–898.
- Moyer, J.R. and Brown, T.H. 1998. Methods for whole-cell recording from visually preselected neurons of perirhinal cortex in brain slices from young and aging rats. *Journal of Neuroscience Methods*. **86**(1), pp.35–54.
- Murphy, T.H., Baraban, J.M., Wier, W.G. and Blatter, L.A. 1994. Visualization of quantal synaptic transmission by dendritic calcium imaging. *Science*. **263**(5146), pp.529–532.
- Nabavi, S., Fox, R., Proulx, C.D., Lin, J.Y., Tsien, R.Y. and Malinow, R. 2014. Engineering a memory with LTD and LTP. *Nature*. **511**(7509), pp.348–352.
- Naghdi, N., Majlessi, N. and Bozorgmehr, T. 2003. The effects of anisomycin (a protein synthesis inhibitor) on spatial learning and memory in CA1

- region of rats hippocampus. *Behavioural brain research*. **139**(1–2), pp.69–73.
- Nair, D., Hosy, E., Petersen, J.D., Constals, A., Giannone, G., Choquet, D. and Sibarita, J.B. 2013. Super-Resolution Imaging Reveals That AMPA Receptors Inside Synapses Are Dynamically Organized in Nanodomains Regulated by PSD95. *Journal of Neuroscience*. **33**(32), pp.13204–13224.
- Navarro, P.P., Stahlberg, H. and Castaño-Díez, D. 2018. Protocols for Subtomogram Averaging of Membrane Proteins in the Dynamo Software Package. *Frontiers in Molecular Biosciences*. **5**, p.82.
- Neyman, S. and Manahan-Vaughan, D. 2008. Metabotropic glutamate receptor 1 (mGluR1) and 5 (mGluR5) regulate late phases of LTP and LTD in the hippocampal CA1 region in vitro. *European Journal of Neuroscience*. **27**(6), pp.1345–1352.
- Nicastro, D., Schwartz, C., Pierson, J., Gaudette, R., Porter, M.E. and McIntosh, J.R. 2006. The molecular architecture of axonemes revealed by cryoelectron tomography. *Science*. **313**(5789), pp.944–948.
- Nickel, M. and Gu, C. 2018. Regulation of Central Nervous System Myelination in Higher Brain Functions. *Neural Plasticity*. **2018**.
- Noble, A.J., Dandey, V.P., Wei, H., Brasch, J., Chase, J., Acharya, P., Tan, Y.Z., Zhang, Z., Kim, L.Y., Scapin, G., Rapp, M., Eng, E.T., Rice, W.J., Cheng, A., Negro, C.J., Shapiro, L., Kwong, P.D., Jeruzalmi, D., Georges, A. des, Potter, C.S. and Carragher, B. 2018. Routine single particle CryoEM sample and grid characterization by tomography. *eLife*. **7**.
- Nogales, E., Wolf, S.G. and Downing, K.H. 1998. Structure of the $\alpha\beta$ tubulin dimer by electron crystallography. *Nature* 1998 391:6663. **391**(6663), pp.199–203.
- Ojemann, G.A. 2003. The neurobiology of language and verbal memory: Observations from awake neurosurgery. *International Journal of Psychophysiology*. **48**(2), pp.141–6.
- Okamoto, K.I., Nagai, T., Miyawaki, A. and Hayashi, Y. 2004. Rapid and persistent modulation of actin dynamics regulates postsynaptic

- reorganization underlying bidirectional plasticity. *Nature neuroscience*. **7**(10), pp.1104–1112.
- O'Rourke, M.B., Smith, C.C., De La Monte, S.M., Sutherland, G.T. and Padula, M.P. 2019. Higher Mass Accuracy MALDI-TOF/TOF Lipid Imaging of Human Brain Tissue in Alzheimer's Disease. *Current protocols in molecular biology*. **126**(1).
- Ortega-de San Luis, C., Pezzoli, M., Urrieta, E. and Ryan, T.J. 2023. Engram cell connectivity as a mechanism for information encoding and memory function. *Current Biology*.
- Ortega-De San Luis, C. and Ryan, T.J. 2022. Understanding the physical basis of memory: Molecular mechanisms of the engram. *Journal of Biological Chemistry*. **298**(5).
- Panja, D., Dagyte, G., Bidinosti, M., Wibrand, K., Kristiansen, Å.M., Sonenberg, N. and Bramham, C.R. 2009. Novel translational control in arc-dependent long term potentiation consolidation in Vivo. *Journal of Biological Chemistry*. **284**(46), pp.31498–31511.
- Park, P., Kang, H., Sanderson, T.M., Bortolotto, Z.A., Georgiou, J., Zhuo, M., Kaang, B.-K. and Collingridge, G.L. 2019. On the Role of Calcium-Permeable AMPARs in Long-Term Potentiation and Synaptic Tagging in the Rodent Hippocampus. *Frontiers in Synaptic Neuroscience*. **11**.
- Park, P., Sanderson, T.M., Amici, M., Choi, S.L., Bortolotto, Z.A., Zhuo, M., Kaang, B.K. and Collingridge, G.L. 2016. Calcium-permeable AMPA receptors mediate the induction of the protein kinase a-dependent component of long- term potentiation in the hippocampus. *Journal of Neuroscience*. **36**(2), pp.622–631.
- Perez-Alvarez, A., Fearey, B.C., O'Toole, R.J., Yang, W., Arganda-Carreras, I., Lamothe-Molina, P.J., Moeyaert, B., Mohr, M.A., Panzera, L.C., Schulze, C., Schreiter, E.R., Wiegert, J.S., Gee, C.E., Hoppa, M.B. and Oertner, T.G. 2020. Freeze-frame imaging of synaptic activity using SynTagMA. *Nature Communications* 2020 11:1. **11**(1), pp.1–16.
- Peters, A. 1991. The fine structure of the nervous system. *Neurons and their supporting cells.*, pp.211–218.

- Peters, A., Palay, S.L., Webster, H. de F. and Delgado-Escueta, A. V. 2015. The Fine Structure of the Nervous System: Neurons and Their Supporting Cells. <https://doi.org/10.1086/417517>. **67**(1), pp.80–80.
- Petersen, J.D., Chen, X., Vinade, L., Dosemeci, A., Lisman, J.E. and Reese, T.S. 2003. Distribution of postsynaptic density (PSD)-95 and Ca²⁺/calmodulin-dependent protein kinase II at the PSD. *The Journal of neuroscience : the official journal of the Society for Neuroscience*. **23**(35), pp.11270–8.
- Pettersen, E.F., Goddard, T.D., Huang, C.C., Couch, G.S., Greenblatt, D.M., Meng, E.C. and Ferrin, T.E. 2004. UCSF Chimera--a visualization system for exploratory research and analysis. *Journal of computational chemistry*. **25**(13), pp.1605–1612.
- Peukes, J., Lovatt, M., Leistner, C., Boulanger, J., Morado, D.R., Kukulski, W., Zhu, F., Komiyama, N., Briggs, J.A.G., Grant, S.G.N. and Frank, R. 2021. The molecular infrastructure of glutamatergic synapses in the mammalian forebrain. *bioRxiv.*, 2021.02.19.432002.
- Plant, K., Pelkey, K.A., Bortolotto, Z.A., Morita, D., Terashima, A., McBain, C.J., Collingridge, G.L. and Isaac, J.T.R. 2006. Transient incorporation of native GluR2-lacking AMPA receptors during hippocampal long-term potentiation. *Nature Neuroscience*. **9**(5), pp.602–604.
- Platel, H. 2005. Functional neuroimaging of semantic and episodic musical memory. *Annals of the New York Academy of Sciences*. **1060**, pp.136–147.
- Plitzko, J., Mahamid, J., Engel, B., Albert, S., Schaffer, M., Arnold, J., Fukuda, Y., Khoshouei, M., Danev, R. and Baumeister, W. 2016. Enabling and doing structural biology in situ. *European Microscopy Congress 2016: Proceedings.*, pp.113–113.
- Poo, M. ming, Pignatelli, M., Ryan, T.J., Tonegawa, S., Bonhoeffer, T., Martin, K.C., Rudenko, A., Tsai, L.H., Tsien, R.W., Fishell, G., Mullins, C., Gonçalves, J.T., Shtrahman, M., Johnston, S.T., Gage, F.H., Dan, Y., Long, J., Buzsáki, G. and Stevens, C. 2016. What is memory? The present state of the engram. *BMC Biology*. **14**(1), p.40.
- Price, J.C., Guan, S., Burlingame, A., Prusiner, S.B. and Ghaemmaghami, S. 2010. Analysis of proteome dynamics in the mouse brain. *Proceedings*

- of the National Academy of Sciences of the United States of America.*
107(32), pp.14508–14513.
- Radecke, J., Seeger, R., Kádková, A., Laugks, U., Khosrozadeh, A., Goldie, K.N., Lučić, V., Sørensen, J.B. and Zuber, B. 2023. Morphofunctional changes at the active zone during synaptic vesicle exocytosis. *EMBO reports.*, pp.1–16.
- Rall, W., Shepherd, G., Reese, T. and Brightman, M. 1966. Dendrodendritic synaptic pathway for inhibition in the olfactory bulb. *Experimental neurology.* **14**(1), pp.44–56.
- Ramirez, S., Tonegawa, S. and Liu, X. 2014. Identification and optogenetic manipulation of memory engrams in the hippocampus. *Frontiers in behavioral neuroscience.* **7**(JAN).
- Ramón y Cajal, S. (1852-1934). A. du texte 1909. Histologie du système nerveux de l'homme et des vertébrés. Cervelet, cerveau moyen, rétine, couche optique, corps strié, écorce cérébrale générale et régionale, grand sympathique / par S. Ramon Cajal,...
- Rao-Ruiz, P., Visser, E., Mitrić, M., Smit, A.B. and van den Oever, M.C. 2021. A Synaptic Framework for the Persistence of Memory Engrams. *Frontiers in Synaptic Neuroscience.* **13**, p.13.
- Rastogi, V., Puri, N., Arora, S., Kaur, G., Yadav, L. and Sharma, R. 2013. Artefacts: A Diagnostic Dilemma – A Review. *Journal of Clinical and Diagnostic Research : JCDR.* **7**(10), p.2408.
- Redondo, R.L., Kim, J., Arons, A.L., Ramirez, S., Liu, X. and Tonegawa, S. 2014. Bidirectional switch of the valence associated with a hippocampal contextual memory engram. *Nature.* **513**(7518), pp.426–430.
- Reilly, J.E., Hanson, H.H. and Phillips, G.R. 2011. Persistence of excitatory shaft synapses adjacent to newly emerged dendritic protrusions. *Molecular and cellular neurosciences.* **48**(2), pp.129–136.
- Reth, M. 2013. Matching cellular dimensions with molecular sizes.
- Richter, K. 1994. Cutting artefacts on ultrathin cryosections of biological bulk specimens. *Micron (Oxford, England : 1993).* **25**(4), pp.297–308.
- Roy, D.S., Park, Y.G., Kim, M.E., Zhang, Y., Ogawa, S.K., DiNapoli, N., Gu, X., Cho, J.H., Choi, H., Kametsky, L., Martin, J., Mosto, O., Aida, T., Chung, K. and Tonegawa, S. 2022. Brain-wide mapping reveals that

- engrams for a single memory are distributed across multiple brain regions. *Nature Communications* 2022 13:1. **13**(1), pp.1–16.
- Ryan, T.A., Li, L., Chin, L.S., Greengard, P. and Smith, S.J. 1996. Synaptic vesicle recycling in synapsin I knock-out mice. *The Journal of Cell Biology*. **134**(5), p.1219.
- Ryan, T.J. and Frankland, P.W. 2022. Forgetting as a form of adaptive engram cell plasticity. *Nature reviews. Neuroscience*. **23**(3), pp.173–186.
- Ryan, T.J., Roy D., S., Pignatelli, M., Arons, S. and Tonegawa, S. 2015. Engram cells retain memory under retrograde amnesia. *Science*. **348**(6238), pp.1007–1014.
- Ryan, T.J., de San Luis, C.O., Pezzoli, M. and Sen, S. 2021. Engram cell connectivity: an evolving substrate for information storage. *Current Opinion in Neurobiology*. **67**, pp.215–225.
- Sakamoto, K., Karelina, K. and Obrietan, K. 2011. CREB: A multifaceted regulator of neuronal plasticity and protection. *Journal of Neurochemistry*. **116**(1), pp.1–9.
- Sanders, J., Cowansage, K., Baumgärtel, K. and Mayford, M. 2012. Elimination of dendritic spines with long-term memory is specific to active circuits. *Journal of Neuroscience*. **32**(36), pp.12570–12578.
- Santos, C.V., Rogers, S.L. and Carter, A.P. 2023. CryoET shows cofilactin filaments inside the microtubule lumen. *bioRxiv*.
- Santuy, A., Tomás-roca, L., Rodríguez, J. and González-soriano, J. 2020. Estimation of the number of synapses in the hippocampus and brain-wide by volume electron microscopy and genetic labeling.
- Savtchenko, L.P. and Rusakov, D.A. 2007. The optimal height of the synaptic cleft. *Proceedings of the National Academy of Sciences of the United States of America*. **104**(6), p.1823.
- Scala, F., Kobak, D., Bernabucci, M., Bernaerts, Y., Cadwell, C.R., Castro, J.R., Hartmanis, L., Jiang, X., LTURNUS, S., Miranda, E., Mulherkar, S., Tan, Z.H., Yao, Z., Zeng, H., Sandberg, R., Berens, P. and Tolias, A.S. 2020. Phenotypic variation of transcriptomic cell types in mouse motor cortex. *Nature* 2020 598:7879. **598**(7879), pp.144–150.
- Scarff, C.A., Fuller, M.J.G., Thompson, R.F. and Iadanza, M.G. 2018. Variations on Negative Stain Electron Microscopy Methods: Tools for

- Tackling Challenging Systems. *Journal of Visualized Experiments : JoVE*. **2018**(132), p.57199.
- Schaffer, M., Pfeffer, S., Mahamid, J., Kleindiek, S., Laugks, T., Albert, S., Engel, B., Rummel, A., Smith, A., Baumeister, W. and Plitzko, J. 2019. A cryo-FIB lift-out technique enables molecular-resolution cryo-ET within native *Caenorhabditis elegans* tissue. *Nature methods*. **16**(8), pp.757–762.
- Schikorski, T. and Stevens, C.F. 1997. Quantitative ultrastructural analysis of hippocampal excitatory synapses. *The Journal of neuroscience : the official journal of the Society for Neuroscience*. **17**(15), pp.5858–5867.
- Schindelin, J., Arganda-Carreras, I., Frise, E., Kaynig, V., Longair, M., Pietzsch, T., Preibisch, S., Rueden, C., Saalfeld, S., Schmid, B., Tinevez, J.Y., White, D.J., Hartenstein, V., Eliceiri, K., Tomancak, P. and Cardona, A. 2012. Fiji: an open-source platform for biological-image analysis. *Nature Methods* 2012 9:7. **9**(7), pp.676–682.
- Schiøtz, O.H., Kaiser, C.J.O., Klumpe, S., Morado, D.R., Poege, M., Schneider, J., Beck, F., Klebl, D.P., Thompson, C. and Plitzko, J.M. 2023. Serial Lift-Out: sampling the molecular anatomy of whole organisms. *Nature Methods* 2023., pp.1–9.
- Schuman, E. and Chan, D. 2004. Fueling Synapses. *Cell*. **119**(6), pp.738–740.
- Scoville, W.B. and Milner, B. 1957. Loss of recent memory after bilateral hippocampal lesions. *Journal of Neurology, Neurosurgery & Psychiatry*. **20**(1), pp.11–21.
- Semon, R. 1909. Die mnemischen Empfindungen in ihren Beziehungen. [Accessed 14 December 2023]. Available from: https://scholar.google.com/scholar_lookup?title=Die%20nmemischen%20Empfindungen&publication_year=1909&author=R.%20Semon.
- Shapiro, L. and Weis, W.I. 2009. Structure and Biochemistry of Cadherins and Catenins. *Cold Spring Harbor Perspectives in Biology*. **1**(3).
- Shen, K. and Meyer, T. 1999. Dynamic control of caMKII translocation and localization in hippocampal neurons by NMDA receptor stimulation. *Science*. **284**(5411), pp.162–166.

- Sheng, M. and Kim, E. 2011. The postsynaptic organization of synapses. *Cold Spring Harbor Perspectives in Biology*. **3**(12).
- Shepherd, G.M.G. and Harris, K.M. 1998. Three-Dimensional Structure and Composition of CA3→CA1 Axons in Rat Hippocampal Slices: Implications for Presynaptic Connectivity and Compartmentalization. *The Journal of Neuroscience*. **18**(20), p.8300.
- Shigeoka, T., Jung, H., Jung, J., Turner-Bridger, B., Ohk, J., Lin, J.Q., Amieux, P.S. and Holt, C.E. 2016. Dynamic Axonal Translation in Developing and Mature Visual Circuits. *Cell*. **166**(1), pp.181–192.
- Shrestha, P., Ayata, P., Herrero-Vidal, P., Longo, F., Gastone, A., LeDoux, J.E., Heintz, N. and Klann, E. 2020. Cell-type-specific drug-inducible protein synthesis inhibition demonstrates that memory consolidation requires rapid neuronal translation. *Nature neuroscience*.
- Silvester, E., Vollmer, B., Pražák, V., Vasishtan, D., Machala, E.A., Whittle, C., Black, S., Bath, J., Turberfield, A.J., Grünwald, K. and Baker, L.A. 2021. DNA origami signposts for identifying proteins on cell membranes by electron cryotomography. *Cell*. **184**(4), pp.1110-1121.e16.
- Sobolevsky, A.I., Rosconi, M.P. and Gouaux, E. 2009. X-ray structure, symmetry and mechanism of an AMPA-subtype glutamate receptor. *Nature*. **462**(7274), pp.745–756.
- Somogyi, P., Tamás, G., Lujan, R. and Buhl, E.H. 1998. Salient features of synaptic organisation in the cerebral cortex. *Brain Research Reviews*. **26**(2–3), pp.113–135.
- Sorra, K.E. and Harris, K.M. 1993. Occurrence and three-dimensional structure of multiple synapses between individual radiatum axons and their target pyramidal cells in hippocampal area CA1. *The Journal of Neuroscience*. **13**(9), p.3736.
- Spence, E.F. and Soderling, S.H. 2015. Actin Out: Regulation of the Synaptic Cytoskeleton Published.
- Squire, L.R. 2004. Memory systems of the brain: A brief history and current perspective. *Neurobiology of Learning and Memory*. **82**(3), pp.171–177.
- Stangor, C. and Walinga, J. 2014. *Introduction to Psychology - 1st Canadian Edition* 1st ed. Victoria: BC Open Text Project.

- Stassart, R.M., Möbius, W., Nave, K.A. and Edgar, J.M. 2018a. The Axon-Myelin unit in development and degenerative disease. *Frontiers in Neuroscience*. **12**(JUL), p.368527.
- Stassart, R.M., Möbius, W., Nave, K.A. and Edgar, J.M. 2018b. The Axon-Myelin unit in development and degenerative disease. *Frontiers in Neuroscience*. **12**(JUL), p.368527.
- Stewart, M.D., Li, J. and Wong, J. 2005. Relationship between Histone H3 Lysine 9 Methylation, Transcription Repression, and Heterochromatin Protein 1 Recruitment. *Molecular and Cellular Biology*. **25**(7), pp.2525–2538.
- Südhof, T.C. 2017. Leading Edge Review Synaptic Neurexin Complexes: A Molecular Code for the Logic of Neural Circuits. *Cell*. **171**(4), pp.745–769.
- Südhof, T.C. 2012. The Presynaptic Active Zone. *Neuron*. **75**(1), p.11.
- Suyama, S., Hikima, T., Sakagami, H., Ishizuka, T. and Yawo, H. 2007. Synaptic vesicle dynamics in the mossy fiber-CA3 presynaptic terminals of mouse hippocampus. *Neuroscience Research*. **59**(4), pp.481–490.
- Syková, E. and Nicholson, C. 2008. Diffusion in brain extracellular space. *Physiological Reviews*. **88**(4), pp.1277–1340.
- Szule, J.A., Harlow, M.L., Jung, J.H., De-Miguel, F.F., Marshall, R.M. and McMahan, U.J. 2012. Regulation of synaptic vesicle docking by different classes of macromolecules in active zone material. *PloS one*. **7**(3).
- Tabone, C.J. and Ramaswami, M. 2012. Is NMDA Receptor-Coincidence Detection Required for Learning and Memory? *Neuron*. **74**(5), pp.767–769.
- Tamada, H., Blanc, J., Korogod, N., Petersen, C.C. and Knott, G.W. 2020. Ultrastructural comparison of dendritic spine morphology preserved with cryo and chemical fixation. *eLife*. **9**, pp.1–15.
- Tanaka, K.Z., Pevzner, A., Hamidi, A.B., Nakazawa, Y., Graham, J. and Wiltgen, B.J. 2014. Cortical Representations Are Reinstated by the Hippocampus during Memory Retrieval. *Neuron*. **84**(2), pp.347–354.
- Tang, A.H., Chen, H., Li, T.P., Metzbower, S.R., MacGillavry, H.D. and Blanpied, T.A. 2016. A transsynaptic nanocolumn aligns neurotransmitter release to receptors. *Nature*. **536**(7615), p.210.

- Tao, C.-L., Liu, Y.-T., Sun, R., Zhang, B., Qi, L., Shivakoti, S., Tian, C.-L., Zhang, P., Lau, P.-M., Zhou, Z.H. and Bi, G.-Q. 2018. Differentiation and Characterization of Excitatory and Inhibitory Synapses by Cryo-electron Tomography and Correlative Microscopy. *The Journal of neuroscience : the official journal of the Society for Neuroscience*. **38**(6), pp.1493–1510.
- Tao, S., Wang, Y., Peng, J., Zhao, Y., He, X., Yu, X., Liu, Q., Jin, S. and Xu, F. 2021. Whole-Brain Mapping the Direct Inputs of Dorsal and Ventral CA1 Projection Neurons. *Frontiers in Neural Circuits*. **15**, p.643230.
- Thompson, R.F., Walker, M., Siebert, C.A., Muench, S.P. and Ranson, N.A. 2016. An introduction to sample preparation and imaging by cryo-electron microscopy for structural biology. *Methods (San Diego, Calif.)*. **100**, p.3.
- Ting, J.T., Lee, B.R., Chong, P., Soler-Llavina, G., Cobbs, C., Koch, C., Zeng, H. and Lein, E. 2018. Preparation of Acute Brain Slices Using an Optimized N-Methyl-D-glucamine Protective Recovery Method. *Journal of visualized experiments : JoVE*. (132).
- Tonegawa, S., Pignatelli, M., Roy, D.S. and Ryan, T.J. 2015. Memory engram storage and retrieval. *Current opinion in neurobiology*. **35**, pp.101–109.
- Tremblay, R., Lee, S. and Rudy, B. 2016. GABAergic interneurons in the neocortex: from cellular properties to circuits. *Neuron*. **91**(2), pp.260–292.
- Trotter, J.H., Hao, J., Maxeiner, S., Tsetsenis, T., Liu, Z., Zhuang, X. and Südhof, T.C. 2019. Synaptic neurexin-1 assembles into dynamically regulated active zone nanoclusters. *The Journal of Cell Biology*. **218**(8), p.2677.
- Tu, L., Zhang, N., Conde, K.M., Bean, J.C., Wang, C. and Xu, Y. 2021. Free-floating Immunostaining of Mouse Brains. *Journal of visualized experiments : JoVE*. (176).
- Tuijtel, M.W., Koster, A.J., Faas, F.G.A. and Sharp, T.H. 2019. Correlated Cryo Super-Resolution Light and Cryo-Electron Microscopy on Mammalian Cells Expressing the Fluorescent Protein rsEGFP2. *Small Methods*., p.1900425.
- Tullis, J.E., Larsen, M.E., Rumian, N.L., Freund, R.K., Boxer, E.E., Brown, C.N., Coultrap, S.J., Schulman, H., Aoto, J., Dell'Acqua, M.L. and Bayer,

- K.U. 2023. LTP induction by structural rather than enzymatic functions of CaMKII. *Nature* 2023., pp.1–8.
- Turrigiano, G. 2012. Homeostatic synaptic plasticity: Local and global mechanisms for stabilizing neuronal function. *Cold Spring Harbor Perspectives in Biology*. **4**(1), p.a005736.
- Valtonen, J., Gregory, E., Landau, B. and McCloskey, M. 2014. New learning of music after bilateral medial temporal lobe damage: evidence from an amnesic patient. *Frontiers in human neuroscience*. **8**, p.694.
- Végh, M.J., Heldring, C.M., Kamphuis, W., Hijazi, S., Timmerman, A.J., Li, K.W., van Nierop, P., Mansvelter, H.D., Hol, E.M., Smit, A.B. and van Kesteren, R.E. 2014. Reducing hippocampal extracellular matrix reverses early memory deficits in a mouse model of Alzheimer's disease. *Acta Neuropathologica Communications*. **2**(1), p.76.
- Vetere, G., Kenney, J.W., Tran, L.M., Xia, F., Steadman, P.E., Parkinson, J., Josselyn, S.A. and Frankland, P.W. 2017. Chemogenetic Interrogation of a Brain-wide Fear Memory Network in Mice. *Neuron*. **94**(2), pp.363-374.e4.
- Vilas, J.L., Oton, J., Messaoudi, C., Melero, R., Conesa, P., Ramirez-Aportela, E., Mota, J., Martinez, M., Jimenez, A., Marabini, R., Carazo, J.M., Vargas, J. and Sorzano, C.O.S. 2020. Measurement of local resolution in electron tomography. *Journal of Structural Biology: X*. **4**, p.100016.
- Vyleta, N.P., Borges-Merjane, C. and Jonas, P. 2016. Plasticity-dependent, full detonation at hippocampal mossy fiber-CA3 pyramidal neuron synapses. *eLife*. **5**(OCTOBER2016).
- Wakayama, S., Kiyonaka, S., Arai, I., Kakegawa, W., Matsuda, S., Ibata, K., Nemoto, Y.L., Kusumi, A., Yuzaki, M. and Hamachi, I. 2017. Chemical labelling for visualizing native AMPA receptors in live neurons. *Nature Communications*. **8**, p.14850.
- Watanabe, S. 2016. Flash-and-freeze: Coordinating optogenetic stimulation with rapid freezing to visualize membrane dynamics at synapses with millisecond resolution. *Frontiers in Synaptic Neuroscience*. **8**(24), p.eCollection2016.

- Willuhn, I. and Steiner, H. 2009. Skill-memory consolidation in the striatum: Critical for late but not early long-term memory and stabilized by cocaine. *Behavioural brain research*. **199**(1), p.103.
- Wolf, S.G., Mutsafi, Y., Dadosh, T., Ilani, T., Lansky, Z., Horowitz, B., Rubin, S., Elbaum, M. and Fass, D. 2017. 3D visualization of mitochondrial solid-phase calcium stores in whole cells. *eLife*. **6**, pp.1–18.
- Woodward, C.L., Mendonça, L.M. and Jensen, G.J. 2015. Direct visualization of vaults within intact cells by electron cryo-tomography. *Cellular and Molecular Life Sciences*. **72**(17), pp.3401–3409.
- Wu, G.-H., Smith-Geater, C., Galaz-Montoya, J.G., Gu, Y., Gupte, S.R., Aviner, R., Mitchell, P.G., Hsu, J., Miramontes, R., Wang, K.Q., Geller, N.R., Hou, C., Danita, C., Joubert, L.-M., Schmid, M.F., Yeung, S., Frydman, J., Mobley, W., Wu, C., Thompson, L.M. and Chiu, W. 2023. CryoET reveals organelle phenotypes in huntington disease patient iPSC-derived and mouse primary neurons. *Nature Communications*. **14**(1), p.692.
- Yang, G., Pan, F. and Gan, W.B. 2009. Stably maintained dendritic spines are associated with lifelong memories. *Nature*. **462**(7275), pp.920–924.
- Yang, N., Chen, Y.B. and Zhang, Y.F. 2023. The rearrangement of actin cytoskeleton in mossy fiber synapses in a model of experimental febrile seizures. *Frontiers in Neurology*. **14**, pp.1107538–1107538.
- Yao, P.J., Eren, E., Petralia, R.S., Gu, J.W., Wang, Y.X. and Kapogiannis, D. 2020. Mitochondrial Protrusions in Neuronal Cells. *iScience*. **23**(9), p.101514.
- Yelshanskaya, M. V., Li, M. and Sobolevsky, A.I. 2014. Structure of an agonist-bound ionotropic glutamate receptor. *Science*. **345**(6200), pp.100–1074.
- Yoon, Y.J., Wu, B., Buxbaum, A.R., Das, S., Tsai, A., English, B.P., Grimm, J.B., Lavis, L.D. and Singer, R.H. 2016. Glutamate-induced RNA localization and translation in neurons. *Proceedings of the National Academy of Sciences of the United States of America*. **113**(44), pp.E6877–E6886.

- Yu, X. and Zuo, Y. 2014. Two-photon in vivo imaging of dendritic spines in the mouse cortex using a thinned-skull preparation. *Journal of Visualized Experiments*. (87), p.51520.
- Yuste, R. and Bonhoeffer, T. 2004. Genesis of dendritic spines: insights from ultrastructural and imaging studies. *Nature Reviews Neuroscience* 2004 5:1. **5**(1), pp.24–34.
- Zhang, D., Ivica, J., Krieger, J.M., Ho, H., Yamashita, K., Stockwell, I., Baradaran, R., Cais, O. and Greger, I.H. 2023. Structural mobility tunes signalling of the GluA1 AMPA glutamate receptor. *Nature* 2023., pp.1–6.
- Zhang, K. 2016. Gctf: Real-time CTF determination and correction. *Journal of Structural Biology*. **193**(1), p.1.
- Zheng, S., Wolff, G., Greenan, G., Chen, Z., Faas, F.G.A., Bárcena, M., Koster, A.J., Cheng, Y. and Agard, D.A. 2022. AreTomo: An integrated software package for automated marker-free, motion-corrected cryo-electron tomographic alignment and reconstruction. *Journal of Structural Biology: X*. **6**.
- Zhu, F., Cizeron, M., Qiu, Z., Benavides-Piccione, R., Kopanitsa, M. V., Skene, N.G., Koniaris, B., DeFelipe, J., Fransén, E., Komiyama, N.H. and Grant, S.G.N. 2018. Architecture of the Mouse Brain Synaptome. *Neuron*. **99**(4), pp.781-799.e10.
- Zhu, S., Stein, R., Yoshioka, C., Lee, C., Goehring, A., Mchaourab, H. and Gouaux, E. 2016. Mechanism of NMDA Receptor Inhibition and Activation. *Cell*. **165**(3), pp.704–714.
- Zhu, Y., Uytiepo, M., Bushong, E., Haberl, M., Beutter, E., Scheiwe, F., Zhang, W., Chang, L., Luu, D., Chui, B., Ellisman, M. and Maximov, A. 2021. Nanoscale 3D EM reconstructions reveal intrinsic mechanisms of structural diversity of chemical synapses. *Cell Reports*. **35**(1), p.108953.
- Zuber, B. and Lučić, V. 2019. Molecular architecture of the presynaptic terminal. *Current Opinion in Structural Biology*. **54**, pp.129–138.
- Zuber, B., Nikonenko, I., Klauser, P., Muller, D. and Dubochet, J. 2005. The mammalian central nervous synaptic cleft contains a high density of periodically organized complexes. *Proceedings of the National Academy of Sciences of the United States of America*. **102**(52), pp.19192–19197.